Tunisian Republic
Ministry of Higher Education,
Scientific Research
and Technology

University of Sfax
National Engineering School of Sfax



Doctoral School
Sciences and Technologies

DOCTORAL THESIS

Electrical Engineering
Order No.: 69 - 2016

THESIS

Submitted to

The National Engineering School of Sfax

For the award of the

DOCTORATE

In the discipline of Electrical Engineering

By

Ferdaous MASMOUDI

(Master's Degree in Electrical Energy Conversion and Renewable Energy)

Optimization of Stand-Alone Photovoltaic Systems

Defended on December 31, 2016, before the jury composed of:

Mr.	**Abdessatar GUERMAZI**	(Professor)	Chair
Mr.	**Mohamed Nejib MANSOURI**	(Associate Professor)	Reviewer
Mr.	**Abderrazak YANGUI**	(Associate Professor)	Reviewer
Mr.	**Mohamed Ben Ali KAMMOUN**	(Professor)	Examiner
Mr.	**Nabil DERBEL**	(Professor)	Examiner
Mr.	**Hafedh TRABELSI**	(Professor)	Thesis Supervisor

University of Sfax
National Engineering School of Sfax *ENIS*
Doctoral School of Sciences and Technologies *EDST*
Control and Energy Management Laboratory *CEMLab*
ENIS, Route de Soukra km 2.5, P.O. Box 1173 - 3038, Sfax, Tunisia
Tel.: +216 74 274 418
Fax: +216 74 275 595
http://www.enis.rnu.tn
http://www.enis.rnu.tn/EDST/index1.php
http://www.cem-lab.info/
https://www.researchgate.net/profile/Ferdaous_Masmoudi
Copyright © Ferdaous MASMOUDI, 2016
Order No.: 69–2016

© Ferdaous Masmoudi, 2016 – All rights reserved

This manuscript was written using LaTeX

Dedication

To my husband ***Zied*** and my son ***Adem***,

to my parents ***Younès*** and ***Hajer***,

to my parents-in-law ***Abd El Waheb*** and ***Ratiba***,

to my sister ***Siwar*** and my brother ***Firas***,

to the ***Masmoudi*** & ***Loukil*** families

and to all those who are dear to me...

© Ferdaous Masmoudi, 2016 – All rights reserved

Acknowledgments

My doctoral research work entitled "Optimization of Stand-Alone Photovoltaic Systems" was carried out within the framework of the Doctoral School of Sciences and Technologies *EDST*, at the Control and Energy Management Laboratory *CEM-LAB* of the National Engineering School of Sfax *ENIS*. I would like to thank the Director of CEM-LAB, ***Mohamed CHTOUROU***, for the trust he placed in me.

I am deeply grateful for the honor bestowed upon me by Professor ***Abdessatar GUERMAZI***, Professor at ENIS, by accepting to chair the jury of my doctoral thesis defense. I express my sincere thanks to him for the interest he has shown in this work.

My gratitude and sincere thanks are addressed to Professor ***Mohamed Nejib MANSOURI***, Associate Professor at the National Engineering School of Monastir and CEO of the ECO Park of BORJ CEDRIA, for accepting to evaluate this work and to participate as a reviewer.

I am very honored that Professor ***Abderrazak YANGUI***, Associate Professor at ENIS, accepted the responsibility of reviewing and evaluating this work. I warmly thank him for his dedication.

I express my sincere thanks to Professor ***Mohamed Ben Ali Kammoun*** of ENIS for accepting to participate in my jury as an examiner. I wish to express to him my deepest respect.

I would like to thank Professor ***Nabil DERBEL*** of ENIS for the honor he has given me by agreeing to examine this thesis. I hereby express my profound gratitude to him.

© Ferdaous Masmoudi, 2016 – All rights reserved

The research project was supervised by Professor ***Hafedh TRABELSI***, Professor at ENIS, to whom I would like to express my deepest gratitude. I sincerely thank him for his constant professional support throughout the development of this work. His advice, his scientific and human qualities, his open-mindedness, the enthusiasm he was able to convey to me, as well as the trust he placed in me, enabled me to accomplish my work under the best possible conditions.

I would especially like to thank Dr. ***Fatma BEN SALEM***, Associate Professor at ISGIS, for the quality of her collaboration, her advice, her human qualities, and the friendly manner in which she supported this work.

I would like to express my sincere thanks to Mr. ***Samir AYEDI***, technician at the Electrical Engineering Laboratory, for the help and support he provided me. I also thank all the staff members and technicians of the Electrical Engineering Department at ENIS.

I also thank all the doctoral students, *Rabeb ABID*, *Jihen LOUKIL*, *Faten AYADI*, *Nesrine BOUJELBEN*, and Dr. *Fatma ABDELHEDI*, with whom I had the opportunity to share and exchange many ideas.

To all the people (the list is too long), whether or not they belong to the CEM-Lab family, who contributed, directly or indirectly, closely or remotely, to the completion of this work, I hereby express my profound gratitude.

Any errors and inconsistencies remain my own.

Sfax, December 31, 2016

Ferdaous MASMOUDI

© Ferdaous Masmoudi, 2016 – All rights reserved

About the Manuscript

This work aims to cover the relevant aspects required to provide an overview of stand-alone photovoltaic systems, with particular emphasis on methods for optimizing the efficiency of photovoltaic conversion chains.

First, a general introduction presents the global situation of renewable energies, particularly photovoltaic energy, worldwide and in Tunisia. It is followed by a general description of the research problem addressed in this work. Then, a significant part is devoted to presenting the state of the art related to the fundamentals of photoelectric conversion and the operating modes of the photovoltaic solar cell.

The work presented in this thesis is structured around three main axes. The first axis is devoted to the study of the photovoltaic generator. Mathematical models of the photovoltaic solar cell were developed and identified using algorithms for estimating the internal parameters of each model, followed by a comparative analysis of the performance of the different models. This study is complemented by the modeling of solar-cell associations allowing the formation of photovoltaic modules and panels. The simulation results of the photovoltaic generator were validated through experimental tests carried out on a typical monocrystalline solar cell as well as on a 50 W monocrystalline solar module.

The second part is devoted to optimizing the efficiency of the photovoltaic module by improving its wiring and optimizing its orientation with respect to solar radiation. In this context, a detailed study of a solar-trajectory tracking system, referred to as a "solar tracking system" or "solar tracker", motorized along two axes and controlled by a microcontroller, is presented. This system is designed to support a 50 W solar module and move it in order to maintain an orientation orthogonal to the solar radiation, thereby making it possible to fully exploit the solar resource available in the environment.

The third part is devoted to the design and sizing of the charge controller. It integrates the DC–DC conversion stage (chopper), which ensures adaptation between the source and the load, the MPPT control enabling optimization of the efficiency of the conversion system, as well as a battery supervision system intended to improve the performance of the storage system.

Finally, a significant part of this thesis is devoted to experimental work related to the designed system. The practical implementation made it possible to validate the theoretical studies and simulation results through the implementation of a prototype of a photovoltaic power-supply chain optimized by a charge controller and a solar tracker.

© Ferdaous Mesmoudi, 2016 – All rights reserved

Contents

Introduction **1**

1 General Overview of Renewable Energy 1

1 .1 Overview of the Current State of Renewable Photovoltaic Energy Worldwide and in Tunisia 2

2 Motivations and Objectives 5

2 .1 Motivations 5

2 .2 Objectives 6

2 .3 Project Limitations 7

2 .4 Main Contributions 7

3 Structure of this Manuscript 8

3 .1 Tools Used 9

3 .2 List of Publications Resulting from this Thesis 10

I The Photovoltaic Generator: Overview, Structures and Operating Modes **11**

I.1 Introduction 12

I.2 Overview of the Photovoltaic Solar Cell 12

I.2 .1 History of the Solar Cell 12

I.2 .2 Solar-Cell Technologies 14

I.2 .3 Application Areas 16

I.3 Structure and Operating Modes of the Solar Cell 18

I.3 .1 Structure of the Solar Cell 19

© Ferdaous Masmoudi, 2016 – All rights reserved

I.3 .2 Operating Modes of the Solar Junction 20
I.3 .3 Electrical Losses in the Solar Cell 24
I.4 Parameters and Characteristics of a Solar Cell 25
I.4 .1 Reference and Operating Systems 25
I.4 .2 Electrical Parameters of the Solar Cell 26
I.4 .3 Test Conditions and Manufacturer Data 27
I.5 Effect of Irradiance and Temperature on Solar-Cell Performance 30
I.5 .1 Effect of Irradiance 30
I.5 .2 Effect of Temperature 31
I.6 Conclusion 31

II Modeling of the Photovoltaic Solar Cell 33

II.1 Introduction 34
II.2 Methods and Experiments 35
II.2 .1 Principle of the Internal-Parameter Identification Procedure 35
II.2 .2 Principle of the Curve-Fitting Procedure 37
II.2 .3 Experimental Measurements of the Solar Cell 38
II.3 Ideal Model 40
II.3 .1 Algorithm for Identifying the Unknown Parameters of the Ideal Model . . 40
II.3 .2 Identification Results of the Ideal-Model Parameters under STC 42
II.3 .3 Effect of Temperature and Irradiance on the Internal Parameters of the Ideal Model 43
II.4 One-Series-Resistance Model: Simplified One-Diode Model 45
II.4 .1 Algorithm for Identifying the Unknown Parameters of the Simplified Model 46
II.4 .2 Identification Results of the One-Series-Resistance Model Parameters under STC 49

© Ferdaous Masmoudi 2016 – All rights reserved

II.4 .3 Effect of Temperature and Irradiance on the Internal Parameters of the One-Series-Resistance Model 50
II.5 One-Diode Model 51
II.5 .1 Algorithm for Identifying the Unknown Parameters of the One-Diode Model 52
II.5 .2 Identification Results of the One-Diode Model Parameters under STC . . 55
II.5 .3 Effect of Temperature and Irradiance on the Internal Parameters of the One-Diode Model 56
II.6 Two-Diode Model 58
II.6 .1 Algorithm for Identifying the Unknown Parameters of the Two-Diode Model 59
II.6 .2 Identification Results of the Two-Diode Model Parameters under STC . . 62
II.6 .3 Effect of Temperature and Irradiance on the Internal Parameters of the Two-Diode Model 63
II.7 Multiple-Diode Models: Three-Diode Case 65
II.7 .1 Search for Unknown Parameters Using the Genetic Algorithm 67
II.7 .2 Search for Unknown Parameters Using the Evolved Gradient Algorithm . 68
II.7 .3 Search Results for the Three-Diode Model Parameters under STC 68
II.7 .4 Effect of Temperature and Irradiance on the Internal Parameters of the One-Diode Model 69
II.8 Simulation Results and Experimental Validation 72
II.8 .1 Comparison of the Solar-Cell Models under STC 73
II.8 .2 Comparison of the Solar-Cell Models outside STC 74
II.8 .3 General Evaluation of the Solar-Cell Models 74
II.8 .4 Effect of Temperature and Irradiance on Solar-Cell Efficiency 75
II.9 Conclusion 77

III Optimal Association and Operation of Solar Cells and Modules 78

III.1 Introduction 79

© Ferdaous Mamoudi, 2016 – All rights reserved

III.2 Associations of Photovoltaic Solar Cells and Modules 80
III.2 .1 Composition of a PV Solar Module 81
III.2 .2 Series Association of Solar Cells 84
III.2 .3 Parallel Association of Solar Cells 85
III.2 .4 Mixed Association of Solar Cells 86
III.2 .5 Characterization of the 50 W Monocrystalline Solar Module Used 87
III.3 Problems Causing PV-Module Losses 88
III.3 .1 Uniform and Partial Shading 89
III.3 .2 Solar-Module Losses Due to the Mismatch Effect 91
III.3 .3 Role of the “Bypass” Diode 94
III.3 .4 Simulation of Total and Partial Shading Effects on a Photovoltaic Solar Module 94
III.4 Solar Resource and Sun-Path Tracking 96
III.4 .1 Solar Resource in Tunisia and Sfax 97
III.4 .2 Sun Motion and Position 99
III.4 .3 Solar Irradiance on Horizontal and Inclined Planes 102
III.4 .4 Simulation of Solar-Tracker Efficiency 104
III.5 Design and Implementation of the Two-Axis Solar Tracker 107
III.5 .1 Description of the Mechanical Structure 107
III.5 .2 Description of the Electrical System 108
III.5 .3 Solar-Tracker Programming Algorithm 109
III.6 Conclusion 111

IV Optimal Design of the Stand-Alone Photovoltaic Conversion and Storage System **112**

IV.1 Introduction 113
IV.2 Principle of Photovoltaic Power Optimization 113

© Ferdaous Mamoudi, 2016 – All rights reserved

IV.3 Characterization of the PV Source and the Load 116
IV.3 .1 Characterization of the PV Source 116
IV.3 .2 Load Characterization 118
IV.4 Characterization and Observation of the Storage System 120
IV.4 .1 Presentation of the Storage Element: 120
IV.4 .2 Presentation of the Battery Model and Identification of Its Parameters . . 121
IV.4 .3 Battery Observation System: 126
IV.5 Design, Modeling, and Sizing of the DC–DC Converter 127
IV.5 .1 Optimal Sizing of Power Converters 127
IV.5 .2 Design of the PV Conversion Chain Using a Boost Converter 130
IV.6 Design and Modeling of the MPPT Control 139
IV.7 Principle of the MPPT Control Strategy 139
IV.7 .1 P&O-Type MPPT Control 140
IV.7 .2 Simulation of the PV Conversion Chain Controlled by the P&O-Type MPPT Strategy 142
IV.8 Conclusion 147

V Experimental Work and Results **148**

V.1 Introduction 149
V.2 Dual-axis solar-tracking system 150
V.2 .1 Real-time data acquisition and conditioning 150
V.2 .2 System installation and experimental results 151
V.3 Charge-control system 152
V.3 .1 Design and implementation of the printed circuit board 153
V.3 .2 Experimental tests 155
V.4 Conclusion 157

Conclusion **158**

© Ferdaous Mastoudi, 2016 – All rights reserved

1 Summary of the Work 158

2 Main Results 159

3 Perspectives 160

© Ferdaous Masmoudi, 2016 – All rights reserved

List of Tables

1 Renewable energy production in Tunisia in 2013.[5] 4

I.1 Chronology of solar-cell development. 13

I.2 Various applications of PV energy.[3, 5, 70] 18

I.3 Specifications of the Standard Test Conditions 28

I.4 Specifications of the Nominal Operating Conditions 28

I.5 Electrical specifications of the "JAC M5SF-2" solar cell under STC 29

II.1 Internal-parameter results for the JAC M5SF-2 cell under STC using the ideal model. 42

II.2 Internal-parameter results for the JAC M5SF-2 cell under STC using the one-series-resistance model. 50

II.3 Internal-parameter results for the JAC M5SF-2 cell under STC using the one-diode model. 55

II.4 Internal-parameter results for the JAC M5SF-2 cell under STC using the two-diode model. 62

II.5 Internal-parameter results for the JAC M5SF-2 cell under STC using the triple-diode model. 69

II.6 Comparison between the simulation characteristics and the reference characteristic. 73

II.7 Evaluation of the monocrystalline solar-cell models. 74

III.1 Technical specifications of the 50 W solar module under STC 87

III.2 Example of shading-factor evaluation 95

© Ferdaous Masmoudi, 2016 _ All rights reserved

III.3 Comparison between the different types of solar-module orientation 105

IV.1 Evaluation of R_m in the vicinity of the MPP of the 50 W solar module under STC ($G = 1000W/m^2$ and $T = 25°C$). 118

IV.2 Comparison of the characteristics of various well-known battery technologies [96]. 121

IV.3 Electrical specifications of the "Power Kingdom PS7-12" Lead-Acid battery. . . . 123

IV.4 Results of the parameter-extraction methods for the "Power Kingdom PS7-12" Lead-Acid battery. 125

IV.5 Electrical diagrams of the converter topologies considered. [104] 128

IV.6 State matrices of the converter topologies considered [104]. 130

IV.7 Mathematical expressions of the parameters of the different converter topologies considered [104]. 131

IV.8 Numerical calculation of the parameters of the different converter topologies studied. 131

© Ferdaous Masmoudi, 2016 - All rights reserved

List of Figures

1 Evolution of PV energy worldwide. (a) annually installed power (GW). (b) cumulative power (GW).[3] IEA-PVPS: member countries of the PVPS program of the International Energy Agency IEA. 2

2 Global production of PV solar modules worldwide in 2014 (48 961 MW). (a) By country. (b) By technology. (c) By manufacturer.[4] 3

3 Autonomous Mobile Robot Design. (a) Compact drawing. (b) Exploded drawing. 6

4 Synoptic diagram of the PV solar-energy supply system. 6

I.1 Development of silicon-junction quality. 14

I.2 Development of solar-cell efficiency records over the last 40 years (source: NREL). 15

I.3 Architecture of the different types of PV chains: (a) Direct Coupling. (b) Stand-Alone System. (c) Grid-Connected System. (d) Hybrid System. 17

I.4 Section of a typical solar cell. (a) Perspective diagram. (b) Cross section. [7] . . 19

I.5 Electrical losses in the solar cell. 24

I.6 Four-quadrant $(I-V)$ characteristics of the solar cell according to the reference system. (a) Load reference system. (b) Generator reference system. 25

I.7 Characteristic of a solar cell in the dark and under illumination. 26

I.8 Manufacturer electrical $(I-V)$ characteristic of the "JAC M5SF-2" solar cell under STC. 29

I.9 Electrical $(I-V)$ characteristics of the "JAC M5SF-2" solar cell under several climatic conditions. 30

II.1 Key points of the solar-cell $(I-V)$ characteristic. 36

© Ferdaous Masmoudi, 2016 – All rights reserved

II.2 Explanatory diagram of the curve-fitting method. 38
II.3 Explanatory diagram of the measurement method for the "JAC M5SF-2" solar cell. 39
II.4 Experimental test bench of the "JAC M5SF" solar cell. 39
II.5 Equivalent electrical circuit of the ideal model. 40
II.6 Search algorithm for the internal parameters of the ideal model. 42
II.7 Variations of the internal parameters of the ideal model of the JAC M5SF-2 solar cell as functions of temperature and irradiance. (a) Variation of n as a function of temperature. (b) Variation of I_s as a function of temperature. (c) Variation of I_{ph} as a function of temperature and irradiance. 45
II.8 Equivalent electrical circuit of the one-series-resistance model. 45
II.9 Search algorithm for the internal parameters of the one-series-resistance, one-diode, and two-diode models. 49
II.10 Variations of the internal parameters of the one-series-resistance model of the JAC M5SF-2 solar cell as functions of temperature and irradiance. (a) Variation of n as a function of temperature. (b) Variation of I_s as a function of temperature. (c) Variation of R_s as a function of temperature. (d) Variation of I_{ph} as a function of temperature and irradiance. 51
II.11 Equivalent electrical circuit of the one-diode model. 52
II.12 Variations of the internal parameters of the one-diode model of the JAC M5SF-2 solar cell as functions of temperature and irradiance. (a) Variation of n as a function of temperature. (b) Variation of I_s as a function of temperature. (c) Variation of R_s as a function of temperature. (d) Variation of R_{sh} as a function of temperature. (e) Variation of I_{ph} as a function of temperature and irradiance. 57
II.13 Equivalent electrical circuit of the two-diode model. 58

© Ferdaous Mamoudi, 2016 – All rights reserved

II.14 Variations of the internal parameters of the two-diode model of the JAC M5SF-2 solar cell as functions of temperature and irradiance. (a) Variation of I_{s1} as a function of temperature. (b) Variation of I_{s2} as a function of temperature. (c) Variation of n_2 as a function of temperature. (d) Variation of R_s as a function of temperature. (e) Variation of R_{sh} as a function of temperature. (f) Variation of I_{ph} as a function of temperature and irradiance. 64

II.15 Equivalent electrical circuits: (a) three-diode model. (b) multi-diode model. . . 65

II.16 Genetic algorithm. 67

II.17 Evolved gradient algorithm. 68

II.18 Variation of I_{ph} as a function of temperature and irradiance using the evolved gradient algorithm. 70

II.19 Variations of the internal parameters of the three-diode model of the JAC M5SF-2 solar cell as functions of temperature. (a) Variation of n_1 as a function of temperature. (b) Variation of I_{s1} as a function of temperature. (c) Variation of n_2 as a function of temperature. (d) Variation of I_{s2} as a function of temperature. (e) Variation of n_3 as a function of temperature. (f) Variation of I_{s3} as a function of temperature. (g) Variation of R_{sh} as a function of temperature. (h) Variation of R_s as a function of temperature. 71

II.20 Example of implementation of the solar-cell model in the MATLAB-Simulink environment: triple-diode model. 72

II.21 Comparison between the different models and the reference curve: (a) $(I-V)$ characteristic. (b) $(P-V)$ characteristic. 73

II.22 Comparison between the different models and the experimental curve: (a) $(I-V)$ characteristic. (b) $(P-V)$ characteristic. 74

II.23 Effect of irradiance variation on the solar-cell characteristics: (a) $(I-V)$ characteristic. (b) $(P-V)$ characteristic. 76

© Ferdaous Mamoudi, 2016 – All rights reserved

II.24 Effect of temperature variation on the solar-cell characteristics: (a) $(I-V)$ characteristic. (b) $(P-V)$ characteristic. 77

III.1 Main factors leading to the degradation of PV-generator efficiency. 79

III.2 Illustrations of (a) a solar cell, (b) a solar module, (c) a solar panel, and (d) a solar array. 81

III.3 Illustrations of a typical solar module. (a) Module composition. (b) Electrical interconnections of the cells. 82

III.4 Illustration and demonstration of a series association of N_s solar cells. 85

III.5 Illustration and demonstration of a parallel association of N_p solar cells. 86

III.6 Illustration of a mixed association of $N_s \times N_p$ solar cells. 87

III.7 50 W solar module used. (a) Experimental test bench. (b) Comparison between experimental and simulated electrical characteristics. 88

III.8 Illustrations of solar cells under different irradiance conditions. 89

III.9 Illustration of the mismatch effect on two solar cells connected in series. 91

III.10 Electrical characteristics of mismatch between two solar cells connected in series. (a) $(I-V)$ characteristics. (b) $(P-V)$ characteristics. 92

III.11 Illustration of the "Hot-spot" phenomenon. 92

III.12 Illustration of the mismatch effect on two solar cells connected in parallel. . . . 93

III.13 Electrical characteristics of mismatch between two solar cells connected in parallel. (a) $(I-V)$ characteristics. (b) $(P-V)$ characteristics. 93

III.14 Ideal association of Bypass diodes with solar cells. 94

III.15 Economical association of Bypass diodes with solar cells. 95

III.16 Illustrations of a shaded solar module. (a) Realistic shadow pattern. (b) Simplified shadow pattern. 95

III.17 Comparison between the electrical characteristics of a shaded and an unshaded module. (a) $(I-V)$ characteristics. (b) $(P-V)$ characteristics. 96

© Ferdaous Masmoudi 2016 – All rights reserved

III.18 Example of implementation of a solar-module model accounting for the shading effect in the MATLAB-Simulink environment. 97

III.19 Solar resource in Tunisia. (a) Global Horizontal Irradiation in KWh/m^2 in Tunisia (source: Solargiz). (b) Monthly and annual cumulative Global Irradiation in KWh/m^2 in six Tunisian cities (source: INM). 98

III.20 Solar characteristics of the city of Sfax. (a) Solar-radiation profile for the year 2010 in W/m^2. (b) Temperature-range profile for the year 2010. (Source: INM). 99

III.21 Caption for LOF 100

III.22 Sun trajectory obtained using the SPA algorithm. (a) Flowchart for calculating the sun's position. (b) Daily sun trajectories for the 12 months of the year 2010 at ENIS. 101

III.23 Solar irradiance on a horizontal plane and an inclined plane. (a) Solar irradiance on a horizontal plane at P. (b) Solar irradiance on an inclined plane at P. (Source: ITACA) 102

III.24 Solar characteristics during the best and worst irradiance days of 2010 in Sfax. (a) Flowchart for calculating solar irradiance. (b) Actual and estimated irradiance profiles in W/m^2 (Source: INM). 103

III.25 Meteorological characteristics during the best and worst irradiance days of 2010 in Sfax. (a) Clear-sky-index profile. (b) Measured actual temperature profile (°C) (Source: INM). 105

III.26 Example of implementation of the solar-tracker model in the MATLAB-Simulink environment. 106

III.27 Simulation of solar trackers during the best and worst irradiance days of 2010 in Sfax. (a) Power generated during the best day. (b) Power generated during the worst day. 106

III.28 Mechanical system of the dual-axis tracker. (a) Structure for vertical motion. (b) Structure for horizontal motion. 108

© Ferdaous Maamoudi, 2016 – All rights reserved

III.29 Schematic representation of the solar-tracker electrical system. 109

III.30 Overall algorithm of the two-axis solar tracker. 110

IV.1 Intersections between the EMF levels of a 24 V battery and various resistive loads with the $(I-V)$ and $(P-V)$ characteristics of a PV generator: operating points under direct coupling. 114

IV.2 Principle of the designed PV conversion chain. 116

IV.3 Linearization of the source in the vicinity of the MPP. (a) $(I-V)$ characteristic. (b) Equivalent circuits. 117

IV.4 Simplification of the PV conversion chain in the vicinity of the MPP. 119

IV.5 Composition of the storage element. (a) Electrochemical cell. (b) Electrochemical battery. [95] 120

IV.6 Electrical battery model from the *SimPowerSystems* toolbox. (a) Symbol. (b) Electrical diagram. 122

IV.7 Discharge characteristic of the "Power Kingdom PS7-12" Lead-Acid battery at 25°C. 124

IV.8 Experimental measurements of the "Power Kingdom PS7-12" battery. (a) Explanatory measurement diagram. (b) Experimental test bench. 125

IV.9 Explanatory diagram of the curve-fitting method used to identify the parameters of the "Power Kingdom PS7-12" battery. 125

IV.10 Comparison of the discharge characteristics of the "Power Kingdom PS7-12" battery. 126

IV.11 Battery-observer algorithm. 127

IV.12 Efficiency comparison of the different converter topologies. 132

IV.13 Structure of the boost converter. 132

IV.14 Diagrams of the boost-converter operating sequences. 133

IV.15 Simulation model of the PV chain using ideal components. 134

© Ferdaous Mashoudi, 2016 - All rights reserved

IV.16 Simulation results of the boost converter using ideal components. (a) PV-module voltage V_{pv}. (b) PV-module current I_{pv}. (c) PV-module power P_{pv}. (d) Inductor current I_L. (e) Output voltage V_S. (f) Output current I_S. (g) Output power P_S. (h) Battery current I_{bat}. 136

IV.17 Simulation model of the PV chain taking power losses into account. 137

IV.18 Simulation results of the boost converter taking power losses into account. (a) PV-module voltage V_{pv}. (b) PV-module current I_{pv}. (c) PV-module power P_{pv}. (d) Inductor current I_L. (e) Output voltage V_S. (f) Output current I_S. (g) Output power P_S. (h) Battery current I_{bat}. 138

IV.19 Different situations considered by the MPPT strategy. 140

IV.20 Algorithm of the P&O-type MPPT control strategy. 141

IV.21 Implementation of the MPPT model in the MATLAB–Simulink environment. . 142

IV.22 Effect of load variation on the electrical quantities of the PV conversion chain. (a) Duty cycle. (b) Input voltage V_{pv} and output voltage V_S. (c) Input current I_{pv} and output current I_S. (d) Input power P_{pv} and output power P_S. 143

IV.23 Effect of irradiance variation on the electrical quantities of the PV conversion chain. (a) Irradiance profile. (b) Duty cycle. (c) Input voltage V_{pv} and output voltage V_S. (d) Input current I_{pv} and output current I_S. (e) Input power P_{pv} and output power P_S. 144

IV.24 Effect of temperature variation on the electrical quantities of the PV conversion chain. (a) Temperature profile. (b) Duty cycle. (c) Input voltage V_{pv} and output voltage V_S. (d) Input current I_{pv} and output current I_S. (e) Input power P_{pv} and output power P_S. 146

V.1 Prototype of the PV solar-energy power-supply system dedicated to embedded applications. 149

V.2 Hardware part of the solar tracker. 150

© Ferdaous Mamoudi, 2016 – All rights reserved

V.3 Data-acquisition process. 151
V.4 Graphical interface of the Web Service. 151
V.5 Experimental results of the solar tracker on November 6, 2016. 152
V.6 Flowchart of the states and transitions of the charge-controller program state machine. 153
V.7 Design and manufacturing stages of the charge-controller system. 154
V.8 Test of the charge-control system. 155
V.9 Frequency and duty cycle of the MOSFET PWM control. 156
V.10 Oscilloscope display of the experimental test of the Boost converter with a 15 V voltage source. 156
V.11 Oscilloscope display of the experimental test of the Boost converter with the PV module. 157

© Ferdaous Masmoudi, 2016 – All rights reserved

General Introduction

This introduction presents the general context and the main motivation of the work documented in this thesis. It includes an overview of the current state of renewable photovoltaic energy worldwide and in Tunisia. It is followed by the motivations, the objectives and the limitations of this thesis project, as well as the main contributions made through our work. Finally, the main outlines of this manuscript are listed.

1 General Overview of Renewable Energy

Due to the rapid increase in global energy demand, the development of renewable energy is undergoing continuous evolution. At the same time, the depletion of fossil fuel reserves has further driven several research and development projects to compensate for this deficit using alternative energy sources.

Regarding petroleum-based resources, such as coal, oil and natural gas, they were for a long time the only available energy sources. However, because of their dispersion and random non-uniform distribution across territories, as well as their limited availability, they have represented a source of conflict and the reason for competition among nations since the 18^{th} century. Moreover, conventional energy sources of fossil origin can be exploited for only a few decades. In addition, waste from nuclear power plants creates other pollution problems in terms of radioactive waste.

However, to meet global energy needs, it has become necessary to identify solutions and diversify energy sources. Currently, research is focused on finding and developing new, renewable, inexhaustible and environmentally friendly energy sources. Nevertheless, energy extraction techniques from these resources require more in-depth research and development strategies aimed at improving efficiency and reliability. Renewable energy can be classified into three main families: mechanical energy (wind, hydraulic, and wave hydrodynamic energy), electrical energy (photovoltaic conversion and thermoelectric conversion) and thermal energy (geothermal and solar thermal energy).

The sun, regarded as a promising source of clean energy, has been at the center of interest of several research teams throughout the world for several decades. It is considered an inexhaustible source of energy with the greatest development potential compared with other sources. Thus, the photovoltaic (PV) generator is cited as the most widespread conversion system of solar origin. Unlike conventional systems, the PV generator produces electrical energy silently, cleanly and

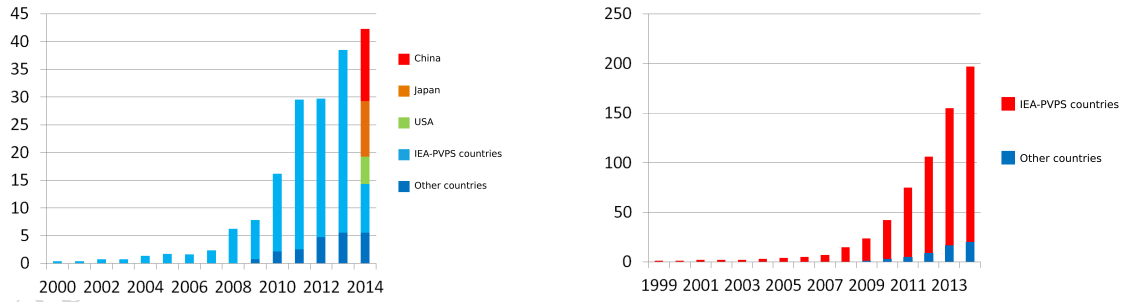
© Ferdaous Masmoudi - 2016 - All rights reserved

efficiently by exposing its constituent photovoltaic cells to solar radiation. There are many advantages that encourage the use of PV systems, namely:

- Solar energy is free. It consumes no fuel. Likewise, PV systems do not release harmful substances into the air or polluted water into nature. They do not produce dioxide emissions and do not endanger human health.
- Solar photovoltaic systems can operate in grid-connected mode or stand-alone mode. In addition, a PV system can be built at any size according to energy requirements. Indeed, the PV system is expandable when an increase in energy production is sought by associating PV modules to obtain the desired voltages and powers.
- The cells operate reliably for long periods with practically no maintenance. Indeed, solar panels have a long operational lifetime, with most manufacturers guaranteeing their solar panels for up to 20 years of operation, with a notable exception for stand-alone systems whose batteries must be replaced every 8 to 10 years.

1 .1 Overview of the Current State of Renewable Photovoltaic Energy Worldwide and in Tunisia

Photovoltaics is a rapidly expanding market [1]. This can be observed through the increasing activity of solar markets and the international trade in solar equipment. One example is the online platform *PvXchange*[1]. The annual growth rate of photovoltaic installations was approximately 44 % from 2000 to 2014 (44 GW in 2014 alone). More than twenty years of PV market development resulted in the deployment of more than 177 GW of PV systems around the world [2]. The bar chart in Figure 1.a shows the evolution of annually installed power, while Figure 1.b shows the cumulative PV power worldwide from 2000 to 2014.



(a) (b)

Figure 1: Evolution of PV energy worldwide. (a) annually installed power (GW). (b) cumulative power (GW).[3]
IEA-PVPS: member countries of the PVPS program of the International Energy Agency IEA.

The participation volume of each country in the PV power installed in 2014 is shown in the pie charts of Figure 2.

[1]PvXchange is one of the world's largest brokerage platforms for solar modules, inverters, and other PV components. It is a leader in the solar market worldwide. Further details can be found by the reader on its website http://www.PvXchange.com

© Feraoun Mehdi, 2016 – All rights reserved

Regarding photovoltaic module production in 2014, the pie chart in Figure 2.a indicates that China leads with a share of 66 %. All of Europe contributed a share of 8%. Japan and Malaysia ranked third with 6% and 5%, respectively.
In the same context, according to Figure 2.b, silicon-based photovoltaic technology represented approximately 92% of PV cell production in 2014. The share of polycrystalline technology is now approximately 56% of total production, followed by monocrystalline technology at 26%. This figure tends to increase according to several studies in the coming years, given the increase in the efficiency of this technology and the decrease in its production cost.
Figure 2.c presents the share of each manufacturer in PV cell production in 2014. The manufacturer "JA Solar" already holds a significant market share of approximately 3% annually.

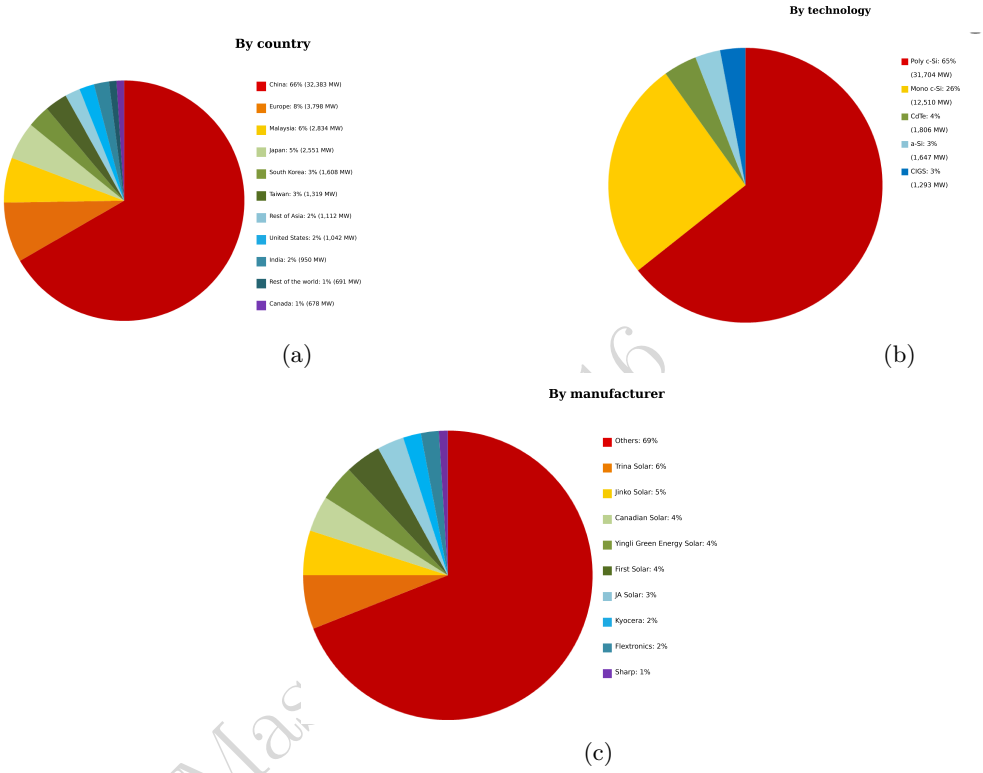


Figure 2: Global production of PV solar modules worldwide in 2014 (48 961 MW). (a) By country. (b) By technology. (c) By manufacturer.[4]

Following the path of developed countries, Tunisia is one of the few developing countries that has been fully committed since 1980 (Hammam Biadha Project) to the energy-transition strategy by adopting a proactive energy-management policy aimed at encouraging the development of the renewable-energy sector. To achieve this objective, ambitious measures and bold investment policies have been initiated over the years. This policy accelerated particularly from the mid-2000s onward with the sharp rise in fuel prices and the emergence of an increasing energy deficit.

Electricity production at the national level reached 19 952 GWh in 2016 and is estimated by forecasts to reach 23 515 GWh in 2021. Only 430 GWh of the produced energy comes from renewable sources (without taking private installations into account) [5]. Table 1 presents indicative figures on the types of renewable-energy sources available and active in Tunisia between

© Ferdaous Maâ reserved

2013 and 2014, the total installed capacities, the average of their annual production, as well as the savings achieved in oil equivalent (unit: kilotonne of oil equivalent; ktoe). This table shows a low contribution of solar PV energy to total renewable production, especially at the level of public installations (absence of large-scale PV solar power plants).

Table 1: Renewable energy production in Tunisia in 2013.[5]

Renewable source type	Power produced GWh/year	Installed power MW	Savings achieved ktoe/year
Wind	358	233	150
Hydraulic	60	62	38.44
Solar Photovoltaic	Public: 9 Private: 31.5 (14,000 households)	13 21	3.72 31.5
Solar Water Heater	——— ———	500,000 m^2 (installed area)	31

Committing the State to the training of qualified skills in the fields of renewable energy requires immediate action in scientific research and university education.

In Tunisia, several university institutions teach subjects related to energy management. Among the active research structures in the fields of renewable energy is the Borj Cedria Technopark *TBC* [2], which hosts the Research and Energy Technologies Center CRTEn [3], concerned with energy efficiency and renewable energy. The center focuses on the use of photovoltaic systems for lighting, irrigation and water desalination using renewable energy, the use of solar and wind energy, and research on materials for photovoltaic applications.

The National Engineering School of Sfax *ENIS* has also become involved in the policy of incorporating the theme of renewable energy into higher education and research organizations. The work carried out in this thesis represents one among several contributions of the *CEM LAB* laboratory toward motivating, promoting and encouraging the scientific mastery of renewable-resource technologies.

© Ferdaous Masmoudi 2016 - All rights reserved

[2] http://www.ecopark.tn/
[3] http://www.crten.rnrt.tn

2 Motivations and Objectives

2 .1 Motivations

The thesis topic presented in this manuscript falls within the framework of the integration and exploitation of renewable-energy sources in the design of embedded and mechatronic systems. Indeed, this topic is part of a broad research project at ENIS that proposes the design of an Autonomous Mobile Robot through a collective effort combining the various research areas. Thus, the studies carried out and planned address the following themes:

Robotics and Embedded Systems : The design of the embedded robotic system and the synthesis of the tools and action diagrams required for real-time data analysis, as well as the control and command of the different components and peripherals.

Electrical Systems Computing : The development of optimized algorithms for subsystem control and real-time data transfer.

Automatic Control : The development of advanced automatic-control approaches for robot motion control and trajectory tracking, taking into account obstacles and arising constraints.

Renewable Energy and Power Electronics : The design of an energy-conversion system and the power stages required to exploit renewable-energy sources.

Storage System : Battery charging and a system for managing and observing the stored energy, as well as a view of the state of charge, state of life and diagnosis of the battery under charge.

Motors and Electrical Machines : The modeling and control of electrical machines, as well as the management and optimization of their electrical-energy consumption.

The autonomous mobile robot is designed around a motorized mobile base that supports a manipulator arm and is equipped with a PV system for autonomous solar-energy supply. The first prototype of the robot was launched during the 2015-2016 academic year. Figure 3 shows the mechanical design of the system developed using *SolidWorks* software.

Such a robotic system can be used in various applications. The robot can be exploited for educational purposes as well as for industrial missions (for example, moving loads and objects over long trajectories), and it can be navigated as an exploration robot in places where human intervention is dangerous or impossible. It can also be assigned surveillance and information-collection missions.

It is also possible to use the PV power-supply system separately in stand-alone systems such as public lighting or mobile charging stations. It can therefore be used to supply intelligent embedded systems and connected objects within the framework of implementing the “Smart City”.

© Ferdaous Mamoudi, 2016 – All rights reserved

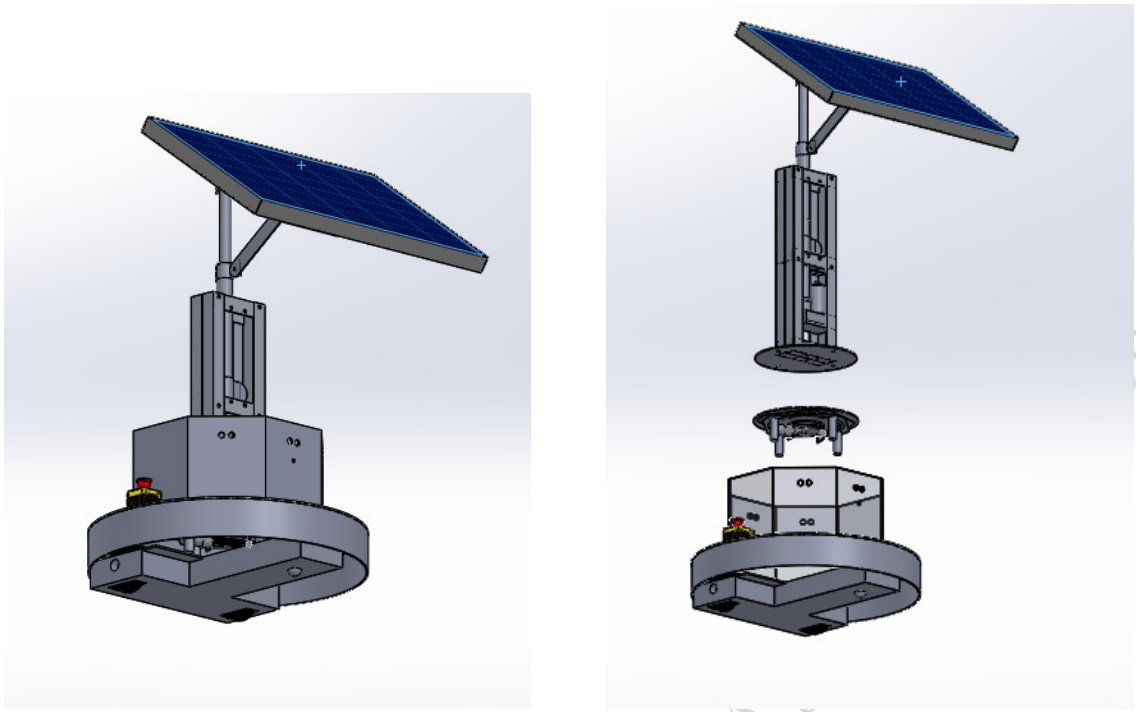


Figure 3: Autonomous Mobile Robot Design. (a) Compact drawing. (b) Exploded drawing.

2 .2 Objectives

The work carried out during this thesis is structured around the development of the electrical-energy supply part of the robot described previously. Total autonomy of the robot is proposed from the standpoint of electrical-energy production and consumption by using a renewable, clean, silent and safe energy source.

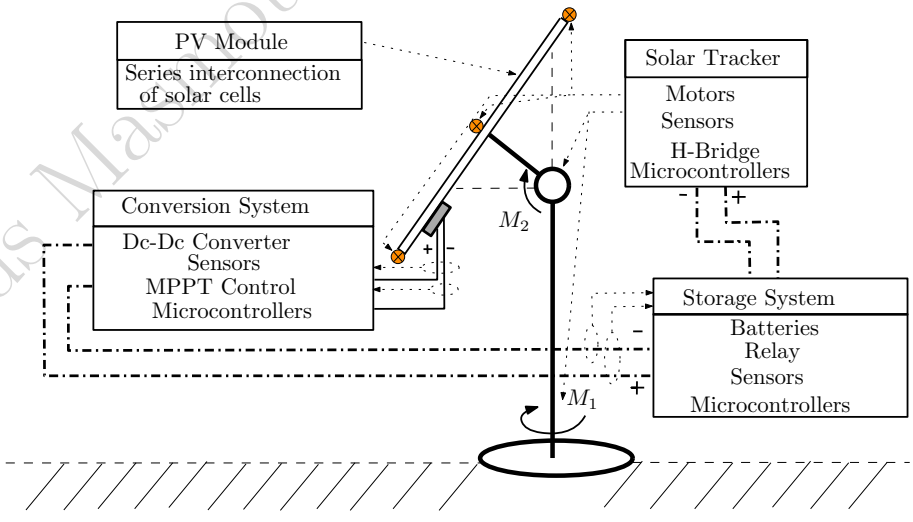


Figure 4: Synoptic diagram of the PV solar-energy supply system.

This work presents the design of a PV solar-energy supply system dedicated to embedded and robotic applications. The energy efficiency of the PV modules used is optimized by various methods with the aim of maximizing the exploitation, without loss, of the electrical energy

© Ferdaous Mabrouki, 2016 – All rights reserved

available from the PV equipment.

A simplified synoptic diagram of the designed system, summarizing the different blocks developed in this thesis, is presented in Figure 4.

At the end of this thesis, a practical implementation of the theoretically studied system is also presented through the fabrication of a preliminary prototype.

It is nevertheless appropriate to emphasize the problems of modeling solar cells and modules and studying their efficiencies under continuous climatic disturbances, as well as studying the techniques and means for the appropriate and optimal exploitation of photovoltaic generators.

2 .3 Project Limitations

Although there are many types and technologies of solar cells and modules, only the monocrystalline type was adopted and used in the form of a single module (without associations of several modules), and the study was limited to a stand-alone PV system connected to a battery storage element (Lead-Acid).

The modeling and study of PV cells and modules did not take into account the effect of aging and the degradation of device efficiency caused by mechanical and physical defects in the junction structure.

The designed energy-conversion system is intended to operate under normal conditions without taking into account unexpected accidental faults such as breakdown of the switching cell or damage to sensors, etc.

The proposed work did not address environmental noise acting on the systems or parasitic emissions disturbing the operation and endurance of the PV chain.

2 .4 Main Contributions

The main contributions of this thesis are structured around the following points:

- The problem of photovoltaic solar-cell modeling was discussed in detail in the second chapter by developing five equivalent electrical models while identifying their internal parameters using careful iterative algorithms. The work carried out resulted in the publication of two journal articles [1-2] and two conference papers [4-5].
- The optimization of solar-module efficiency is achieved first through module protection, as well as through the optimal positioning of their surfaces with respect to incident irradiance. In the third chapter, a prototype of a two-axis motorized solar tracker controlled by an appropriate algorithm for tracking the sun's trajectory was proposed. Part of the work carried out was the subject of a conference paper [6].
- The use of a battery model to simulate the PV chain requires experimental identification of the storage element and deduction of its internal parameters. In Chapter 4, a battery-identification method is proposed, together with the design of a battery-observation system. The identification work was the subject of a journal article [3] and a paper published in a conference [7].

© Ferdaous Mahmoudi, 2016 – All rights reserved

- In the fourth chapter, the design of a power converter with its appropriate MPPT control was detailed, and in the fifth chapter a prototype of the designed electronic board mounted on the "PV Module−Solar Tracker−Charge Controller" system was presented. Some parts of this work were the subject of three papers published in international conferences [8-9-10].

3 Structure of this Manuscript

The present manuscript, which constitutes a synthesis of the above-mentioned work, is organized into five chapters. The present chapter introduces a general overview of the position of photovoltaic energy worldwide and in Tunisia and describes the problems and motivations that initiated this work. The main intended objectives and the contributions made are also presented.

First, the first chapter provides an overview of photovoltaic solar technology and its electrical characteristics. A historical review is presented, together with the different currently existing photovoltaic technologies and applications. Fundamental concepts concerning the internal structure of the solar cell are provided, and the chapter concludes with a description of the electrical parameters and the operating principle of the solar device.

The second chapter discusses the problem of photovoltaic solar-cell modeling and the synthesis of equivalent electrical models. We then proceed with the development of algorithms for searching the internal parameters of the considered models and conclude with the analysis of some simulation results, as well as a comparative study of the proposed models.

The third chapter is devoted to the analysis of solar-cell associations with the aim of forming photovoltaic modules and panels. The different possible cell groupings are described, as well as the problems that may arise during their connections. This is followed by the synthesis of methods for optimizing the energy exploitation of photovoltaic generators through the design of a motorized solar tracker that tracks incident solar radiation in open-loop and closed-loop modes.

The fourth chapter deals with the energy-adaptation and conversion system that serves as an interface between the PV generator and the load or storage element. Methods for linearizing the PV source and the output load used are presented, as well as the modeling and identification of the storage-battery parameters. The operation of static power-chopper converters is then studied and the various existing topologies are discussed. The Boost chopper is adopted, and detailed sizing and modeling are presented while taking into account the parasitic elements of this architecture. Optimization of the efficiency of the adaptation stage is achieved through the synthesis of the appropriate MPPT control strategy.

The fifth chapter is dedicated to describing the experimental work carried out. It presents the different stages of design and implementation of the fabricated prototype. A sample of the experimental results obtained during the first tests of the system is also presented.

This manuscript concludes with a brief conclusion highlighting the significant results obtained from this thesis and opening perspectives on new problems that ensure the continuity and improvement of the project.

© Ferdaous Masmoudi 2016 _ All rights reserved

3 .1 Tools Used

In order to simulate the behavior of the different parts, the designed photovoltaic system was implemented in the "*MATLAB/Simulink*" environment using the "*SimPowerSystems*" toolbox to model the power converter, while the identification algorithms for the solar-cell models were developed by programming in the "*MATLAB*" language in an "*Mfile*" document using various toolboxes such as the "*Optimization toolbox*" and the "*Symbolic Math toolbox*".

Regarding the prototype of the implemented PV system, the solar tracker is equipped with an electronic data-acquisition layer established on the "*ARDUINO Nano*" board built around the "*AVR Atmega328*" microcontroller (a product of "*Atmel*"). Considering the control of the solar-tracker motors and the sun-trajectory tracking algorithm, a System on Chip ("*SoC*") board of the "*Raspberry Pi*" type was used, given its high parallel-computing power and its ability to communicate with several peripherals.

The control and command system of the PV charge controller was implemented using an "*ARDUINO Mega*" board with an "*AVR Atmega2560*" microcontroller because of its high programming flexibility, as well as its high computing capacity. The development of the electronic board of the Boost-type DC-DC converter was carried out using "*Proteus 8 Professional*" software with its "*ISIS*" and "*ARES*" interfaces, as well as board routing and preparation of the artwork.

Data centralization and subsequent transfer are ensured from the "*Raspberry Pi*" board through the use of cloud computing (in Anglo-Saxon terms "*Cloud Computing*"), which aims to create a delocalized telecommunications network facilitating information sharing. Thus, storage of the acquired system-state data on remote servers is carried out through the "*Wifi*" interface and the "*Internet*" network using the "*Web Service*" protocol.

The mechanical design of the robot prototype equipped with the solar tracker was developed in collaboration with the company for the development of mechatronic engineering solutions *Novel-Ti* [4] (SFAX).

© Ferdaous Masmoudi, 2016 – All rights reserved

[4] http://www.novelti.com.tn

3 .2 List of Publications Resulting from this Thesis

Articles

[1] Ferdaous Masmoudi, Hafedh Trabelsi, Nabil Derbel. "Comparative study of photovoltaic solar cell models with identification of internal parameters and experimental ascertainment." DE GRUYTER (Germany). Advances on Systems, Signals, and Devices (ASSD) (accepted December 2016).

[2] Ferdaous Masmoudi, Fatma Ben Salem, Nabil Derbel. "Identification of Internal Parameters of a Monocrystalline Photovoltaic Cell Models and Experimental Ascertainment." International Journal of Renewable Energy Research (IJRER), (Published September 2014).

[3] Jihen Loukil, Ferdaous Masmoudi, Nabil Derbel. "Third Order Model Identification of Lead-Acid Battery Using Genetic Algorithm and Experimental Measurements." DE GRUYTER (Germany). Advances on Systems, Signals, and Devices (ASSD) (accepted December 2016).

Conferences

[4] Ferdaous Masmoudi, Fatma Ben Salem, Nabil Derbel. "Simple models design for one monocrystalline photovoltaic cell by identification of internal parameters." IEEE Annual Seminar on Automation. Industrial Electronics and Instrumentation (SAAEI), Morocco, Tangier, June (2014).

[5] Ferdaous Masmoudi, Fatma Ben Salem, Nabil Derbel. "Single and Double Diode Models for Conventional Mono-Crystalline Solar Cell with Extraction of Internal Parameters." IEEE International Multi-Conference on Systems Signals and Devices (SSD'16), Leipzig, Germany, March (2016).

[6] Ferdaous Masmoudi, Hafedh Trabelsi, Nabil Derbel. "Simulation and Design of Dual Axis Solar Tracker System for Photovoltaic Power Optimization." (Submitted November 2016).

[7] Jihen Loukil, Ferdaous Masmoudi, Nabil Derbel. "Modeling of Internal Parameters of a Lead Acid Battery with Experimental Validation." IEEE International Multi-Conference on Systems Signals and Devices (SSD'16), Leipzig, Germany, March (2016).

[8] Rabeb Abid, Ferdaous Masmoudi, Fatma Ben Salem, and Nabil Derbel. "Design and Realization of a Photovoltaic System Controlled by an MPPT Algorithm." IEEE International Conference on Sciences and Techniques of Automatic Control and Computer Engineering (STA'15), Monastir, Tunisia, December (2015).

[9] Rabeb Abid, Ferdaous Masmoudi, Fatma Ben Salem, Nabil Derbel. "Modeling and Simulation of Conventional DC-DC Converters Dedicated to Photovoltaic Applications." The International Renewable Energy Congress (IREC), Hammamet, Tunisia, March (2016).

[10] Rabeb Abid, Ferdaous Masmoudi, Nabil Derbel. "Comparative Study of Fundamental Variable Input Converters used for PV Conversion Systems." (Submitted November 2016).

© Ferdaous Masmoudi, 2016 – All rights reserved

Chapter I

The Photovoltaic Generator: Overview, Structures and Operating Modes

Abstract: *This first chapter aims to introduce electrical energy of photovoltaic origin. First, a general introduction is presented, followed by a historical review of the development of the solar-cell structure. The different PV-cell technologies currently available are then introduced, followed by a classification of the most significant PV applications worldwide. The second part deals with the investigation of the internal structure of the solar cell as well as the analysis of the fundamental physical mechanisms governing the solar junction. The chapter concludes with an examination of the characteristics and operating modes of the solar cell while detailing its fundamental electrical parameters.*

Keywords: Photoelectric effect – photovoltaics,
Cell – Generator – Photovoltaic system,
p-n junction: emitter – base – space-charge region,
Generation – Recombination – Diffusion phenomena,
Characteristics – Electrical parameters,

© Ferdaous Masmoudi, 2016 – All rights reserved

I.1 Introduction

The term photovoltaic (PV) is a combination of the Greek word "phós" (light), or "phōtós" (of light), and the name of the Italian physicist "*Alessandro Volta*" (1745–1825), who discovered the first electrochemical battery, after whom the functional unit of electricity (Volt) was named. Thus, one translation of the word photovoltaic could be "light battery", "light source", or even "light converter" [6]. More generally, the word photovoltaic refers to the direct conversion of solar radiation into electrical energy.

The elementary component constituting the photovoltaic generator (PVG) is the solar cell. It is generally manufactured from silicon, a semiconductor also used for diodes, transistors, and integrated circuits.

A solar cell, when not exposed to light, behaves exactly like a diode which, when the p-n junction is forward biased, allows current to flow from the p-region to the n-region. When the diode is exposed to light, it behaves as a photovoltaic cell; a photonic current is generated and then diffuses from the n-region toward the p-region.

This results in the creation of a potential difference (approximately 0.5 V) between the two terminals of the cell. The released current varies according to the radiation and the surface area of the cell, as well as its manufacturing technology and conversion efficiency (from 5 to 9 A for a conventional cell with a surface area of 125 mm×125 mm). In order to obtain a usable voltage in the range of 20 to 50 V, many cells must be interconnected to form a solar module.

I.2 Overview of the Photovoltaic Solar Cell

Following this introduction, an overview of the history of the photovoltaic cell is presented, together with its different technologies and application areas.

I.2 .1 History of the Solar Cell

The chronology of solar cells begins in the 19$^{\text{th}}$ century, when father and son "*Becquerel*" observed, during an electrochemical experiment (a cell), that the presence of sunlight stimulates the generation of electrical energy between platinum electrodes immersed in an electrolyte. The motion effect exerted by light on the electrons of a body is called the photoelectric effect. Later, combining the concept of p-n junctions (bringing into contact two doped semiconductors, generally silicon-based) with the photoelectric effect led to the appearance of the first solid-state solar cells called "photovoltaic" cells.

Solar cells continued to be used in many applications. Historically, they were used in situations where power supply through the electrical grid was inaccessible (stand-alone – isolated photovoltaic system), such as Hammam Biadha in Tunisia for several decades.

The chronological timeline in Table I.1 shows the most particular dates concerning the development of photovoltaic technology.

© Ferdaous Mosmoudi, 2016 – All rights reserved

Table I.1: Chronology of solar-cell development.

1839	"Alexandre Edmond Becquerel" observed the photovoltaic effect through an electrochemical experiment exposed to light.
1873	"Willoughby Smith" discovered the photoconductivity of selenium Se.
1877	"W.G. Adams" and "R.E. Jour" observed the photovoltaic effect in solidified selenium and published the first document on the selenium cell.
1883	"Charles Fritts" developed a solar cell using selenium on a thin layer of gold to form a device with an efficiency of less than 1%.
1887	"Heinrich Hertz" discovered the photoelectric effect caused by ultraviolet light; at the same time, "James Moser" reported sensitized photoelectrochemical cells.
1888	"Aleksandr Stoletov", "Melvin Severy", and then "Harry Reagan" received the first patents for manufacturing solar cells between 1888 and 1897.
1904	"Wilhelm Hallwachs" built the first solar cell based on a semiconductor junction (copper and copper oxide).
1905	"Albert Einstein" published a paper explaining the photoelectric effect from the viewpoint of quantum physics.
1918	"Jan Czochralski" developed a method for growing metal single crystals. This method was later adapted to produce monocrystalline silicon.
1948	"Gordon Teal" and "John Little" adapted the "Czochralski" crystal-growth method to produce monocrystalline germanium and, later, silicon.
1950	"Bell Labs", the American scientific research and development company, produced solar cells for space activities.
1954	"Bell Labs" announced the invention of the first practical silicon solar cell. Shortly afterward, it presented cells with an efficiency of about 6%. The "New York Times" predicted that solar cells would lead to an unlimited source of energy from the sun.
1955	"Western Electric", an electrical-engineering company, was the first to receive permission to commercialize solar cells. The company "Hoffman Electronics-Semiconductor" then created and marketed a solar cell with 2% efficiency for 25 \$/cell, i.e. 1.785 \$/watt.
1958	"Vanguard I", the first solar-powered satellite, was launched with 100 cm^2 of PV cells.
1960	"Hoffman Electronics" created a solar cell with an efficiency of 14%.
1977	Following the 1973 oil crisis, solar PV was used as an alternative terrestrial energy source and global production exceeded 500 kW.
1983	Global photovoltaic production exceeded 21.3 megawatts, and sales exceeded 250 million \$.
1991	President "George H. W. Bush" directed the United States Department of Energy and founded the National Renewable Energy Laboratory "NREL".
1994	"NREL" developed the two-junction GaInP/GaAs solar concentrator (180 suns), which became the first solar cell with an efficiency greater than 30%.
1999	The total installed photovoltaic power worldwide reached 1000 megawatts.
2006	"Boeing" and "Spectrolab" announced a new solar-cell efficiency record that reached 40%.
2016	A worldwide solar-cell efficiency race was launched among solar-energy laboratories. The German institute "Fraunhofer ISE" recently announced a new record of 46%.

© Ferdaous Masmoudi 2016 – All rights reserved

I.2 .2 Solar-Cell Technologies

Photovoltaic cells represent the smallest unit in a solar-energy production device. According to their manufacturing technology, cells can generally be classified into five major categories:

- Crystalline silicon type (monocrystalline silicon, polycrystalline silicon, etc.).
- Thin-film type, also called compound semiconductor (amorphous, Cadmium-Telluride CaTd, etc.).
- Multijunction type (concentrator, GaInP2/GaAs/Ge, etc.).
- Single-junction GaAs type (concentrator, crystalline, etc.).
- Emerging type, which groups together all new technologies currently under development and improvement (organic, inorganic, perovskite, Grätzel, etc.).

The use of materials for silicon cells has been significantly reduced over the last 10 years. Figure I.1 shows the improvement in junction quality in terms of thickness and amount of material used, moving from approximately 400μm with 16g/W_c to less than 150μm with 6g/W_c; this provides thinner *wafers* with higher efficiency.

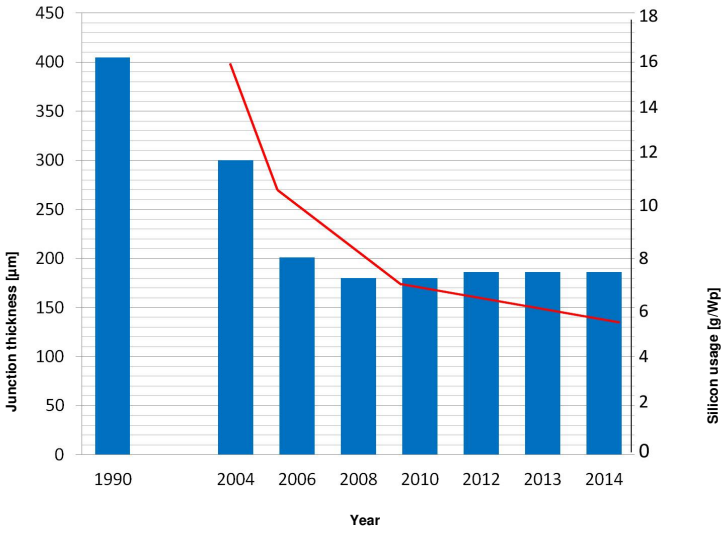


Figure I.1: Development of silicon-junction quality.

Currently, crystalline-silicon cell technologies are the most widely manufactured and commercialized (see Figure 2.b). Cell-efficiency records show the increase in efficiency of the different cell types. Figure I.2 summarizes the different solar-cell technologies currently available and their inventors, as well as the progress in efficiency recorded over the last 40 years.

© Ferdaous N... 6 _ All rights reserved

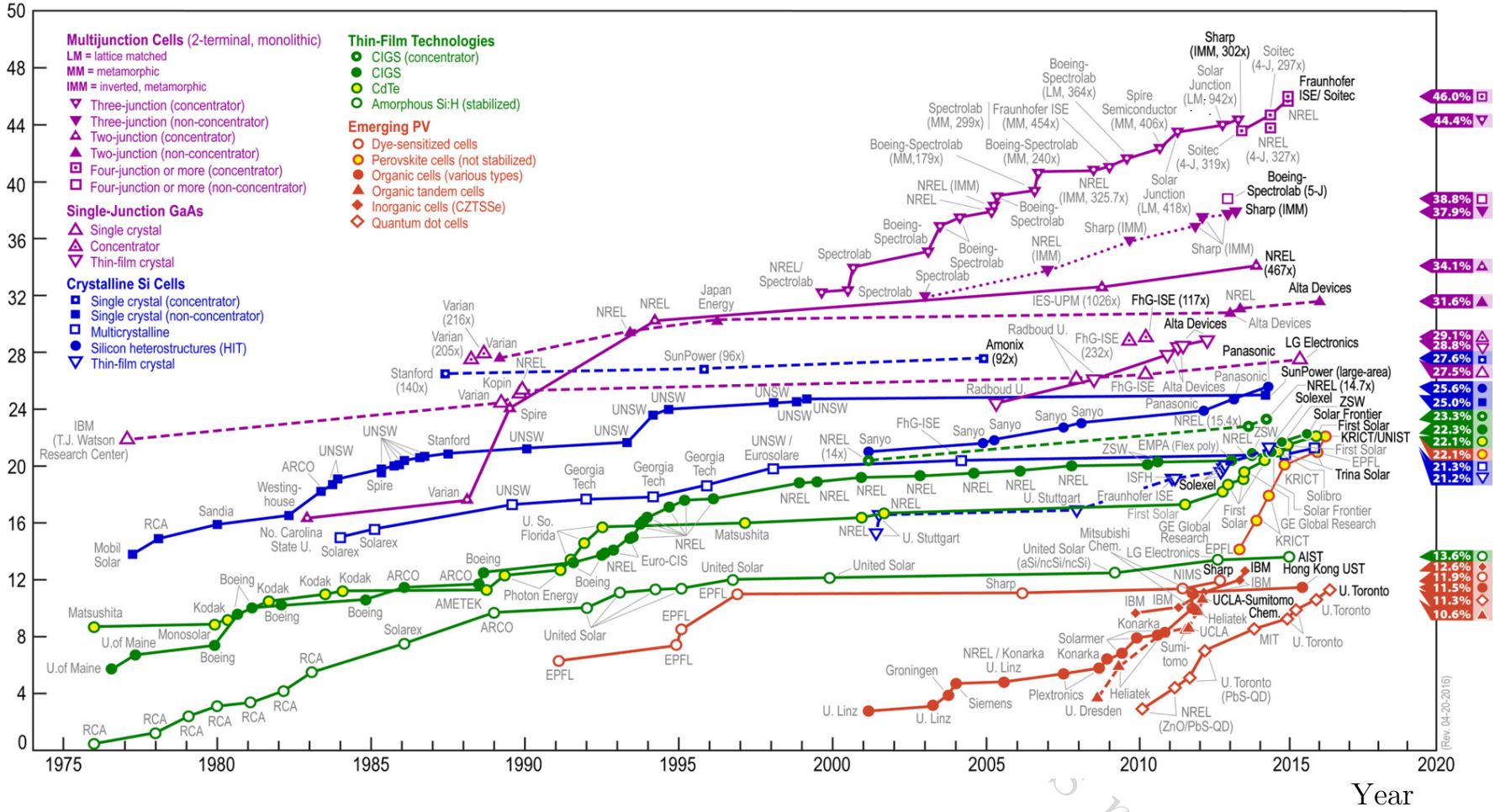


Figure I.2: Development of solar-cell efficiency records over the last 40 years (source: NREL).

© Fe
5 reserved

At the forefront of the efficiency race are obviously the high-concentration multijunction solar cells, which can reach an efficiency of 46%. For crystalline cells, the *PERL* architecture cell holds the leading position with an efficiency of 25%. Organic cells occupy the last position with an efficiency of about 9%. However, the efficiency gain over the last five years is clearly visible, rising from 3% to 12% currently.

I.2 .3 Application Areas

Initially, the exploitation of photovoltaic solar energy was confined to extraterrestrial applications (satellites, exploration robots, etc.), given the high cost of this technology (1000 times more expensive than the current price). Today, the photovoltaic field covers a multitude of diversified applications and has the greatest development potential compared with other renewable resources. Applications can be classified into four major categories [7]:

- **Direct coupling of the photovoltaic system**: This type of system, represented by Figure I.3.a, which can also be considered a stand-alone system, is the simplest coupling system. Moreover, it is independent of the grid. The DC output of the PV module is directly connected to the DC load. With this coupling, the load operates only during sunshine hours. While its advantage is simplicity of use, the main drawback of this type is the impossibility of benefiting from the maximum energy produced by the PV generator, as well as the absence of a storage system that allows energy to be recovered during the night.

- **Stand-Alone Photovoltaic System**: The stand-alone system, represented by Figure I.3.b, is generally used in isolated sites in the absence of an electrical grid or when the cost of grid connection is too high. This system includes charge controllers and storage systems in its chain. The batteries must have sufficient capacity to store the energy produced during the day for use at night and during periods of bad weather.

- **Grid-Connected Photovoltaic System**: Although, initially, the main uses of photovoltaic energy were stand-alone, grid-connected systems now play a predominant role. These systems do not require storage elements because the grid acts as a reservoir for excess energy. During periods of insufficient photovoltaic-energy production, the grid also supplies the required energy (Figure I.3.c).

- **Hybrid System**: A hybrid system is a combination of different methods of electricity production. This combination, shown in Figure I.3.d, includes renewable energy sources (such as water, wind, solar, etc.) as well as conventional non-renewable sources (gas, coal, oil, etc.) in order to balance periods of bad weather and even seasonal fluctuations. Hybrid systems generally require more sophisticated control systems than stand-alone or grid-connected PV systems. For example, in the case of a PV/diesel system, the diesel engine must be started when the battery reaches a given discharge level and stopped again

© Ferdaous Masmoudi, 2016 – All rights reserved

when the battery reaches an adequate state of charge. The backup generator can be used solely to recharge the batteries as well as to supply the load.

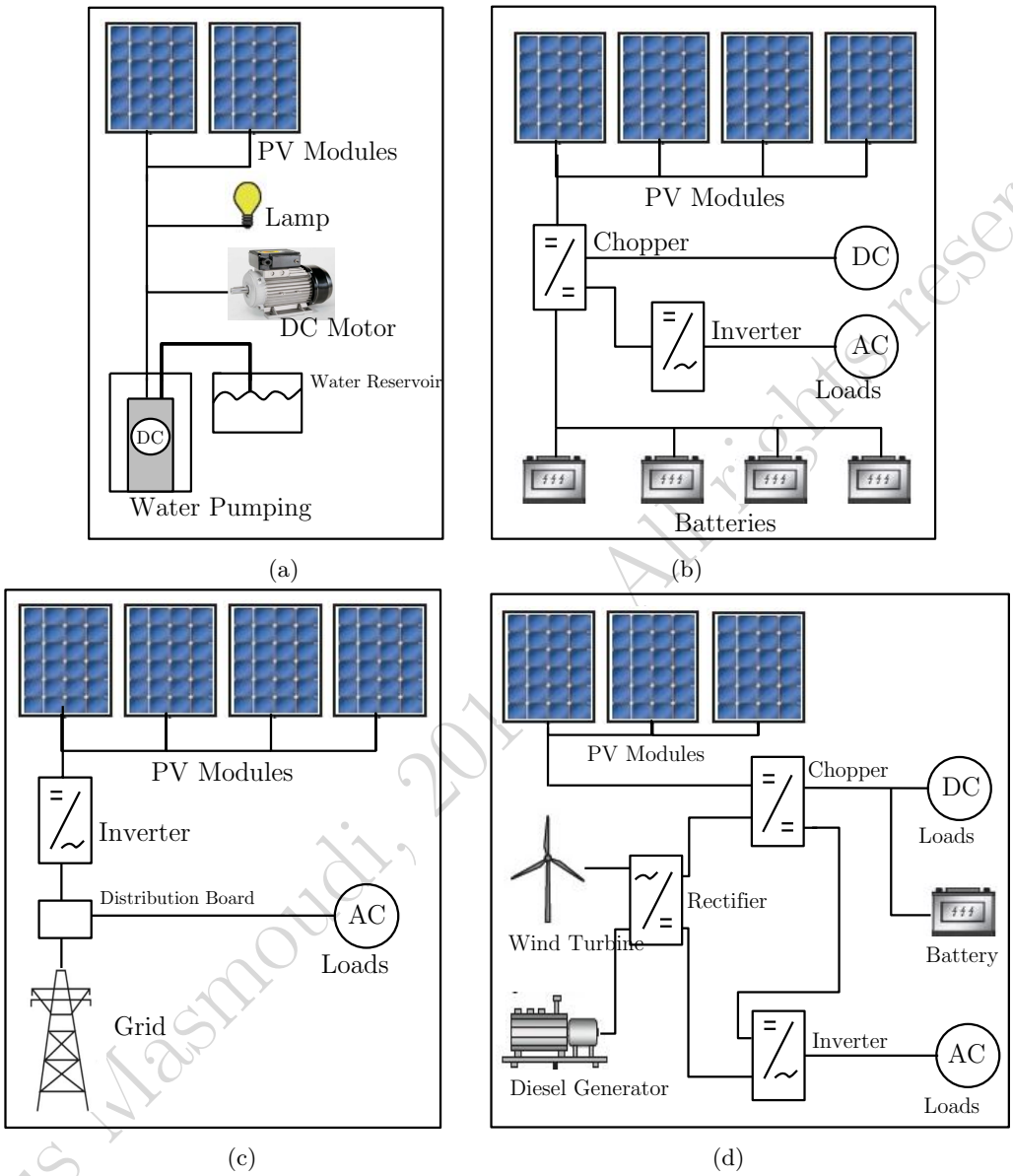


Figure I.3: Architecture of the different types of PV chains: (a) Direct Coupling. (b) Stand-Alone System. (c) Grid-Connected System. (d) Hybrid System.

Table I.2 summarizes the most significant photovoltaic applications existing worldwide.

© Ferdaous Masmoudi, 2014 All rights reserved

Table I.2: Various applications of PV energy.[3, 5, 70]

Systems PV Stand-Alone	Very Small Systems Pico-System $\sim <$ 10 peak-watt (W_c)	- Phone charger - Laptop computer - Radio - Flashlight - Security (security system) - Fan - Watch-calculator-sensors
	Small Systems $\sim <$ 1 KW_c	- Public lighting - Telecommunication and signaling system - Solar car - Solar water pumping - Satellites - mobile robot - macaronic system
	Medium Systems a few tens of KW_c	- Power supply for isolated sites Example: Hammem Biadha in Siliana - Tunisia = $30KW_c$
Systems PV Grid-Connected Systems	Small or Medium Systems Residential or Commercial a few tens of KW_c $\rightarrow$ a few MW_c	- Rooftop system - Ground-mounted system - Building-integrated system
	Large Systems $\sim >$ 10 MW_c	- Large-scale utility: Solar Generation Station; Solar Park; Solar Farm; Solar Power Plant; Solar Plant, etc. Examples: - "Solar Star" station of 579 MW_c extending over $13Km^2$ (California, USA) - "Perovo Solar" park of 100 MW_c extending over $2Km^2$ (Perovo, Crimea, Ukraine) - "Wald Polenz Solar" park of 52 MW_c extending over $22Km^2$ (Leipzig, Germany)
Hybrid Systems	Systems Medium or Large (mainly on islands) a few hundred KW_c $\rightarrow$ a few tens of MW_c	- PV/T: Photovoltaic - Thermal - CPV/T: PV Concentrator - Thermal - PV/Diesel: Photovoltaic - diesel engine - PV/wind: Photovoltaic - Wind - Various existing combinations, etc. Examples: - "Pellwor" island in Germany (PV-Diesel-Wind) - "Kythnos" island in Greece (PV-Wind)

© Ferdaous Masmoudi, 2016 – All rights reserved

I.3 Structure and Operating Modes of the Solar Cell

The solar cell is an electronic device manufactured from semiconductor materials in the form of a p-n junction. When illuminated, the material absorbs light, which causes the excitation

of electrons and the generation of electron-hole pairs. The released electrons can therefore be exploited by moving them, which constitutes electrical energy.

This chapter aims to identify the fundamental phenomena acting on the solar cell, without entering into the details of semiconductor physics, as well as to explore its internal structure; this will allow an adequate understanding of the operating modes of PVGs and their modeling.

I.3 .1 Structure of the Solar Cell

The structure of a crystalline solar cell is fundamentally composed of a doped-silicon p-n junction, as shown in Figure I.4 [56].

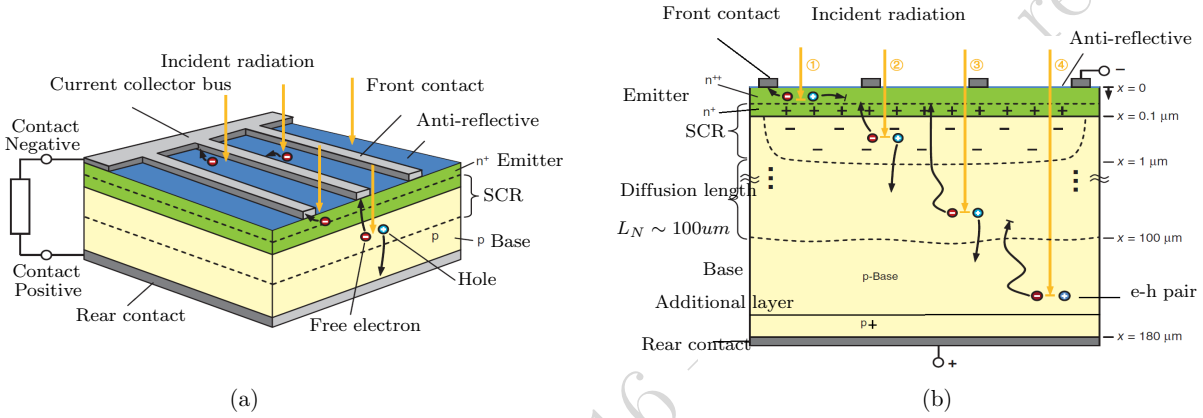


Figure I.4: Section of a typical solar cell. (a) Perspective diagram. (b) Cross section. [7]

The bottom of the structure constitutes the *Base* of the junction, formed mainly by two layers: heavily doped p^+ silicon followed by p-doped silicon from bottom to top. At the top is the *Emitter* of the junction, also formed by two layers: heavily doped n^+ silicon followed by n-doped silicon from top to bottom. The terms *Base* and *Emitter* are bipolar-transistor terms also used for solar cells. In the middle, a diffusion electric field is established between the *Base* and the *Emitter*, forming the space-charge region SCR, also called the depletion region.

On the *Emitter* surface, a front grid of metallic conductors is placed to collect the electrons generated on the surface of the structure. The current-collector bars (busbars) serve to collect all the energy produced and transfer it to the positive terminal of the cell. Similarly, the rear of the cell (rear contact) is covered with a metal-semiconductor interface devoted to the recombination of electron-hole pairs; this constitutes the negative terminal of the cell.

When the cell is illuminated, each absorbed photon generates an electron-hole pair. Connecting a load to the two terminals of the solar cell allows electrical energy to be extracted. In fact, the particles (electrons and holes) are separated by the electric field of the SCR and then moved toward the terminals: the holes through the *Base* and then toward the rear contact, and the electrons through the *Emitter* toward the front contacts. After passing through the load, each electron reunites with a hole and thus completes the circuit. The generation of a potential difference at the terminals of a junction between two different materials in response to solar radiation is called the *photovoltaic effect*. The generated current depends mainly and

© Ferdaous Maamoudi, 2016 - reserved

directly on the quantity of photons absorbed by the structure, in other words, on the intensity of the light incident on the junction. This current is called the *photocurrent* or the *photoelectric current*.

I.3 .2 Operating Modes of the Solar Junction

All solar cells contain junctions between different materials with different doping levels. Given the fundamental role of these junctions in solar-cell operation, their physical behavior is analyzed in this section. In general, four types of p-n junctions are distinguished:

p-n Homojunction : This is a p-n junction manufactured from the same semiconductor material, such as c-Si (case of monocrystalline solar cells).

Heterojunction : This is a p-n junction formed by two chemically different semiconductors.

p-i-n Junction : This is a junction in which the internal-electric-field region is extended by inserting an intrinsic i layer between the p-type layer and the n-type layer. The i layer behaves as a capacitor that extends the electric field formed by the p-n junction.

MS Junction : This is a junction between a metal and a semiconductor, such as the Schottky contact formed at the metal/semiconductor interface.

In what follows, the homojunction type is adopted to study the internal physics of the monocrystalline solar cell.

I.3 .2 .1 Generation, Diffusion and Recombination

Radiative generation is the fundamental phenomenon of electron-hole-pair generation. When light penetrates a material (by analogy, heat), it is (partially) absorbed as it propagates through the structure. If the energy of the photon (phonon in the case of heat) is greater than the band-gap energy of the semiconductor, it is capable of breaking the valence bond and exciting an electron toward the conduction band, leaving behind a hole in the valence band. This is the generation process (thermal generation), which is the essential cause of the appearance of the photonic (thermal) current [35].

Diffusion is a process in which particles tend to spread from regions of high particle-doping concentration toward regions of low particle-doping concentration because of random thermal motion. The driving force of diffusion is a particle-concentration gradient. The current resulting from diffusion is proportional to the particle-concentration gradient. It increases exponentially as a function of the voltage applied across the solar-cell junction. The exponential term is directly related to the $Fermi - Dirac$ distribution function, $f(E)$, which describes the ratio of states occupied by an electron to the other allowed states at a given energy E.

An increase in temperature increases the collision rate of charged particles with the vibrating atoms of molecular lattices. As the number of collisions increases, particle mobility decreases, resulting in degradation of junction efficiency with increasing temperature [10].

© Fernadus Mamoudi, 2016 _ All rights reserved

Recombination is a phenomenon that strongly determines solar-cell efficiency because it reduces the collected current and consequently the current used from the solar cell. In fact, any electron present in the conduction band is in an unstable state and will eventually stabilize at a lower-energy position in the valence band. When this occurs, the electron occupies a vacant position in the valence band, thereby effectively eliminating a hole. This process is called recombination. There are three main types of recombination in the bulk of a monocrystalline semiconductor.

- Direct recombination
- Auger recombination
- Shockley-Read-Hall (SRH) recombination

The last recombination mechanism (SRH) is the most important for the solar cell because it is the dominant recombination process in semiconductors under most operating conditions. When the crystal is impure because of foreign atoms, defects occur in the crystal lattice. These recombination centers introduce allowed trap states. An electron can be trapped in such a defect and recombine with a hole attracted by the trapped electron. As a result, the excess energy is dissipated into the lattice as heat [11].

The photogeneration rate is often much higher than the recombination rate, so the recombination effect can be considered negligible. However, the recombination rate strongly determines the saturation-current density. A high saturation-current density has a detrimental effect on solar-cell voltage and therefore on its energy-conversion efficiency.

I.3 .2 .2 Solar Junction at Equilibrium

When p-type and n-type semiconductors are brought together, the large difference in electron and hole concentrations between the two regions first causes a diffusion current of electrons from the n-type material across the metallurgical junction (the interface between the n-type and p-type regions) toward the p-type material, and conversely a diffusion current of holes from the p-type material toward the n-type material. Because of this diffusion process in the region near the metallurgical junction, this region becomes almost completely depleted of mobile charge carriers. The depletion of charge carriers creates a space-charge region, SCR, also called the depletion region. The regions outside the SCR, in which charge neutrality is preserved, are referred to as quasi-neutral regions. The SCR around the metallurgical junction results from the formation of an internal electric field that forces charge carriers to move in the direction opposite to that of the concentration gradient. The diffusion currents continue to flow until the forces acting on the charge carriers (the concentration gradient and the internal electric field) compensate each other. At that moment, the driving force for charge transport disappears and no current flows through the p-n junction [12].

The p-n junction represents a system of charged particles in diffusion equilibrium in which the electrochemical potential is constant and independent of position. Because of the electric field,

© Ferdaous Masmoudi, 2016 – All rights reserved

an electrostatic potential difference is created between the boundaries of the space-charge region. Across the depletion region, changes in charge-carrier concentration are compensated by changes in electrostatic potential. In the quasi-neutral regions, the electron and hole concentrations are the same as in isolated doped semiconductors.

In the depletion region of the n-type semiconductor, it is the concentration of positively charged donor atoms N_D that determines the space charge in this region. In the p-type semiconductor, the concentration of negatively charged acceptor atoms N_A determines the space charge in the depletion region.

I.3 .2 .3 Solar Junction under Illumination

When a p-n junction is illuminated, additional electron-hole pairs are generated in the semiconductor. The concentration of minority carriers (electrons in the p-type region and holes in the n-type region) increases sharply. This increase in minority-carrier concentration causes them to flow through the depletion region toward the quasi-neutral regions. Electrons flow from the p-type region toward the n-type region and holes from the n-type region toward the p-type region. The flow of photogenerated carriers causes the photogeneration current I_{ph}, which is added to the thermal-generation current I_{gen}. When no external contact is established between the n-type and p-type regions (the junction is open-circuited), no current can flow inside the p-n junction. This means that the current resulting from the flow of photogenerated and thermally generated carriers must be balanced by the reverse recombination current [7].

The recombination current I_{rec} increases as the electrostatic-potential barrier across the depletion region decreases. The electrostatic-potential barrier across the junction is lowered by an amount V_{oc} (where V_{oc} denotes the open-circuit voltage). Under illumination, when the n-type and p-type regions are short-circuited, the photogenerated current flows through the external circuit. Under the short-circuit condition, the electrostatic-potential barrier does not change, but the strong variation of the quasi-Fermi level inside the depletion region confirms that current flows inside the semiconductor. When a load is connected to the terminals of the p-n junction, only a fraction of the photogenerated current flows through the external circuit. The electrochemical-potential difference between the n-type region and the p-type region is reduced by a voltage drop across the load. This, in turn, reduces the electrostatic potential below the depletion region, resulting in an increase in the recombination current. In the superposition approximation, the net current flowing through the load is determined as the sum of the thermal- and photonic-generation currents and the recombination current. The voltage drop across the load can be simulated by applying a forward-bias voltage to the junction. Consequently, the equation describing the behavior of the junction under applied voltage is included to describe the net current under p-n-junction illumination.

$$I(V) = I_{rec}(V) - I_{gen} - I_{ph} \tag{I.1}$$

Equation (I.1) is called the *Shockley* equation, which describes the current-voltage ($I - V$) characteristic of an ideal p-n diode. It is the fundamental equation of microelectronic-

© Ferdaous Masmoudi, 2016 _ All rights reserved

device physics. The illuminated $I-V$ characteristic of the p-n junction is the same as the dark characteristic, but it is shifted downward by the photogenerated-current density I_{ph}. The detailed derivation of the photogenerated-current density of the p-n junction is presented in the literature [35]. Its value under a uniform generation rate, G_u, is

$$I_{ph} = q \cdot A \cdot G_u \cdot (L_N + W + L_P) \tag{I.2}$$

With:

$$G_u = \alpha \cdot N_u \cdot e^{-\alpha X} \tag{I.3}$$

where:

- L_N: minority-carrier diffusion length for electrons.
- L_P: minority-carrier diffusion length for holes.
- W: width of the depletion region.
- α: absorption coefficient in surface units (cm^{-1}).
- X: depth distance in the semiconductor material.
- N_u: uniform photon flux at the surface (photons/surface unit/s).
- A: cell surface area.
- q: charge of an electron.

This means that only carriers generated in the depletion region and in the regions extending up to the minority-carrier diffusion length from the depletion region contribute to the photogenerated current. When designing the thickness of a solar cell, the absorber thickness must not be greater than the region from which carriers contribute to the photogenerated current, where I_s is the saturation-current density of the p-n junction, given by:

$$I_s = q n_i^2 \left(\frac{D_N}{L_N N_A} + \frac{D_P}{L_P N_D} \right) \tag{I.4}$$

With:

- D_N: diffusion constant of electrons in the P region.
- D_p: diffusion constant of holes in the N region.
- N_A: acceptor concentration.
- N_D: donor concentration.
- n_i: intrinsic concentration.

© Ferdaous Mesmoudi, 2016 _ All rights reserved

The detailed derivation of the saturation-current density of the p-n junction is available in the literature [7]. The saturation-current density depends in a complex manner on the fundamental semiconductor parameters. Ideally, the saturation-current density should be as low as possible, and this requires an optimal and balanced design of the p-type and n-type semiconductor properties. For example, an increase in dopant concentration decreases the minority-carrier diffusion length; this means that the optimal product of these two quantities requires a delicate balance between these two properties.

The recombination of majority carriers due to the diffusion of minority carriers injected into most of the quasi-neutral regions causes a decrease in the majority-carrier concentration compared with equilibrium. The decrease in majority-carrier concentration is compensated by the flow of majority carriers from the electrodes into the bulk. In this way, current flows through the p-n junction under forward-bias voltage. For high reverse-bias voltage, the *Boltzmann* factor in Equation I.1 becomes very small and can be neglected. The current density is given by:

$$I(V) = -I_s - I_{ph} \tag{I.5}$$

and I_s represents the flow of thermally generated minority carriers through the junction.

I.3 .3 Electrical Losses in the Solar Cell

Solar-cell efficiency is limited by a set of losses caused by various phenomena (Figure I.5). Optical losses are not part of our research. We are interested only in electrical losses.

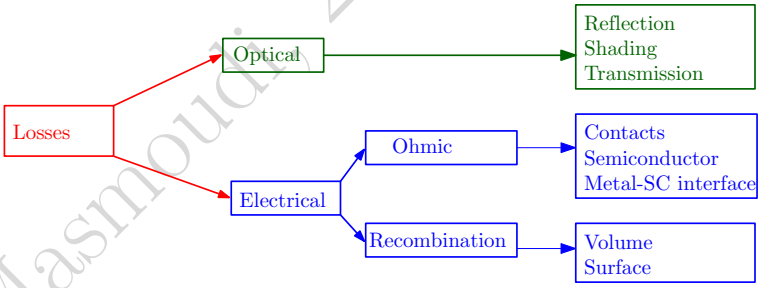


Figure I.5: Electrical losses in the solar cell.

Ohmic Losses

There are electrical losses in the fingers of the front metallic-conductor grid on the cell surface. In addition, ohmic losses also occur in the semiconductor material because the conductivity of the doped material is limited. High currents must be directed toward the front contacts, particularly with thin emitters. Finally, losses exist at the metal/semiconductor junction (Schottky contact).

Recombination Losses

The most important mechanism is recombination due to imperfection. It occurs when the theoretically ideal crystal is impure because of foreign atoms, errors in the crystal structure, or similar effects. In this case, the forbidden band is no longer empty because it contains additional levels. For an electron, the additional levels act like step levels on which a descent into the valence band becomes easier and therefore more probable. Recombination centers caused by

© Ferdaous Masmoudi 2016 – All rights reserved

foreign atoms are also called traps. In addition to foreign atoms, crystal errors such as a vacant lattice site or crystal displacements also lead to increased recombination. A crystal surface is a disturbance of the infinitely extended ideal crystal. The electrons of the outer atoms do not find bonding partners and necessarily remain in open bonds. These then lead to undesirable surface recombination.

I.4 Parameters and Characteristics of a Solar Cell

I.4 .1 Reference and Operating Systems

Figures I.6.a and I.6.b present two reference systems (Load/Generator) for four-quadrant operation of a p-n junction in the dark and under illumination.

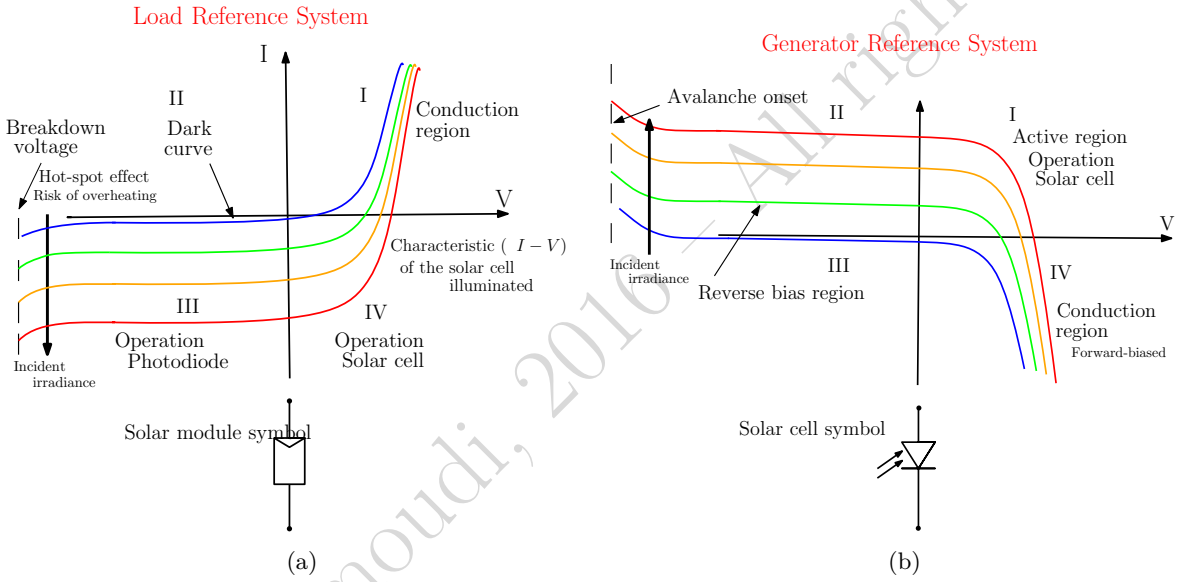


Figure I.6: Four-quadrant $(I-V)$ characteristics of the solar cell according to the reference system. (a) Load reference system. (b) Generator reference system.

In the load reference system (Figure I.6.a), the voltage V is applied to the device, and the current I, considered positive, flows from the voltage source toward the p-n junction. As long as no light shines on the p-n junction, it behaves as an unbiased diode. Only under reverse voltage do small reverse-current flows occur, often called dark currents. As soon as light shines on the diode, a photoelectric current independent of the voltage V is added to the diode's $(I-V)$ characteristic curve. Because it flows in the opposite direction, it shifts the $(I-V)$ curve downward. The use of the photodiode in quadrant III is called photodiode operation. Photodiodes are generally used with a reverse voltage, for example, to serve as detectors for optical-data receivers. In quadrant IV, the photodiode is used as a solar cell: with a positive applied voltage, the result is a negative current.

The characteristic curve of a solar cell corresponds to the principle of a p-n junction and, more specifically, a photodiode. However, with the solar cell, the generator reference system is

© Ferdaous Masmoudi, 2016 – All rights reserved

most often selected. In the generator reference system, the voltage V is measured at the energy source, which is the solar cell, and the positive current I flows from the cell toward the external load. Compared with Figure I.6.a, the voltage axis is retained; only the sign of the current is reversed. Energy generation now takes place in the first quadrant and, for this reason, only the first-quadrant characteristic curve of the solar cell is usually represented. Instead of the photodiode symbol, the special solar-cell symbol has become standard (see Figure I.6).

I.4 .2 Electrical Parameters of the Solar Cell

The main parameters used to characterize solar-cell performance are the peak power P_m, short-circuit current I_{sc}, open-circuit voltage V_{oc}, and fill factor FF. These parameters are determined from the electrical $(I-V)$ characteristic under illumination, as illustrated in Figure I.7; the conversion efficiency η can be determined from these parameters.

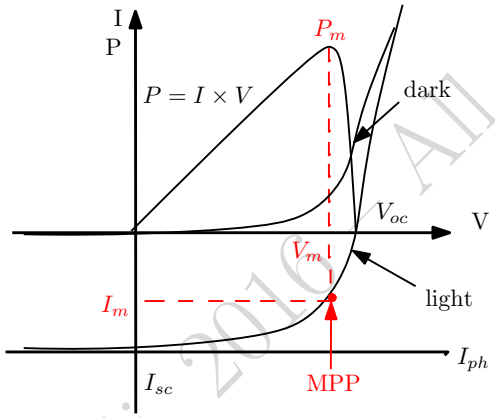


Figure I.7: Characteristic of a solar cell in the dark and under illumination.

Short-Circuit Current

The short-circuit current I_{sc} is the current that flows through the external circuit when the solar-cell electrodes are short-circuited. The short-circuit current of a solar cell depends on the incident photon-flux density, determined by the spectrum of the incident light. During measurements of conventional solar cells, the spectrum is normalized to the $AM1.5$ spectrum. In the ideal case, I_{sc} is equal to the photonic current I_{ph} ($I_{sc} = I_{ph}$); in a real solar cell, electrical losses influence the short-circuit current.

In laboratory monocrystalline solar cells, a current I_{sc} greater than $42 mA/cm^2$ is measured, whereas the commercial solar cell has an I_{sc} current greater than 35 mA/cm^2.

Open-Circuit Voltage

The open-circuit voltage is the voltage at which no current flows in the external circuit. It is the maximum voltage that a solar cell can supply. V_{oc} corresponds to the forward-bias voltage during which the dark current compensates the photocurrent. In the ideal case, the open-circuit voltage can be calculated from the following equation:

$$V_{oc} = \frac{KT}{q} \ln\left(1 + \frac{I_{ph}}{I_s}\right) \tag{I.6}$$

© Ferdaous Masmoudi, 2016 All rights reserved

This equation shows that V_{oc} depends on the photogenerated-current density I_{ph} and the saturation current I_s of the solar cell.

The saturation current I_s depends on the recombination rate in the solar cell. Consequently, V_{oc} is a measure of the amount of recombination in the device.

Laboratory monocrystalline-silicon solar cells have a V_{oc} voltage of about 720 mV under standard AM1.5 conditions, whereas commercialized solar cells generally have a V_{oc} voltage greater than 600 mV.

Maximum Power Point

The solar cell supplies different powers in relation to the actual operating point at which it is operated. The point at which the power reaches a maximum value is called the maximum power point MPP (*Maximum Power Point*).

Since the power P at an operating point is equal to the product $V \times I$, this power reaches its maximum P_m at the MPP. This case is represented in Figure I.7; the associated current and voltage values at the MPP are called I_m and V_m.

Fill Factor

The fill factor FF describes the relationship between the maximum power P_m at the MPP and the product of the open-circuit voltage V_{oc} and the short-circuit current I_{sc} (see Figure I.7). The FF indicates the size of the area at the MPP operating point relative to the area $V_{oc} \times I_{sc}$. The fill factor can be expressed as:

$$FF = \frac{V_m I_m}{V_{oc} I_{sc}} = \frac{P_m}{V_{oc} I_{sc}} \tag{I.7}$$

The fill factor is a measure of cell quality. Typical values for monocrystalline-silicon cells range from 0.75 to 0.85, and for thin-film cells they range from 0.6 to 0.75.

Conversion Efficiency

The conversion efficiency η is calculated as the ratio between the maximum generated power P_m and the incident optical power P_{opt}. The irradiance value P_{opt} of 1000 W/m^2 for the $AM1.5$ spectrum has become a standard for measuring the conversion efficiency of solar cells:

$$\eta = \frac{P_m}{P_{opt}} = \frac{V_m I_m}{P_{opt}} = \frac{V_{oc} I_{sc} FF}{P_{opt}} \tag{I.8}$$

Typical values of the conversion efficiency of a crystalline-silicon solar cell lie in the range from 17% to 21%.

I.4 .3 Test Conditions and Manufacturer Data

I.4 .3 .1 Standard Test Conditions: *STC*

Problems in comparing the measured characteristics of different solar cells led to the concept of Standard Test Conditions STC. In fact, using this reference standard to test solar-cell performance makes it possible to compare them objectively within restricted error and uncertainty limits.

© Ferdaous Masmoudi, 2016 - All rights reserved

This performance test is covered by multiple European (IEC 60904-1) and international (ASTM E948) standards and provides a recognized method for testing and reporting the electrical behavior of photovoltaic cells.

The STC includes cell temperature, incident global irradiance, and the spectral distribution of the reference light. Table I.3 summarizes the specifications of the STC.

Table I.3: Specifications of the Standard Test Conditions

Test Conditions	Symbol	Value
Irradiance	G_{ref}	1000 W/m^2
Cell temperature	T_{ref}	25 °C
Light spectrum	AM_{ref}	1.5

I.4 .3 .2 Nominal Operating Cell Temperature: *NOCT*

Temperature strongly influences the performance of a PV module. While the level of incident irradiance can easily be determined by measuring it with a pyranometer, the temperature reached inside the cell is very difficult to evaluate.

In order to provide an estimate of the average operating temperature of the cell junction, manufacturers also provide, together with the STC performance, the Nominal Operating Cell Temperature, called $NOCT$. This value corresponds to the performance of a cell under the conditions summarized in Table I.4.

Table I.4: Specifications of the Nominal Operating Conditions

Test Conditions	Symbol	Value
Irradiance	G_{NOCT}	800 W/m^2
Ambient temperature	T_a	20 °C
External wind speed	$Vitesse_{Vent}$	1 m/s

Simplified thermal models use a linear relationship between the incident solar irradiance G and the difference between the cell-junction temperature and the ambient temperature $(T - T_a)$, where the NOCT is used as a reference point:

$$T = T_a + \left(\frac{T_{NOCT} - 20}{800} G\right) \tag{I.9}$$

I.4 .3 .3 Manufacturer Data

The photovoltaic cell (reference cell) proposed for study in the simulation and experimental work is the monocrystalline cell marketed under the reference *JA Solar, JAC M5SF-2*.

The electrical performance of the photovoltaic cell provided by the manufacturer consists of measuring the electrical current as a function of voltage, i.e. the electrical $(I - V)$ characteristic, when it is illuminated by an appropriate stable light source and maintained at a fixed temperature level, that is, under the Standard Test Conditions, STC.

© Ferdaous Mastouri 2016 – All rights reserved

Table I.5: Electrical specifications of the "JAC M5SF-2" solar cell under STC

Electrical quantities	Symbol	Value
Maximum power	P_{mref}	2.97 W
Voltage at the maximum power point	V_{mref}	0.537 V
Current at the maximum power point	I_{mref}	5.531 A
Open-circuit voltage	V_{ocref}	0.637 V
Short-circuit current	I_{scref}	5.888 A
Power temperature coefficient	K_p	-0.370 % /K
Voltage temperature coefficient	K_v	-0.241 % /K
Current temperature coefficient	K_i	0.033 % /K
$\frac{dI}{dV}\|_{I=I_{sc}}$	$\Delta_{I_{sc}}$	-0.003945 S
$\frac{dI}{dV}\|_{V=V_{oc}}$	$\Delta_{V_{oc}}$	-150.6667 S
Fill factor (in %)	FF	79.19 %
Efficiency	η	19.2~20 %
Nominal operating cell temperature	$NOCT$	45 °C

The electrical specifications of the reference cell under STC are summarized in Table I.5.

The photovoltaic-cell manufacturer provides, in the product datasheet, the evolution of the PV-cell $(I-V)$ characteristic under STC, as shown in Figure I.8.

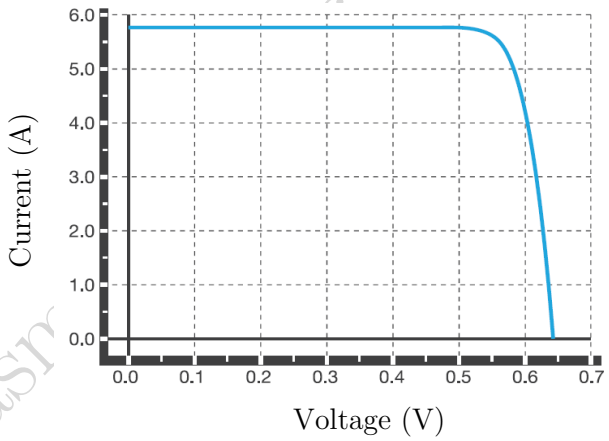


Figure I.8: Manufacturer electrical $(I-V)$ characteristic of the "JAC M5SF-2" solar cell under STC.

Two additional parameters must be deduced from the $(I-V)$ curve of Figure I.8 provided in the datasheet: the derivative of current with respect to voltage near the short-circuit point $\frac{dI}{dV}|_{(0,I_{sc})}$ and the derivative of current with respect to voltage near the open-circuit point $\frac{dI}{dV}|_{(V_{oc},0)}$. In this case, a commonly used software package called "*Scanlt*" is used to reproduce the datasheet curve and define the derivatives at the indicated points. The calculated parameters are added to the electrical specifications in Table I.5.

© Ferdaous Masr — All rights reserved

I.5 Effect of Irradiance and Temperature on Solar-Cell Performance

The PV-module installer is generally not interested in the nominal power (known as peak power) given by the supplier under STC. In fact, the Standard Test Conditions (STC) of PV modules are not representative of their actual operating conditions. For example, higher levels of incident solar radiation can cause the temperature of a module to increase by several degrees above the STC temperature (25°C), which means degradation of module performance. In order to efficiently estimate real-time energy production from a set of ambient data and parameters, it is essential to account for the effect of variations in temperature and irradiance on solar-generator efficiency. Figure I.9 shows the $(I-V)$ characteristics of the reference solar cell under STC, with a decrease in irradiance to 500 W/m^2 and then with an increase in temperature to 50°C.

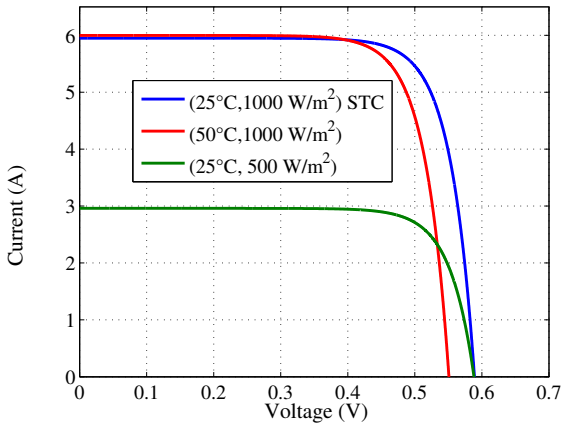


Figure I.9: Electrical $(I-V)$ characteristics of the "JAC M5SF-2" solar cell under several climatic conditions.

I.5 .1 Effect of Irradiance

Intuitively, the performance of a solar cell decreases considerably as the intensity of the light incident on the module decreases relative to STC. The cause of this degradation is due to the dependence of the open-circuit voltage and short-circuit current on the incident light, as described in Section 1.4.2. However, evaluating the extent of this reduction is not trivial, since the solar-module manufacturer does not explicitly provide an efficiency-reduction factor for all light-intensity levels. Nevertheless, Figure I.9 explicitly shows the proportionality of the current with respect to irradiance. Indeed, at an illumination of 500 W/m^2, the current becomes almost half that of the characteristic at 1000 W/m^2 (STC). This is due to the proportionality of the generated photonic current I_{ph} to the incident light; this result is shown physically (see Section 1.3.2.3) and leads to the establishment of Relation I.10. In the case of the ideal solar-cell model, the photonic current exactly coincides with the short-circuit current and Relation I.10 can therefore be used for any current. For the more accurate models, several types of current

© Ferdaous Mamouda, all rights reserved

losses exist, especially at the junction, which leads to more complicated current expressions.

$$I_{ph}(G,T) = \frac{G}{G_{ref}} I_{ph}(G_{ref},T) \tag{I.10}$$

Where

- G is the current irradiance.
- T is the current junction temperature.
- $\frac{G}{G_{ref}}$ is the proportionality factor.

I.5 .2 Effect of Temperature

Similarly, the behavior of solar modules with respect to temperature changes is also of great interest. Figure I.9 shows the decrease in the open-circuit voltage V_{oc} at a temperature of 50°C compared with the characteristic at 25°C (STC), and the same applies to all voltage values. On the other hand, it can be observed that the current values increase slightly with increasing temperature.

Roughly, the slight increase in short-circuit current at higher temperatures is completely compensated by the marked decrease in open-circuit voltage. The overall effect is a general linear decrease in the resulting maximum power and therefore a decrease in cell efficiency and fill factor. This effect is due to an increase in intrinsic-carrier concentration at higher temperatures, which in turn leads to an increase in the intensity I_s of the reverse saturation current, which represents a measure of carrier leakage across the cell junction. As explained previously, the exponential temperature dependence of I_s is the main cause of the linear reduction in V_{oc} with temperature.

Furthermore, the slight increase in generated current is due to a moderate increase in photoelectric current resulting from an increase in the number of thermally generated carriers. The overall reduction in power at high temperature shows that cold and sunny climates are the best environments for installing a solar system.

The deviation of a module characteristic due to a temperature change relative to the reference state (STC) is expressed by the temperature coefficients (K_i, K_v, K_p) given by the manufacturer in its technical document. When the values of the temperature coefficients are known, the value of certain parameters can be estimated by applying the following generalized relationships: For currents:

$$I(G_{ref},T) = I_{ref} + K_i(T - T_{ref}) \tag{I.11}$$

For voltages:

$$V(G_{ref},T) = V_{ref} + K_v(T_c - T_{ref}) \tag{I.12}$$

I.6 Conclusion

This first chapter provided an overview of the different technologies and applications of the photovoltaic solar cell, as well as a study of its fundamental characteristics. First, an overview

© Ferdaous Maghnoudi, 2016 – All rights reserved

of the history of the solar cell and the development of its technologies, together with its various applications, was presented. Subsequently, the fundamentals of semiconductor physics were reviewed, and the structure and operating mode of a monocrystalline solar cell in the dark and under illumination were studied. The following part focused on the characteristic parameters of the solar cell as well as on the manufacturer data under the Standard Test Conditions "STC" and under the Nominal Operating Cell Temperature conditions "NOCT".

© Ferdaous Masmoudi, 2016 – All rights reserved

Chapter II

Modeling of the Photovoltaic Solar Cell

Abstract: *This chapter deals with the modeling of the photovoltaic solar cell using five equivalent electrical models: the ideal model, the one-series-resistance model, the one-diode model, the two-diode model, and the three-diode model. For each of these models, the determination of its unknown internal parameters is carried out according to two search methods, namely: (i) the identification method, and (ii) the fitting method. This chapter concludes with simulation results concerning the comparison between the different models studied as well as their theoretical and experimental validations.*

Keywords: Photovoltaic solar cell
Identification method, fitting method
Equivalent electrical models,
Ideal model,
One-series-resistance model (Simplified),
One-diode model,
Two-diode model,
Three-diode model (multi-diode),
Newton algorithms, Genetic Algorithm, Evolved Gradient Algorithm,

© Ferdaous Masmoudi, 2016 – All rights reserved

II.1 Introduction

The best use of the energy provided by a PV generator and the optimization of its efficiency require the development of an appropriate power-conversion system, followed by the development of an effective control and command technique that is consistent with the electrical characteristics of the photovoltaic generator used. At this level, the importance of the modeling and simulation phases becomes apparent. Indeed, the association of solar modules with conversion stages requires a good knowledge of the behavior of these modules, which may, in the event of improper use, damage or reduce the efficiency of the system. Simulation makes it possible to reproduce the various real physical phenomena that may occur, thereby allowing an optimally performing system to be designed. This step therefore proves indispensable before undertaking any experimental implementation or manufacturing procedure, because it saves losses of time, effort, and especially money.

In order to be able to develop a simulation model of a photovoltaic conversion system that integrates the photovoltaic solar generator, the DC–DC or DC–AC adaptation stage, the load and the storage system together with its control device, it is essential to define an equivalent electrical model of the photovoltaic generator.

In the literature, several mathematical models describe the operation and behavior of the photovoltaic generator. To date, and after several years of research in this field, there has been no definitive model that perfectly describes the operation occurring inside the solar wafer. Indeed, the solar cell is a dynamic multiphysics device. Moreover, a multitude of interactions take place around and across the solar junction. Each solar-cell model design aims to highlight a specific behavior of the device. By considering certain assumptions, it is possible to neglect secondary effects in order to focus only on the main effect under study. Countless types of models can be found, including, for example, chemical models [14], physical models [15], thermal models [16], optical models [17], as well as electrical models [18, 19, 20, 21], which constitute the main subject of this study.

The main objective of this chapter is the development of different models that can be implemented. In order to define an equivalent electrical model of the photovoltaic cell, a system of equations must be established and solved to determine the unknown parameters that characterize the properties of the cell.

A proper definition of an equivalent electrical model involves determining the internal parameters of the model that fit the PV generator of interest. For this purpose, two approaches are proposed in the literature:

- Parametric identification approach [22]: based on data corresponding to key points obtained mainly from the technical document (datasheet) of the photovoltaic generator concerned.

- Curve-fitting approach [23]: based on the best fit of the $(I-V)$ or $(P-V)$ curves obtained by means of the model to the reference data resulting from PV-module tests.

© Ferdaous Masmoudi, 2016 _ All rights reserved

A multitude of equivalent electrical models have been studied in the literature. The ideal model was discussed by "*VILLALVA*" [24], who proposed identifying the parameter I_s instead of using the physical relation as a function of the band energy. The one-series-resistance model was proposed by "*XIAO*" and "*DUNFORD*" [25], who assumed that all parameters depend on irradiance and temperature. The one-diode model was initially proposed by "*KENNERUD*" [26], then by "*PHANG*" and "*CHAN*" [27], who suggested the identification method based on experimental measurements. This model has been widely discussed in the literature, but no one took climatic variation into account. The two-diode model was also proposed by "*PHANG*" and "*CHAN*" [28], where they used rather complicated mathematical formulations but obtained more accurate results. "*GOW*" and "*MANNING*" [29] also used the double-diode model, but by resorting to identification constants as well as experimental measurements. This model has also been widely discussed while neglecting the effect of climatic variation. As for multi-diode models, their appearance is recent and related to the spread of evolutionary algorithms. We cite "*JIN JUN*" [30], who proposed a generalized multidimensional model, and "*KHANNA*" [31], who studied the triple-diode model; both used the PSO algorithm (*Particle Swarm Optimization*). Other works target multijunction cells and use other algorithms, without, however, taking variations in climatic conditions into account.

In this chapter, a brief introduction to the methods for searching for internal parameters is presented, together with an experimental measurement method for the solar-cell $(I - V)$ characteristic. Subsequently, five equivalent electrical models are detailed, with their internal parameters searched for by one of the two methods while considering the variation of the junction temperature T and the variation of irradiance G. The results of the search algorithms will make it possible to evaluate the internal parameters of each model as a function of temperature variation. These parameters will be used to implement the solar-cell models in Matlab-Simulink/SimpowerSystems. This chapter concludes with a comparative study of the different models using the simulation results.

II.2 Methods and Experiments

II.2 .1 Principle of the Internal-Parameter Identification Procedure

The fundamental principle adopted to identify the internal parameters of the photovoltaic cell is to use the values of the electrical characteristics $\left(V_{oc}, I_{sc}, V_m, I_m, K_i, K_v, \Delta_{I_{sc}}, \Delta_{V_{oc}}\right)$ provided in the manufacturer's datasheet or directly measured from the PV cell. Depending on the selected solar-cell model, up to six unknown electrical parameters may need to be identified to define the model. The determination of these quantities is based on solving a system of nonlinear equations while considering only the datasheet information reported in Table I.5.

The electrical-characteristic $(I - V)$ curve of the solar cell is presented in Figure II.1. It illustrates the key points for the parametric-identification principle, namely:

- The short-circuit point, with coordinates $(V, I) = (0, I_{sc})$.

© Fernando Masmoudi, 2016 - All rights reserved

- The open-circuit point, with coordinates $(V, I) = (V_{oc}, 0)$.
- The maximum-power point, with coordinates $(V, I) = (V_m, I_m)$.
- The slope of the $(I - V)$ characteristic in the vicinity of the short-circuit point $\left.\frac{dI}{dV}\right|_{I=I_{sc}}$.
- The slope of the $(I - V)$ characteristic in the vicinity of the open-circuit point $\left.\frac{dI}{dV}\right|_{V=V_{oc}}$.
- The slope of the $(P - V)$ characteristic in the vicinity of maximum power $\left.\frac{dP}{dV}\right|_{P=P_m}$.

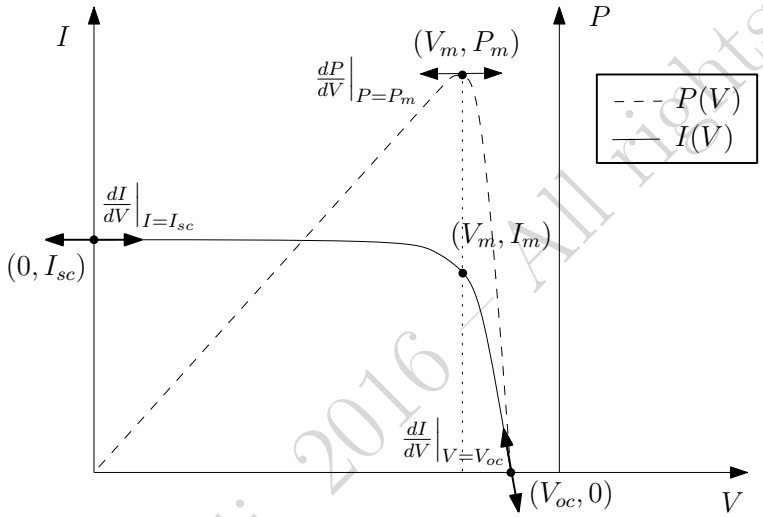


Figure II.1: Key points of the solar-cell $(I - V)$ characteristic.

In order to formulate the slopes of the $(I-V)$ and $(P-V)$ characteristics, and starting from the implicit relation linking I and V and from the expression of the power P:

$$I = f(I, V) \tag{II.1}$$

$$P = I.V \tag{II.2}$$

we write:

$$dI = \frac{\partial f}{\partial V} dV + \frac{\partial f}{\partial I} dI \tag{II.3}$$

The derivative of the current I with respect to the voltage V is written as follows:

$$\frac{dI}{dV} = \frac{\dfrac{\partial f}{\partial V}}{1 - \dfrac{\partial f}{\partial I}} \tag{II.4}$$

Thus, the derivative of the power P with respect to the voltage V is written as follows:

$$\frac{dP}{dV} = I + V \frac{\dfrac{\partial f}{\partial V}}{1 - \dfrac{\partial f}{\partial I}} \tag{II.5}$$

© Ferdaous Masmoudi, 2016 - All rights reserved

With the development of numerical computing tools and platforms, the iterative calculation process becomes a fairly accessible task. Depending on the selected programming tool, a program can be developed that solves nonlinear equations to a desired accuracy. This work proposes two calculation methods in the MATLAB environment:

1. Either the predefined nonlinear-equation-solving functions in the MATLAB environment are used through the *Optimization Toolbox*[1], such as the commands *fzero* and *fsolve*.
2. Or a recursive calculation program is developed based on one or more mathematical optimization programming theories. In this work, the *Newton* method (*Newton-Raphson*) is proposed.

II.2 .2 Principle of the Curve-Fitting Procedure

Another approach for searching for the internal parameters of solar-cell models consists of extracting them by means of the curve-fitting method.
Curve fitting, known as "*Curve fitting*", is a process for constructing a curve or mathematical function that provides the best fit to a series of reference data points. It is also called parameter fitting (the "Franglais" expression "*fitter* a curve" may also be used, meaning "to fit a curve").

For curve fitting, an optimization algorithm is used to find the set of parameters (p_1, p_2, $\cdots$, p_n) such that the performance criterion (or evaluation) is minimal. In this case, error-minimization algorithms are considered.
For modeling, a function f with n parameters (p_1, p_2, $\cdots$, p_n) is defined, according to the selected model, linking the voltage V (abscissa) to the current I (ordinate), such that:

$$I = f(p_1, p_2, \cdots, p_n, I, V) \tag{II.6}$$

The simulation provides:

$$\begin{bmatrix} (x_1, y_1^{sim}) \\ (x_2, y_2^{sim}) \\ \vdots \\ (x_m, y_m^{sim}) \end{bmatrix}$$

which are compared with the m reference points:

$$\begin{bmatrix} (x_1, y_1^{ref}) \\ (x_2, y_2^{ref}) \\ \vdots \\ (x_m, y_m^{ref}) \end{bmatrix}$$

Depending on the nature of the evaluation criterion, two types of fitting are distinguished:

- Algebraic fitting aims to minimize the vertical deviation (ordinate) between the mathematical-model curve and the reference curve inserted in the form of a database. The evaluation criterion is expressed by $J = \min_{1 \le i \le m} \left(\mid y^{ref} - y^{sim} \mid \right)$.

[1]For more information about this toolbox, type >> *optimtool* in the MATLAB command window, or consult the online *Mathworks* guide: http://www.mathworks.com/products/optimization/

© Ferdaous Masmoudi, 2016 - All rights reserved

- Geometric fitting aims to minimize the distance perpendicular to the mathematical-model curve. In this case, there are many formulations. Quadratic regression may be used by minimizing the criterion $J = \sum_{i=1}^{m} (y^{ref} - y^{sim})^2$.

In general, optimization methods can be divided into two different categories: exact methods (Gauss, Newton, Gradient, etc.) and non-exact methods (evolutionary algorithms). Research has shown that when the complexity of a problem increases, non-exact methods are more appropriate than exact methods.

Non-exact methods, such as numerical, heuristic, and metaheuristic methods, involve fundamental and simplified calculation formulations. Even though they cannot guarantee an optimal solution, most can reach a near-optimal solution.

This work proposes two fitting methods developed from (i) a heuristic algorithm represented by the genetic algorithm and (ii) a metaheuristic algorithm represented by the evolved gradient algorithm. In general, for non-exact optimization methods, an evaluation function is used to assess the performance of a probable solution, often called "fitness". Since, by convention, a higher fitness value denotes a better solution, the fitness function is then defined by $f = \frac{1}{J}$.

The reference data may be obtained either from experimental measurements of the solar cell or from the $(I - V)$ characteristic often plotted in the technical document provided by the manufacturer. The principle of the curve-fitting procedure is explained in Figure II.2.

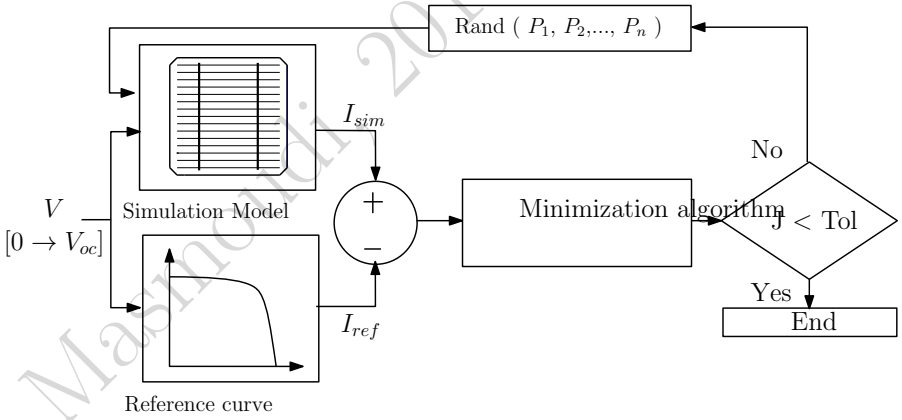


Figure II.2: Explanatory diagram of the curve-fitting method.

II.2 .3 Experimental Measurements of the Solar Cell

In order to experimentally validate the models implemented later in this chapter, a practical test bench was developed to investigate the reference solar cell marketed under the designation JA M5SF-2 (Table I.5). The measurements are intended mainly to plot the experimental $(I - V)$ characteristic of an individual solar cell and subsequently compare it with the simulation results of the developed models. The experimental work is described by the explanatory diagram in Figure II.3.

© Ferdaous Masmoudi 2016 - All rights reserved

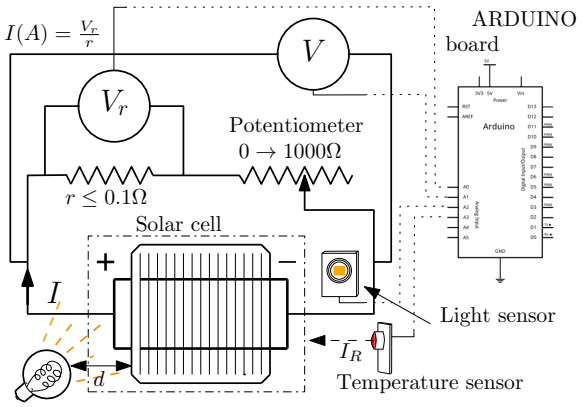


Figure II.3: Explanatory diagram of the measurement method for the "JAC M5SF-2" solar cell.

The test bench shown in Figure II.4 is essentially composed of the following elements:

- A monocrystalline solar cell: JA Solar JAC M5SF-2,
- A light source: full-spectrum lamp,
- Very-low-value resistors: less than 0.1 Ω,
- A voltage sensor: for voltage and current measurement,
- A potentiometer: to change the connected resistance value (0 Ω ∼ 1KΩ),
- A digital light sensor: to measure the value of the incident light,
- An infrared temperature sensor: to measure the cell junction temperature,
- An ARDUINO microcontroller for acquiring the data from the sensors and recording the measurements.

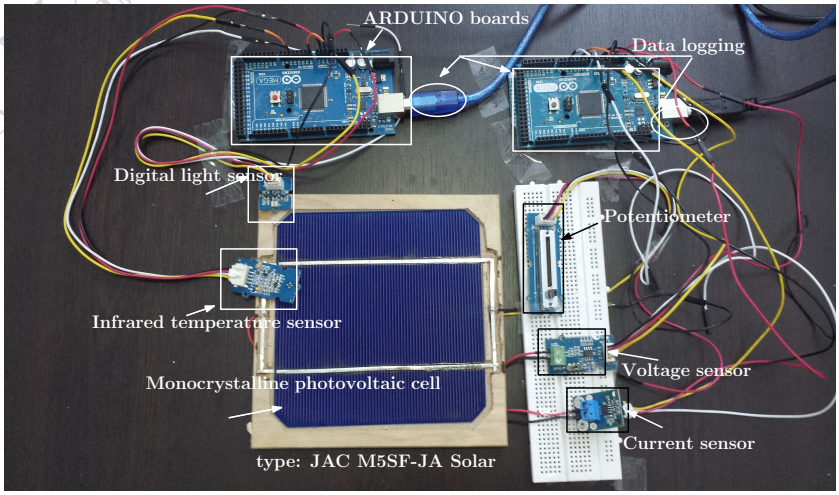


Figure II.4: Experimental test bench of the "JAC M5SF" solar cell.

© Ferdaous Kasmoudi, 2016 – All rights reserved

II.3 Ideal Model

The simplest electrical model of a solar cell is represented by a current source in parallel with a single diode. The configuration of the ideal equivalent electrical circuit of the solar cell is given in Figure II.5. This equivalent model consists of a current source that generates the photogenerated current I_{ph} and a diode carrying a current I_d.

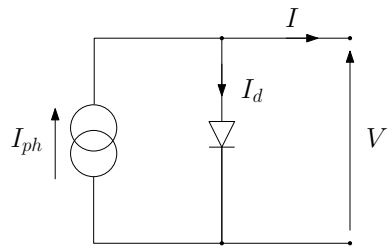


Figure II.5: Equivalent electrical circuit of the ideal model.

The current I delivered by the cell can be expressed in terms of the photocurrent I_{ph} and the current I_d through the diode according to the following relation:

$$I = I_{ph} - I_d \tag{II.7}$$

The relationship between the current I delivered by the cell and the voltage V across its terminals is described by:

$$I = I_{ph} - I_s \left(\exp\left(\frac{V}{nV_t} \right) - 1 \right) \tag{II.8}$$

with:

$$V_t = \frac{kT}{q} \tag{II.9}$$

where:

- I_{ph}: the photocurrent (photoelectric current) generated by the cell,
- I_s: the saturation current of the cell junction,
- n: the diode ideality factor, which ranges from 1 to 2,
- T: the junction temperature during operation (K),
- k: the Boltzmann constant ($k = 1.38 \times 10^{-23}$ J/K),
- q: the charge of an electron ($q = 1.6 \times 10^{-19}$ C).

II.3 .1 Algorithm for Identifying the Unknown Parameters of the Ideal Model

The unknown parameters of the ideal model are I_{ph}, I_s, and n. Searching for these three unknowns requires solving a system of three equations. The identification procedure explained below is adopted at three key points as follows.

© Ferdaous Masmoudi, 2016 _ All rights reserved

By applying Equation II.8 at the short-circuit point, the following relation is obtained:

$$I_{sc} = I_{ph} - I_s \left(\exp\left(\frac{0}{nV_t}\right) - 1 \right) \tag{II.10}$$

At the open-circuit point, Equation II.8 is written as follows:

$$0 = I_{ph} - I_s \left(\exp\left(\frac{V_{oc}}{nV_t}\right) - 1 \right) \tag{II.11}$$

By rewriting Equation II.8 at the maximum-power point, we obtain:

$$I_m = I_{ph} - I_s \left(\exp\left(\frac{V_m}{nV_t}\right) - 1 \right) \tag{II.12}$$

The aim is to simplify the system of equations in order to highlight the unknown parameters. Thus, taking Relation II.10 into account, the photocurrent I_{ph} is expressed as follows:

$$I_{ph} = I_{sc} \tag{II.13}$$

Thus, the saturation current I_s can be expressed using Equation II.11 as follows:

$$I_s = \frac{I_{sc}}{\exp\left(\frac{V_{oc}}{nV_t}\right) - 1} \tag{II.14}$$

Rewriting Equation II.12, with the currents I_{ph} and I_s replaced by their expressions, yields the following relation for the current I_m at the maximum-power point:

$$I_m = I_{sc} \left(1 - \frac{\exp\left(\frac{V_m}{nV_t}\right) - 1}{\exp\left(\frac{V_{oc}}{nV_t}\right) - 1} \right) \tag{II.15}$$

Using Equations II.13 and II.14, the currents I_{ph} and I_s can be readily calculated and determined solely from the information in the manufacturer's datasheet and the unknown n. However, the parameter n is determined by numerically solving Relation II.15. Since the relation is nonlinear and difficult to solve, a numerical algorithm is developed to search for n.

To solve Equation II.15 of the ideal solar-cell model, the MATLAB *fzero* command can be used, or the Newton algorithm can be developed for a single nonlinear equation, expressed as follows for $n_0 = 1$ and $i \in \mathbb{N}$:

$$n_{i+1} = n_i - \frac{g(n_i)}{g'(n_i)} \tag{II.16}$$

with:

$$g(n) = I_m - I_{sc} \left(1 - \frac{\exp\left(\frac{V_m}{nV_t}\right) - 1}{\exp\left(\frac{V_{oc}}{nV_t}\right) - 1} \right) \tag{II.17}$$

and

$$g'(n) = \frac{\partial g(n)}{\partial n} = \frac{(I_{sc} - I_m)V_{oc}}{I_{sc}(n^2 V_t)} \exp\left(\frac{V_{oc}}{nV_t}\right) - \frac{V_m}{n^2 V_t} \exp\left(\frac{V_m}{nV_t}\right) \tag{II.18}$$

Figure II.6 presents the algorithm adopted for identifying the unknown n. The inputs of this algorithm are previously summarized in Table I.5.

© Ferdaous Masrioudi, 2016_ All rights reserved

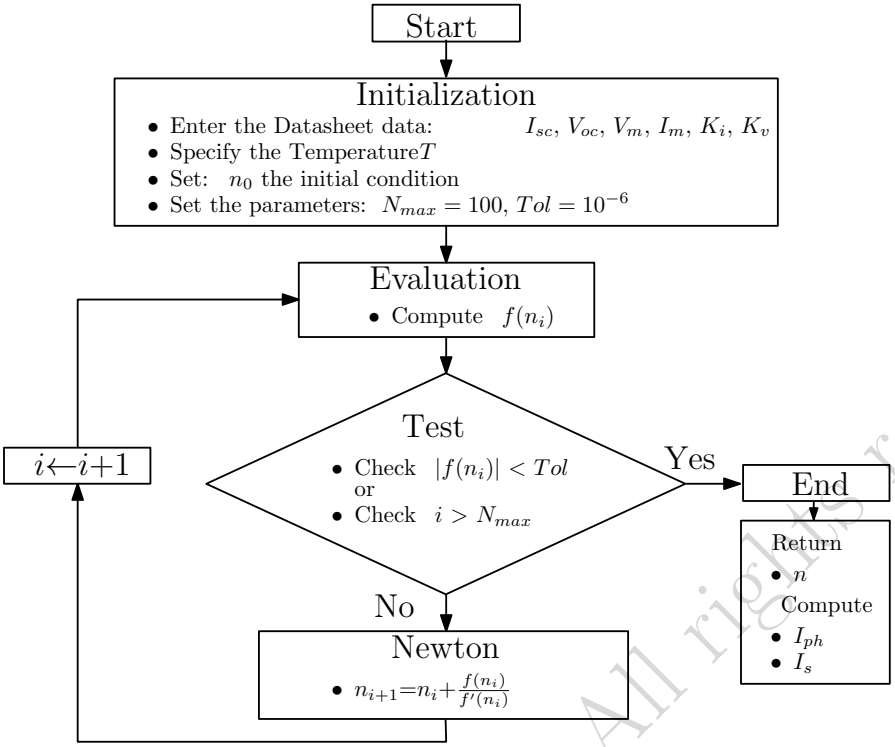


Figure II.6: Search algorithm for the internal parameters of the ideal model.

II.3 .2 Identification Results of the Ideal-Model Parameters under STC

Under standard test conditions, the algorithm input data (I_{sc}, V_{oc}, I_m, V_m) take the reference values from the datasheet summarized in Table I.5 as (I_{scref}, V_{ocref}, I_{mref}, V_{mref}).

The execution[2] of the programs for searching the internal parameters of the ideal model, by inserting the characteristics of the reference monocrystalline cell (JA JAC M5SF-2), makes it possible to obtain the values of the unknown parameters under STC. Since the parameters sought are under STC, they can be denoted by (I_{phref}, I_{sref}, n_{ref}). The results are summarized in Table II.1.

Table II.1: Internal-parameter results for the JAC M5SF-2 cell under STC using the ideal model.

Parameter	*fzero*	*Newton*
I_{phref} (A)	5.8880	5.8880
I_{sref} (A)	1.037×10^{-7}	1.037×10^{-7}
n_{ref}	1.3886	1.3886
N iterations	8	3
Time (s)	0.814	1.62
Method	bisection/interpolation	simple Newton

These results show the convergence of the two algorithms toward the same values. The Newton algorithm converges in a competitive time when compared with the predefined MATLAB

[2]The program is executed on a computer with an Intel(R) Core(TM) i3-3120M CPU @ 2.50 GHz, 4.00 GB RAM, a 64-bit operating system, and an x64 processor.

© Ferdaous Mamouri 2016 – All rights reserved

fzero function. The reduced number of iterations also demonstrates the speed and efficiency of the method. The tolerated accuracy is 10^{-6}, which can be considered sufficiently precise. It is observed that the Newton algorithm performs fewer iterations; however, it consumes more calculation time. This demonstrates the importance of code optimization[3] in computer programming.

II.3 .3 Effect of Temperature and Irradiance on the Internal Parameters of the Ideal Model

The results previously described in Table II.1 represent the internal parameters of the solar cell under STC. However, it was previously shown (I.2.2.8) that under other climatic factors, where the temperature differs from 25°C and the irradiance is no longer 1000 $W.m^{-2}$, the quantities (V_{oc}, I_{sc}, V_m, I_m) take other values, which requires adjusting these quantities before executing the program.

It is assumed that temperature variation causes changes in the quantities related to the internal structure of the cell, for this model $n(T)$, $I_s(T)$, and $I_{ph}(T)$. It is nevertheless important to emphasize that irradiance variation affects only the generated photoelectric current $I_{ph}(G,T)$. Rewriting the general expression II.8 of the ideal model as a function of T and G gives the following relation:

$$I(G,T) = \frac{G}{G_{ref}} I_{ph}(T) - I_s(T)\left(\exp\left(\frac{V(G,T)}{n(T)V_t}\right) - 1\right) \tag{II.19}$$

To execute the algorithm while taking the variation of the junction temperature T into account, the system of equations formed by Relations II.13, II.14, and II.15 is reconsidered, and the factors K_v and K_i provided by the manufacturer are used to adjust the input-parameter values (V_{oc}, I_{sc}, V_m, I_m). It is recalled that for small temperature variations:

$$I_{sc}(T) = I_{scref} + K_i(T - T_{ref}) \tag{II.20}$$

$$V_{oc}(T) = V_{ocref} + K_v(T_c - T_{ref}) \tag{II.21}$$

$$I_m(T) = I_{mref} + K_i(T - T_{ref}) \tag{II.22}$$

$$V_m(T) = V_{mref} + K_v(T - T_{ref}) \tag{II.23}$$

For irradiance variation, the current I_{ph} should be adjusted.

$$I_{ph}(G,T) = \frac{G}{G_{ref}} I_{ph}(T) \tag{II.24}$$

For this ideal model, it can be stated that:

$$I_{ph}(G,T) = \frac{G}{G_{ref}}[I_{scref} + K_i(T - T_{ref})] \tag{II.25}$$

[3]Code optimization (*program optimization*, *software optimization*) is the discipline that teaches the practice of modifying algorithmic code optimally, allowing the program to execute more efficiently while using fewer resources (memory storage, etc.) and consuming less energy.

© Ferdaous Masmoudi 2016 – All rights reserved

Figures II.7.a and II.7.b show the variations of the parameters n and I_s of the reference solar cell as a function of temperature variations.

The $n(T)$ curve has a decreasing shape. According to semiconductor theory [32, 33, 34, 35], the ideality factor n is very close to unity at low doping and high temperatures. However, it can deviate significantly from unity when the doping level increases or when the temperature decreases. The $I_s(T)$ curve is increasing, and its exponential shape is also justified by junction theory.

Figure II.7.c presents the variations of the photoelectric current I_{ph} as a function of temperature and irradiance. The shape of the surface shows a straightforward double linearity justified by Relation II.24. However, the weak effect of temperature on the increase in the photogenerated current can be observed.

Following identification of the internal parameters of the ideal model $n(T)$, $I_s(T)$, and $I_{ph}(G,T)$, the variations of the short-circuit current $I_{sc}(G,T)$ and open-circuit voltage $V_{oc}(G,T)$ as functions of irradiance and temperature can be expressed based on Relation II.19. For the ideal model, one obtains:

$$I_{sc}(G,T) = \frac{G}{G_{ref}} I_{sc}(T) = \frac{G}{G_{ref}} \left[I_{scref} + K_i (T - T_{ref}) \right] \tag{II.26}$$

$$V_{oc}(G,T) = n(T) V_t \ln \left(\frac{G}{G_{ref}} \frac{I_{ph}(T)}{I_s(T)} + 1 \right) \tag{II.27}$$

© Ferdaous Masmoudi, 2016 - All rights reserved

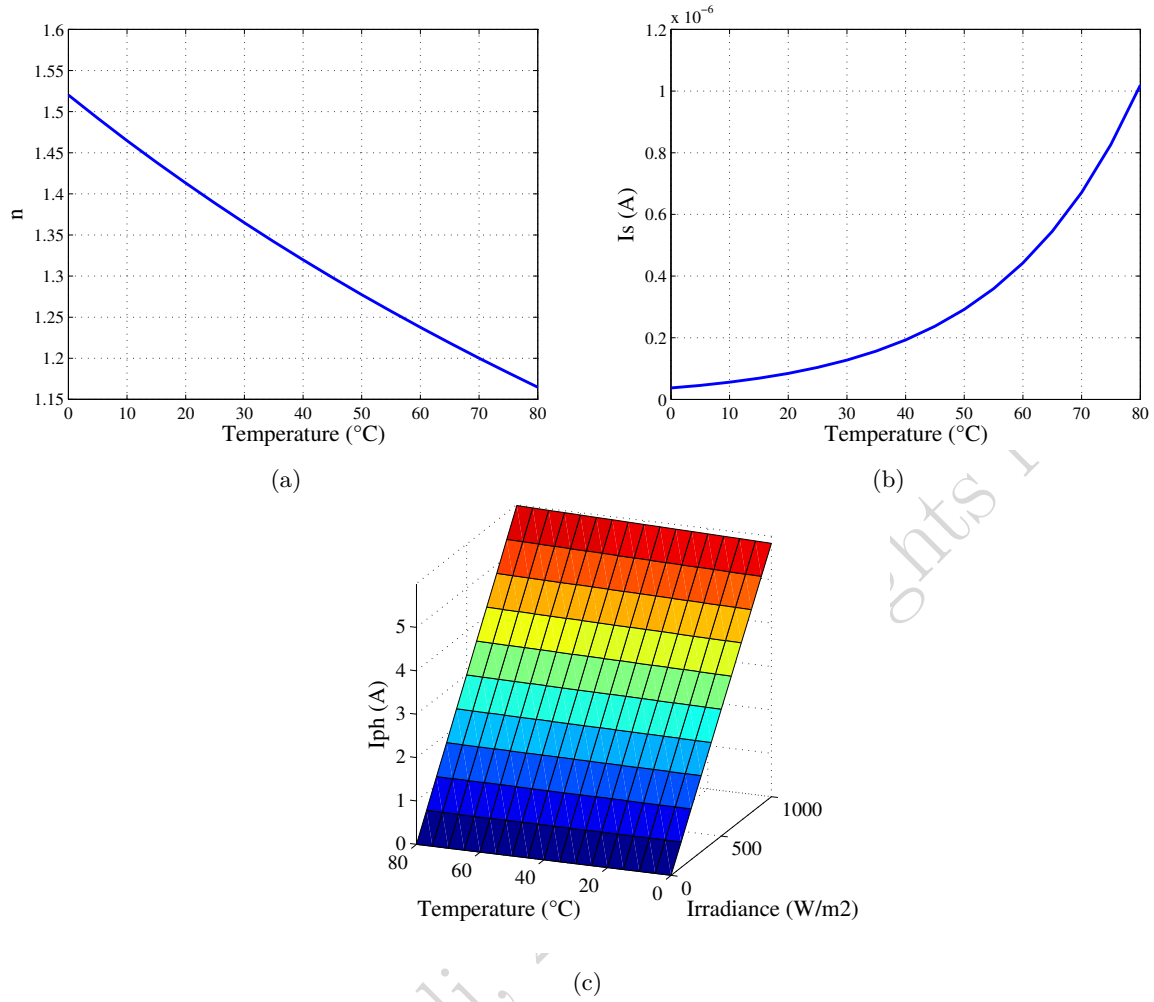


Figure II.7: Variations of the internal parameters of the ideal model of the JAC M5SF-2 solar cell as functions of temperature and irradiance. (a) Variation of n as a function of temperature. (b) Variation of I_s as a function of temperature. (c) Variation of I_{ph} as a function of temperature and irradiance.

II.4 One-Series-Resistance Model: Simplified One-Diode Model

Greater accuracy can be introduced into the previous model by adding a series resistance. Figure II.8 shows the equivalent circuit of the simplified one-diode model with a single resistance R_s connected in series, which combines the different connection resistances throughout the cell structure.

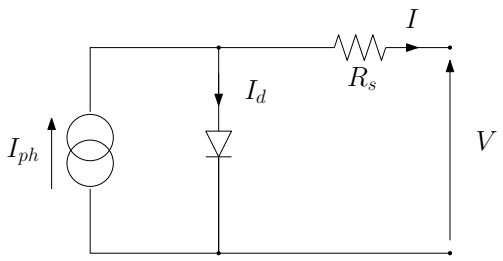


Figure II.8: Equivalent electrical circuit of the one-series-resistance model.

© Ferdaous Masmoudi, All rights reserved

This model is commonly used in many studies and offers a compromise between accuracy and simplicity.

Like the ideal model, the current of this simplified model can also be expressed by II.28:

$$I = I_{ph} - I_d \tag{II.28}$$

The relationship between the diode current I_d and the voltage V across its terminals is described by II.29:

$$I_d = I_s \left(\exp\left(\frac{V + R_s I}{n V_t} \right) - 1 \right) \tag{II.29}$$

By substituting the current I_d with its expression, Equation II.28 becomes:

$$I = I_{ph} - I_s \left(\exp\left(\frac{V + R_s I}{n V_t} \right) - 1 \right) \tag{II.30}$$

with:

$$V_t = \frac{kT}{q} \tag{II.31}$$

where:

- I_{ph}: the photocurrent (photoelectric current) generated by the cell,
- I_s: the saturation current of the cell junction,
- n: the diode ideality factor, which ranges from 1 to 2,
- R_s: the series resistance combining the different substrate resistances in the cell structure,
- T: the junction temperature during operation (K),
- k: the Boltzmann constant ($k = 1.38 \times 10^{-23}$ J/K),
- q: the charge of an electron ($q = 1.6 \times 10^{-19}$ C).

II.4 .1 Algorithm for Identifying the Unknown Parameters of the Simplified Model

Determining the four unknown parameters of the one-series-resistance model, namely (I_{ph}, I_s, R_s, and n), requires the use of a system of four equations. The identification procedure is adopted at the following four key points.

Applying Equation II.30 at the short-circuit point gives the following relation:

$$I_{sc} = I_{ph} - I_s \left(\exp\left(\frac{R_s I_{sc}}{n V_t} \right) - 1 \right) \tag{II.32}$$

At the open-circuit point, Equation II.30 gives:

$$0 = I_{ph} - I_s \left(\exp\left(\frac{V_{oc}}{n V_t} \right) - 1 \right) \tag{II.33}$$

© Ferdaous Jamoudi, 2016 – All rights reserved

Rewriting Equation II.30 at the maximum-power point leads to the following relation:

$$I_m = I_{ph} - I_s \left(\exp\left(\frac{V_m + R_m I_m}{n V_t} \right) - 1 \right) \tag{II.34}$$

Furthermore, taking into account Relation II.5 for the derivative of power with respect to voltage at the maximum-power point, one can write:

$$\left.\frac{dP}{dV}\right|_{P=P_m} = I_m + V_m \frac{\left.\frac{\partial f}{\partial V}\right|_{\substack{V=V_m \\ I=I_m}}}{1 - \left.\frac{\partial f}{\partial I}\right|_{\substack{V=V_m \\ I=I_m}}} = 0 \tag{II.35}$$

The identification of the unknown parameters (I_{ph}, I_s, R_s, n) of the equivalent electrical model is developed by solving the system of equations formed by Relations II.32, II.33, II.34, and II.35. Considering the following relations:

$$e_1 = \exp\left(\frac{V_{oc}}{n V_t} \right) \tag{II.36}$$

$$e_2 = \exp\left(\frac{R_s I_{sc}}{n V_t} \right) \tag{II.37}$$

$$e_3 = \exp\left(\frac{V_m + R_m I_m}{n V_t} \right) \tag{II.38}$$

Simplifying the system of equations gives the following relations. First, subtracting Relation II.33 from Relation II.32 gives the following result:

$$I_{sc} = I_s \left(\exp\left(\frac{V_{oc}}{n V_t} \right) - \exp\left(\frac{R_s I_{sc}}{n V_t} \right) \right) = I_s (e_1 - e_2) \tag{II.39}$$

Consequently, the saturation current I_s is expressed by:

$$I_s = \frac{I_{sc}}{e_1 - e_2} \tag{II.40}$$

Then, taking Equation (II.33) into account, the photocurrent I_{ph} is expressed as:

$$I_{ph} = I_s \left(\exp\left(\frac{V_{oc}}{n V_t} \right) - 1 \right) = I_s (e_1 - 1) \tag{II.41}$$

Substituting the saturation current I_s obtained from Equation (II.40) into the expression of the photocurrent I_{ph} (II.41) leads to:

$$I_{ph} = I_{sc} \, \frac{e_1 - 1}{e_1 - e_2} \tag{II.42}$$

Relations (II.40) and (II.42) are expressed in terms of the two other unknown parameters, R_s and n. To solve this problem, Equations (II.34) and (II.35) are used.

By rewriting Equation (II.34), with the currents I_{ph} and I_s replaced by their expressions, the following relation for the current I_m at the maximum-power point is obtained:

$$I_m = I_{sc} \, \frac{e_1 - e_3}{e_1 - e_2} \tag{II.43}$$

© Ferdaous Masmoudi 2016 - All rights reserved

Equation (II.35) for the derivative of power with respect to voltage at the maximum-power point is necessary to find the fourth unknown parameter.

Considering Relation II.30, one obtains:

$$\frac{\partial f}{\partial V} = -\frac{I_s}{nV_t}\exp\left(\frac{V+R_sI}{nV_t}\right) \tag{II.44}$$

$$\frac{\partial f}{\partial I} = -\frac{R_sI_s}{nV_t}\exp\left(\frac{V+R_sI}{nV_t}\right) \tag{II.45}$$

By substituting Relations (II.44) and (II.45) into Equation (II.5) developed previously, one obtains:

$$\frac{dP}{dV} = I + V\frac{-\frac{I_s}{nV_t}\exp\left(\frac{V+R_sI}{nV_t}\right)}{1+\frac{R_sI_s}{nV_t}\exp\left(\frac{V+R_sI}{nV_t}\right)} \tag{II.46}$$

At the maximum-power point, Equation (II.46) becomes:

$$\left.\frac{dP}{dV}\right|_{P=P_m} = I_m + V_m\frac{-\frac{I_s}{nV_t}\exp\left(\frac{V_m+R_sI_m}{nV_t}\right)}{1+\frac{R_sI_s}{nV_t}\exp\left(\frac{V_m+R_sI_m}{nV_t}\right)} = 0 \tag{II.47}$$

By rewriting Equation (II.47) and replacing I_s by its expression, one obtains:

$$\left.\frac{dP}{dV}\right|_{P=P_m} = I_m - \frac{V_mI_{sc}e_3}{nV_t(e_1-e_2)+R_sI_{sc}e_3} = 0 \tag{II.48}$$

As for the ideal model, determining the unknown parameters of the one-series-resistance model requires the development of a numerical search algorithm. For this model, the system of equations formed by Relations (II.43) and (II.48) is more complicated because it contains two non-linear equations and aims to determine the two unknown parameters R_s and n.

Two calculation methods are adopted to solve this system, either through the MATLAB *fsolve* function or by using the Newton algorithm, written this time for two equations and expressed as follows:

$$X_{i+1} = X_i + J^{-1}(X_i)g(X_i), \quad \text{where}: \quad i \in \mathbb{N} \tag{II.49}$$

with X the vector sought:

$$X = \begin{bmatrix} n \\ R_s \end{bmatrix} \tag{II.50}$$

and g is the vector of objective functions:

$$g = \begin{bmatrix} F(n,R_s) \\ G(n,R_s) \end{bmatrix} = \begin{bmatrix} I_m - I_{sc}\frac{e_1-e_3}{e_1-e_2} \\ I_m - \frac{V_mI_{sc}e_3}{V_t(e_1-e_2)+R_sI_{sc}e_3} \end{bmatrix} = 0 \tag{II.51}$$

The term J^{-1} corresponds to the inverse Jacobian matrix of the system under study. The Jacobian is formed by:

$$J = \begin{bmatrix} \frac{\partial F(n,R_s)}{\partial n} & \frac{\partial F(n,R_s)}{\partial R_s} \\ \frac{\partial G(n,R_s)}{\partial n} & \frac{\partial G(n,R_s)}{\partial R_s} \end{bmatrix} \tag{II.52}$$

© Ferdaous Masmoudi, 2016 - All rights reserved

For the calculation of the partial derivatives of the Jacobian matrix, the "*jacobian*" function of the MATLAB *Symbolic Math Toolbox*[4] can be used. Similarly, the *inv* function is used to determine the inverse Jacobian J^{-1}.

For the first estimate, the following vector X_0 is chosen:

$$X_0 = \begin{bmatrix} n_0 \\ R_{s0} \end{bmatrix} = \begin{bmatrix} 1 \\ 0.01 \end{bmatrix} \tag{II.53}$$

Figure II.9 presents the algorithm adopted for identifying the unknowns R_s and n. The inputs of this algorithm are the manufacturer's data previously summarized in Table I.5.

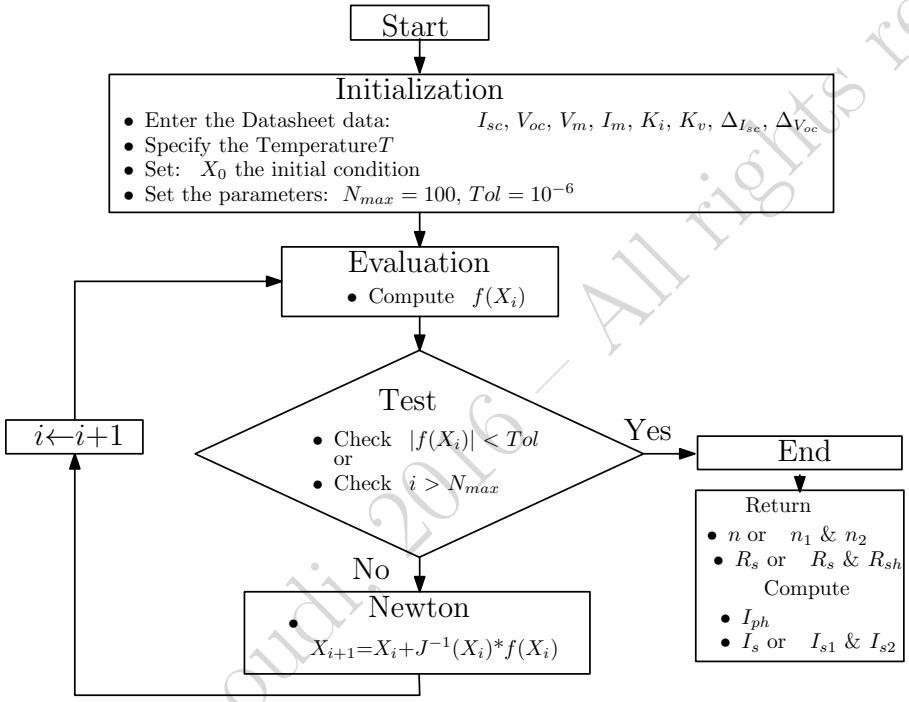


Figure II.9: Search algorithm for the internal parameters of the one-series-resistance, one-diode, and two-diode models.

II.4 .2 Identification Results of the One-Series-Resistance Model Parameters under STC

Analogously to what was done for the ideal model, Table II.2 presents the results of the algorithms for searching the unknown parameters of the one-series-resistance model applied to the reference cell JA JAC MS5F-2 under standard measurement conditions, STC.

The results in Table II.2 show that the two methods converge toward the same values, which demonstrates their accuracy. However, the Newton algorithm performs fewer iterations and consumes more time. The tolerated accuracy is 10^{-6}, which can be considered sufficiently precise.

[4]For more information about this toolbox, type >> *helpsymbolic* in the MATLAB command window, or consult the online *Mathworks* guide: http://www.mathworks.com/products/symbolic/

© Ferdaous Masmoudi 2016 _ All rights reserved

Table II.2: Internal-parameter results for the JAC M5SF-2 cell under STC using the one-series-resistance model.

Parameter	*fsolve*	*Newton*
I_{phref} (A)	5.8880	5.8880
I_{sref} (A)	5.4506×10^{-8}	5.45055×10^{-8}
n_{ref}	1.3403	1.3403
R_{sref} (Ω)	6.2863×10^{-4}	6.2864×10^{-4}
N iterations	6	4
Time (s)	0.514	1.535
Method	Trust-region-dogleg	simple Newton

II.4 .3 Effect of Temperature and Irradiance on the Internal Parameters of the One-Series-Resistance Model

In the following, the influence of temperature and irradiance on the model parameters ($n(T)$, $I_s(T)$, $R_s(T)$, and $I_{ph}(G,T)$) is presented. The general expression of the one-series-resistance model as a function of G and T is expressed by:

$$I(G,T) = \frac{G}{G_{ref}} I_{ph}(T) - I_s(T) \left(\exp\left(\frac{V(G,T) + R_s(T) I(G,T)}{n(T) V_t} \right) - 1 \right) \tag{II.54}$$

Analogously to what was established for the ideal model (II.4.2), and taking Relations (II.20), (II.21), (II.22), and (II.23) into account, Figure II.10 shows the variations of the model parameters as a function of climatic changes.

Figure II.10.a shows a decreasing shape of the $n(T)$ curve, which reaches values below unity at high temperatures. Figure II.10.b shows the shape of the $I_s(T)$ curve, which is also decreasing, paradoxically with respect to junction theory. The $R_s(T)$ curve in Figure II.10.c increases linearly; however, it is negative at low temperatures, which has no physical meaning.

The variations of the photoelectric current $I_{ph}(G,T)$ shown in Figure II.10.d exhibit a surface with a shape identical to that of the ideal model, reflecting the negligible effect of the exponential terms in the expression of I_{ph}.

© Ferdaous Mamaoui 2016 — All rights reserved

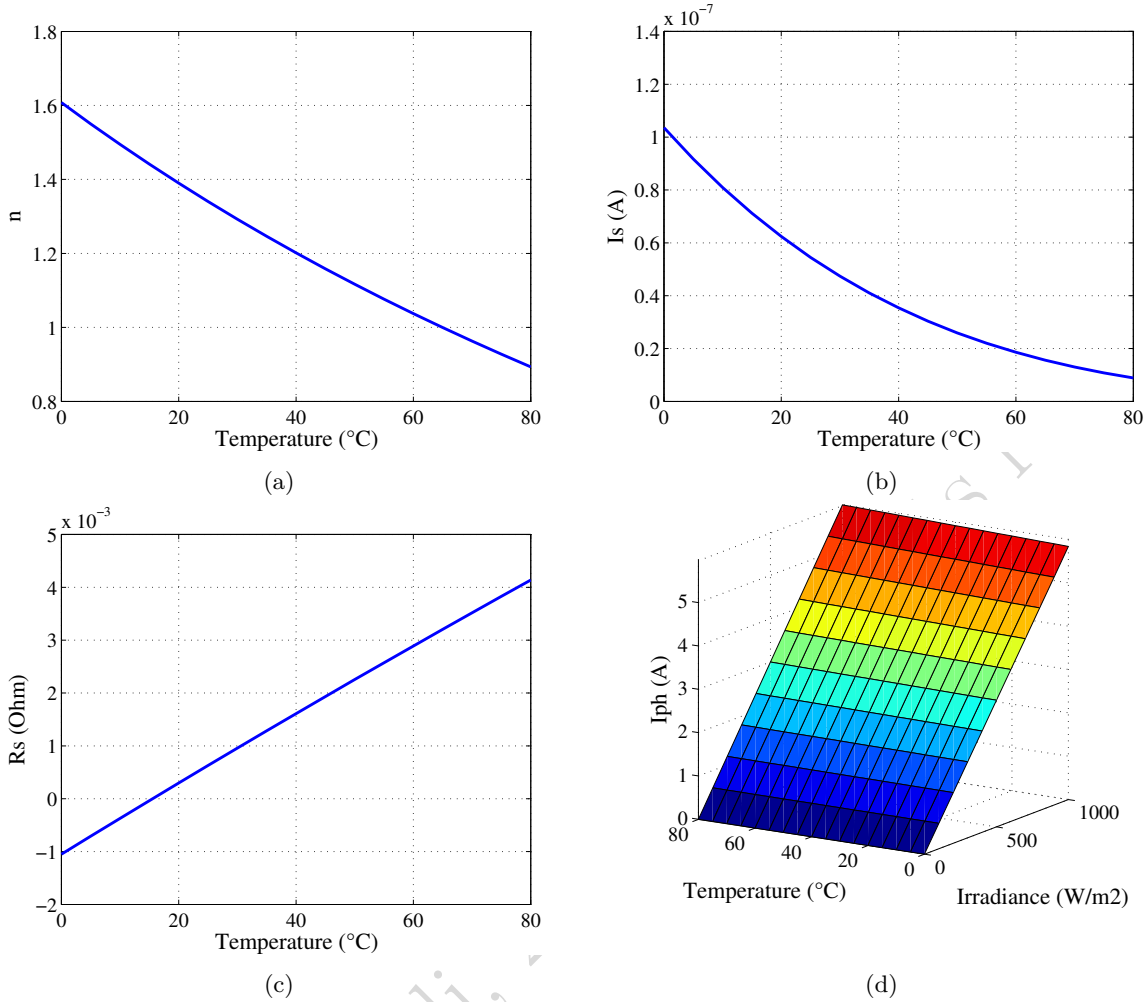


Figure II.10: Variations of the internal parameters of the one-series-resistance model of the JAC M5SF-2 solar cell as functions of temperature and irradiance. (a) Variation of n as a function of temperature. (b) Variation of I_s as a function of temperature. (c) Variation of R_s as a function of temperature. (d) Variation of I_{ph} as a function of temperature and irradiance.

II.5 One-Diode Model

The equivalent one-diode (1D) model of a solar cell consists of a current source generating the photocurrent I_{ph} in parallel with a single diode carrying a current I_d, a parallel resistance R_{sh}, and a series resistance R_s. The parallel (shunt) resistance R_{sh} produces the leakage current I_{sh} and represents current losses in defects and impurities within the solar-cell structure. The electrical configuration of this model is shown in Figure II.11 [23-32].

© Ferdaous Masrouri, ...

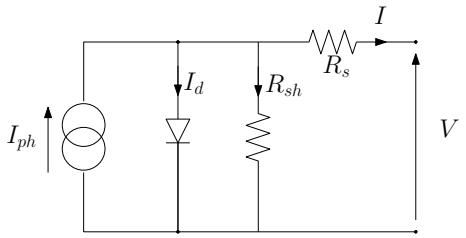


Figure II.11: Equivalent electrical circuit of the one-diode model.

Under irradiance G, the current I delivered by the cell can be expressed in terms of the photocurrent I_{ph}, the current I_d through the diode, and the leakage current I_{sh} by the following relation:

$$I = I_{ph} - I_d - I_{sh} \tag{II.55}$$

The relationship between the diode current I_d and the voltage V across its terminals is described by the following equation:

$$I_d = I_s \left(\exp\left(\frac{V + R_s I}{n V_t} \right) - 1 \right) \tag{II.56}$$

The current I_{sh} through the shunt resistance R_{sh}, as a function of the voltage V across the cell terminals, can be expressed as follows:

$$I_{sh} = \frac{V + R_s I}{R_{sh}} \tag{II.57}$$

By substituting the currents I_d and I_{sh} with their expressions, Equation (II.55) becomes:

$$I = I_{ph} - I_s \left(\exp\left(\frac{V + R_s I}{n V_t} \right) - 1 \right) - \frac{V + R_s I}{R_{sh}} \tag{II.58}$$

with

$$V_t = \frac{kT}{q} \tag{II.59}$$

and where:

- R_{sh}: the parallel resistance combining the effect of the different leakage currents through the cell structure.

II.5 .1 Algorithm for Identifying the Unknown Parameters of the One-Diode Model

The unknown parameters of this model are (I_{ph}, I_s, n, R_s, and R_{sh}). Determining these five unknown parameters of the one-diode model requires the use of a system of five equations. The identification procedure is adopted at five key points as follows. Applying Equation (II.58) at the short-circuit point gives the following relation:

$$I_{sc} = I_{ph} - I_s \left(\exp\left(\frac{R_s I_{sc}}{n V_t} \right) - 1 \right) - \frac{R_s I_{sc}}{R_{sh}} \tag{II.60}$$

At the open-circuit point, Equation (II.58) takes the following form:

$$0 = I_{ph} - I_s \left(\exp\left(\frac{V_{oc}}{n V_t} \right) - 1 \right) - \frac{V_{oc}}{R_{sh}} \tag{II.61}$$

© Ferdaous Masmoudi, 2016 – All rights reserved

Rewriting Equation (II.58) at the maximum-power point leads to the following relation:

$$I_m = I_{ph} - I_s \left(\exp\left(\frac{V_m + R_s I_m}{n V_t} \right) - 1 \right) - \frac{V_m + R_s I_m}{R_{sh}} \tag{II.62}$$

Considering Expression (II.58), the partial derivatives of I with respect to V and then I are expressed by the following relations:

$$\frac{\partial I(V,I)}{\partial V} = -\frac{I_s}{n V_t} \exp\left(\frac{V + R_s I}{n V_t} \right) - \frac{1}{R_{sh}} \tag{II.63}$$

$$\frac{\partial I(V,I}{\partial I} = -\frac{R_s I_s}{n V_t} \exp\left(\frac{V + R_s I}{V_t} \right) - \frac{R_s}{R_{sh}} \tag{II.64}$$

By substituting (II.63) and (II.64) into Equation (II.4), one obtains:

$$\frac{dI}{dV} = \frac{-\frac{I_s}{n V_t} \exp\left(\frac{V + R_s I}{n V_t} \right) - \frac{1}{R_{sh}}}{1 + \frac{R_s I_s}{n V_t} \exp\left(\frac{V + R_s I}{n V_t} \right) + \frac{R_s}{R_{sh}}} \tag{II.65}$$

Simplifying Equation II.65 gives:

$$\frac{dI}{dV} = \frac{-R_{sh} I_s \exp\left(\frac{V + R_s I}{n V_t} \right) - n V_t}{n V_t R_{sh} + R_s R_{sh} I_s \exp\left(\frac{V + R_s I}{V_t} \right) + n V_t R_s} \tag{II.66}$$

The identification of the unknown internal parameters of the one-diode model, I_{ph}, I_s, n, R_{sh}, and R_s, is based on solving the system of equations formed by Relations (II.60), (II.61), (II.62), and (II.66), written in the vicinity of the short-circuit point $I = I_{sc}$ and the open-circuit point $V = V_{oc}$. The following relations are considered:

$$e_1 = \exp\left(\frac{V_{oc}}{n V_t} \right) \tag{II.67}$$

$$e_2 = \exp\left(\frac{R_s I_{sc}}{n V_t} \right) \tag{II.68}$$

$$e_3 = \exp\left(\frac{V_m + R_m I_m}{n V_t} \right) \tag{II.69}$$

The aim is now to simplify this system of equations.

Subtracting Relation (II.60) from Relation (II.61) leads to the following relation:

$$I_{sc} = I_s (e_1 - e_2) + \frac{V_{oc} - I_{sc} R_s}{R_{sh}} \tag{II.70}$$

Consequently, the saturation current I_s is expressed as follows:

$$I_s = \frac{I_{sc}(R_s + R_{sh}) - V_{oc}}{R_{sh}(e_1 - e_2)} \tag{II.71}$$

Taking Relation (II.61) into account, the photocurrent I_{ph} is expressed as follows:

$$I_{ph} = I_s (e_1 - 1) + \frac{V_{oc}}{R_{sh}} \tag{II.72}$$

© Ferdaous Masmoudi, 2016 - All rights reserved

By substituting I_s with its expression, Equation (II.72) becomes:

$$I_{ph} = I_{sc}\left(\frac{(R_s + R_{sh})(e_1 - 1)}{R_{sh}(e_1 - e_2)}\right) + \frac{V_{oc}}{R_{sh}}\left(1 - \frac{(e_1 - 1)}{(e_1 - e_2)}\right) \tag{II.73}$$

By rewriting Equation (II.62) in terms of I_{ph} and I_s, one obtains:

$$I_m - I_{ph} + I_s\,(e_3 - 1) + \frac{V_m + R_s I_m}{R_{sh}} = 0 \tag{II.74}$$

By replacing I_{ph} and I_s by their expressions, Relation (II.74) becomes:

$$I_{sc}\left(\frac{(R_s + R_{sh})(e_3 - e_1)}{R_{sh}(e_1 - e_2)}\right) - \frac{V_{oc}}{R_{sh}}\left(1 + \frac{(e_3 - e_1)}{(e_1 - e_2)}\right) + \frac{V_m}{R_{sh}} + I_m\left(1 + \frac{R_s}{R_{sh}}\right) = 0 \tag{II.75}$$

Relations (II.71), (II.73), and (II.75) are expressed as functions of two other unknown parameters, R_s and R_{sh}. Relation (II.66) is therefore used for $(V, I) = (0, I_{sc})$ and for $(V, I) = (V_{oc}, 0)$ in order to identify them.

At the short-circuit point $(V, I) = (0, I_{sc})$, Equation (II.66) becomes:

$$\left.\frac{dI}{dV}\right|_{I=I_{sc}} = \frac{-R_{sh}I_s e_2 - nV_t}{nV_t R_{sh} + R_s R_{sh} I_s e_2 + nV_t R_s} = \Delta I_{sc} \tag{II.76}$$

One then writes:

$$-R_{sh}I_s e_2 - nV_t - \Delta I_{sc}\,[nV_t(R_{sh} + R_s) + R_s R_{sh} I_s e_2] = 0 \tag{II.77}$$

At the open-circuit point $(V, I) = (V_{oc}, 0)$, Equation (II.66) is written as:

$$\left.\frac{dI}{dV}\right|_{V=V_{oc}} = \frac{-R_{sh}I_s e_1 - nV_t}{nV_t R_{sh} + R_s R_{sh} I_s e_1 + nV_t R_s} = \Delta V_{oc} \tag{II.78}$$

Similarly, one writes:

$$-R_{sh}I_s e_1 - nV_t - \Delta V_{oc}\,[nV_t(R_{sh} + R_s) + R_s R_{sh} I_s e_1] = 0 \tag{II.79}$$

The system of five equations is formed by Relations (II.71), (II.72), (II.75), (II.77), and (II.79). It is sufficient to determine R_{sh}, R_s, and n for the currents I_{ph} and I_s to be readily calculated. Furthermore, determining these parameters is based on numerically solving the following three nonlinear relations: (II.75), (II.77), and (II.79). A search algorithm is developed using two calculation methods, either with the MATLAB $fsolve$ function or using the Newton algorithm to search for the three parameters n, R_s, and R_{sh}:

$$X_{i+1} = X_i + J^{-1}(X_i)g(X_i), \quad i \in \mathbb{N} \tag{II.80}$$

where X is the vector of parameters sought:

$$X = \begin{bmatrix} n \\ R_s \\ R_{sh} \end{bmatrix} \tag{II.81}$$

© Ferdaous Masmoudi, 2016 – All rights reserved

and g is the vector of objective functions:

$$g = \begin{bmatrix} F(n, R_s, R_{sh}) \\ G(n, R_s, R_{sh}) \\ H(n, R_s, R_{sh}) \end{bmatrix} = \begin{bmatrix} I_{sc}\left(\frac{(R_s+R_{sh})(e_3-e_1)}{R_{sh}(e_1-e_2)}\right) - \frac{V_{oc}}{R_{sh}}\left(1+\frac{(e_3-e_1)}{(e_1-e_2)}\right) + \frac{V_m}{R_{sh}} + I_m\left(1+\frac{R_s}{R_{sh}}\right) \\ -R_{sh}I_s e_2 - nV_t - \Delta I_{sc}\left(nV_t(R_{sh}+R_s) + R_s R_{sh} I_s e_2\right) \\ -R_{sh}I_s e_1 - nV_t - \Delta V_{oc}\left(nV_t(R_{sh}+R_s) + R_s R_{sh} I_s e_1\right) \end{bmatrix} = 0 \quad \text{(II.82)}$$

The term J^{-1} corresponds to the inverse Jacobian matrix of the system under study. The Jacobian is formed by:

$$J = \begin{bmatrix} \frac{\partial F(n,R_s,R_{sh})}{\partial n} & \frac{\partial F(n,R_s,R_{sh})}{\partial R_s} & \frac{\partial F(n,R_s,R_{sh})}{\partial R_{sh}} \\ \frac{\partial G(n,R_s,R_{sh})}{\partial n} & \frac{\partial G(n,R_s,R_{sh})}{\partial R_s} & \frac{\partial G(n,R_s,R_{sh})}{\partial R_{sh}} \\ \frac{\partial H(n,R_s,R_{sh})}{\partial n} & \frac{\partial H(n,R_s,R_{sh})}{\partial R_s} & \frac{\partial H(n,R_s,R_{sh})}{\partial R_{sh}} \end{bmatrix} \quad \text{(II.83)}$$

For the first estimate, the following vector X_0 is chosen:

$$X_0 = \begin{bmatrix} n_0 \\ R_{s0} \\ R_{sh0} \end{bmatrix} = \begin{bmatrix} 1 \\ 0.001 \\ 100 \end{bmatrix} \quad \text{(II.84)}$$

Figure II.9 also presents the algorithm adopted for identifying the unknowns R_{sh}, R_s, and n of the one-diode model.

II.5 .2 Identification Results of the One-Diode Model Parameters under STC

Table II.3 presents the results of the algorithms for searching the unknown parameters of the one-diode model applied to the reference cell (JA JAC M5SF-2) under standard measurement conditions, *STC*. The two parameters ΔI_{sc} and ΔV_{oc} are added to the input quantities I_{scref}, V_{ocref}, I_{mref}, and V_{mref} (the effect of climatic conditions on the slopes of the electrical characteristic is assumed negligible).

Table II.3: Internal-parameter results for the JAC M5SF-2 cell under STC using the one-diode model.

Parameter	*fsolve*	*Newton*
I_{phref} (A)	5.888	5.88808
I_{sref} (A)	3.9945×10^{-8}	3.9945×10^{-8}
n_{ref}	1.3182	1.3182
R_{sref} (Ω)	8.828×10^{-4}	8.828×10^{-4}
R_{shref} (Ω)	253.5729	253.5729
N iterations	9	4
Time (s)	0.414	14.0278
Method	Trust-region-dogleg	simple Newton

© Ferdaous Mahmoudi, 2016 – All rights reserved

The results in Table II.3 show that the two methods converge toward the same values, which demonstrates their accuracy. The Newton algorithm is more efficient in terms of the number of iterations; however, it requires considerably more time, especially when evaluating the Jacobian matrix. The tolerated error criterion is less than 1e-6, which can be considered sufficiently precise.

II.5 .3 Effect of Temperature and Irradiance on the Internal Parameters of the One-Diode Model

The influence of temperature and irradiance on the model parameters ($n(T)$, $I_s(T)$, $R_s(T)$, $R_{sh}(T)$, and $I_{ph}(G,T)$) is presented. The general expression of the one-diode model as a function of G and T is:

$$I(G,T) = \frac{G}{G_{ref}} I_{ph}(T) - I_s(T)\left(\exp\left(\frac{V(G,T)+R_s(T)I(G,T)}{n(T)V_t}\right)-1\right) - \frac{V(G,T)+R_s(T)I(G,T)}{R_{sh}(T)} \quad \text{(II.85)}$$

Analogously to what was established for the ideal model (II.4.2), and taking Relations (II.20), (II.21), (II.22), and (II.23) into account, Figure II.12 shows the variations of the unknown model parameters as a function of climatic changes.

The shapes of the curves shown in Figure II.12 are fully consistent with junction theory and semiconductor physics, particularly doped silicon [32, 33, 34, 35].

The variations of the photoelectric current $I_{ph}(G,T)$ shown in Figure II.12.e exhibit a surface with a shape identical to that of the ideal model, reflecting the negligible effect of the exponential terms in the expression of I_{ph}.

© Ferdaous Masmoudi, 2016 _ All rights reserved

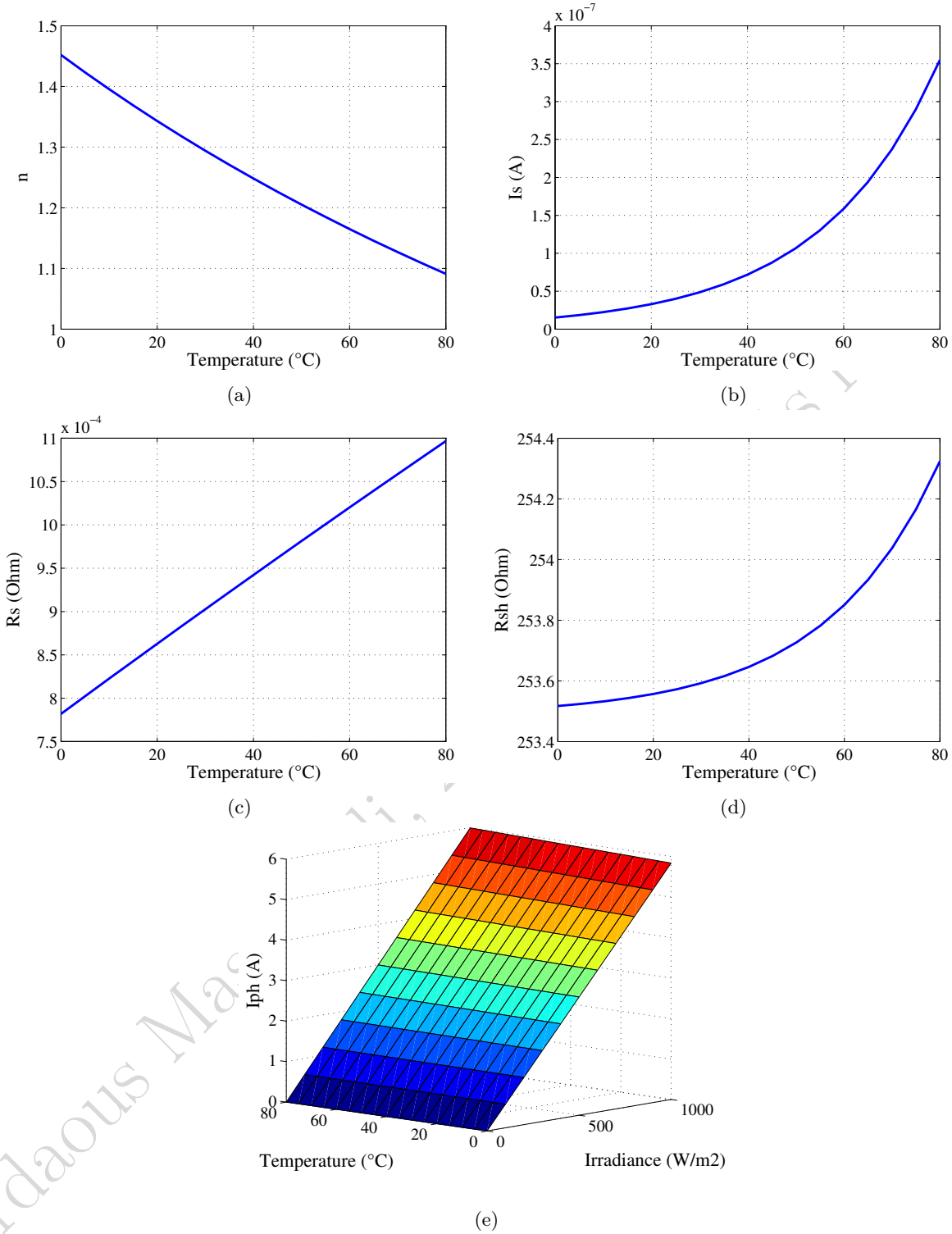


Figure II.12: Variations of the internal parameters of the one-diode model of the JAC M5SF-2 solar cell as functions of temperature and irradiance. (a) Variation of n as a function of temperature. (b) Variation of I_s as a function of temperature. (c) Variation of R_s as a function of temperature. (d) Variation of R_{sh} as a function of temperature. (e) Variation of I_{ph} as a function of temperature and irradiance.

© Ferdaous Ma

II.6 Two-Diode Model

The model presented in this section is the two-diode (∼double-diode) model, which takes the recombination phenomenon in the space-charge region into account and provides better accuracy for the $I-V$ characteristic. It gives more physically credible values for the internal parameters that may reflect the phenomena occurring inside the solar cell.

The equivalent electrical circuit of the double-diode (2D) solar-cell model consists of a current source generating the photocurrent I_{ph} in parallel with two diodes carrying the currents I_{d1} and I_{d2}. The leakage current of the shunt resistance R_{sh} is represented by the current I_{sh}, and R_s represents the series resistance. The equivalent electrical-circuit configuration is shown in Figure II.13 [33-37].

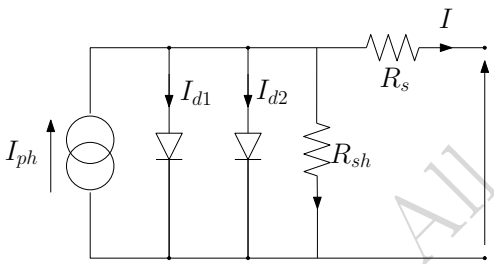


Figure II.13: Equivalent electrical circuit of the two-diode model.

Under irradiance G, the solar-cell $I-V$ characteristic is expressed by the following equation:

$$I = I_{ph} - I_{d1} - I_{d2} - I_{sh} \tag{II.86}$$

The relationship between the current I_{d1} and the voltage V across the cell terminals is described by the following equation:

$$I_{d1} = I_{s1}\left(\exp\left(\frac{V+R_sI}{n_1V_t}\right)-1\right) \tag{II.87}$$

Similarly, the relationship between the current I_{d2} and the voltage V is described as follows:

$$I_{d2} = I_{s2}\left(\exp\left(\frac{V+R_sI}{n_2V_t}\right)-1\right) \tag{II.88}$$

The relationship between the current I_{sh} and the voltage V across the cell terminals can be expressed as follows:

$$I_{sh} = \frac{V+R_sI}{R_{sh}} \tag{II.89}$$

By substituting the currents I_{d1}, I_{d2}, and I_{sh} with their expressions, Equation (II.86) becomes:

$$I = I_{ph} - I_{s1}\left(\exp\left(\frac{V+R_sI}{n_1V_t}\right)-1\right) - I_{s2}\left(\exp\left(\frac{V+R_sI}{n_2V_t}\right)-1\right) - \frac{V+R_sI}{R_{sh}} \tag{II.90}$$

- I_{s1}: the junction saturation current associated with diffusion-recombination phenomena in the quasi-neutral region,
- I_{s2}: the junction saturation current associated with the recombination phenomenon in the space-charge region,

© Ferdaous Masmoudi, 2016 – All rights reserved

- n_1: the ideality factor of diode 1, equal to 1 for this model,
- n_2: the ideality factor of diode 2, considered significantly greater than 1.

II.6 .1 Algorithm for Identifying the Unknown Parameters of the Two-Diode Model

The unknown parameters of this model are (I_{ph}, I_{s1}, n_1, I_{s2}, n_2, R_s, and R_{sh}). According to previous research on classical semiconductor physics and $p-n$ junctions, the quality factor n_1 associated with diffusion and recombination phenomena in the quasi-neutral region is generally estimated to be equal to 1 [51], whereas the quality factor n_2, related to recombination theory in the depletion region, is assumed to be significantly greater than 1 [52]. The remainder of the work consists of adopting the identification procedure for six unknown parameters of the double-diode model and developing a search algorithm to identify them.

Determining the six unknown parameters of the double-diode model, namely I_{ph}, I_{s1}, I_{s2}, n_2, R_s, and R_{sh}, requires the use of a system of six equations developed as follows.

Applying Equation (II.90) at the short-circuit point gives the following relation:

$$I_{sc} = I_{ph} - I_{s1}\left(\exp\left(\frac{R_s I_{sc}}{V_t}\right) - 1\right) - I_{s2}\left(\exp\left(\frac{R_s I_{sc}}{n_2 V_t}\right) - 1\right) - \frac{R_s I_{sc}}{R_{sh}} \tag{II.91}$$

At the open-circuit point, Equation (II.90) is written as follows:

$$0 = I_{ph} - I_{s1}\left(\exp\left(\frac{V_{oc}}{V_t}\right) - 1\right) - I_{s2}\left(\exp\left(\frac{V_{oc}}{n_2 V_t}\right) - 1\right) - \frac{V_{oc}}{R_{sh}} \tag{II.92}$$

Rewriting Equation (II.90) at the maximum-power point leads to the following relation:

$$\begin{aligned} I_m = {} & I_{ph} - I_{s1}\left(\exp\left(\frac{V_m + R_s I_m}{V_t}\right) - 1\right) \\ & - I_{s2}\left(\exp\left(\frac{V_m + R_s I_m}{n_2 V_t}\right) - 1\right) - \frac{V_m + R_s I_m}{R_{sh}} \end{aligned} \tag{II.93}$$

Considering Expression (II.90), the partial derivatives of I with respect to V and then I are expressed by the following relations:

$$\frac{\partial I(I,V)}{\partial V} = -\frac{I_{s1}}{V_t}\exp\left(\frac{V + R_s I}{V_t}\right) - \frac{I_{s2}}{2V_t}\exp\left(\frac{V + R_s I}{n_2 V_t}\right) - \frac{1}{R_{sh}} \tag{II.94}$$

$$\frac{\partial I(I,V)}{\partial I} = R_s \frac{\partial I(I,V)}{\partial V} \tag{II.95}$$

By substituting Relations (II.94) and (II.95) into Equation (II.4), one obtains:

$$\frac{dI}{dV} = \frac{-\frac{I_{s1}}{V_t}\exp\left(\frac{V+R_s I}{V_t}\right) - \frac{I_{s2}}{n_2 V_t}\exp\left(\frac{V+R_s I}{n_2 V_t}\right) - \frac{1}{R_{sh}}}{1 + \frac{R_s I_{s1}}{V_t}\exp\left(\frac{V+R_s I}{V_t}\right) + \frac{R_s I_{s2}}{n_2 V_t}\exp\left(\frac{V+R_s I}{n_2 V_t}\right) + \frac{R_s}{R_{sh}}} \tag{II.96}$$

Simplifying Relation (II.96) gives the following relation:

$$\frac{dI}{dV} = \frac{-n_2 R_{sh} I_{s1}\exp\left(\frac{V+R_s I}{V_t}\right) - R_{sh} I_{s2}\exp\left(\frac{V+R_s I}{n_2 V_t}\right) - n_2 V_t}{n_2 V_t (R_s + R_{sh}) + R_s R_{sh}\left(n_2 I_{s1}\exp\left(\frac{V+R_s I}{V_t}\right) + I_{s2}\exp\left(\frac{V+R_s I}{n_2 V_t}\right)\right)} \tag{II.97}$$

© Ferdaous Masmoudi, 2016 – All rights reserved

The expression of the derivative of power P with respect to voltage V given by Relation (II.5) is expressed for this model by the following relation:

$$\frac{dP}{dV} = I + V\left(\frac{-n_2 R_{sh} I_{s1}\exp\left(\frac{V+R_s I}{V_t}\right) - R_{sh} I_{s2}\exp\left(\frac{V+R_s I}{n_2 V_t}\right) - n_2 V_t}{n_2 V_t(R_s+R_{sh}) + R_s R_{sh}\left(n_2 I_{s1}\exp\left(\frac{V+R_s I}{V_t}\right) + I_{s2}\exp\left(\frac{V+R_s I}{n_2 V_t}\right)\right)}\right) \quad \text{(II.98)}$$

The identification of the unknown parameters I_{ph}, I_{s1}, I_{s2}, n_2, R_s, and R_{sh} of the equivalent model is developed by solving the system formed by Relations (II.91), (II.92), (II.93), (II.98), and (II.97), written in the vicinity of the short-circuit point $I = I_{sc}$ and the open-circuit point $V = V_{oc}$. The following relations are considered:

$$e_1' = \exp\left(\frac{V_{oc}}{V_t}\right) \quad \text{(II.99)}$$

$$e_1'' = \exp\left(\frac{V_{oc}}{n_2 V_t}\right) \quad \text{(II.100)}$$

$$e_2' = \exp\left(\frac{R_s I_{sc}}{V_t}\right) \quad \text{(II.101)}$$

$$e_2'' = \exp\left(\frac{R_s I_{sc}}{n_2 V_t}\right) \quad \text{(II.102)}$$

$$e_3' = \exp\left(\frac{V_m + R_s I_m}{V_t}\right) \quad \text{(II.103)}$$

$$e_3'' = \exp\left(\frac{V_m + R_s I_m}{n_2 V_t}\right) \quad \text{(II.104)}$$

Subtracting Relation (II.91) from Relation (II.92) gives the following result:

$$I_{sc} = I_{s1}(e_1' - e_2') + I_{s2}(e_1'' - e_2'') + \frac{V_{oc} - I_{sc}R_s}{R_{sh}} \quad \text{(II.105)}$$

Thus, the saturation current I_{s1} can be expressed in terms of I_{s2} using Equation (II.105) as follows:

$$I_{s1} = \frac{I_{sc}(R_s+R_{sh}) - V_{oc}}{R_{sh}(e_1' - e_2')} - I_{s2}\frac{(e_1'' - e_2'')}{(e_1' - e_2')} \quad \text{(II.106)}$$

Subtracting Relation (II.93) from Relation (II.92) gives the following result:

$$I_m = I_{s1}(e_1' - e_3') + I_{s2}(e_1'' - e_3'') + \frac{V_{oc} - V_m - I_m R_s}{R_{sh}} \quad \text{(II.107)}$$

Thus, the saturation current I_{s2} can be expressed in terms of I_{s1} using Equation II.107 as follows:

$$I_{s2} = \frac{I_m R_{sh} - V_{oc} + V_m + I_m R_s}{R_{sh}(e_1'' - e_3'')} - I_{s1}\frac{(e_1' - e_3')}{(e_1'' - e_3'')} \quad \text{(II.108)}$$

Substituting and simplifying the saturation current I_{s1} obtained from Equation (II.106) in the expression of the saturation current I_{s2} given by Equation (II.108) leads to:

$$\begin{aligned} I_{s2} &= I_m\frac{(R_s+R_{sh})(e_1' - e_2')}{R_{sh}A} - I_{sc}\frac{(R_s+R_{sh})(e_1' - e_3')}{R_{sh}A} \\ &\quad + V_{oc}\frac{(e_2' - e_3')}{R_{sh}A} + V_m\frac{(e_1' - e_2')}{R_{sh}A} \end{aligned} \quad \text{(II.109)}$$

© Ferdaous Masmoudi, 2016. All rights reserved

with:

$$A = (e_1'' - e_3'')(e_1' - e_2') - (e_1'' - e_2'')(e_1' - e_3') \tag{II.110}$$

By replacing the result of Equation (II.109) in the expression of the diffusion saturation current I_{s1} in Equation (II.106), one obtains:

$$\begin{aligned} I_{s1} &= I_{sc}\frac{(R_s + R_{sh})}{R_{sh}(e_1' - e_2')}[1 + \frac{(e_1' - e_3')(e_1'' - e_2'')}{A}] - I_m\frac{(R_s + R_{sh})(e_1'' - e_2'')}{R_{sh}A} \\ &\quad -V_m\frac{(e_1'' - e_2'')}{R_{sh}A} - V_{oc}\frac{1}{R_{sh}(e_1' - e_2')}[1 + \frac{(e_2' - e_3')(e_1'' - e_2'')}{A}] \end{aligned} \tag{II.111}$$

Taking Equation (II.92) into account, the expression of the photocurrent I_{ph} is written in terms of I_{s1} and I_{s2} as follows:

$$I_{ph} = I_{s1}(e_1' - 1) + I_{s2}(e_1'' - 1) + \frac{V_{oc}}{R_{sh}} \tag{II.112}$$

Relations (II.111), (II.109), and (II.112) are expressed in terms of the three other unknown parameters: n_2, R_s, and R_{sh}. To find them, Equation (II.97) is written for $(V, I) = (0, I_{sc})$ and for $(V, I) = (V_{oc}, 0)$, and Equation (II.98) is then used in the vicinity of the maximum-power point $(V, I) = (V_m, I_m)$.

At the short-circuit point, Equation (II.97) is written:

$$\left.\frac{dI}{dV}\right|_{I=I_{sc}} = \frac{-n_2R_{sh}I_{s1}e_2' - R_{sh}I_{s2}e_2'' - n_2V_t}{n_2V_tR_{sh} + n_2R_sR_{sh}I_{s1}e_2' + R_sR_{sh}I_{s2}e_2'' + n_2V_tR_s} = \Delta_{I_{sc}} \tag{II.113}$$

At the open-circuit point, Equation (II.97) is written:

$$\left.\frac{dI}{dV}\right|_{V=V_{oc}} = \frac{-n_2R_{sh}I_{s1}e_1' - R_{sh}I_{s2}e_1'' - n_2V_t}{n_2V_tR_{sh} + n_2R_sR_{sh}I_{s1}e_1' + R_sR_{sh}I_{s2}e_1'' + n_2V_tR_s} = \Delta_{V_{oc}} \tag{II.114}$$

At the maximum-power point, Equation (II.98) is written:

$$\left.\frac{dP}{dV}\right|_{\substack{V=V_m \\ I=I_m}} = I_m + V_m\left(\frac{-n_2R_{sh}I_{s1}e_3' - R_{sh}I_{s2}e_3'' - n_2V_t}{n_2V_t(R_s + R_{sh}) + R_sR_{sh}\,(n_2I_{s1}e_3' + I_{s2}e_3'')}\right) = 0 \tag{II.115}$$

The system of six equations is formed by Relations (II.111), (II.109), (II.112), (II.113), (II.114), and (II.115). The currents I_{ph}, I_{s1}, and I_{s2} can be readily calculated and determined by implementing the information in the manufacturer's datasheet. Furthermore, determining these parameters is based on numerically solving the following three nonlinear relations: (II.113), (II.114), and (II.115). Thus, a search algorithm is developed using two calculation methods, either with the MATLAB *fsolve* function or by applying the Newton algorithm:

$$X_{i+1} = X_i + J^{-1}(X_i)g(X_i), \;\; i \in \mathbb{N} \tag{II.116}$$

where X is the design vector:

$$X = \begin{bmatrix} n_2 \\ R_s \\ R_{sh} \end{bmatrix} \tag{II.117}$$

© Ferdaous Masmoudi 2016 – All rights reserved

and g is the vector of objective functions:

$$g = \begin{bmatrix} F(n_2, R_s, R_{sh}) \\ G(n_2, R_s, R_{sh}) \\ H(n_2, R_s, R_{sh}) \end{bmatrix} = \begin{bmatrix} I_{sc}\left(\frac{(R_s + R_{sh})(e_3 - e_1)}{R_{sh}(e_1 - e_2)}\right) - \frac{V_{oc}}{R_{sh}}\left(1 + \frac{(e_3 - e_1)}{(e_1 - e_2)}\right) + \frac{V_m}{R_{sh}} + I_m\left(1 + \frac{R_s}{R_{sh}}\right) \\ -R_{sh}I_s e2 - nV_t - \Delta_{I_{sc}}\left(nV_t(R_{sh} + R_s) + R_s R_{sh} I_s e2\right) \\ -R_{sh}I_s e1 - nV_t - \Delta_{V_{oc}}\left(nV_t(R_{sh} + R_s) + R_s R_{sh} I_s e1\right) \end{bmatrix} = 0 \quad \text{(II.118)}$$

The term J^{-1} corresponds to the inverse Jacobian matrix of the system under study. The Jacobian is formed by:

$$J = \begin{bmatrix} \frac{\partial F(n_2, R_s, R_{sh})}{\partial n_2} & \frac{\partial F(n_2, R_s, R_{sh})}{\partial R_s} & \frac{\partial F(n_2, R_s, R_{sh})}{\partial R_{sh}} \\ \frac{\partial G(n_2, R_s, R_{sh})}{\partial n_2} & \frac{\partial G(n_2, R_s, R_{sh})}{\partial R_s} & \frac{\partial G(n_2, R_s, R_{sh})}{\partial R_{sh}} \\ \frac{\partial H(n_2, R_s, R_{sh})}{\partial n_2} & \frac{\partial H(n_2, R_s, R_{sh})}{\partial R_s} & \frac{\partial H(n_2, R_s, R_{sh})}{\partial R_{sh}} \end{bmatrix} \quad \text{(II.119)}$$

For the first estimate, the following vector X_0 is chosen:

$$X_0 = \begin{bmatrix} n_{20} \\ R_{s0} \\ R_{sh0} \end{bmatrix} = \begin{bmatrix} 2 \\ 0.001 \\ 100 \end{bmatrix} \quad \text{(II.120)}$$

Figure II.9 also presents the algorithm adopted for identifying the unknowns R_{sh}, R_s, and n_2 of the two-diode model.

II.6 .2 Identification Results of the Two-Diode Model Parameters under STC

Table II.4 presents the results of the algorithms for searching the unknown parameters of the one-diode model applied to the reference cell (JA JAC M5SF-2) under standard measurement conditions, *STC*.

Table II.4: Internal-parameter results for the JAC M5SF-2 cell under STC using the two-diode model.

Parameter	$fsolve$	$Newton$
I_{phref} (A)	5.88802	5.888
I_{s1ref} (A)	1.92927×10^{-11}	1.92926×10^{-11}
I_{s2ref} (A)	6.2819×10^{-8}	6.2818×10^{-8}
n_{1ref}	1	1
n_{2ref}	1.36658	1.36655
R_{sref} (Ω)	1.0637×10^{-3}	1.0636×10^{-3}
R_{shref} (Ω)	253.6219	253.622
N iterations	27	20
Time (s)	0.931	20.546
Method	Trust-region-dogleg	simple Newton

The results in Table II.4 show that the two methods converge toward the same values. The $Newton$ algorithm converged after only 20 iterations; in contrast, the $fsolve$ function was able to

© Ferdaous Masmoudi, 2016 – All rights reserved

converge in 0.931 seconds. It can be observed that the returned values, especially the saturation currents I_{s1ref} and I_{s2ref}, are highly consistent with the theory of silicon $p-n$ junctions.

II.6 .3 Effect of Temperature and Irradiance on the Internal Parameters of the Two-Diode Model

The influence of temperature and irradiance on the model parameters ($n_2(T)$, $I_{s1}(T)$, $I_{s2}(T)$, $R_s(T)$, $R_{sh}(T)$, and $I_{ph}(G,T)$) is presented. The general expression of the two-diode model as a function of G and T is:

$$\begin{aligned} I(G,T) &= \frac{G}{G_{ref}} I_{ph}(T) - I_{s1}(T)\left(\exp\left(\frac{V(G,T)+R_s(T)I(G,T)}{V_t}\right)-1\right) \\ &\quad -I_{s2}(T)\left(\exp\left(\frac{V(G,T)+R_s(T)I(G,T)}{n_2(T)V_t}\right)-1\right) - \frac{V(G,T)+R_s(T)I(G,T)}{R_{sh}(T)} \end{aligned} \quad \text{(II.121)}$$

Analogously to what was established for the other models, and taking Relations (II.20), (II.21), (II.22), and (II.23) into account, Figure II.14 shows the variations of the unknown model parameters as a function of climatic changes.

© Ferdaous Masmoudi, 2016 – All rights reserved

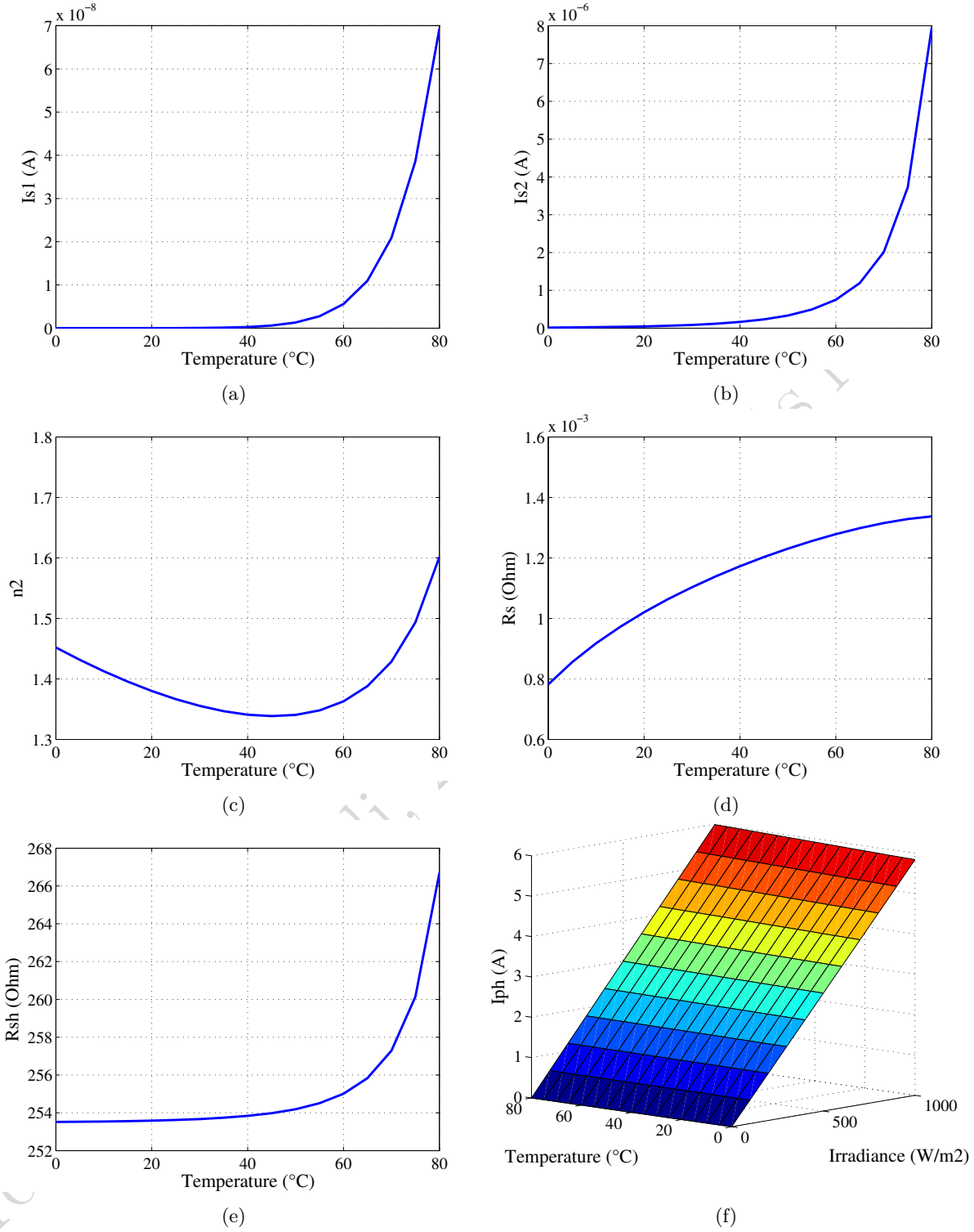


Figure II.14: Variations of the internal parameters of the two-diode model of the JAC M5SF-2 solar cell as functions of temperature and irradiance. (a) Variation of I_{s1} as a function of temperature. (b) Variation of I_{s2} as a function of temperature. (c) Variation of n_2 as a function of temperature. (d) Variation of R_s as a function of temperature. (e) Variation of R_{sh} as a function of temperature. (f) Variation of I_{ph} as a function of temperature and irradiance.

The shapes of the curves presented in Figure II.14 are fully consistent with junction theory and semiconductor physics, particularly doped silicon [32, 33, 34, 35].

Figures II.14.a and II.14.b show increasing trends for the $I_{s1}(T)$ and $I_{s2}(T)$ curves. However, the saturation current of the first diode has negative values for temperatures below 32°C, which contradicts junction theory. Figures II.14.c, II.14.d, and II.14.e show reasonable trends with respect to the literature.

The variation of the photoelectric current $I_{ph}(G,T)$ shown in Figure II.14.f exhibits a surface with a shape identical to those of the previous models, reflecting the negligible effect of the exponential terms in the expression of I_{ph} for this model as well.

II.7 Multiple-Diode Models: Three-Diode Case

Multiple-diode models are models whose equivalent electrical circuits contain more than one diode in parallel with the photogenerated-current source (Figure II.15.a). This is intended to better describe the underlying physics acting within the internal structure of the photovoltaic cell. Multi-diode models make it possible to obtain greater accuracy when simulating solar-cell behavior. However, searching for the unknown parameters of these models requires more complicated algorithms that are considerably more expensive in terms of the amount of computation because of the additional diodes [40-42].

The appropriate choice of the number of associated diodes depends mainly on the type of cell and its manufacturing technology. Since increasing the number of diodes leads to an increase in the number of unknown internal parameters of the electrical model (> 6 parameters), it becomes impossible to use the identification method employed previously, because the datasheet parameters are no longer sufficient.

The search for the unknown parameters of multiple-diode models is developed from the curve-fitting method explained in II.2.2.

As a case study, the triple-diode (3D) model illustrated in Figure II.15.b is used. This model provides an additional improvement over the double-diode model by introducing a third diode. This makes it possible to model correctly the effects of grain boundaries and the leakage current due to the peripheries [56].

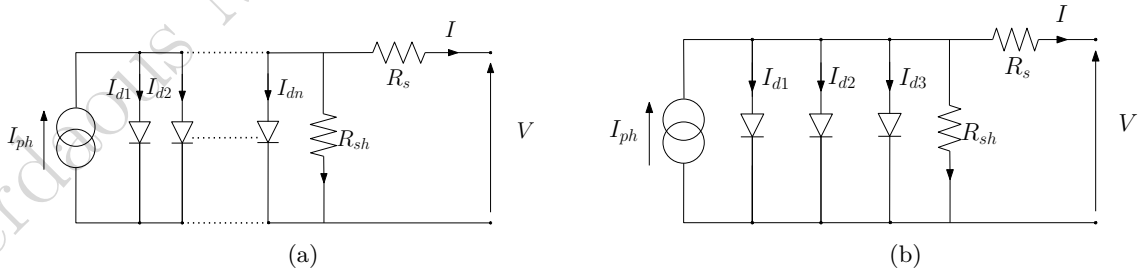


Figure II.15: Equivalent electrical circuits: (a) three-diode model. (b) multi-diode model.

The equivalent electrical circuit of the triple-diode solar-cell model consists of a current source generating the photocurrent I_{ph} in parallel with three diodes carrying the currents I_{d1}, I_{d2}, and I_{d3}, while considering two resistances: the shunt resistance R_{sh} and the series resistance R_s.

© Ferdaous Mastouri, 2016 – All rights reserved

Under irradiance G, the solar-cell $(I-V)$ characteristic is expressed by the following equation:

$$I = I_{ph} - I_{d1} - I_{d2} - I_{d3} - I_{sh} \tag{II.122}$$

The relationship between the current I_{d1} and the voltage V across the cell terminals is described by the following equation:

$$I_{d1} = I_{s1}\left(\exp\left(\frac{V + R_s I}{n_1 V_t}\right) - 1\right) \tag{II.123}$$

Similarly, the relationship between the current I_{d2} and the voltage V is described as follows:

$$I_{d2} = I_{s2}\left(\exp\left(\frac{V + R_s I}{n_2 V_t}\right) - 1\right) \tag{II.124}$$

Likewise, the relationship between the current I_{d3} and the voltage V is described as follows:

$$I_{d2} = I_{s3}\left(\exp\left(\frac{V + R_s I}{n_3 V_t}\right) - 1\right) \tag{II.125}$$

The relationship between the current I_{sh} and the voltage V across the cell terminals can be expressed as follows:

$$I_{sh} = \frac{V + R_s I}{R_{sh}} \tag{II.126}$$

By substituting the currents I_{d1}, I_{d2}, I_{d3}, and I_{sh} with their expressions, Equation (II.122) becomes:

$$\begin{aligned} I \;=\; & I_{ph} - I_{s1}\left(\exp\left(\frac{V + R_s I}{n_1 V_t}\right) - 1\right) - I_{s2}\left(\exp\left(\frac{V + R_s I}{n_2 V_t}\right) - 1\right) \\ & - I_{s3}\left(\exp\left(\frac{V + R_s I}{n_3 V_t}\right) - 1\right) - \frac{V + R_s I}{R_{sh}} \end{aligned} \tag{II.127}$$

with:

- I_{s1}: the junction saturation current associated with diffusion-recombination phenomena in the quasi-neutral region,
- I_{s2}: the junction saturation current associated with the recombination phenomenon in the space-charge region,
- I_{s3}: the saturation current associated with the recombination phenomenon in defect regions and grain-boundary sites,
- n_1: the ideality factor of diode 1, generally ranging from 1 to 2,
- n_2: the ideality factor of diode 2, considered to range from 1 to 5,
- n_3: the ideality factor of diode 3, considered to range from 2 to 5.

The unknown parameters of this model are (I_{ph}, I_{s1}, n_1, I_{s2}, n_2, I_{s3}, n_3, R_s, and R_{sh}). The remainder of the work consists of implementing a curve-fitting procedure in order to estimate the nine unknown parameters of the triple-diode model.

© Ferdaous Masmoudi 2016 – All rights reserved

II.7 .1 Search for Unknown Parameters Using the Genetic Algorithm

The genetic algorithm (GA) [57] is a heuristic adaptive optimization tool whose search technique is inspired by Darwinian principles of survival of the fittest in biological genetics. The GA, originally introduced by Holland (1975), simulates the evolutionary process of a living species by means of typical biological-genetics operations such as selection (*Selection*), mutation (*Mutation*), and crossover (*Crossover*).

Genetic algorithms have been applied in several fields. They do not require auxiliary information or specific knowledge as other exact optimization methods do. Consequently, they are highly practical for complex applications.

The principle of the genetic algorithm is based on using multiple simultaneous search points (Population) on which genetic operations are applied. This procedure is applied iteratively until the convergence criterion is satisfied. The population P contains N individuals X_i. Each individual is composed of D elements $x_{i,j}$ corresponding to the unknown parameters of the model. The population at iteration T can be represented by the following matrix:

$$P^T = \begin{pmatrix} X_1^T \\ \vdots \\ X_i^T \\ \vdots \\ X_N^T \end{pmatrix} = \begin{pmatrix} x_{1,1}^T & \cdots & x_{1,j}^T & \cdots & x_{1,D}^T \\ \vdots & \ddots & \vdots & \ddots & \vdots \\ x_{i,1}^T & \cdots & x_{i,j}^T & \cdots & x_{i,D}^T \\ \vdots & \ddots & \vdots & \ddots & \vdots \\ x_{N,1}^T & \cdots & x_{N,j}^T & \cdots & x_{N,D}^T \end{pmatrix} \text{ with: } \begin{cases} i \in [1, N] \\ j \in [1, D] \\ T \in [1, T_{max}] \end{cases} \tag{II.128}$$

The flowchart of the developed genetic algorithm is presented in Figure II.16.

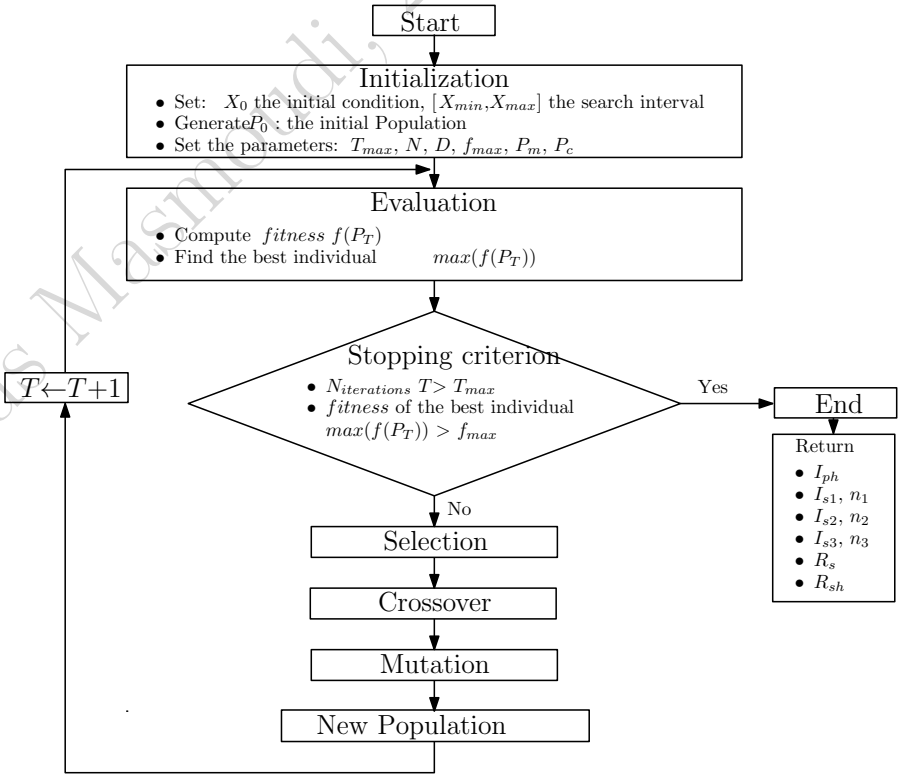


Figure II.16: Genetic algorithm.

© Ferdaous Masmoudi, 2016 - All rights reserved

II.7 .2 Search for Unknown Parameters Using the Evolved Gradient Algorithm

The evolved gradient (GE) algorithm [58] presents a new metaheuristic method derived from the gradient method. In an exact optimization method, the gradient is used to find optima. This method uses the gradient as an updating rule.

The GE algorithm explores the search space by means of a set of vectors and includes three main operators: Updating vector (*Updatin*), Jumping vector (*Jumping*), and Refreshing vector (*Refreshing*). The updating vector represents the main rule acting on the population of probable solutions. The search direction is determined using the Newton-Raphson method. The Jumping and Refreshing vectors make it possible to avoid local optima. The flowchart of the evolved gradient algorithm is presented in Figure II.17.

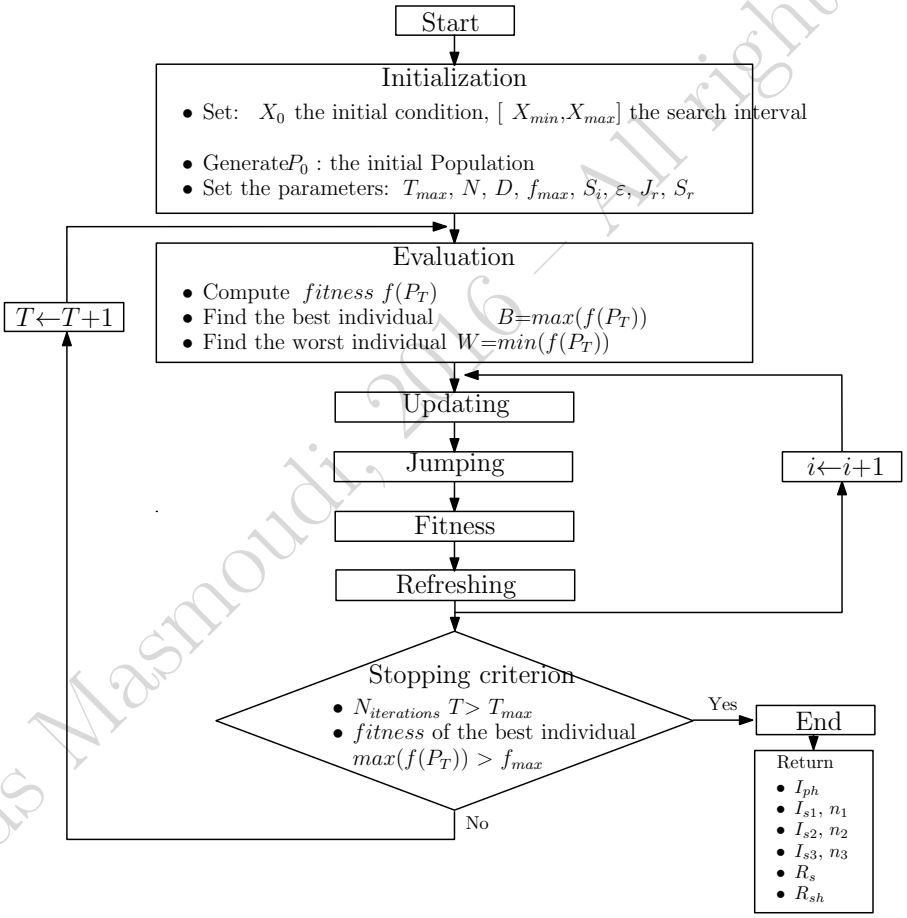


Figure II.17: Evolved gradient algorithm.

II.7 .3 Search Results for the Three-Diode Model Parameters under STC

Table II.5 presents the results of the algorithms for searching the unknown parameters of the three-diode model applied to the reference cell (JA JAC M5SF-2) under standard measurement conditions, *STC*.

© Ferdaous Masmoudi, 2016 — All rights reserved

Table II.5: Internal-parameter results for the JAC M5SF-2 cell under STC using the triple-diode model.

Parameter	Genetic	Evolved Gradient
I_{ph} (A)	5.8883	5.8893
I_{s1} (A)	2.906×10^{-10}	2.5101×10^{-10}
I_{s2} (A)	5.2373×10^{-5}	3.4669×10^{-5}
I_{s3} (A)	5.0407×10^{-3}	3.5558×10^{-3}
n_1	1.0492	1.046
n_2	2.7627	2.4222
n_3	4.3131	4.9479
R_s (Ω)	0.001894×10^{-4}	0.001398
R_{sh} (Ω)	374.6215	157.6793
$fitness$	10.121	11.543
N iterations	501	101
Time (s)	1829.125	3111.209

The results in Table II.5 show that the two algorithms converge toward slightly different values, which can nevertheless be considered fairly close. These results can be improved by increasing the number of iterations; however, this results in a longer computation time.

It can be observed that the genetic algorithm executes a large number of iterations in a shorter time, unlike the evolved gradient algorithm, which performs fewer iterations but requires a longer computation time because of the complexity of the operations performed.

At this stage, the evolved gradient algorithm can be considered more efficient in searching for the internal parameters, since its fitness is higher than that of the genetic algorithm.

II.7 .4 Effect of Temperature and Irradiance on the Internal Parameters of the One-Diode Model

The influence of temperature and irradiance on the model parameters (I_{ph}, I_{s1}, n_1, I_{s2}, n_2, I_{s3}, n_3, R_s, and R_{sh}) is presented. Taking Relations (II.20), (II.21), (II.22), and (II.23) into account, Figure II.19 presents the variation of the unknown model parameters as a function of climatic changes.

© Ferdaous Massaoudi, 2016 – All rights reserved

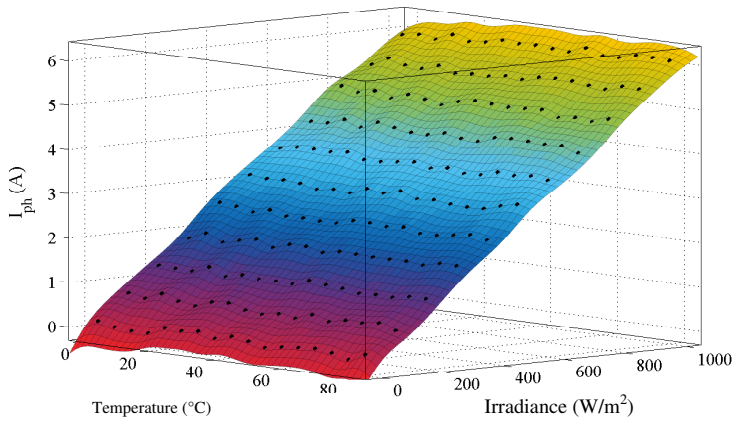


Figure II.18: Variation of I_{ph} as a function of temperature and irradiance using the evolved gradient algorithm.

The evolved gradient algorithm was used repeatedly (from 3 to 8 trials) and for different values of irradiance G and temperature T. Since the algorithm does not reach the same high fitness factor at every point, the MATLAB *Curve Fitting Toolbox*[5] was used to fit the shapes of the curves by interpolation. Figure II.18 shows the variation of the photogenerated current I_{ph} as a function of climatic changes. It can be observed that the general shape of the 3D-model surface is similar to the shapes obtained with the previous models and is fully consistent with the theoretical study already carried out.

Similarly, the two algorithms studied (Genetic and Evolved Gradient) were used repeatedly and for different values of irradiance and temperature to determine the parameters of the 3D model as functions of climatic changes. Figure II.19 presents the results obtained. The plotted points indicate the results of the various trials performed, and the curves are estimated by appropriate interpolation using the *cftool* toolbox.

Overall, the curves show complete consistency with doped-silicon junction theory, especially in terms of the saturation currents I_{s1}, I_{s2}, and I_{s3} (Figures II.19.b, II.19.d, and II.19.f) and their orders of magnitude. Consequently, the values of the resistances R_{sh} and R_s (Figures II.19.g and II.19.h) are reasonable, and the curves show an increase as temperature rises, which has been experimentally verified by several studies [32, 33, 34, 35].

Regarding the ideality factors n_1, n_2, and n_3 (Figures II.19.a, II.19.c, and II.19.e), it can be observed that the value of n_1 tends toward unity as temperature increases, whereas n_2 and n_3 exhibit parabolic curve shapes. These shapes can be justified by the limitation of the solar junction in withstanding high temperatures. Indeed, the junction ideality coefficient is related to several factors, such as the silicon doping level and the intrinsic defects of the crystal lattice. These factors become particularly apparent at high temperatures (temperature promotes intermolecular vibration of the crystal lattice and accelerates collisions between free particles) and modify the conduction quality of the monocrystalline material.

[5]For more information about this toolbox, type >> *cftool* in the MATLAB command window, or consult the online *Mathworks* guide: http://fr.mathworks.com/products/curvefitting/.

© Ferdaous Mamouni, 2016 - All rights reserved

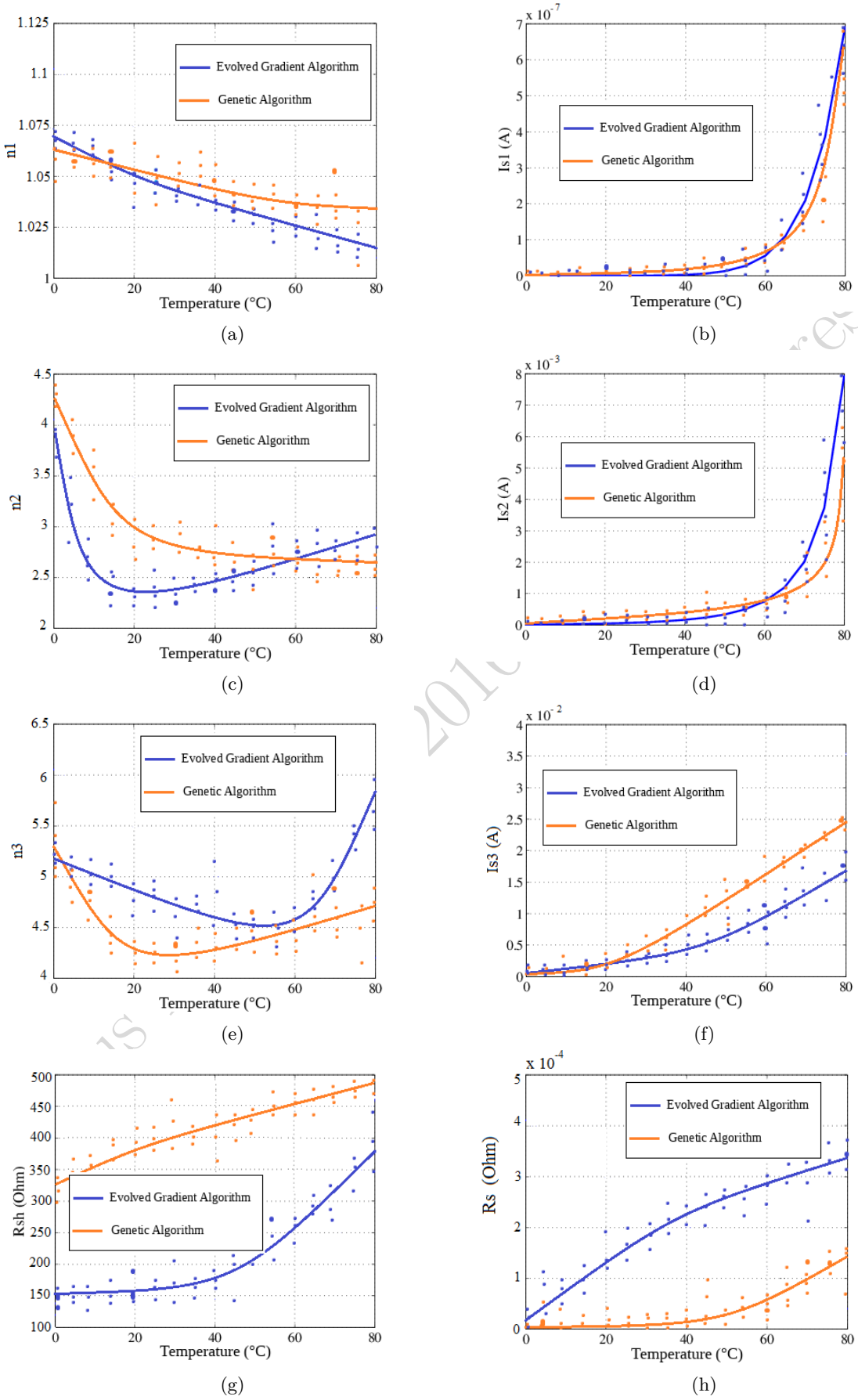


Figure II.19: Variations of the internal parameters of the three-diode model of the JAC M5SF-2 solar cell as functions of temperature. (a) Variation of n_1 as a function of temperature. (b) Variation of I_{s1} as a function of temperature. (c) Variation of n_2 as a function of temperature. (d) Variation of I_{s2} as a function of temperature. (e) Variation of n_3 as a function of temperature. (f) Variation of I_{s3} as a function of temperature. (g) Variation of R_{sh} as a function of temperature. (h) Variation of R_s as a function of temperature.

II.8 Simulation Results and Experimental Validation

In this section, the aim is to present and then discuss the simulation results of the previously detailed solar-cell models, which are implemented in the Matlab Simulink/SimpowerSystems environment, as shown in Figure II.20.

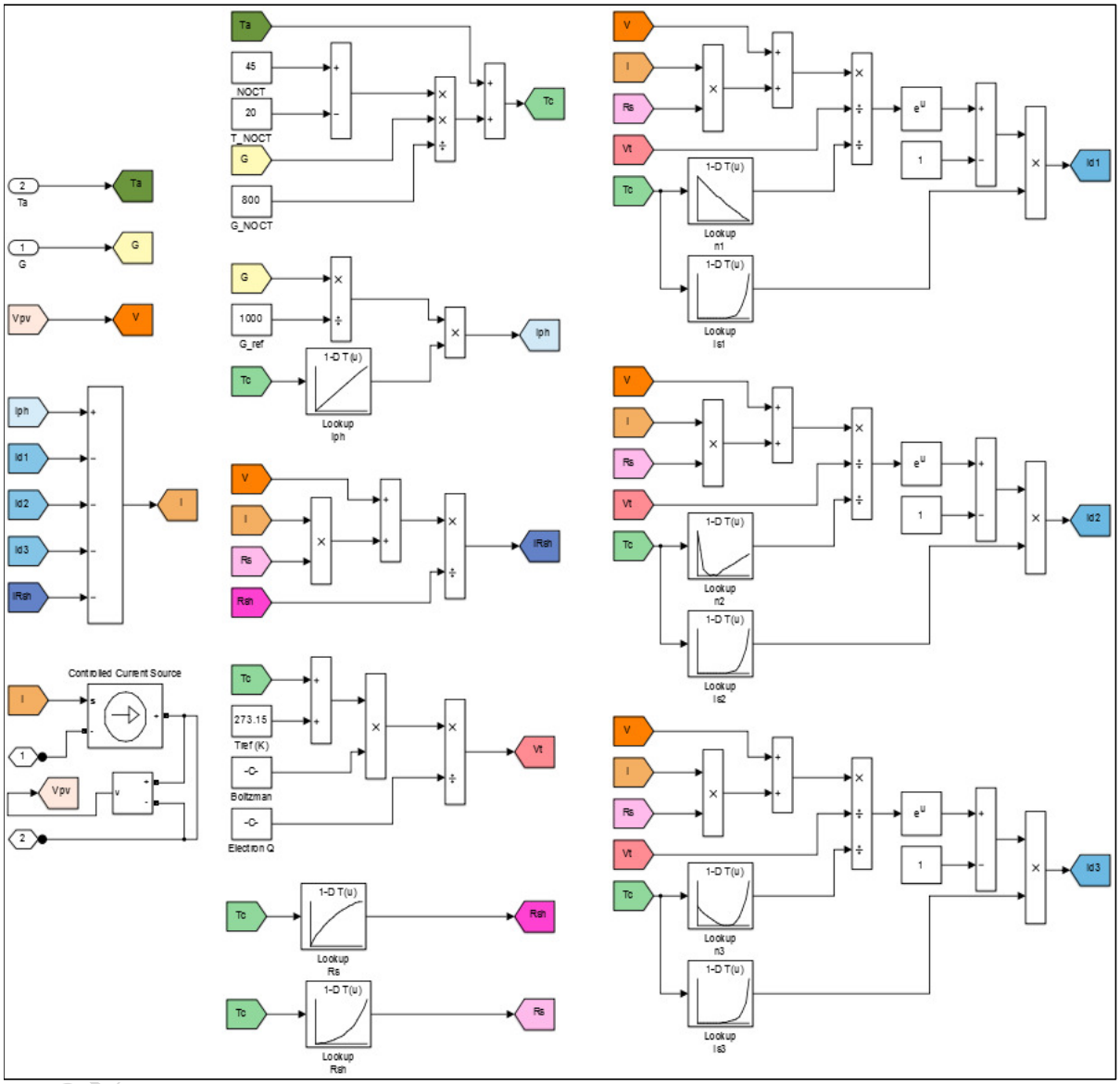


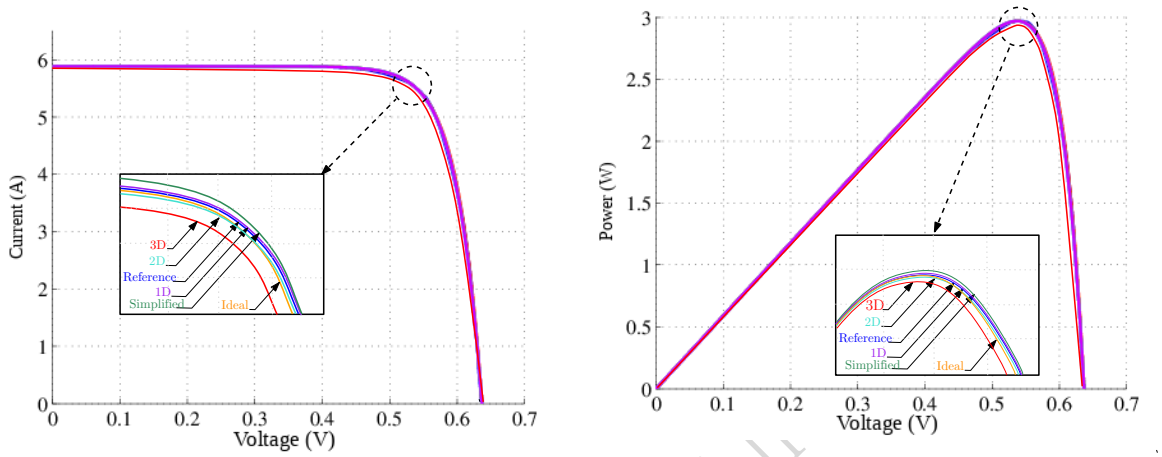
Figure II.20: Example of implementation of the solar-cell model in the MATLAB-Simulink environment: triple-diode model.

A comparison is presented between the five models applied to the reference solar cell under STC and then outside STC. The effect of irradiance and temperature on solar-cell performance is detailed. Finally, the five models studied are applied to a set of photovoltaic generators of different types, and the validity of the models for any solar-cell technology is demonstrated.

© Ferda

II.8 .1 Comparison of the Solar-Cell Models under STC

Figure II.21 illustrates the $(I-V)$ and $(P-V)$ characteristics obtained by simulation from the five solar-cell models studied, comparing them with the reference characteristics of the JA JAC MS5f monocrystalline reference cell provided by the manufacturer in the datasheet.



(a) (b)

Figure II.21: Comparison between the different models and the reference curve: (a) $(I-V)$ characteristic. (b) $(P-V)$ characteristic.

Analysis of the figure highlights the ability of the different models to reproduce the characteristic provided by the manufacturer. Better agreement in favor of the one-diode model can be observed, perceptible only at high magnification.

For a quantitative evaluation, the maximum error between the simulated characteristics and the reference characteristic is analyzed together with the fill factor FF, indicated in the datasheet as being equal to 79.19%. The maximum error between the two curves is determined from Relation II.129:

$$\xi_r = max(|P^{sim} - P^{ref}|) \tag{II.129}$$

The fill factor FF of the solar cell can be evaluated from Expression II.130:

$$FF = \frac{P_m}{V_{oc} I_{sc}} \tag{II.130}$$

A summary of the errors and fill factors is presented in Table II.6. The results confirm the good agreement of the models, with a slight improvement observed for the one-diode model.

Table II.6: Comparison between the simulation characteristics and the reference characteristic.

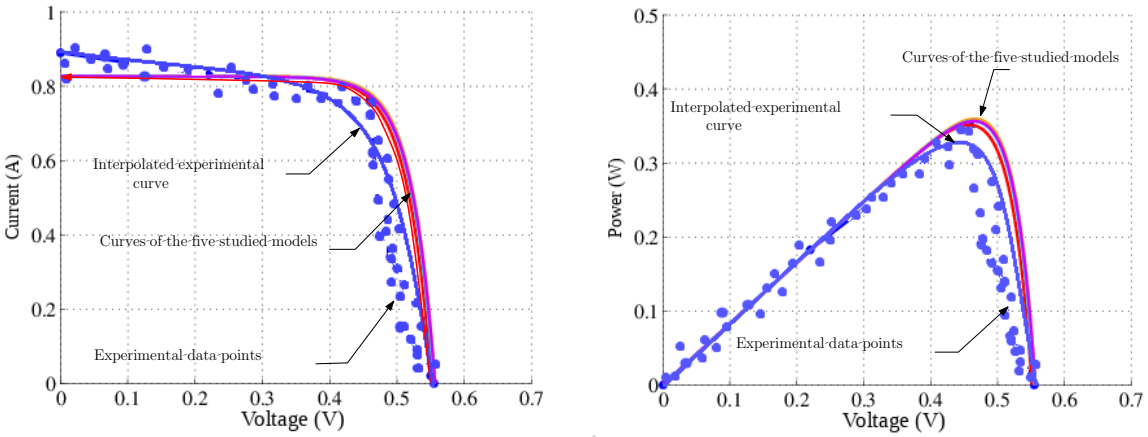
	ξ_r	FF (%)
Ideal model	0.064	77.48
Simplified model	0.0785	77.09
1D model	0.0534	78.68694
2D model	0.0607	78.16661
3D model	0.089	76.8146

© Ferdaous Masmoudi, 2016 - All rights reserved

II.8 .2 Comparison of the Solar-Cell Models outside STC

The experimental measurements performed on the JA JAC MS5f-2 monocrystalline solar cell, described in Section I.2.3, are presented in Figure II.22. For an ambient temperature of $T_a = 28°\text{C}$ and an irradiance of $G = 500\ \text{W/m}^2$, the simulated $(I-V)$ and $(P-V)$ characteristics of the different models are also represented.

The comparison between the experimental results and the simulations confirms the validity of the models outside standard test conditions, particularly at the characteristic points.



(a) (b)

Figure II.22: Comparison between the different models and the experimental curve: (a) $(I-V)$ characteristic. (b) $(P-V)$ characteristic.

II.8 .3 General Evaluation of the Solar-Cell Models

The comparative results of the different solar-cell models reveal a strong similarity, with the error deviation between them remaining limited.

However, significant differences appear in terms of complexity and the physical meaning of the parameters specific to each model.

Table II.7 presents a summary evaluation of the different models according to several criteria.

Table II.7: Evaluation of the monocrystalline solar-cell models.

Models	Number of Parameters	System Complexity	Execution Time	Model Accuracy	Physical Meaning
Ideal model	+++	+++	+++	+	+
Simplified model	++	++	++	+	-
1D model	+	+	+	+++	+++
2D model	+	+	+	++	++
3D model	++++	-	-	++	++

For monocrystalline solar cells, the simulations show that the one-diode model is the most appropriate and the most faithful for reproducing their actual behavior. It provides a good compromise between accuracy and complexity.

© Ferdaous Mahmoudi, 2016

The ideal model also proves effective considering its simplicity and the reduced number of initial parameters required to execute the search algorithm. It provides acceptable accuracy with a short execution time, and its parameters also retain consistent physical meaning.

However, the one-series-resistance model contains parameters that lack rigorous physical meaning; nevertheless, this does not affect the overall accuracy of the model, which remains satisfactory. This model remains simple and requires a limited number of initial parameters.

Regarding the two-diode model, its complexity as well as the long execution time of the search algorithm are explicitly observable. Nevertheless, it correctly represents the monocrystalline solar cell, particularly from the standpoint of the physical consistency of the parameters.

The least accurate models in this study are the multi-diode models, particularly the triple-diode model. Based on the fitting method, it appears more complex than the models resulting from the identification method. Nevertheless, this model remains an appropriate approach for modeling multiple-diode solar cells. It is also relevant for new-generation multijunction solar cells as well as concentrator photovoltaic systems.

In general, the fitting method remains applicable to the other solar-cell models (ideal, simplified, 1D, and 2D) in the absence of manufacturer data or when the module under study undergoes an aging phenomenon. In this context, establishing a reliable model requires recent and accurate experimental measurements.

II.8 .4 Effect of Temperature and Irradiance on Solar-Cell Efficiency

In order to highlight the influence of irradiance G on solar-cell behavior, Figure II.23 illustrates the simulated $(I-V)$ and $(P-V)$ characteristics for different values of irradiance G. The results lead to the following observations:

- the short-circuit current I_{sc} is proportional to irradiance G,
- the open-circuit voltage V_{oc} remains relatively high, even for low values of G,
- the maximum power P_m varies with the voltage V_m according to a nonlinear law, particularly at low irradiance values G.

© Ferdaous Masmoudi, 2016 – All rights reserved

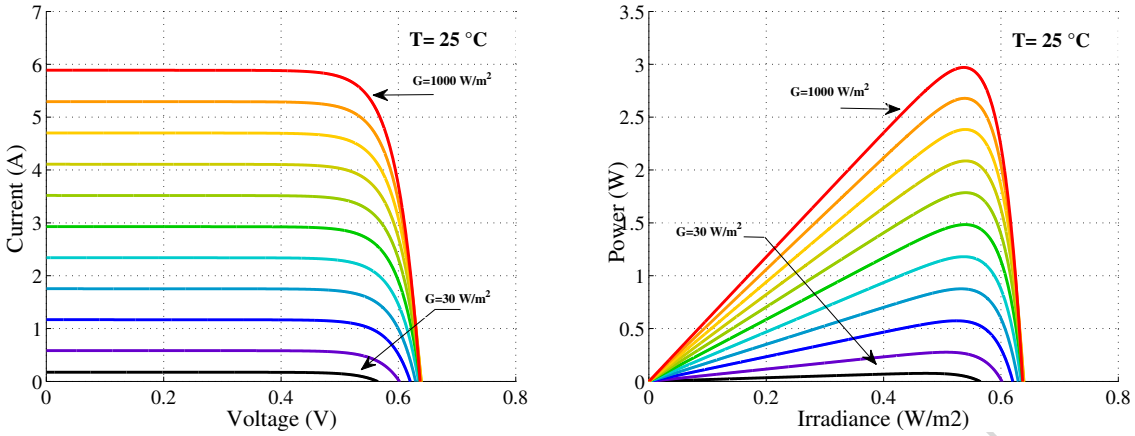


Figure II.23: Effect of irradiance variation on the solar-cell characteristics: (a) $(I-V)$ characteristic. (b) $(P-V)$ characteristic.

In order to analyze the influence of the junction temperature T on solar-cell behavior, Figure II.24 presents the $(I-V)$ and $(P-V)$ characteristics simulated using the solar-cell model for different values of T. Analysis of the results highlights that:

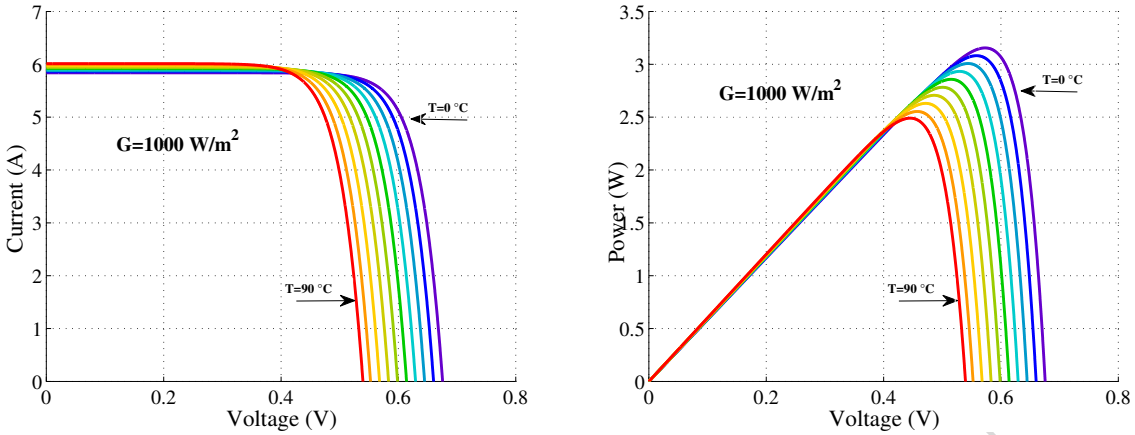
- the point (V_m,I_m) of maximum power P_m decreases as the temperature T_c increases; this phenomenon is due to the decrease in the voltage V_m across the cell terminals, while the variation of I_m remains negligible,
- the maximum power P_m varies almost linearly as a function of the voltage V_m for all values of T_c.

The joint study of the influence of irradiance G and temperature T on the solar cell shows that a decrease in G or an increase in T leads to degradation of solar-cell performance.

This loss of efficiency is mainly due to:

- the decrease in the current I produced by the solar generator, which is highly sensitive to the irradiance intensity G,
- the decrease in the voltage V across the solar-generator terminals, which is closely related to the junction temperature T_c.

© Ferdaous Masmoudi, 2016 – All rights reserved



(a) (b)

Figure II.24: Effect of temperature variation on the solar-cell characteristics: (a) $(I-V)$ characteristic. (b) $(P-V)$ characteristic.

II.9 Conclusion

This chapter dealt with the modeling of photovoltaic solar cells through the study of five distinct electrical models. The methods for identifying the internal parameters were presented while taking into account the variation of temperature T and irradiance G.

The results obtained confirm the validity of the different models while highlighting the advantages and limitations specific to each one.

The implementation of the models in Matlab-Simulink made it possible to reproduce the behavior of the solar cell with satisfactory accuracy. The models were also applied to different photovoltaic-cell technologies, confirming their robustness and consistency.

The developed model can be integrated into the complete simulation of photovoltaic conversion chains, in association with other blocks such as converters, inverters, batteries, loads, etc.

© Ferdaous Masmoudi, 2016 - All rights reserved

Chapter III

Optimal Association and Operation of Solar Cells and Modules

Abstract: *This chapter introduces the association of solar cells as well as the composition of a PV solar module. The fundamental problems responsible for improper operation of the solar module are discussed. The available solar resource in the environment, which depends on the geographical location, is then studied, and the advantages and energy benefits associated with tracking the sun's trajectory are highlighted. The work presented in this chapter concludes with the design and implementation of an intelligent two-axis motorized solar tracker programmed in closed loop.*

Keywords: PV Solar Cell / Module,
Series / Parallel / Mixed Associations,
Uniform and Partial Shading,
Mismatch / Hot-Spot Effect,
Solar Resource and Radiation,
Intelligent Solar Tracker.

© Ferdaous Messaoudi, 2016 – All rights reserved

III.1 Introduction

During its daily operation, the PV generator is subject to several constraints affecting its efficiency and safety. The diagram in Figure III.1 summarizes the main factors that can influence the performance of a PV module [59, 60, 61, 62].

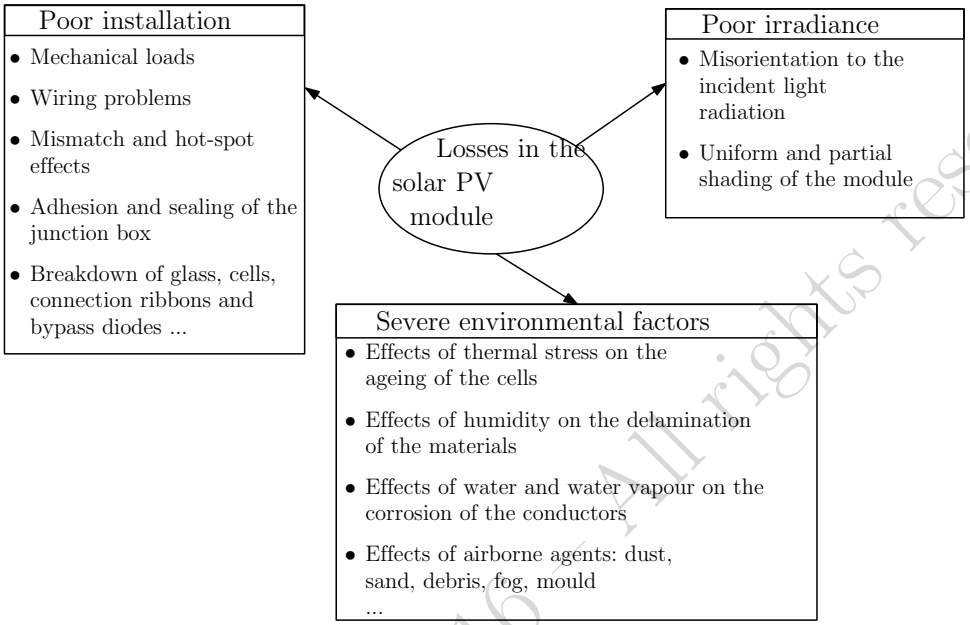


Figure III.1: Main factors leading to the degradation of PV-generator efficiency.

Installing a PV generator that ensures optimal efficiency is mainly governed by adequate avoidance of the different sources of losses. It is understood that this work does not aim to optimize the PV generator from a physical and chemical standpoint by improving the quality of the solar junction itself; rather, the objective is to improve the operation and protection of the solar equipment in order to extract the maximum amount of energy, extend its lifetime, and maintain a high efficiency. From the diagram in Figure III.1, three actions can be identified for optimizing solar efficiency:

Maintenance and Repair: Certain mechanical and electrical damage, as well as natural atmospheric deposits on the PV module, can only be addressed through scheduled routine maintenance of the equipment in order to carefully monitor the condition of the module and remove or repair the various forms of damage.

Risk Prevention: PV-module operation involves identifiable and predictable risks, mainly related to the electrical quantities characterizing the solar generator. To overcome these risks, theoretical studies and simulation work are carried out in order to anticipate and assess the losses, identify the origin of faults, and subsequently develop affordable solutions.

Regulation through Monitoring and Control: This action is generally undertaken following the prevention stage. An anomaly affecting the PV module and studied theoretically can be mitigated by an appropriate regulation system. Such a system must obviously

© Ferdaous Masmoudi, 2016 - All rights reserved

include fault-detection sensors required for the monitoring stage, as well as actuators capable of intervening mechanically and electrically to prevent damage. The control stage is handled by a processing unit (generally a microcontroller) capable of processing the information acquired by the sensors, making decisions through appropriate computations, and transmitting control signals to the actuators.

The work carried out in this chapter contributes to the topics of risk prevention and PV-system regulation, first by simulating the behavior of an association of solar cells under various environmental factors, and then by designing and implementing a regulation system (an intelligent solar tracker) programmed in closed loop to optimize the efficiency of the PV module.

First, the different forms of PV generators (cell, module, panel, and array) and the mechanical composition of a solar module are presented. The different types of solar-cell associations are then studied rigorously in order to model a 50 W solar module having electrical characteristics comparable to the module used in practice. Experimental tests are conducted on the 50 W solar module in order to validate the simulation results. It should be noted that, throughout this work, only one module is considered, and associations of several solar modules are not studied.

Next, with the aim of taking preventive action, the key parameters affecting solar-module efficiency are studied, mainly the effects of shading, mismatch, and hot spots. A simulation model of a solar module is therefore developed to highlight these different problems.

The third part concerns the study of the solar resource and solar radiation available in the environment and their characteristics with a view to their optimal exploitation. For this purpose, a general overview of the solar-resource situation in Tunisia, and particularly in Sfax, is presented. This is followed by a study of the movement and position of the sun relative to the Earth. The solar radiation incident on an inclined plane is then studied, considering the case of the city of Sfax, and a simulation model is developed to highlight the importance and interest of tracking the sun's trajectory with the PV module in order to generate maximum electrical power.

The fourth and final part concerns the design and implementation of an intelligent two-axis motorized solar tracker programmed in closed loop, capable of detecting the position of the sun while performing the necessary regulation to avoid all sources of shading.

III.2 Associations of Photovoltaic Solar Cells and Modules

Photovoltaic energy can be used for both small- and large-scale applications depending on the desired total power. For this purpose, solar cells (Figure III.2.a) can be associated in series and/or in parallel to increase the required operating voltage and/or current [13].

A photovoltaic module (Figure III.2.b) consists of several photovoltaic cells connected in series or in parallel (manufacturers generally prefer to use only a series association within a single module). A photovoltaic panel, as illustrated in Figure III.2.c, consists of several modules electrically connected in series or in parallel and mounted together on the same mechanical support. Finally, a photovoltaic network, array, or field consists of several solar panels electrically

© Ferdaous Masmoudi 2016 - All rights reserved

connected in series or in parallel, as shown in Figure III.2.d. In what follows, the composition of a PV solar module is first presented, followed by a study of the influence of solar-cell associations on the electrical output quantities of the resulting PV generator.

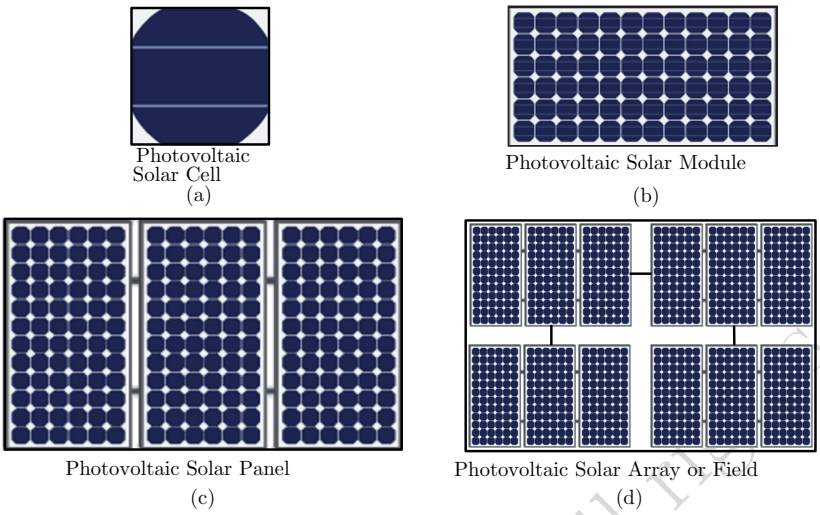


Figure III.2: Illustrations of (a) a solar cell, (b) a solar module, (c) a solar panel, and (d) a solar array.

III.2 .1 Composition of a PV Solar Module

A PV module consists of several interconnected solar cells (typically 36 cells connected in series) encapsulated in a single robust and durable unit. The main purpose of encapsulating the electrically connected solar cells is to protect both the cells and their metallic interconnection wires (ribbons) from the harsh environment in which they are used. Indeed, relatively thin solar cells are very fragile and are subject to mechanical damage unless they are properly protected. In addition, the front metal grid of the solar cell and the metallic interconnection ribbons linking the different cells may be corroded by water or water vapor. The two main functions of encapsulation are therefore protection against mechanical damage and corrosion [7, 56].

There are many types of photovoltaic modules with different structures suited to the nature of the solar cells used. For example, amorphous-silicon solar cells are often encapsulated in a flexible material, whereas silicon solar cells are generally packaged within rigid layers with a durable glass front surface.

The lifetime of these modules is largely determined by the way in which they are protected from the surrounding environment. Some suppliers specify a lifetime of 30 years and provide warranties of 5 to 10 years ensuring that the module produces 90% of its rated power during the first 10 years. It should therefore be noted that optimizing the efficiency of a solar module first requires appropriate protection and maintenance of the equipment throughout its operating life.

A conventional solar module generally consists of several robustly encapsulated protective layers, as illustrated in Figure III.3.a [63].

Front-Surface Material: The front surface of a silicon PV module must have high light transmission over the wavelength range from 350 nm to 1200 nm.

© Ferdaous Maamoudi, 2016 – All rights reserved

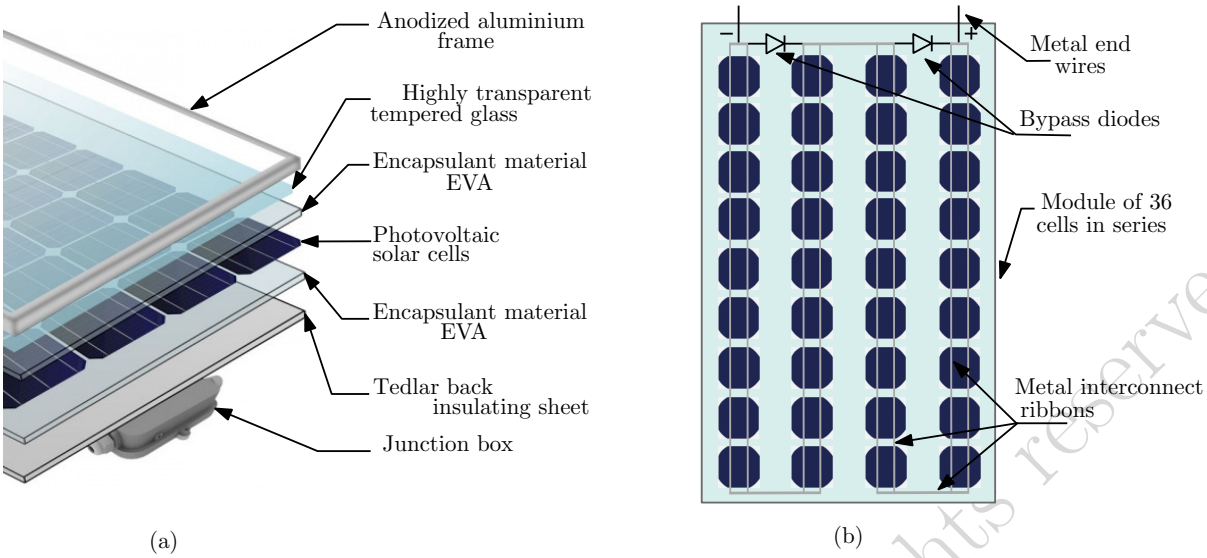


Figure III.3: Illustrations of a typical solar module. (a) Module composition. (b) Electrical interconnections of the cells.

In addition, reflection at the front surface must be low. This reflection could be reduced by applying an antireflection coating to the upper surface. However, such a coating is not sufficiently robust to withstand the harsh environmental conditions in which most photovoltaic systems are used. Another technique for reducing reflection is to roughen or texture the surface. In this case, however, dust and dirt are more likely to adhere to the upper surface and less likely to be removed by wind or rain. Such modules are no longer "self-cleaning", and the benefits of reduced reflection are quickly offset by losses due to increased soiling of the front surface.

In addition to its reflection and transmission properties, the upper-surface material must be impermeable to water, have good mechanical impact resistance, be sufficiently rigid to support the solar cells and wiring, remain stable under prolonged exposure to ultraviolet (UV) radiation, and have low thermal resistivity.

Several choices are available for the upper-surface material, including polymers, acrylics, and tempered glass. Low-iron tempered glass is often the most widely used material because it is inexpensive, strong, stable, highly transparent, impermeable to water and gases, and has good self-cleaning properties.

Rear-Surface Material: The main characteristics required of the rear surface of a photovoltaic module are low thermal resistance and sealing against penetration by water and water vapor. In most modules, a thin polymer sheet, typically *polyvinyl fluoride* (PVF), commonly known by the trade name "Tedlar", is used as the rear surface. Some photovoltaic modules, known as bifacial modules, are designed to accept light from both the front and rear of the solar cell. In this case, both surfaces must be optically transparent.

Encapsulation Material: An encapsulation material is used to ensure adhesion among the

© Ferdaous Maghnouji, 2016 – All rights reserved

solar cells, the upper surface, and the rear surface of the photovoltaic module. The encapsulant must remain stable at high temperatures and under strong UV exposure. It should also be optically transparent and have low thermal resistance. *Ethylene-vinyl acetate* (EVA) is the most commonly used encapsulation material. EVA is supplied in thin sheets that are inserted between the solar cells, the upper surface, and the rear surface. This sandwich is then heated to 150 °C to polymerize the EVA and bond the entire module.

Frame: The border or frame is the final structural component of the module. It is typically made of aluminum, and the frame structure is free of protrusions that could lead to the accumulation of water, dust, or other materials. Plastic frames are also designed for thin-film silicon module technology.

Junction Box: A junction box is the output interface of a solar module. It contains the electrical connections and the ends of the metallic ribbons linking the solar cells, as well as the "Bypass" diodes that protect the module against reverse currents when it is in darkness (Figure III.3.b). The photovoltaic junction box is a sealed plastic enclosure attached to the rear of the solar panel using silicone adhesive. It protects the terminal connections from corrosion by preventing the penetration of external intrusions.

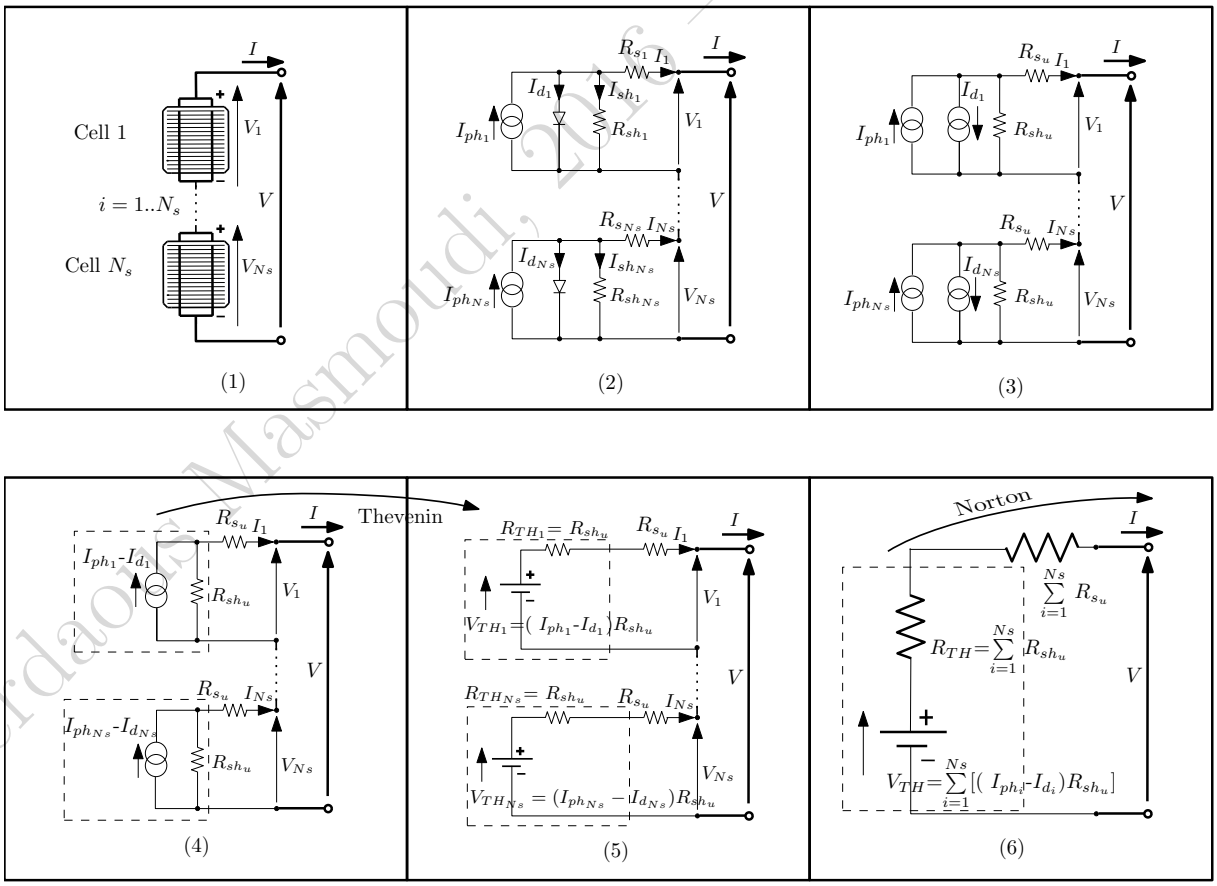
© Ferdaous Masmoudi, 2016 – All rights reserved

III.2 .2 Series Association of Solar Cells

For a number N_s of solar cells connected in series, the voltages delivered by each cell V_i, $i = 1..N_s$, are added together, and their sum gives the resulting voltage V. Furthermore, all cells are traversed by the same current, and the total current I resulting from a series association of solar cells depends on the currents I_i generated by each cell. In order to determine the exact mathematical relations of the electrical quantities resulting from a series association of N_s solar cells, Figure III.4 provides an illustration and demonstration of the calculation procedure for the equivalent electrical circuit.

The assumptions considered in this demonstration are as follows:

- All cells are assumed to be of the same type, exactly identical, and equivalent to a unit cell; their internal parameters related to junction quality are therefore equal, giving: I_{s_i}=I_{s_u}, R_{s_i}=R_{s_u}, R_{sh_i}=R_{sh_u}, n_i=n_u, for $i = 1..N_s$.
- The additional resistances due to the interconnection wires linking the cells are neglected.
- The equivalent parallel diode is considered as a current source with $I_{di} = I_{s_u}\left(\exp\left(\frac{V_i+R_{s_u}I_i}{n_u V_t}\right) - 1\right)$.



The mathematical equations of the electrical quantities resulting from such an association are

© Feridaoui Masmoudi, 2016 – All rights reserved

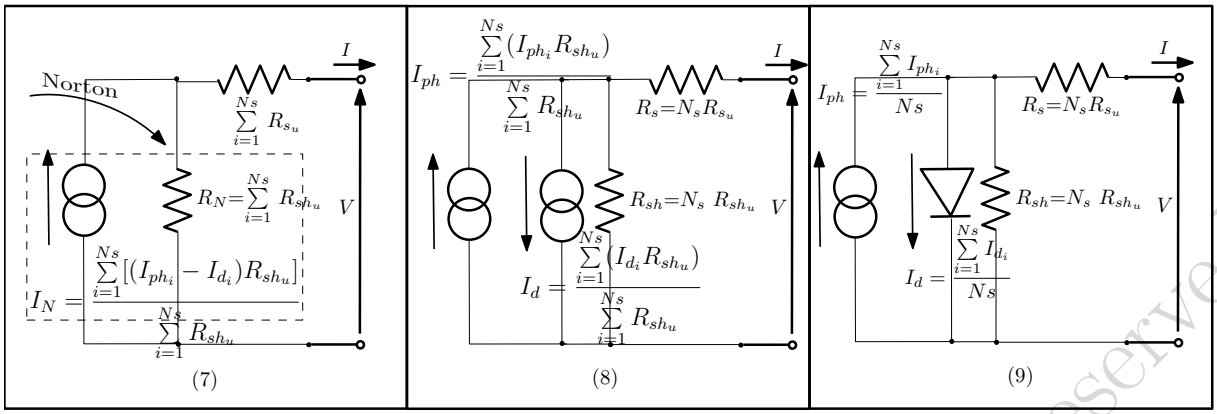


Figure III.4: Illustration and demonstration of a series association of N_s solar cells.

written as follows:

$$V = \sum_{i=1}^{N_s} V_i \tag{III.1}$$

$$I = \frac{\sum_{i=1}^{Ns} I_{ph_i}}{Ns} - \frac{\sum_{i=1}^{Ns} \left[I_{s_u} \left(\exp\left(\frac{V_i + R_{s_u} I_i}{n_u V_t} \right) - 1 \right) \right]}{Ns} - \frac{V + N_s R_s I}{N_s R_{sh}} \tag{III.2}$$

For typical monocrystalline solar cells (such as the cell used in this work) with a conventional front metal grid, a series connection is established by connecting the metal-grid busbars on the front side to the rear metal contact of the neighboring cell.

III.2 .3 Parallel Association of Solar Cells

For a number N_p of solar cells connected in parallel, the currents delivered by each cell I_j, $j = 1..N_p$, are added together, and their sum gives the resulting current I. In addition, all cells are connected across the same potential difference, and the resulting voltage V in a parallel association of solar cells depends on the voltages V_j generated by each cell.

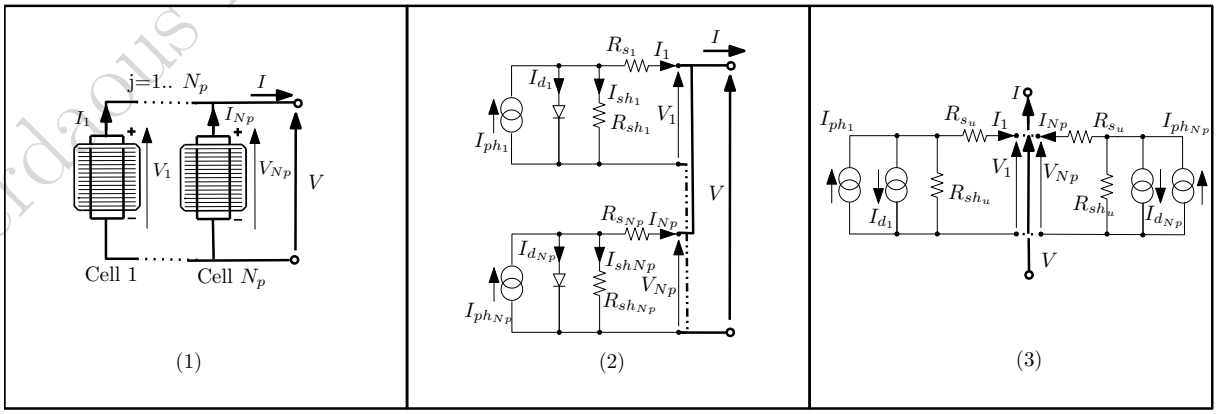


Figure III.5 illustrates and demonstrates the calculation procedure for the equivalent electrical circuit. The same assumptions considered for the series association are retained.

© Feridaous Masmoudi, 2016 – All rights reserved

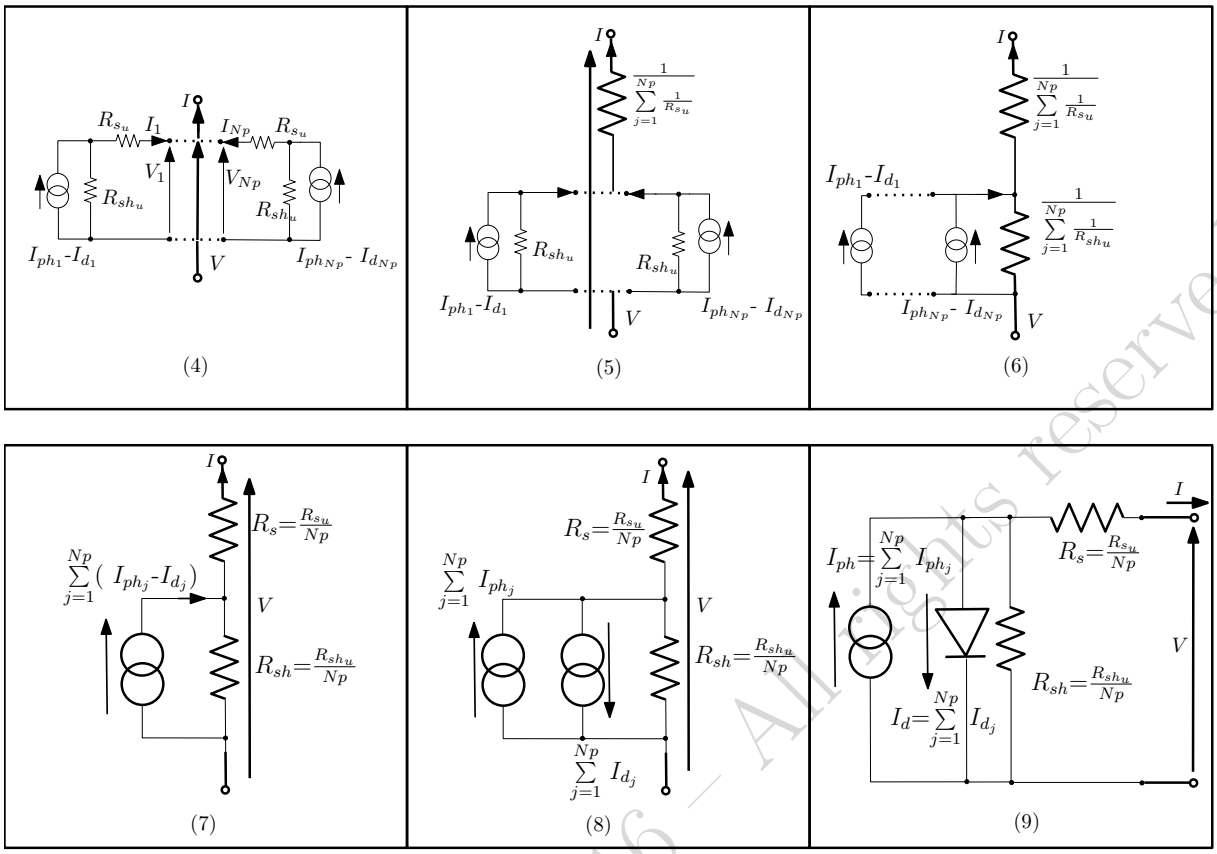


Figure III.5: Illustration and demonstration of a parallel association of N_p solar cells.

The mathematical equations of the electrical quantities resulting from the parallel association are written as follows:

$$I = \sum_{j=1}^{N_p}(I_j) = \sum_{j=1}^{Np} I_{ph_j} - \sum_{j=1}^{Np}\left[I_{s_u}\left(\exp\left(\frac{V_j + R_{s_u} I_j}{n_u V_t}\right) - 1\right)\right] - \frac{V + \frac{R_{s_u}}{N_p} I}{\frac{R_{sh_u}}{N_p}} \tag{III.3}$$

It follows that:

$$V = \left(\left[\sum_{j=1}^{Np} I_{ph_j} - \sum_{j=1}^{Np} I_{d_j} - I\right]\frac{R_{s_u}}{N_p}\right) - \frac{R_{s_u}}{N_p} I \tag{III.4}$$

III.2 .4 Mixed Association of Solar Cells

A photovoltaic module can be formed by connecting in parallel N_p strings of N_s cells. Figure III.6 illustrates the equivalent electrical circuits of a mixed association of solar cells.

Based on the relations established for the series and parallel associations, the mathematical equations of the electrical quantities of a mixed association are written as follows:

$$I = \sum_{j=1}^{N_p} I_j = \sum_{j=1}^{Np}\left(\frac{\sum_{i=1}^{Ns} I_{ph_{ij}}}{Ns}\right) - \sum_{j=1}^{Np}\left(\frac{\sum_{i=1}^{Ns} I_{d_{ij}}}{Ns}\right) - \frac{V + \frac{Ns}{Np} R_{s_u} I}{\frac{Ns}{Np} R_{sh_u}} \tag{III.5}$$

© Ferdaous Masmoudi, 2016 _ All rights reserved

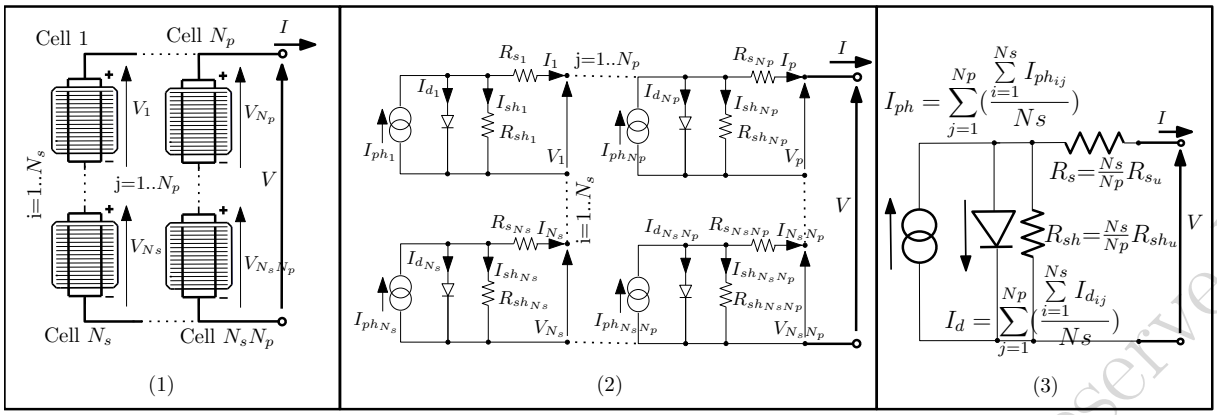


Figure III.6: Illustration of a mixed association of $N_s \times N_p$ solar cells.

We then obtain:

$$V = \sum_{i=1}^{N_s} V_i = \left(\left[\sum_{j=1}^{Np} \left(\frac{\sum_{i=1}^{Ns} I_{ph_{ij}}}{Ns} \right) - \sum_{j=1}^{Np} \left(\frac{\sum_{i=1}^{Ns} I_{d_{ij}}}{Ns} \right) - \sum_{j=1}^{N_p} I_j \right] \frac{Ns}{Np} R_{s_u} \right) - \frac{Ns}{Np} R_{sh_u} \sum_{j=1}^{N_p} I_j \quad \text{(III.6)}$$

III.2 .5 Characterization of the 50 W Monocrystalline Solar Module Used

The photovoltaic solar module used in the experimental work is a 50 W monocrystalline-silicon module composed of 36 cells (the cells have the same reference as the solar cell considered in Chapter 2) connected in series and equipped with two bypass diodes connected in the junction box, as indicated in Figure III.3.b.

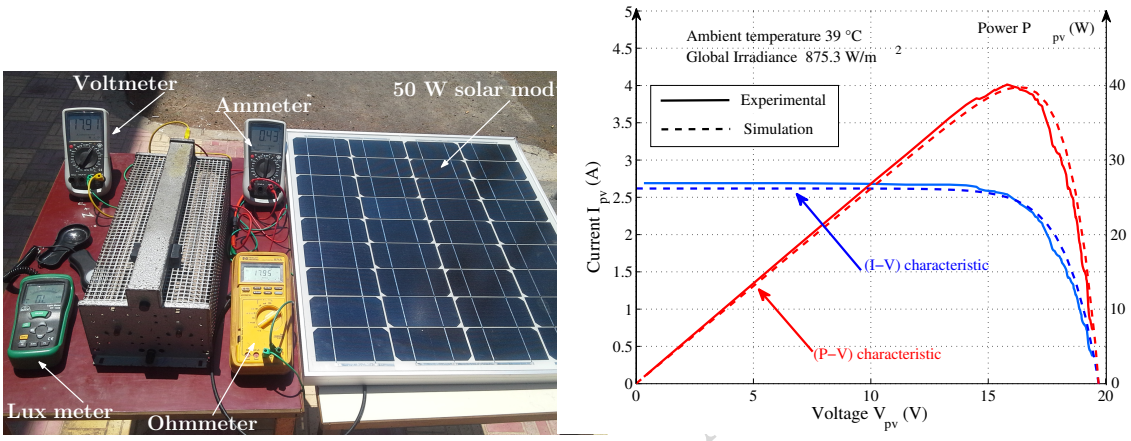
The electrical and mechanical characteristics from the datasheet of the module used are summarized in Table III.1.

Table III.1: Technical specifications of the 50 W solar module under STC

Quantity	Value
Maximum power P_{mref}	53.45 W
Voltage at the maximum power point V_{mref}	19.33 V
Current at the maximum power point I_{mref}	2.765 A
Open-circuit voltage V_{ocref}	22.93 V
Short-circuit current I_{scref}	5.888 A
Number of cells N_s	36 (9×4)
Cell type	Monocrystalline “JAC M5SF-2”
Power temperature coefficient K_p	−0.41 % /K
Voltage temperature coefficient K_v	−0.33 % /K
Current temperature coefficient K_i	0.059 % /K
Efficiency η	19.2∼20 %
Nominal operating cell temperature $NOCT$	45 °C
Dimensions ($l \times L \times H$)	(45 × 45 × 3.5) cm
Weight	4.5 Kg
Number of Bypass diodes	2

© Ferdaous Masmoudi, 2016 - All rights reserved

The module used is experimentally tested in order to obtain its actual electrical characteristics. The test bench is arranged as shown in Figure III.7.a. The tests are carried out during a clear-sky summer day at an average temperature of 39°C, measured using a conventional thermometer, while irradiance is measured using a luxmeter indicating an almost constant value of 156 kLux (luxmeter measurements under diffuse daylight conditions are estimated as equivalent to 1 W/m^2 per 179 lux [64]). The experimental test results are plotted in Figure III.7.b.



(a) (b)

Figure III.7: 50 W solar module used. (a) Experimental test bench. (b) Comparison between experimental and simulated electrical characteristics.

In order to build the MATLAB simulation model of the adopted 50 W module, the one-diode solar-cell model developed in Chapter 2 was used, and 36 cells were connected in series (see the model constructed in Figure III.18). The simulation results for the complete module are plotted in Figure III.7.b. The comparison between the experimental and simulated curves shows remarkable similarity, thereby demonstrating the validity of the model even when cells are associated.

III.3 Problems Causing PV-Module Losses

The PV solar module, composed of several interconnected cells, must be used appropriately, corresponding to operation in the first quadrant of the $(I - V)$ characteristic (Figure I.6). Any problem or severe environmental factor causing damage to the PV module may shift the operating point toward the second or fourth quadrant of the $(I - V)$ characteristic. The module, or some of the cells within it, then become passive loads that absorb energy rather than producing it and dissipate this energy as heat, thereby causing damage that is often irreversible. In order to examine how such scenarios should be handled, the fundamental phenomena and causes underlying these effects are analyzed more closely and an attempt is made to model them.

© Ferdaous Masmoudi, 2016

III.3 .1 Uniform and Partial Shading

The phenomenon of photovoltaic shading may occur because of clouds, environmental obstacles such as trees and buildings, dirt and dust, as well as snow, bird droppings, and often self-shading between parallel rows of panels in the case of associations of several modules.

Shading is considered one of the major problems faced by photovoltaic systems. Indeed, it causes a significant decrease in system efficiency and may, in some cases, damage the cells.

For this reason, optimizing the efficiency of a solar module requires analysis of the causes and effects of shading on the different solar-cell associations in order to prevent their occurrence [65, 66, 67, 68].

Shading is said to be uniform when it is simply caused by a homogeneous reduction in the irradiance level over the entire photovoltaic system, without creating separate shaded and unshaded areas. A typical example of uniform shading is a cloudy sky.

Partial shading is created when a physical object, such as a utility pole or a tree, physically blocks sunlight, resulting in the formation of illuminated and non-illuminated regions on the cell.

III.3 .1 .1 Shading of a Unit Cell

In this part, the effect of shading on a single solar cell is studied, as indicated in Figure III.8. Cell 1 is fully illuminated by radiation with an intensity of 1000 W/m². Cell 2 is uniformly shaded relative to the first cell by a shading factor f_o=0.5, equivalent to an irradiance of 500 W/m². The third cell is partially shaded by a factor f_o=0.5, corresponding to maximum irradiance over half of the cell surface while the other half is completely in darkness.

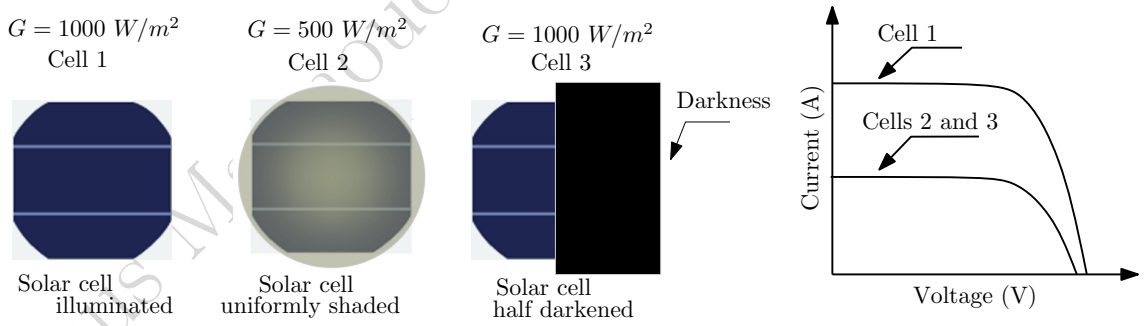


Figure III.8: Illustrations of solar cells under different irradiance conditions.

The electrical characteristics of the different cells show that, for a unit cell, the effect of partial shading is equivalent to uniform shading with an equivalent factor. It is therefore concluded that the output current decreases proportionally to the amount of shading. For a unit solar cell, uniform shading and partial shading produce exactly the same behavior. This result can be considered physically evident because the photocurrent is directly proportional to the surface area and the incident irradiance (Section I.3.2.3, relations 1.2 and 1.3 of Chapter I).

The shading factor f_o is therefore expressed as a function of two components: the surface ratio T_S, which represents the shaded area relative to the total cell surface area (for the cell

© Ferdaous Mahroudi, 2016 – All rights reserved

used, the surface area is $\frac{15.6}{2}$ cm^2), and the shading density D_o, which represents the shading ratio relative to the reference irradiance.

$$f_o = 1 - T_s(1 - D_o) \tag{III.7}$$

with:

$$T_s = \frac{Shaded\ surface}{Total\ surface} \tag{III.8}$$

$$D_o = \frac{Irradiance\ in\ the\ shade}{Ambient\ irradiance} \tag{III.9}$$

Estimating the effect of shading on a solar cell first requires an approximate assessment of the area of the shaded region and of the average shading density within that region. The overall effect is equivalent to that of an irradiance reduced by the same factor. Consequently, relation (II.24) is rewritten by including the shading effect as follows:

$$I_{ph}(G,T) = f_o \times \frac{G}{G_{ref}} \times I_{ph}(T) \tag{III.10}$$

III.3 .1 .2 Shading of an Association of Solar Cells

If shading is uniform, meaning that all cells are subjected to the same irradiance conditions, then the situation is straightforward: the electrical current of all cells decreases by the same shading factor and the power loss is proportional to the shading density.

Under uniform shading, the equations of the solar-cell associations developed in Section III.2 take the following forms:

Series-association case:

$$V = N_s V_u \tag{III.11}$$

$$I = I_u = I_{ph_u} - I_{s_u}\left(\exp\left(\frac{V + R_{s_u} I}{N_s n_u V_t}\right) - 1\right) - \frac{V + N_s R_s I}{N_s R_{sh}} \tag{III.12}$$

Parallel-association case:

$$V = V_u \tag{III.13}$$

$$I = N_p I_u = N_p I_{ph_u} - N_p I_{s_u}\left(\exp\left(\frac{V + R_{s_u} I}{n_u V_t}\right) - 1\right) - \frac{V + \frac{R_{s_u}}{N_p} I}{\frac{R_{sh_u}}{N_p}} \tag{III.14}$$

Mixed-association case:

$$V = N_s V_u \tag{III.15}$$

$$I = N_p I_u = N_p I_{ph_u} - N_p I_{s_u}\left(\exp\left(\frac{V + \frac{N_s}{N_p} R_{s_u} I}{N_s n_u V_t}\right) - 1\right) - \frac{V + \frac{N_s}{N_p} R_{s_u} I}{\frac{N_s}{N_p} R_{sh_u}} \tag{III.16}$$

With:

© Ferdaous Masmoudi, 2016 – All rights reserved

- V_u: the voltage of a unit solar cell,
- I_u: the current of a unit solar cell.

The behavior of a solar module subjected to partial shading is completely different and more complex. Indeed, partial-shading losses are aggravated by the interconnections between the cells and by the module output power. In some cases, these losses are determined by the solar cell having the lowest efficiency. This type of shading causes undesirable effects on the cells of the solar module, such as the mismatch effect and the hot-spot effect.

III.3 .2 Solar-Module Losses Due to the Mismatch Effect

Mismatch losses are caused by interconnecting solar cells or modules that do not have identical properties or that are subjected to different irradiance and temperature conditions.

Differences in any part of the $(I - V)$ curve between one solar cell and another can lead to mismatch losses at certain operating points. The impact of the mismatch between connected cells mainly depends on the configuration of the cell association used [69, 70].

III.3 .2 .1 Mismatch of Series-Connected Cells

This type of mismatch is the most common because most PV modules are composed of a series association of cells, and it can also be easily caused by partial shading of the module. This type is also the most severe.

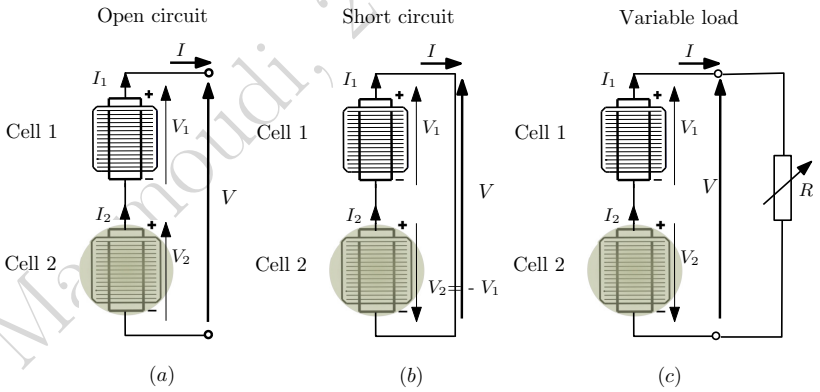


Figure III.9: Illustration of the mismatch effect on two solar cells connected in series.

This scenario can be discussed through an example involving two solar cells connected in series, as shown in Figure III.9. In this case, the two solar cells have different $(I - V)$ characteristics because of a shading effect. The resulting characteristic of this association can be determined graphically, as shown in Figure III.10.a, by first identifying the short-circuit point, which is the intersection of the characteristic of Cell 2 with the characteristic of Cell 1 projected onto the second quadrant, and the open-circuit point, which is the sum of the two open-circuit voltages of the two cells. The remaining points result from adding the voltages of the two cells corresponding to equal currents. It can be observed that the resulting curve is close to the curve

© Ferdaous Mahmoudi, 2016 – All rights reserved

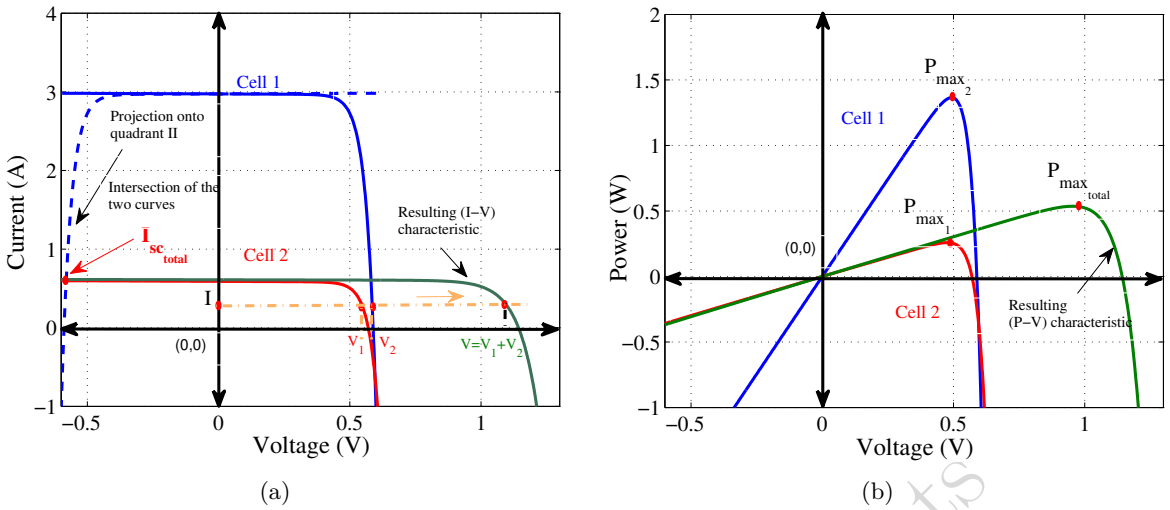


Figure III.10: Electrical characteristics of mismatch between two solar cells connected in series. (a) $(I-V)$ characteristics. (b) $(P-V)$ characteristics.

of the shaded cell along the current axis and is extended by approximately a factor of two along the voltage axis.

Figure III.10.b shows that the maximum power of the resulting $(P-V)$ characteristic of the association does not correspond to the cumulative maximum power of the two cells, but rather approximately to twice the maximum power of the weaker cell.

Under short-circuit conditions, the voltage of the shaded cell is negative because V_2=-V_1. The power produced by Cell 1 is converted into heat in Cell 2, corresponding to operation in the second quadrant. If only two cells are connected in series, Cell 2 can withstand this scenario without difficulty. However, in an association of several cells, the dissipated power becomes significant and the shaded cell can be damaged by the hot-spot phenomenon.

The phenomenon of localized overheating, called the hot-spot effect, occurs [71] when cells are connected in series and one of them produces a very low current compared with the others, as shown in Figure III.11. Near the short-circuit point, part of the power generated by the healthy cells is dissipated by the lower-performance cell. This can lead to highly localized power dissipation, and the resulting local heating may cause irreversible damage to the cell.

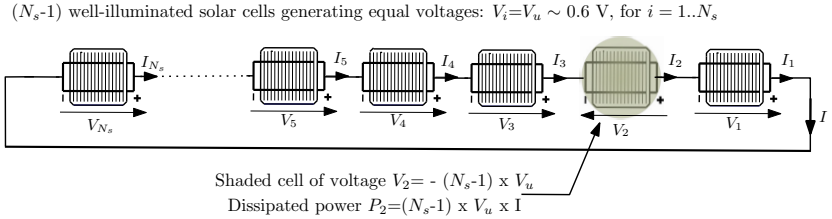


Figure III.11: Illustration of the "Hot-spot" phenomenon.

The mismatch scenario for series-connected cells is less severe for cells of the same type illuminated in a similar manner. Indeed, because of manufacturing tolerances, the junction characteristics of two cells can never be absolutely identical. Consequently, the maximum power

© Ferdaous Mamouri, 2016 - All rights

of series-connected solar cells is always slightly lower than the cumulative maximum power of the individual cells. Manufacturers attempt to minimize these mismatch losses by incorporating into a module only cells having similar characteristics. During manufacturing, each cell is measured after fabrication and then assigned to the appropriate group of cells.

Overall, in a series-cell connection configuration, severe power reductions occur when there is a mismatched cell that produces less current than the healthy cells, especially when the overall association operates near the short-circuit or open-circuit point.

III.3 .2 .2 Mismatch of Parallel-Connected Cells

The current of solar cells connected in parallel is cumulative, whereas the voltage remains the same as for a single cell. As with series-connected solar cells, parallel-connected solar cells having different $(I-V)$ characteristics are subject to critical operating states that must be studied. This scenario is therefore examined through an example involving two solar cells connected in parallel, as shown in Figure III.12.

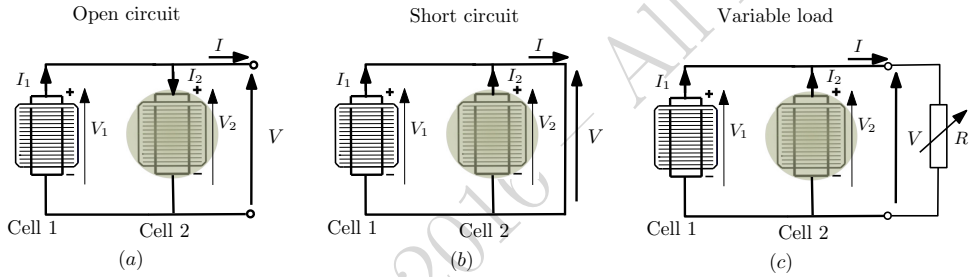


Figure III.12: Illustration of the mismatch effect on two solar cells connected in parallel.

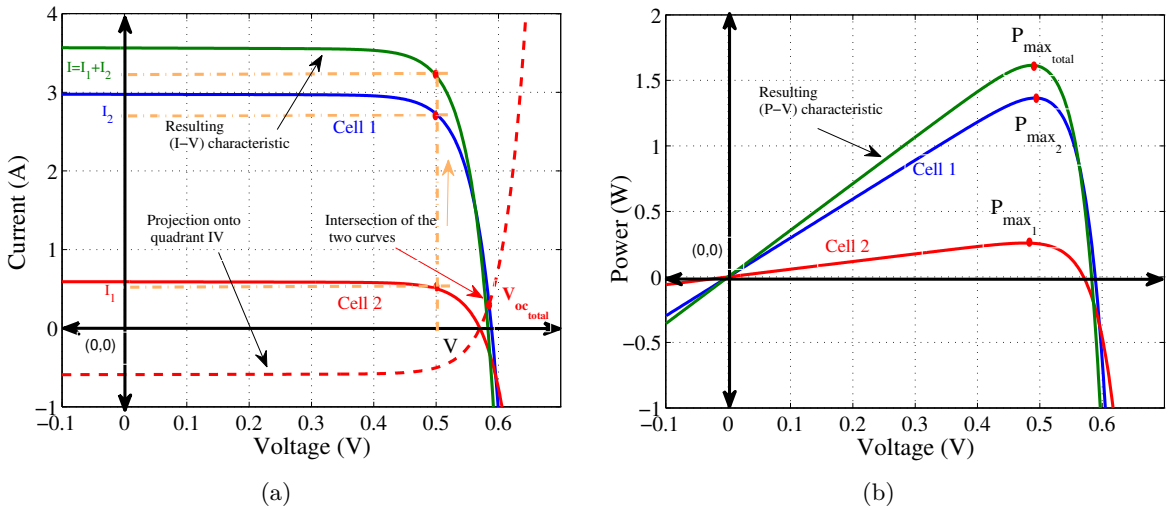


Figure III.13: Electrical characteristics of mismatch between two solar cells connected in parallel. (a) $(I-V)$ characteristics. (b) $(P-V)$ characteristics.

The resulting characteristic of the parallel association can be determined graphically, as shown in Figure III.13.a, by first identifying the short-circuit point, which is the sum of the two

© Fer ... di, 2016 ... All rights reserved

short-circuit currents of the two cells, and the open-circuit point, which is the intersection of the characteristic of Cell 1 with the characteristic of Cell 2 projected onto the fourth quadrant. The remaining points result from adding the currents of the two cells corresponding to equal voltages. It can be observed that the resulting curve is close to the curve of Cell 1, and the power losses shown in Figure III.13.b are much less significant than in the case of series associations. The resulting generated power generally remains higher than the unit power generated by the stronger cell; however, near the open-circuit point, the resulting power decreases considerably and becomes lower than the power of Cell 1.

The greatest danger in this scenario is encountered when the entire module is at open-circuit voltage, such that the voltage generated by the shaded cells is almost equal to the open-circuit voltage. In such a case, the shaded cell is supplied by all the illuminated cells connected adjacent to it.

III.3 .3 Role of the "Bypass" Diode

The destructive effects of the hot-spot phenomenon can be mitigated by using a bypass diode. A bypass diode is connected in parallel with a solar cell, but with opposite polarity. Under normal operation, each solar cell is forward biased and the bypass diode is therefore reverse biased, effectively behaving as an open circuit. However, if a solar cell becomes reverse biased because of severe mismatch, the bypass diode conducts, allowing the current from the healthy solar cells to flow through the external circuit rather than through the faulty cell. The ideal connection of bypass diodes is shown in Figure III.14.

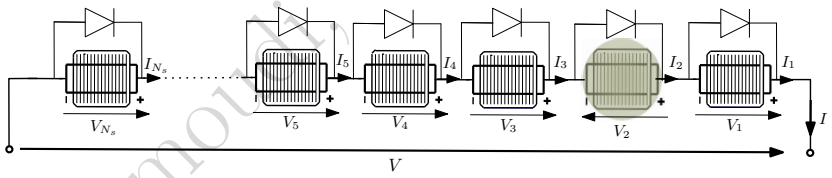


Figure III.14: Ideal association of Bypass diodes with solar cells.

In practice, installing one bypass diode for each solar cell is too costly. For this reason, bypass diodes are placed across groups of solar cells. The permissible number of cells connected in series within each group without causing damage depends on the maximum power, equal to the generation capability of all the cells in the group, that can be dissipated in a single completely dark cell. It is estimated at approximately 15 cells per bypass diode for silicon cells. For a 36-cell module, two bypass diodes should be used to prevent the "hot-spot" effect (Figure III.15).

III.3 .4 Simulation of Total and Partial Shading Effects on a Photovoltaic Solar Module

This part consists of developing a simulation model of a solar module that takes the shading effect into account, highlights mismatch phenomena between cells, and emphasizes the role of bypass diodes in protecting the module.

© Ferdaous Mamouni 2016 – All rights reserved

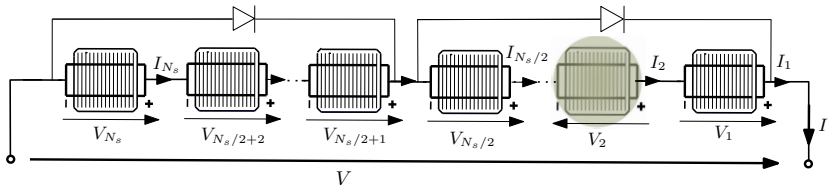
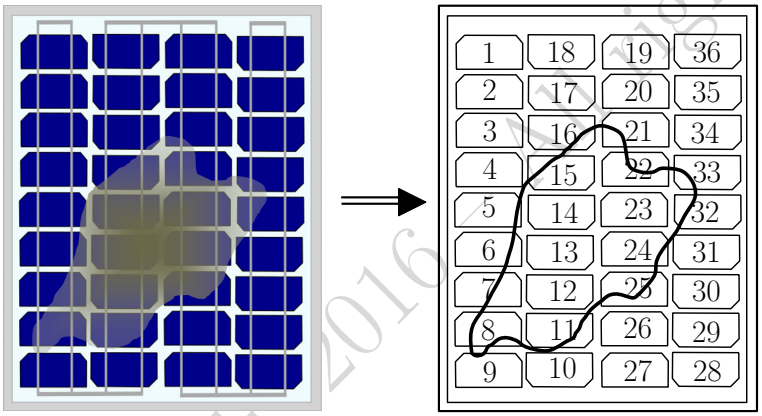


Figure III.15: Economical association of Bypass diodes with solar cells.

During its daily operation, the solar module may be shaded by certain obstacles, especially if the module is designed for a mobile robot that moves throughout its operating area. The general shape of the shadow projected onto the module surface is random and depends on the projection angle. Figure III.16.a presents an example of a shadow pattern on the 50 W solar module. Figure III.16.b provides a simplified schematic representation of the cells affected by the shadow.



(a) (b)

Figure III.16: Illustrations of a shaded solar module. (a) Realistic shadow pattern. (b) Simplified shadow pattern.

The shading factor f_{oi} for each cell is assessed by assigning an estimated value from 0 to 1 to the surface ratio T_{s_i} and shading density D_{o_i} for each affected cell, $i = 1..36$. For this shadow pattern, the following example is presented:

Table III.2: Example of shading-factor evaluation

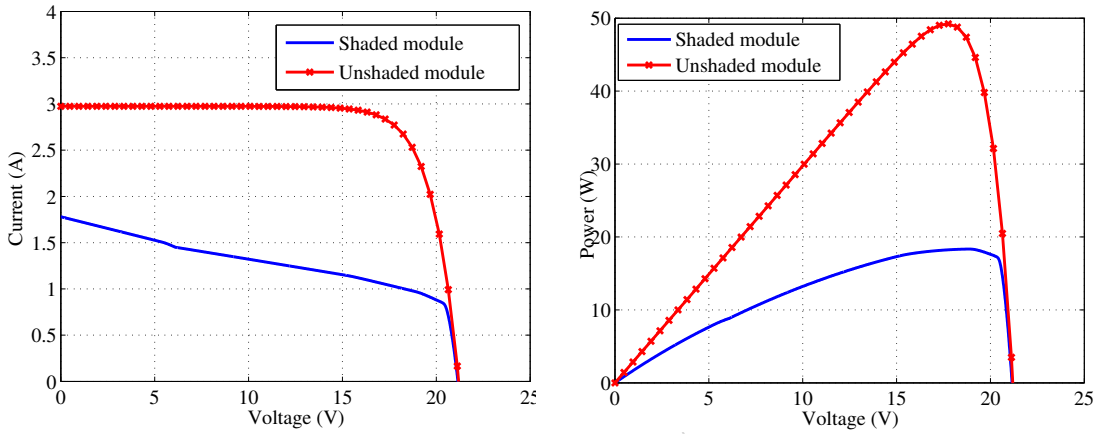
Cell No.	5	6	7	8	11	12	13	14	15
T_s	0.1	0.19	0.42	0.7	0.75	1	1	1	0.75
D_o	0.95	0.95	0.9	0.9	0.8	0.6	0.3	0.34	0.7
f_o	0.995	0.995	0.958	0.93	0.85	0.6	0.3	0.34	0.775
Cell No.	16	21	22	23	24	25	33	32	remaining cells
T_s	0.22	0.23	0.71	1	0.8	0.49	0.21	0.24	1
D_o	0.95	0.95	0.9	0.4	0.4	0.6	0.95	0.95	1
f_o	0.989	0.9885	0.929	0.4	0.52	0.804	0.9895	0.988	1

Figure III.18 presents the implementation of a 36-cell series-connected solar-module model in the MATLAB-Simulink environment while taking into account the shading factor applied to each cell.

© Ferdaous Mahmoudi, 2016 - All rights reserved

Figures III.17.a and III.17.b respectively show the $(I-V)$ and $(P-V)$ characteristics of the shaded module compared with the normally illuminated module.

A remarkable drop in the power generated by the shaded module is observed, reaching 37% of the maximum power, which reflects the importance of this phenomenon and its impact on normal solar-module operation. The discontinuities shown in the characteristics of the shaded module are indeed caused by the alternating operation of bypass diodes 1 and 2.



(a) (b)

Figure III.17: Comparison between the electrical characteristics of a shaded and an unshaded module. (a) $(I-V)$ characteristics. (b) $(P-V)$ characteristics.

III.4 Solar Resource and Sun-Path Tracking

Optimal extraction of photovoltaic energy is mainly related to the availability of sufficient solar radiation in the environment as well as to the appropriate orientation of the module relative to the incident radiation. Therefore, studying solar irradiation and its characteristics is an essential and indispensable step.

This section aims to present general concepts related to solar energy, the available solar-radiation resource, and the trajectory and movement of the sun, or the relative and apparent motion of the sun, in the sky during the day. The Sfax region is used as the case study; nevertheless, this study can be applied to any location on Earth.

In this part, algorithms widely described in the scientific literature are used to model the apparent motion of the sun and the solar irradiation received at the Earth's surface. The discussion of the sun's motion is therefore carried out in the context of identifying the best orientation of the solar module relative to the sun at any location on Earth and at any time. Similarly, the discussion of solar radiation is conducted in the context of evaluating the energy gain achieved by regulating the orientation of the PV module.

An automated mechanism can be designed to regulate the orientation of the solar module and track the sun's trajectory in order to optimize the energy efficiency of the PV module. The concept of the relative motion of the sun helps to implement sun-positioning algorithms

© Ferdaous Masmoudi, 2016

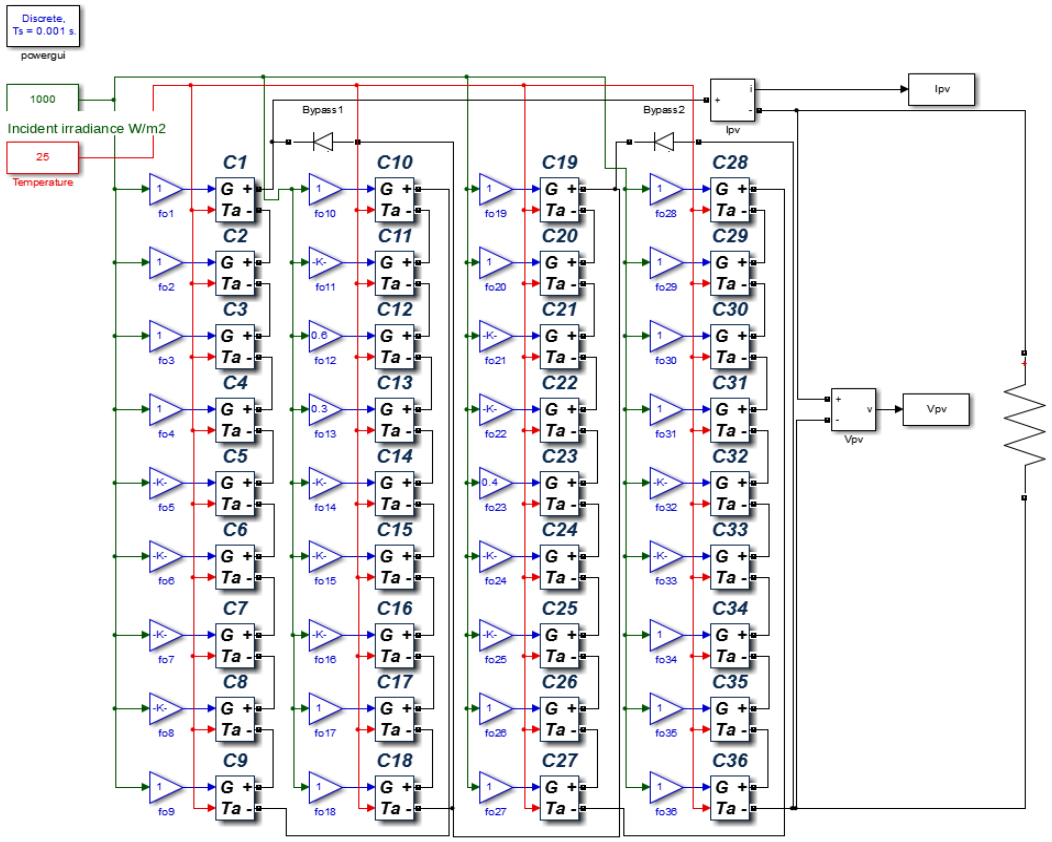


Figure III.18: Example of implementation of a solar-module model accounting for the shading effect in the MATLAB-Simulink environment.

in microcontroller programming and to use them for automatic regulation of the solar-tracking system.

The sun emits energy in the form of electromagnetic energy, and the intensity of the electromagnetic radiation reaching the Earth is often referred to as solar irradiance or insolation; its unit in the International System is "W/m^2". The term radiation is generally used to define the amount of solar energy per unit area received over a given period of time, with "Wh/m^2" as its SI unit. The solar energy received by a surface on Earth as daily irradiation varies according to location, season, and time. The extraterrestrial solar-energy level, namely the average extraterrestrial solar irradiance at the edge of the atmosphere, is estimated by the solar constant at approximately 1367 W/m^2. As solar electromagnetic energy passes through the Earth's atmosphere, the intensity of the direct radiation decreases considerably and reaches a rounded maximum of 1 kW/m^2 at the Earth's surface. Thus, for each square meter of photovoltaic-cell surface placed facing the sun, the system is able to collect approximately 1000 W of solar energy, which can provide 200 W of generated PV power if cells with an efficiency of 20% are considered.

III.4 .1 Solar Resource in Tunisia and Sfax

Throughout the world, many regions are rich in solar resources, particularly countries and regions around the equator. Africa is therefore well known as one of the continents located within the

© Fernaoui Masmoudi, 2016 Reserved

most favorable solar belt. Some African countries, including Tunisia, have very high potential for harvesting solar energy and show good prospects for developing solar-energy projects.

Tunisia is characterized by a semi-arid climate that receives direct solar radiation because of limited cloud cover and precipitation. The solar-resource map in Figure III.19.a is calculated from observations made by meteorological satellites between 1994 and 2010 and shows the average cumulative global irradiation on a horizontal plane. This map reveals that the solar energy received annually by one square meter of surface is estimated at approximately 1600 KWh/m^2 in the north-west of the country, whereas it exceeds 2000 KW/m^2 in the southern regions, representing a significant solar-energy resource.

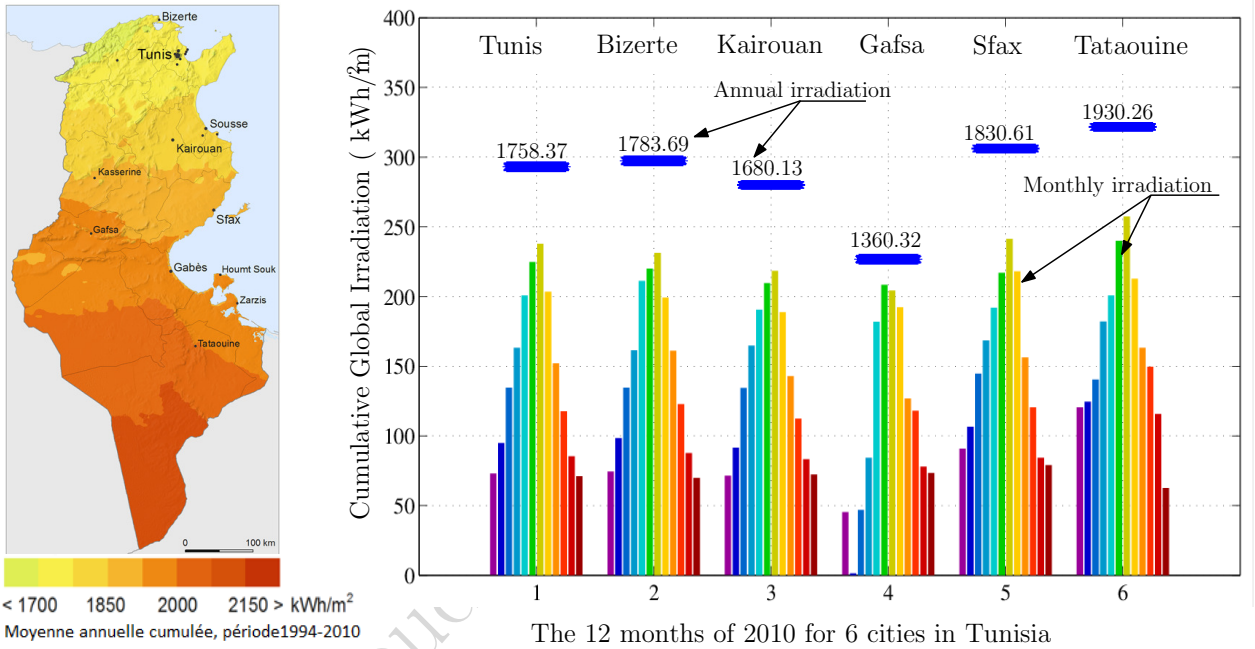


Figure III.19: Solar resource in Tunisia. (a) Global Horizontal Irradiation in KWh/m^2 in Tunisia (source: Solargiz). (b) Monthly and annual cumulative Global Irradiation in KWh/m^2 in six Tunisian cities (source: INM).

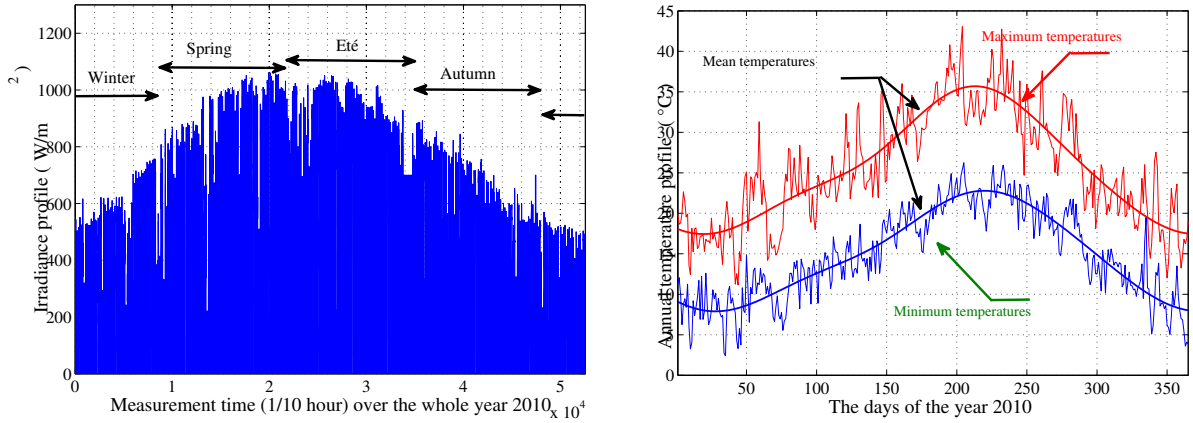
These results are confirmed by regional measurements from the Tunisian National Institute of Meteorology[1], referred to as "INM". The data presented in Figure III.19.b are plotted from the database of actual solar-radiation measurements recorded by meteorological stations located throughout the country and provided by the INM, and they concern only the year 2010. This figure illustrates the significance of the monthly and annual cumulative solar resource in several regions of Tunisia and highlights the solar richness of southern regions such as Tataouine and Sfax, particularly during the winter season.

The city of Sfax has a significant solar-energy resource exceeding 1800 KWh/m^2/year. Monthly cumulative radiation is also significant even in winter, reaching its maximum in July and its minimum in December.

[1]INM: http://www.meteo.tn/

© Ferdaous Mamouri

The Global Irradiance profile on a horizontal plane measured by the INM throughout the entire year at a measurement frequency of 1/10 hour is shown in Figure III.20.a. The overall curve has a sigma-shaped profile, essentially due to the annual motion of the Earth relative to the sun and to the variation in the Earth–Sun distance. The temperature range throughout the year follows the same sigma-shaped profile because of the dependence between solar radiation and ambient temperature. Figure III.20.b plots the minimum and maximum temperatures measured by the meteorological stations in Sfax. These values exhibit continuous variations because temperature also depends on other climatic factors such as wind, albedo[2], and humidity. Temperatures vary between a minimum of 4°C in winter and a maximum of 43°C in summer, which constitutes a favorable environment for solar-module operation.



(a) (b)

Figure III.20: Solar characteristics of the city of Sfax. (a) Solar-radiation profile for the year 2010 in W/m^2. (b) Temperature-range profile for the year 2010. (Source: INM).

III.4 .2 Sun Motion and Position

The position of the sun in the sky as viewed from any point P on the Earth's surface can essentially be defined using four angles.

Any point P on the Earth's surface is defined in terms of longitude and latitude. The latitude (ϕ) of a point P is the angle between a radius extending from point O at the center of the Earth to point P and a radius drawn from the center of the Earth to the equator, as illustrated in Figure III.21.a. Values range from 0° to 90° North and from 0° to 90° South, where 0° is the latitude of any point on the equator.

The longitude (L) of a point is the angle between the Greenwich meridian, or prime meridian, and the meridian passing through point P. A meridian is a circumference passing through both poles. Longitude values range from 0° to 90° East and from 0° to 90° West, where 0° is the longitude of a point on the Greenwich meridian.

[2]Albedo is the reflectivity of a surface, that is, the ratio of reflected light energy to incident light energy. It is a dimensionless quantity ranging from 0 to 1: a perfect black body that absorbs all wavelengths would have zero albedo, whereas a perfect mirror that reflects all wavelengths would have an albedo equal to 1. The Earth has a relatively high albedo of 0.3 to 0.35.

© Ferdaous Masmoudi, 2018 reserved

The declination angle (δ) and the hour angle (ω) are more easily identified from an external view of the Earth. The declination angle is the same for the entire Earth on a given day. The hour angle at a point P on the Earth's surface is the angle between the meridian containing point P and the meridian perpendicular to the sun's rays. The hour angle is negative in the morning, becomes zero at solar noon, when point P faces the sun, and becomes positive in the afternoon. It should be noted that the hour angle is the same for all points on the corresponding meridian, that is, points having the same longitude.

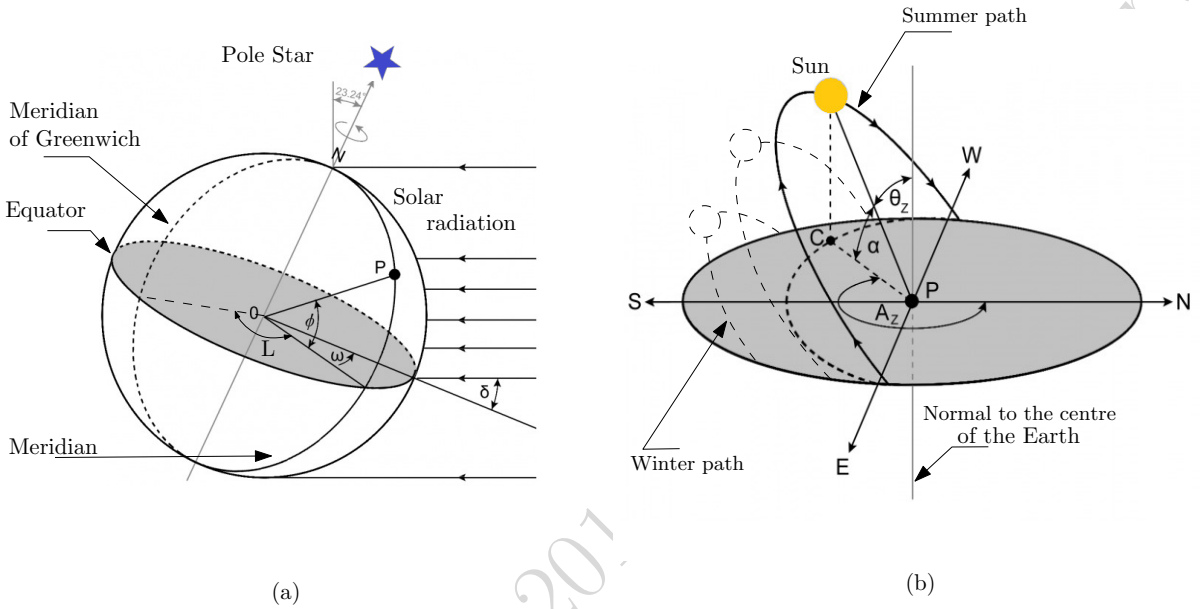


Figure III.21: Apparent motion of the sun. (a) Angles defining a point P on the Earth. (b) Solar angles viewed from point P. (Source: ITACA)[3]

Other angles are defined by considering the path of the sun in the sky as viewed from point P on the Earth's surface. Figure III.21.b shows the solar zenith angle (θ_Z), the solar altitude angle (α), and the solar azimuth angle (A_Z). The elevation of the sun in the sky at any instant can be described either by the angle α measured from the horizon or by θ_Z measured from a line normal to the center of the Earth at point P; the relation $\alpha + \theta_Z = 90°$ always holds.

The astronomical model and the fundamental equations used to calculate the position of the sun were developed in 1988 by "*Michalsky*" [72]. One of the most accurate algorithms for calculating the position of the sun using the "*Michalsky*" approach was developed under the responsibility of the NREL laboratory of the U.S. Department of Energy by "*Reda and Andreas*" [73]. This algorithm is known as the "*Solar Position Algorithm*" (SPA) and calculates the position of the sun with high accuracy, with a maximum error of 0.01%. The complete source code[4] written in C, together with all relevant comments, is made publicly available by NREL; this constitutes a valuable tool for integration into solar-tracking systems.

According to the geographical location of the photovoltaic system (L, ϕ), the day, the month of the year, and the time in hours, minutes, and seconds, the position of the sun moving in the

[3]ITACA: http://www.itacanet.org/the-sun-as-a-source-of-energy/.
[4]SPA code source: http://www.nrel.gov/midc/spa/.

© Fernando Machado 201

sky relative to the Earth can be estimated in terms of the solar angles (α, A_Z) using the SPA algorithm, as shown by the flowchart in Figure III.22.a.

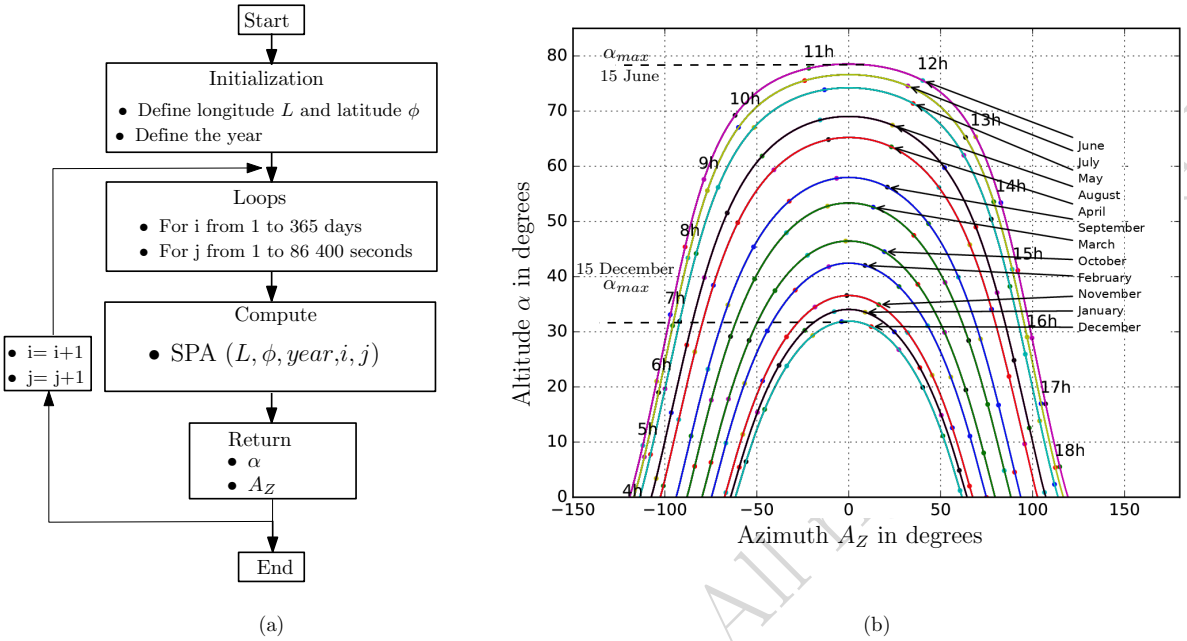


Figure III.22: Sun trajectory obtained using the SPA algorithm. (a) Flowchart for calculating the sun's position. (b) Daily sun trajectories for the 12 months of the year 2010 at ENIS.

Figure III.22.b shows the solar trajectories calculated for the geographical site of ENIS in Sfax (Longitude $L = 10.745°$, Latitude $\phi = 34.783°$) for the 15th day of each month of the year 2010. In this figure, the horizontal axis corresponds to the horizontal plane on which the solar module is installed. The vertical axis corresponds to the height between the Earth's surface and the position of the sun. The sun trajectories are plotted as contours projected onto the vertical plane. This figure defines the annual solar window seen by the solar module installed facing it.

The solar trajectories are symmetrical with respect to the azimuth angle 0°, which corresponds to south, and this angle is limited between -120° East and 120° West, forming an annual angular range of 240° (A_Z∈[-120°,120°]). The daily altitude varies between 0° at night and α_{max}, which depends on the day number of the year. It can be observed that α_{max} varies between a minimum of 30° in winter and reaches 80° in summer.

From this figure, it can be concluded that the best orientation selected for a fixed PV module is defined by the pair of angles (A_{Zm},α_m)=(0°,30°). In this way, the module is guaranteed to receive energy throughout the day, particularly during the winter season.

Nevertheless, fixing a solar module at a single orientation does not allow all the energy provided by the sun to be utilized because the solar radiation is not perpendicular to the module surface at all times, particularly at sunrise and sunset.

Therefore, the idea of tracking the sun's trajectory appears appropriate for optimizing incident radiation and collecting the maximum irradiance throughout the day.

© Ferdaous Masmoudi, 2016 - All rights reserved

III.4 .3 Solar Irradiance on Horizontal and Inclined Planes

The amount of energy reaching the Earth's surface every hour is greater than the amount of energy used by the Earth's population during an entire year. The sun produces an enormous and relatively constant amount of energy. At the surface of the sun, the intensity of solar radiation is approximately 63.3 MW/m^2. As the sun's rays propagate through space, the radiation becomes less intense, and by the time the rays reach the edge of the Earth's atmosphere they can be considered parallel, as shown in Figure III.23.a.

The sun's incident rays on the Earth do not have the same intensity at every point P because they are affected by the inclination angle between the tangent at P and the normal directed toward the center of the sun. Figure III.23.a shows three plane surfaces:

- Plane A: the horizontal plane, tangent at point P on the Earth's surface.
- Plane B: the plane parallel to Plane A but located at the edge of the Earth's atmosphere.
- Plane C: the plane perpendicular to the sun's rays, often referred to as the normal plane.

Let I_0 denote the irradiance intensity at Plane C. The value of I_0 is considered to be the same at every point on the Earth's surface, but not all points are perpendicular to the sun's rays. Let I_{0h} denote the extraterrestrial radiation intensity on Plane B tangent to point P. The irradiance on such a surface is lower than I_0 because of the cosine effect associated with θ_Z between Planes B and C.

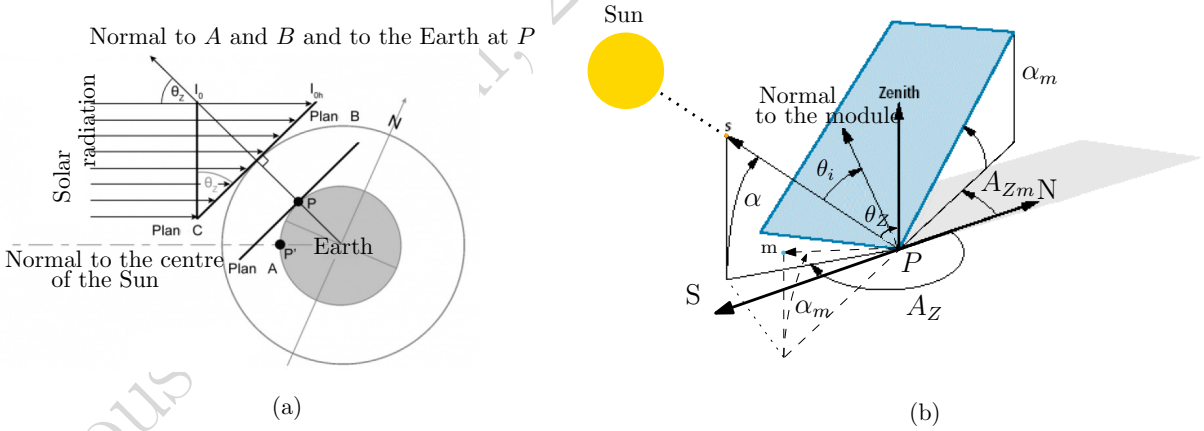


Figure III.23: Solar irradiance on a horizontal plane and an inclined plane. (a) Solar irradiance on a horizontal plane at P. (b) Solar irradiance on an inclined plane at P. (Source: ITACA)

Figure III.23.b makes it possible to visualize the solar angles at point P and the orientation angles of the solar-module surface at the same point. The module azimuth angle (A_{Zm}), the module altitude angle (α_m), and the incidence angle (θ_i) are identified; these angles define the position of an inclined surface relative to the incident solar radiation.

The intensity of the irradiance incident on a PV module depends not only on the intensity of the solar radiation but also on the angle (θ_i) between the module and the sun. When the module surface and sunlight are perpendicular to one another, the irradiance intensity on the

© Ferdaous ..., 2016 – All rights reserved

surface is equal to that of the light and is therefore maximal. However, because the incidence angle between the sun and a fixed module changes continuously throughout the day, the solar radiation received by the fixed PV module is lower than the incident solar radiation. Therefore, it can be stated that regulating the orientation of the solar-module surface is beneficial in order to collect the maximum amount of energy from solar radiation.

While extraterrestrial incident solar radiation is relatively constant, radiation at the Earth's surface varies considerably because of atmospheric effects including absorption, scattering, pressure, site altitude, and local atmospheric variations such as water vapor, clouds, and pollution. These factors make estimating irradiance at a point P on Earth a fairly complex task. Indeed, meteorological variables such as cloud movement and ground albedo at each instant can only be determined from actual measurements. Figure III.24.b shows actual recordings of irradiance values on the horizontal plane during the best and worst days, in terms of irradiance, of the year 2010 in the Sfax region, as provided by the INM.

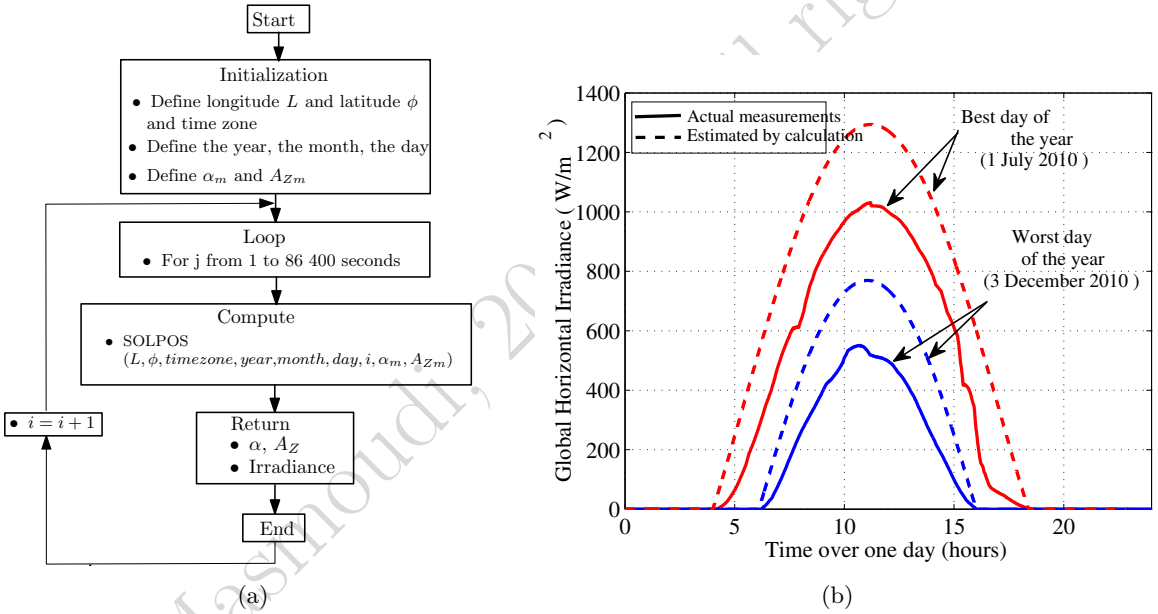


Figure III.24: Solar characteristics during the best and worst irradiance days of 2010 in Sfax. (a) Flowchart for calculating solar irradiance. (b) Actual and estimated irradiance profiles in W/m^2 (Source: INM).

A mathematical model and an algorithm for approximately estimating solar-irradiance intensity on an inclined plane while accounting for atmospheric parameters, but without considering site-specific meteorological parameters, were proposed by the NREL team under the name *Solar Position and Intensity* (SOLPOS). The complete source code[5] written in C, together with all relevant references and comments, is made publicly available by NREL.

Using the SOLPOS algorithm, as shown by the flowchart in Figure III.24.a, the maximum irradiance that can reach a surface at a given orientation can be approximately estimated according to the geographical location, season of the year, and time of day. Figure III.24.b shows

[5]SOLPOS code source: http://rredc.nrel.gov/solar/codesandalgorithms/solpos/.

© Ferdaous Masmoudi, 20 rights reserved

estimates of irradiance on the horizontal plane for the previously described best and worst days of 2010 in Sfax. It can be observed that the actual irradiance obtained from meteorological-station measurements is clearly lower than the estimated irradiance, highlighting the significant effect of meteorological conditions such as clouds and albedo on the resulting irradiance.

In order to estimate irradiance on an inclined plane while accounting for meteorological conditions, the "*Clear Sky Index*" [74, 75] can be used, expressed as:

$$K_c = \frac{Gh_{mes}}{Gh_{est}} \tag{III.17}$$

with:

- Gh_{mes}: horizontal irradiance measured by meteorological stations.
- Gh_{est}: horizontal irradiance estimated by a calculation algorithm.

We then obtain:

$$Gi = K_c \times Gi_{est} \tag{III.18}$$

with:

- Gi: estimated irradiance on an inclined plane accounting for meteorological conditions.
- Gi_{est}: irradiance estimated on an inclined plane by a calculation algorithm.

III.4 .4 Simulation of Solar-Tracker Efficiency

In this part, the power efficiency of several types of sun-tracking systems, commonly called "Solar Trackers", is studied in order to evaluate the energy benefit and power gain resulting from the use of each type.

Four solar-module orientation methods are considered:

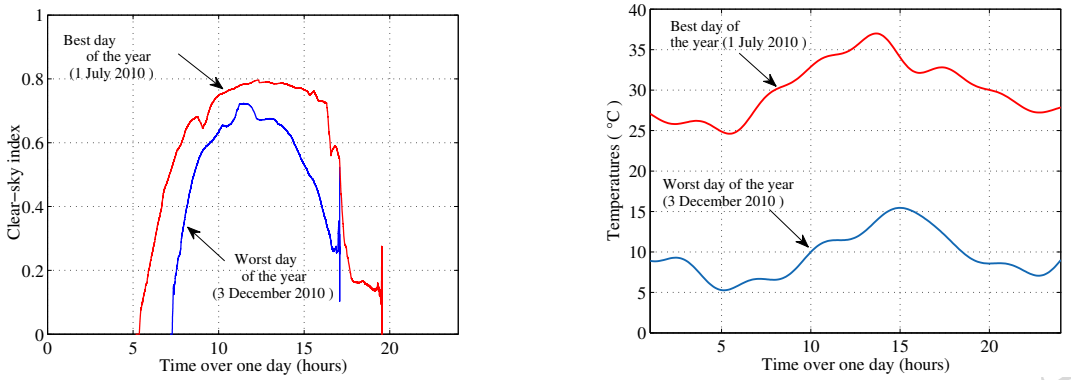
Fixed Module For PV installations mounted on house roofs, solar modules are generally oriented toward an annual optimum position estimated by the pair of module angles (A_{Zm},α_m)=(180°,30°).

Horizontal Solar Tracker This is a single-axis solar tracker with one degree of freedom operating around a horizontal rotation axis relative to the ground. The module azimuth angle is programmed to follow the solar azimuth, whereas the module elevation is fixed at α_m=30°.

Vertical Solar Tracker This is a single-axis solar tracker with one degree of freedom operating around a vertical rotation axis relative to the ground. It therefore follows the solar elevation while keeping the azimuth component fixed at A_{Zm}=180°.

Dual-Axis Solar Tracker This is a two-axis solar tracker with two degrees of freedom corresponding to two rotational axes. These axes are perpendicular to one another. The azimuth axis is perpendicular to the ground and allows the module azimuth to vary so as

© Ferdaous Masmoudi, 2016 - All rights reserved



(a) (b)

Figure III.25: Meteorological characteristics during the best and worst irradiance days of 2010 in Sfax. (a) Clear-sky-index profile. (b) Measured actual temperature profile (°C) (Source: INM).

to coincide with the solar azimuth. The elevation axis is parallel to the ground and allows the system to follow the solar elevation.

In order to accurately evaluate the power generated by the solar module while accounting for the actual evolution of temperature and the clear-sky factor during the day, the data plotted in Figures III.25.a and III.25.b are used, and the performance of the solar trackers is studied during the best and worst irradiance days of the year 2010 at the ENIS site.

The implementation of the solar-tracker simulation model using the SOLPOS algorithm in the MATLAB-Simulink environment is shown in Figure III.26.

Simulating the power generated by the solar module using the four orientation methods described above during the best and worst days of the year 2010 produces the curves shown in Figures III.27.a and III.27.b.

A summary of the maximum efficiency calculation, relative to the input irradiance, and the daily energy gain, relative to the horizontal orientation, for each type of solar-module orientation is presented in Table III.3.

Table III.3: Comparison between the different types of solar-module orientation

Orientation type	Efficiencies in winter and summer (%)	Energy gains in winter and summer (KWh/day)
Fixed module	14.24 – 17.116	0.3563 – 0.371
Vertical tracker	14.49 – 17.125	0.3859 – 0.598
Horizontal tracker	13.03 – 17.21	0.372 – 1.048
Dual-axis tracker	14.64 – 17.32	0.933 – 1.402

The results highlight the superiority of the two-axis solar tracker for optimizing the energy generated by the solar module. Indeed, it can be observed that a solar module fixed at an orientation of 180° south and an elevation of 30° is always less efficient than a PV module equipped with a solar tracker. Comparison between the different solar trackers shows that the vertical tracker is more advantageous in winter, with an efficiency of 14.46% and an energy gain

© Ferdaous Mahmoudi, 2016 – All rights reserved

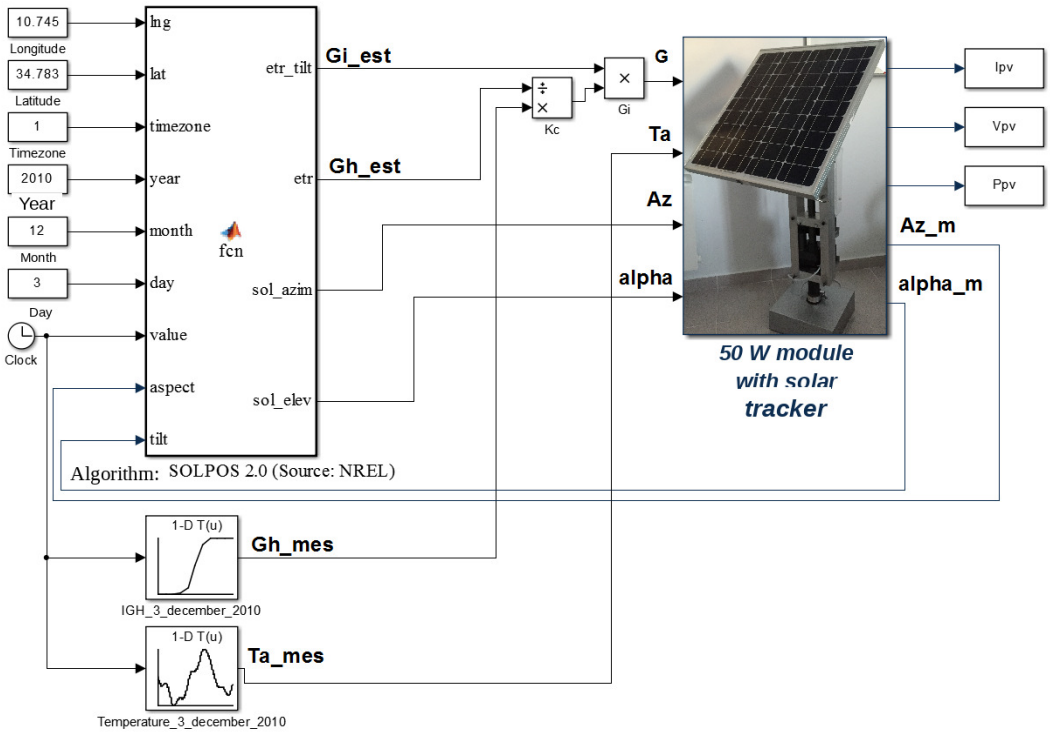
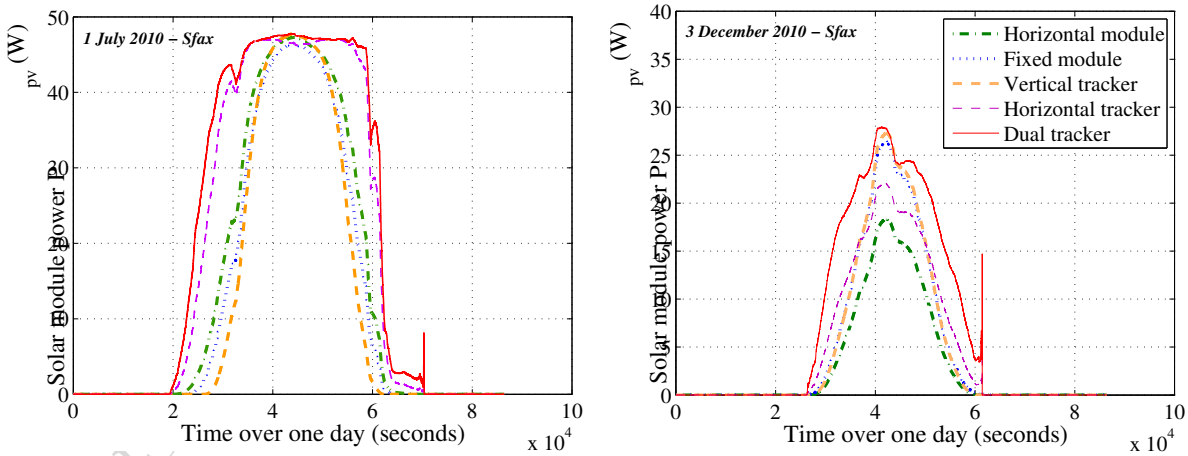


Figure III.26: Example of implementation of the solar-tracker model in the MATLAB-Simulink environment.



(a) (b)

Figure III.27: Simulation of solar trackers during the best and worst irradiance days of 2010 in Sfax. (a) Power generated during the best day. (b) Power generated during the worst day.

of 0.386 KWh/day, than a horizontal tracker, which has an efficiency of 13.03% and provides an energy gain of 0.372 KWh/day. In summer, the horizontal tracker shows a higher energy benefit than the vertical tracker, with a gain of 1.048 KWh/day compared with 0.598 KWh/day for the vertical tracker. Regarding the two-axis solar tracker, the results demonstrate its effectiveness and its ability to increase the power generated by the PV module. The dual-axis tracker is always more advantageous than the other tracker types, whether in winter or summer, with an

efficiency ranging from 14.64% to 17.32% and an energy gain ranging from 0.933 KWh/day in winter to 1.402 KWh/day in summer.

III.5 Design and Implementation of the Two-Axis Solar Tracker

Nature has developed the principle of the sunflower, which orients itself toward the sun during the day. This is a simple but remarkable principle that can be used as inspiration for optimizing the efficiency of solar-energy systems [76, 77, 78, 79].

In the previous section, it was shown that the generated photovoltaic power is a function of the solar-module orientation and that optimization of PV-sensor efficiency can only be achieved using a system that tracks the sun's trajectory. Simulation also demonstrated that the two-axis solar tracker provides an interesting energy benefit compared with the other types.

The objective of this part is therefore to design a two-axis motorized mobile platform that ensures appropriate movement of the solar module so that it follows the sun's trajectory as it moves across the sky, thereby allowing the maximum amount of solar radiation to be collected throughout the day.

The solar-tracker platform is equipped with a set of sensors required to perform advanced functions that allow not only proper system regulation but also exploration of the environment. This system is designed to track the sun's trajectory and to detect and then avoid shaded regions projected onto the module. The first manufactured prototype and the first recorded results are presented in Chapter V.

III.5 .1 Description of the Mechanical Structure

This part describes the mechanical system designed as the basis of the solar tracker. The mechanical platform provides mobility of the solar module according to a spherical reference frame by acting on the two PV-module angles α_m and A_{Zm}. The system is therefore composed of two complementary parts providing rotation about the axis parallel to the horizontal plane and the axis normal to the horizontal plane.

The complete mechanical system typically includes the following elements and components:

Vertical-Motion Structure It supports the PV module by fastening it to its frame, as shown in Figure III.28.a. The vertical base structure maintains a distance between the module and the ground, thereby providing a certain freedom of movement. Rotational movement is provided by a linear actuator housed in the vertical structure. Actuation of the linear actuator produces vertical translational movement of its piston. A link mechanism converts the translational movement into rotation about an axis parallel to the horizontal plane. The rotational movement can vary the module elevation angle α_m between 0° (horizontal) and 90° (vertical).

Horizontal-Motion Structure It supports the vertical support by fastening it to its rotating platform, as shown in Figure III.28.b. Rotational movement is provided by a direct-current

© Ferdaous Masmoudi, 2016 - All rights reserved

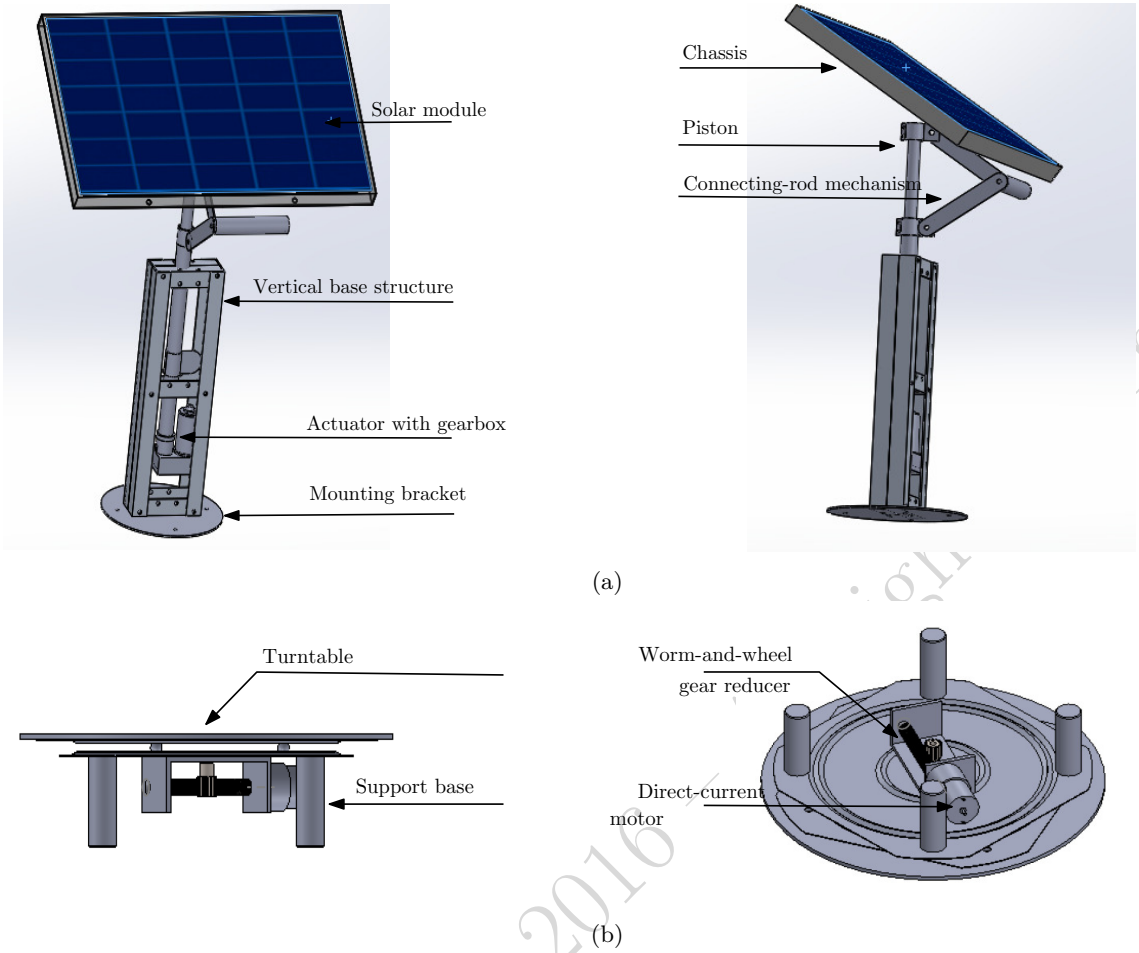


Figure III.28: Mechanical system of the dual-axis tracker. (a) Structure for vertical motion. (b) Structure for horizontal motion.

motor mounted on the back of the platform and connected through its shaft to a worm-gear mechanism acting as a speed reducer. The rotational movement can vary the module azimuth angle A_{Zm} over a full revolution from 0° to 360°.

III.5 .2 Description of the Electrical System

This part describes the electrical system integrated into the mechanical platform and responsible for electrically monitoring and controlling the solar tracker in an appropriate manner. The system is therefore composed of a set of electrical and electronic peripherals communicating with one another and providing various advanced functions of the solar tracker.

Based on Figure III.29, the following components are identified in this system:

- Power-supply batteries: they serve as the power source for the complete system. They supply the motors at 24 V and the remainder of the electronic system at 5 V through a conversion stage (24 V–5 V).
- Actuators: the horizontal direct-current motor *MCC* (24 V) and the vertical actuator based on a *MCC* (24 V) are controlled through two H-bridges acting as direction reversers

© Ferdaous Masmoudi, 2016

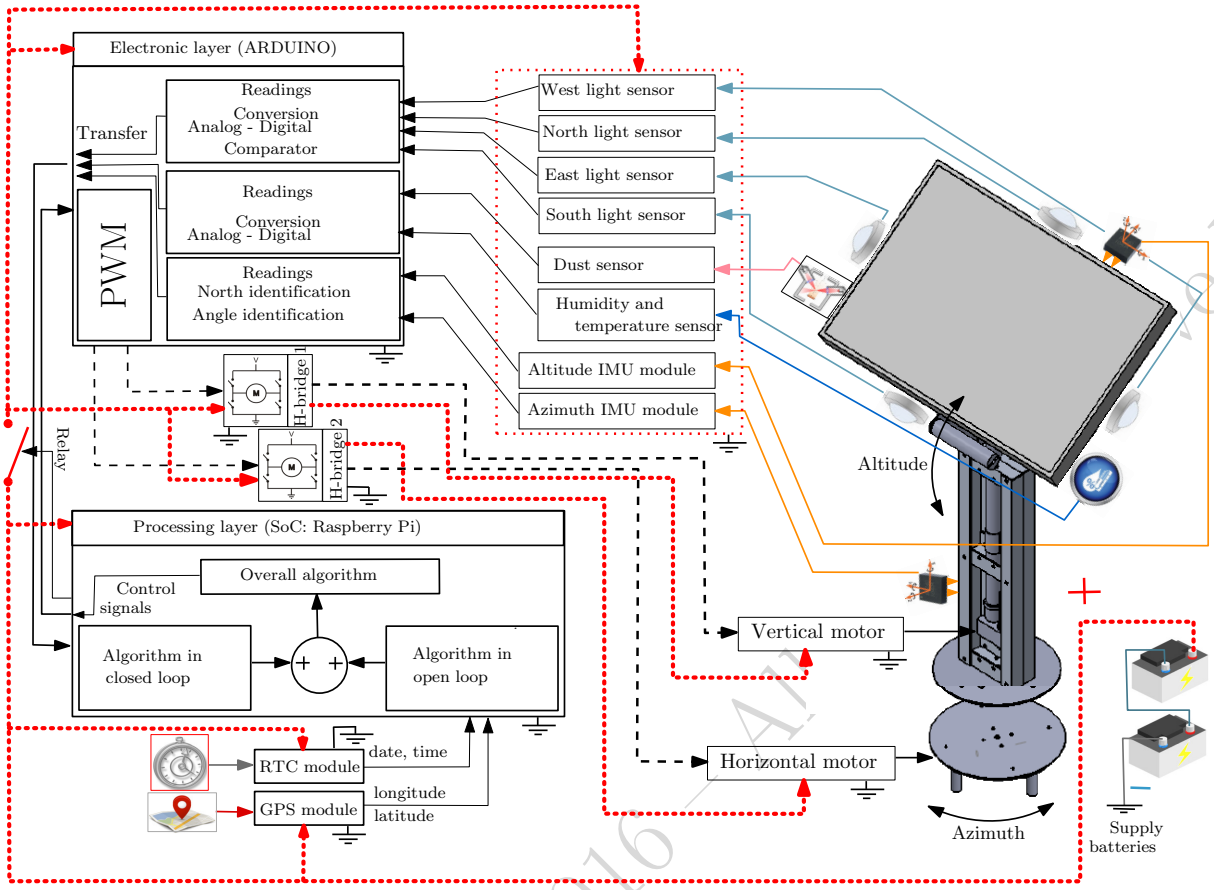


Figure III.29: Schematic representation of the solar-tracker electrical system.

and speed controllers.

- Sensors: the system is equipped with a set of sensors capable of exploring the environment and determining its position in time and space in real time.
- Decentralized electronic layer: it consists of a set of ARDUINO boards used for data acquisition, data transfer, and control of the H-bridges through PWM mode.
- Data-processing layer: it consists of the central *SOC* electronic board of Raspberry Pi type, capable of managing the different peripherals and the different functions in parallel through the overall algorithm implemented on the board.

III.5 .3 Solar-Tracker Programming Algorithm

The solar-tracker system is designed as an embedded system capable of operating automatically and autonomously without requiring any human intervention. For this purpose, this part is devoted to describing the central control algorithm of the solar tracker. The Raspberry board is equipped with an overall program written in "Python" that provides several operating modes depending on the date, time, and state of the system.

Five operating modes are distinguished, as shown in the flowchart in Figure III.30.

© Ferdaous Masmoudi, 2016 - All rights reserved

Night Mode: The overall algorithm is capable of detecting the date and time in real time and determining sunrise and sunset times. Therefore, during the night, the system automatically enters standby mode by acting on the remotely controlled power-supply relay.

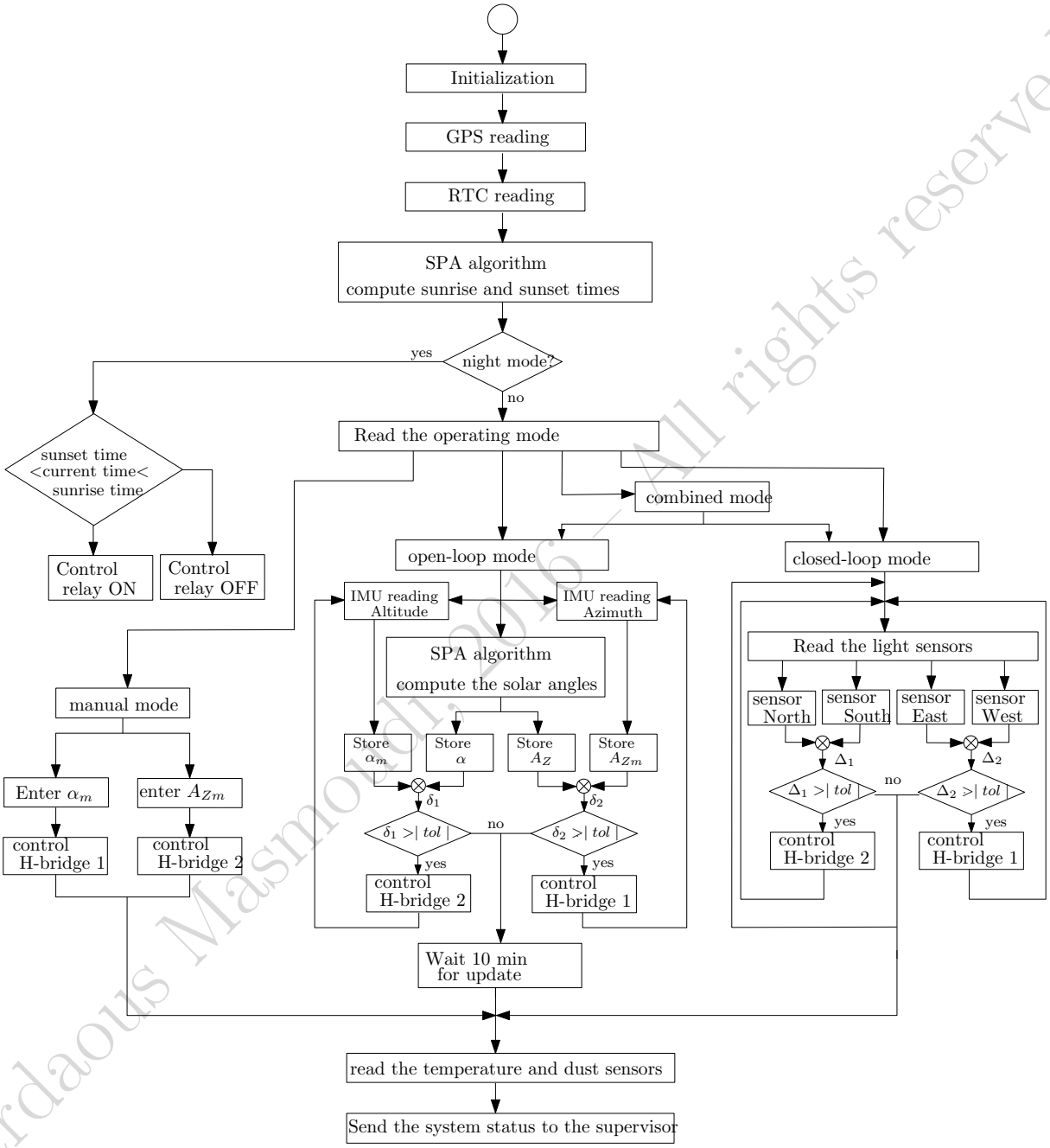


Figure III.30: Overall algorithm of the two-axis solar tracker.

Manual Mode: The system allows manual intervention by the user by switching the operating mode to manual mode, in which the PV module is directly oriented toward the position entered by the user.

Open-Loop Control Mode: This operating mode allows the module to move chronologically

© Ferdaous Masmoudi 2016 — All rights reserved

by identifying and following the sun's path according to the date, time, and geographical position. This control of the solar tracker is considered open-loop control because it does not take the system response into account. The module follows the solar trajectory blindly.

Closed-Loop Control Mode: This operating mode allows movement of the solar module by comparing the amounts of irradiance measured by each light sensor. The four light sensors are responsible for evaluating the amount of light on the four sides of the module. Shaded regions can thus be identified, and the orientation can be regulated so that the sensor values always remain close to one another. This control is considered closed-loop control because it monitors the evolution of the sensor states at each sample and continuously regulates the orientation of the PV module.

Combined Control Mode: This operating mode combines open-loop control and closed-loop control in order to exploit the advantages of each mode and benefit from the maximum amount of solar radiation.

III.6 Conclusion

This chapter was devoted to optimizing the efficiency of a PV generator through improved operation and protection of the solar collector. In the first part, solar-cell associations were studied, and the model of a PV module composed of an association of $(N_s \times N_p)$ solar cells was successfully defined mathematically. The simulation results of the model implemented in MATLAB-Simulink were validated experimentally. The second part was devoted to studying the shading problem and its impact on the different types of associations; the various problems causing PV-generator power losses were therefore presented, and a simulation model was proposed for this effect. The solar resource in Tunisia, and particularly in Sfax, was presented in the third part. The path and position of the sun in the sky were then studied, and the solar irradiance measured on the inclined surface of the solar module was discussed. The simulation work focused on comparing three types of solar trackers with a fixed module, and the energy benefit resulting from the use of a two-axis solar tracker and its importance in optimizing PV-module efficiency were demonstrated. The chapter concluded with the presentation of the complete designed solar-tracker system. The mechanical assembly and the electrical and electronic system were described, and the overall programming algorithm for the complete system was developed.

© Ferdaous Mahmoudi 2016 - All rights reserved

Chapter IV

Optimal Design of the Stand-Alone Photovoltaic Conversion and Storage System

Abstract: *This fourth chapter investigates the design, sizing, synthesis, and analysis of a power-conversion chain dedicated to photovoltaic applications. First, a method for linearizing the nonlinear characteristics of the load and the source around the maximum power point is presented. Next, the modeling and identification of the internal parameters of the Lead-Acid storage battery are addressed. The sizing and synthesis of DC–DC converters operating in continuous conduction mode are then discussed. The final part deals with the development of the P&O control strategy for the converter. The chapter ends with simulation results devoted to studying the performance of the conversion chain under various changes in operating conditions.*

Keywords: PV conversion chain,
Linearization around the MPP,
Lead-Acid battery modeling,
Converter sizing and synthesis,
Boost converter,
P&O MPPT control,

© Ferdaous Mastoudi, 2016 – All rights reserved

IV.1 Introduction

The optimal design of a PV conversion system is strongly required for maximum utilization of solar energy [80]. This necessarily requires going through the sizing and then the simulation stages. To develop a simulation model of the overall PV conversion chain that integrates: (i) the photovoltaic solar generator, (ii) the DC–DC adaptation stage, (iii) the load and storage system, and (iv) its associated control device, it is essential to properly model each component of the BOS system (*in Anglo-Saxon terminology, Balance Of System*: this term is used to summarize all components required in addition to the solar modules to build a complete photovoltaic system) [81].

This chapter provides an overview of the work carried out to initiate the design and modeling of the PV chain described in Figure IV.2. First, the principle of optimizing PV conversion chains is presented and linearizations of the PV source and the coupled load around the maximum power point (MPP) are introduced with a view to adequately sizing the adaptation stage. Subsequently, a characterization of the storage element (lead-acid battery) and its associated observation system is proposed. The third part deals with the sizing procedure and modeling work for the DC–DC power converter. Simulation results for PV conversion chains using a Boost converter are then presented. The fourth and final part concerns the MPPT control strategy. The design and modeling of a P&O (*Perturb and Observe*) MPPT control are therefore presented. The chapter concludes with the simulation results of the system.

IV.2 Principle of Photovoltaic Power Optimization

In the previous chapters, accurate models of the solar cell and then of the solar module (formed by an association of cells) were successfully developed. This chapter continues this work. Accordingly, the possibilities for adapting the PV generator to the available electrical load are examined, together with the identification and modeling of each component constituting the chain. The emphasis of this chapter is on stand-alone PV systems (not connected to the electrical grid).

PV generators are almost always associated with power-electronic devices. Even in the case of a direct connection between a solar module and a battery, a blocking diode is required [82].

The need to optimize the efficiency of a PV module is essential because of its sensitivity to continuous changes in weather conditions and, above all, because of the nonlinearity of its current–voltage ($I-V$) and power–voltage ($P-V$) characteristics. There is only one operating point P_m at which power production is maximum, for a voltage level equal to V_m and a generated current equal to I_m. However, the coordinates of such a point vary with climatic conditions, essentially the level of radiation incident on the panel surface and the evolution of ambient temperature during the day [83].

When a PV module is connected directly to a resistive load or a battery, there is little chance that it will operate at the optimal operating point corresponding to maximum power. Figure IV.1 shows the intersections of several electromotive-force levels (V_1, V_2, V_3, and V_4) of

© Ferdaous Masmoudi, 2016 - All rights reserved

a 24 V battery and the intersections of several resistive-load characteristics (R_1, R_2, R_3, and R_4) with the $(I-V)$ and $(P-V)$ characteristics of a PV module. These different types of loads always have their own requirements for the voltages and currents supplied by the source. Consequently, a significant amount of clean electrical energy is lost because of poor matching between the source and the load. For this reason, an adaptation stage must be inserted to make the connection appropriate [84].

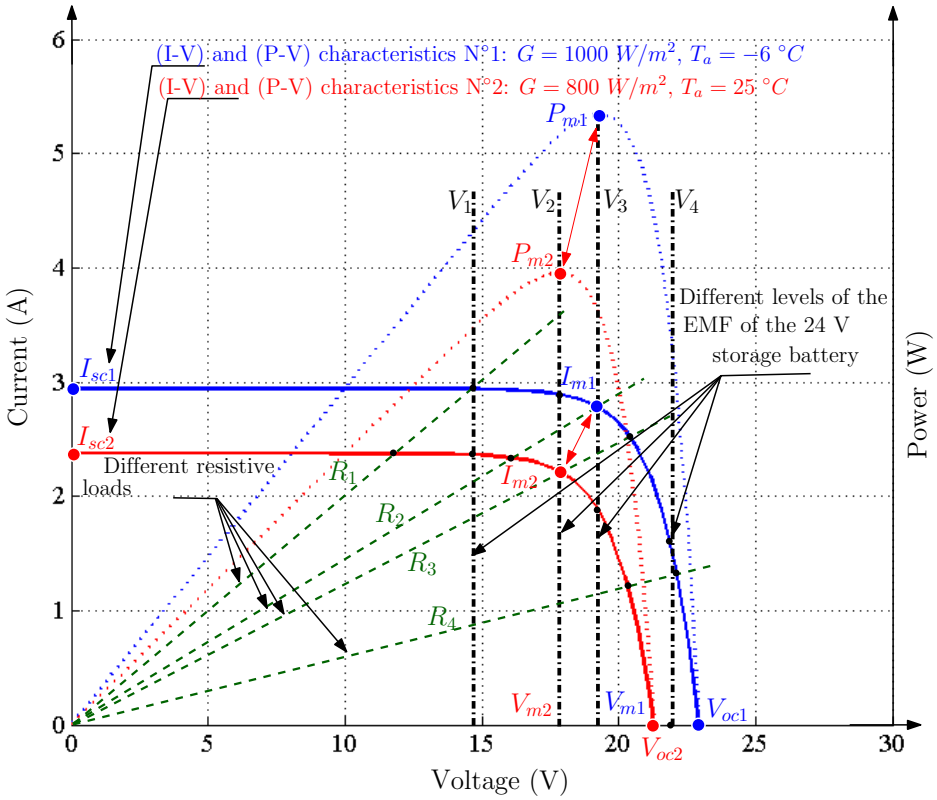


Figure IV.1: Intersections between the EMF levels of a 24 V battery and various resistive loads with the $(I-V)$ and $(P-V)$ characteristics of a PV generator: operating points under direct coupling.

Figure IV.1 shows an infinite number of operating points corresponding to the intersection of the $(I-V)$ characteristic of the PV module with the battery EMF levels or with the different loads, but only one point can coincide with the pair (I_m, V_m), which gives the maximum power P_m.

Thus, in order to improve the efficiency of a photovoltaic conversion system and overcome the disadvantages of direct coupling, a power- electronic converter is required to adapt the electrical frequency and voltage level to the intended use. Moreover, rational use of photovoltaic generators is possible only in association with power-electronic converters so as to regulate the photovoltaic-generator voltage at a maximum power point, independently of the system output voltage.

With the development of power-electronic devices dedicated to photovoltaic applications, several electrical conversion systems have been designed. These systems make it possible to

© Fercaous Masri

convert electrical energy from DC form into DC or AC electrical energy, depending on the type of load to be supplied [85].

Since the solar panel supplies direct current and the load also requires electrical energy in DC form, the system used as an interface between the photovoltaic generator and the load is a DC–DC converter, often called a chopper, which forces the photovoltaic generator at each instant to operate at the desired reference voltage by varying the duty cycle (d) of the control signal, regardless of irradiance and temperature disturbances.

Rigorous control of the adaptation stage, particularly of the duty cycle d, makes it possible to match the load voltage V with the voltage V_m corresponding to the maximum power P_m and guarantees optimization of electrical-energy transfer from the source to the load. The method for controlling converters dedicated to PV systems is often called MPPT (*Maximum Power Point Tracking*). The MPPT control strategy consists of comparing the powers generated by the PV generator at different instants and acting on the converter duty cycle by increasing or decreasing it according to the resulting power difference. Successive repetition of this iteration leads, after a short time, to tracking the desired maximum power.

Obviously, the use of the power-conversion stage and its MPPT control strategy only makes sense in the presence of a storage element (generally a battery) capable of storing the surplus energy recovered. Nevertheless, integrating such equipment requires particular monitoring.

A battery is an electrochemical device that requires slightly more potential to charge and less potential to discharge. However, it has strict voltage and current limits that are fundamental to its optimal performance.

To prevent battery damage, a special protection technique commonly called a "battery observer" (in Anglo-Saxon terminology, BMS: *Battery Management System*) is used. This technique allows the battery to be used over a long period through several charge and discharge cycles while being protected against overcharge, deep discharge, and unwanted discharge. The battery observer is also used to manage and monitor its state of charge SOC (*State Of Charge*) and to maintain its state of health SOH (*State Of Health*).

The system resulting from the association of the BOS system and its MPPT control with the battery observer BMS is generally known and commercialized as a "Charge Controller" [86, 87, 88, 89].

In this context, the objective of this work is to propose the optimal sizing and modeling of a charge controller dedicated to a 50 W PV module for supplying loads (motors, lamps, control boards) with DC voltage.

The principle of the designed PV chain (PV Generator–Charge Controller–Battery–Load) is illustrated by the block diagram in Figure IV.2. The first manufactured prototype of the charge controller and the first results obtained are presented in Chapter V.

© Ferdaous Masmoudi, 2016 – All rights reserved

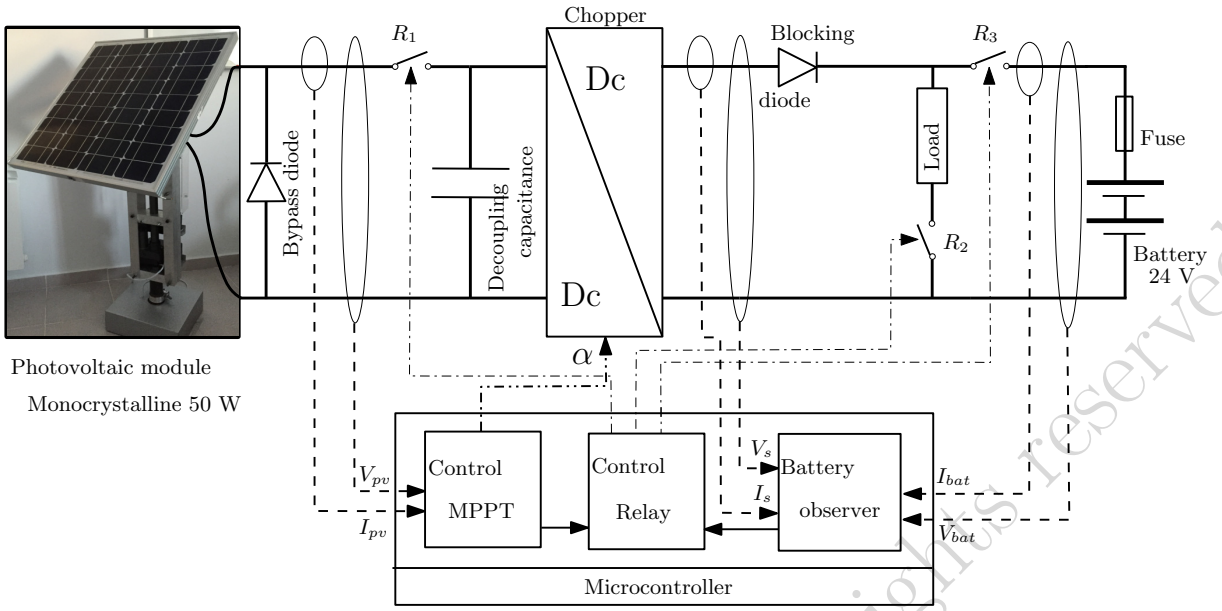


Figure IV.2: Principle of the designed PV conversion chain.

IV.3 Characterization of the PV Source and the Load

Optimal sizing of a power converter for photovoltaic applications is a rather complicated task. This is because the electrical quantities generated by the input source (photovoltaic module) vary during the day (the voltage varies from 0 to V_{oc}, the current varies from 0 to I_{sc}, and V_{oc} and I_{sc} vary as functions of temperature and irradiance).

Likewise, the output load is not constant. First, the voltage across the storage battery changes according to its state of charge. Furthermore, the motors and control boards do not operate continuously at the same rate. To overcome this problem during the sizing stage, the source and load are characterized around a well-defined operating point.

However, given the objective of designing an MPPT control for this system, the module must operate around the operating point that provides maximum power, referred to as the Maximum Power Point (MPP).

In order to optimize converter performance during the sizing stage, the characterizations are carried out around the MPP under STC conditions (irradiance of 1000 W/m^2 and temperature of 25 $°C$) [90, 91, 92].

IV.3 .1 Characterization of the PV Source

The electrical behavior of a photovoltaic solar module is highly nonlinear. This is explicitly visible in its $(I-V)$ characteristic in Figure IV.3a. Indeed, the photovoltaic source behaves as a current source in the low-voltage region, i.e., in the upper part of its characteristic. It behaves as a voltage source in the low-current region, i.e., in the lower part of the characteristic. Between these two regions lies the maximum power point (MPP). In the vicinity of this point, the current and voltage are nearly constant and equal to I_m and V_m, respectively.

© Ferdaous Mastouli, 2016 – All rights reserved

The solar-module characteristic can be simplified by adopting an equivalent circuit around a well-defined operating point. Figure IV.3b presents the Thevenin and Norton equivalent circuits used to linearize the electrical characteristics of the solar module. Around the MPP, the two circuits are exactly equivalent.

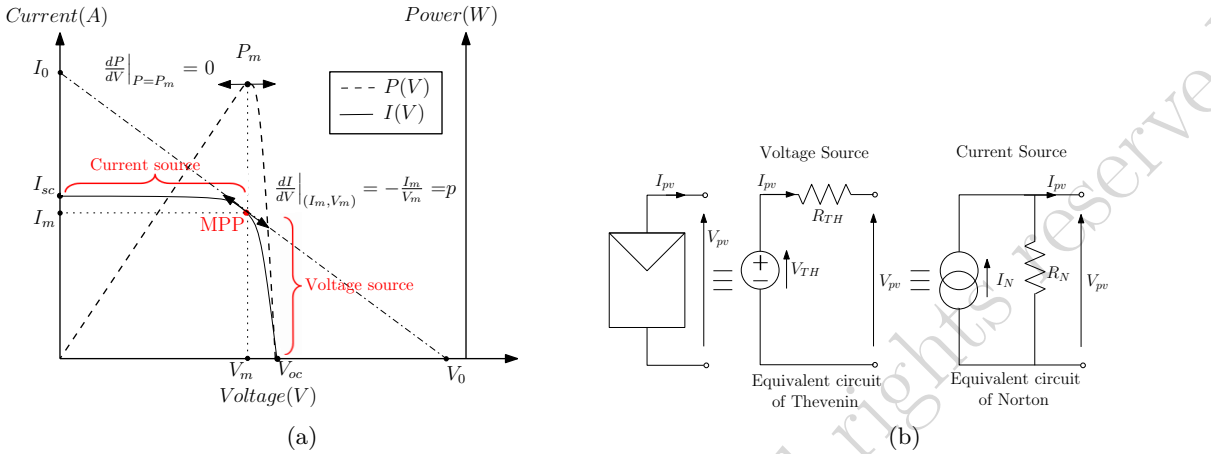


Figure IV.3: Linearization of the source in the vicinity of the MPP. (a) $(I-V)$ characteristic. (b) Equivalent circuits.

The proposed equivalent circuits can be identified from the line tangent to the $(I-V)$ characteristic at the MPP. The intersection of this line with the abscissa axis gives the value of the voltage source V_0. Its intersection with the ordinate axis gives the value of the current source I_0. The slope p of this line can be calculated from the MPP as follows:

$$\left.\frac{dP}{dV}\right|_{P=P_m} = I_m + V_m \left.\frac{dI}{dV}\right|_{\substack{V=V_m \\ I=I_m}} = 0 \tag{IV.1}$$

thus:

$$p = \left.\frac{dI}{dV}\right|_{\substack{V=V_m \\ I=I_m}} = -\frac{I_m}{V_m} \tag{IV.2}$$

The equation of the tangent to the $(I-V)$ characteristic at the MPP is written as follows:

$$I = \left.\frac{dI}{dV}\right|_{\substack{V=V_m \\ I=I_m}} (V - V_m) + I_m \tag{IV.3}$$

$$= -\frac{I_m}{V_m}(V - V_m) + I_m \tag{IV.4}$$

$$= -\frac{I_m}{V_m} V + 2I_m \tag{IV.5}$$

The following particular points of this tangent are therefore obtained: $(0, 2\ I_m)$, $(2V_m, 0)$. If we consider:

$$V_m = R_m \cdot I_m \tag{IV.6}$$

then:

$$R_m = R_{TH} = R_N = -\frac{1}{p} = \frac{V_m}{I_m} \tag{IV.7}$$

R_m is the equivalent resistance of the input source around the maximum power point MPP.

© Ferdaous Masmoudi, 2016 – All rights reserved

The evaluation of the equivalent resistance R_m estimated in the vicinity of the MPP under STC for the 50 W solar module is presented in Table IV.1.

Table IV.1: Evaluation of R_m in the vicinity of the MPP of the 50 W solar module under STC ($G = 1000W/m^2$ and $T = 25°C$).

Quantity	Value
V_m (V)	19.332
I_m (A)	2.7655
R_m (Ω)	6.9904

IV.3 .2 Load Characterization

When a load is directly connected to the PV module, the operating point is determined by the intersection of the module characteristic and the electrical characteristic of the load, as previously shown in Figure IV.1. In order to bring the operating point toward the maximum power point (MPP), a $DC - DC$ converter is inserted to provide matching between the PV source and the load. The converter is controlled by an MPPT strategy that evaluates the appropriate duty cycle d_m for maintaining the MPP. The duty cycle d_m sought by the MPPT varies according to changes in climatic conditions acting on the PV module and according to the continuous fluctuation of the output load.

Unlike the general case in which $DC-DC$ converters are used to regulate the output voltage, here it is instead the input voltage that is regulated. The output voltage is fixed according to the requirements of the storage element (for a 12 V battery, the manufacturer recommends a maximum charging voltage V_{Sm} of 15 V). The desired converter is therefore used to regulate the variable input voltage, which is the origin of its designation as a "Variable Input Converter" [93].

By establishing an MPPT regulator that controls the converter, the maximum available power supplied by the generator can be utilized. In this way, the maximum input power P_m is entirely transferred to the output. The connected load consumes the current it requires and the remaining energy is transferred to the storage element. From this reasoning, it follows that the output quantities are no longer variable. Around the MPP, the output voltage is always equal to the battery voltage V_{S_m}m and the transferred current is always the constant I_{S_m}, regardless of load fluctuation. The problem becomes linear and is represented by an overall equivalent load R_{S_m}, and the conversion chain can be represented simply by Figure IV.4.

Throughout this analysis, the principle of power conservation is considered and the various losses in the conversion stage are neglected.

Obviously, the expressions of the voltage and current gains change according to the type of converter used in the DC–DC adaptation stage (the different converter types considered in this study and their gains are presented in Table IV.7). We denote: voltage gain

$$G_V(d) = \frac{V_s}{V_{pv}} \tag{IV.8}$$

© Ferdaous Miasmoudi, 2016 – All rights reserved

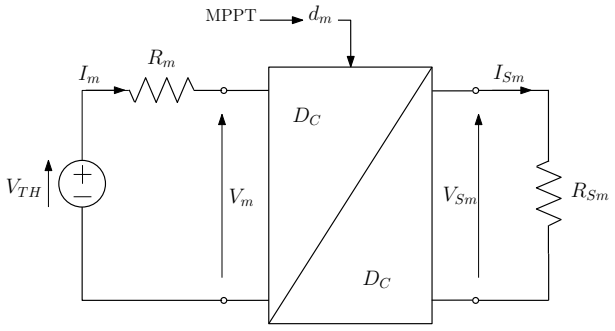


Figure IV.4: Simplification of the PV conversion chain in the vicinity of the MPP.

Voltage gain in the vicinity of the MPP:

$$G_{Vm}(d_m) = \frac{V_{Sm}}{V_m} \tag{IV.9}$$

Power conservation:

$$P_{pv} = P_s V_{pv} \times I_{pv} = V_s \times I_s \tag{IV.10}$$

Current gain of a converter:

$$G_i(d) = \frac{I_s}{I_{pv}} = \frac{1}{G_v(d)} \tag{IV.11}$$

Current gain in the vicinity of the MPP:

$$G_{im}(d_m) = \frac{I_{Sm}}{I_m} = \frac{1}{G_{Vm}} \tag{IV.12}$$

hence:

$$I_{Sm} = \frac{I_m}{G_{Vm}} \tag{IV.13}$$

Equivalent output resistances at the MPP:

$$V_m = R_m \times I_m V_{Sm} = R_{Sm} \times I_{Sm} \tag{IV.14}$$

Recall that:

$$\frac{V_{Sm}}{V_m} = \frac{R_m}{R_{Sm}} \times \frac{I_m}{I_{Sm}} \tag{IV.15}$$

The equivalent output resistance becomes:

$$R_{Sm} = \frac{V_{Sm}}{V_m} \cdot \frac{I_m}{I_{Sm}} \cdot R_m R_S = G_{Vm}(d_m)^2 \cdot R_m \tag{IV.16}$$

Depending on the type of converter used, the optimal duty cycle d_m that provides the MPP under STC can be determined. For example, in the case of a boost converter, where G_v is given by:

$$G_V(d) = \frac{1}{1-d} \tag{IV.17}$$

The optimal duty cycle d_m is then obtained as follows:

$$d_m = 1 - \frac{1}{G_{Vm}} = 1 - \frac{V_m}{V_{Sm}} \tag{IV.18}$$

The evaluation of the equivalent output electrical quantities (R_{Sm}, I_{Sm}, d_m) estimated in the vicinity of the MPP under STC for the 50 W solar module and for various types of converters is presented in Table IV.8.

© Ferdaous Masmoudi, 2016 _ All rights reserved

IV.4 Characterization and Observation of the Storage System

The use of a storage element is required in stand-alone PV systems in order to store the electrical energy produced by the solar generator and to supply energy to electrical loads. This equipment is capable of supplying electrical loads at stable voltages and currents for certain periods. However, it can often cause overvoltages or high current peaks, which requires continuous monitoring [94].

IV.4 .1 Presentation of the Storage Element:

The electrochemical cell is the elementary unit used either to generate electrical energy from stored chemical energy or to store electrical energy in the form of chemical energy. As shown in Figure IV.5.a, it consists of two positive and negative electrodes immersed in a container filled with an electrolyte that provides the essential ionic conductivity between the cell electrodes. The separator, which is permeable to ions and electrically nonconductive, or a spacer, prevents short-circuiting between the positive and negative electrodes of the cell.

A battery is obtained, as shown in Figure IV.5.b, when two or more cells are connected in an appropriate series/parallel arrangement to obtain the required operating voltage and the capacity of a given load.

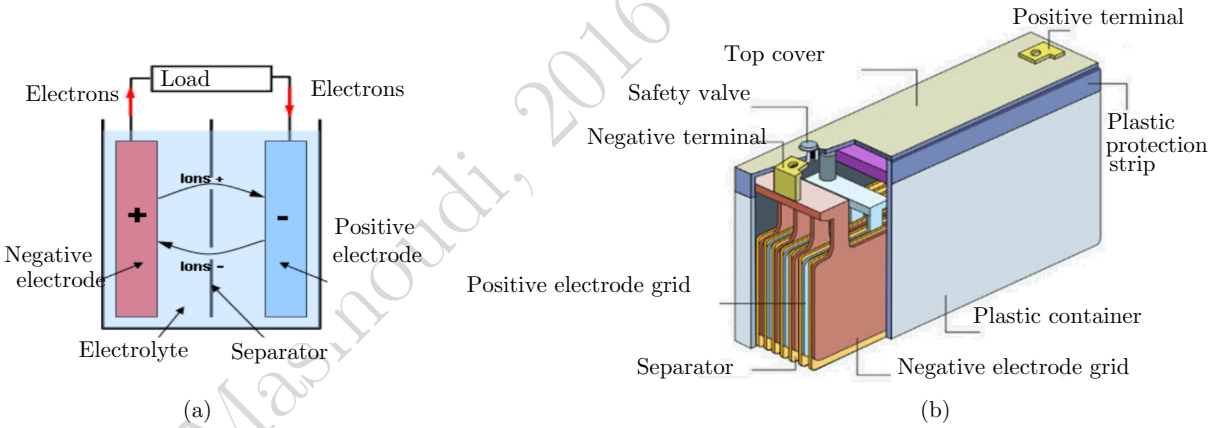


Figure IV.5: Composition of the storage element. (a) Electrochemical cell. (b) Electrochemical battery. [95]

There are several types of batteries, and most of them are still being improved through new research and development. In photovoltaic systems, several battery types can be used. Table IV.2 presents a comparison of some characteristics of the batteries most commonly used for renewable-energy applications.

Lead-acid batteries are the most widely used in photovoltaic applications, particularly in stand-alone power systems, because of their affordable price, robustness, reliability, and ease of maintenance.

However, the use of this type of battery in PV systems can cause limiting operating modes such as excessive overcharge and deep discharge, thereby resulting in electrolyte losses and irreversible chemical-bond failures.

© Ferdaous Masmoudi, 2016 – All rights reserved

Table IV.2: Comparison of the characteristics of various well-known battery technologies [96].

Battery	Lead-acid	NiCd	NiZn	Zebra	Lithium-ion
Cell voltage (V)	2	1.2	1.65	2.6	3.7
Energy density (Wh/Kg)	30−50	45−80	50−60	125	110−160
Number of cycles	500−1200	800−2000	>1000	800	500−1000
Charging time (h)	8−16	1	2−4	4−6	2−4
Self-discharge (%/month)	5	20	30	12	10
Maintenance	3−6 months	30−60 days	60−90 days	None	None
Recycling	yes	no	yes	yes	yes
Safety	stable	stable	stable	hot	explosive
Typical price ($/cycle)	0.04	0.1	0.12	0.5	0.14

In the following, the model used for the lead-acid battery is presented together with adequate identification of its internal parameters. The state-of-charge estimation method and the battery observer implemented in the charge controller are then presented.

IV.4 .2 Presentation of the Battery Model and Identification of Its Parameters

In the literature, batteries are generally represented by three categories of models: (i) experimental models, (ii) electrochemical models, and (iii) electrical models. Nevertheless, because a battery is a complex electrochemical device that is difficult to model, the battery model required for this study must be an electrical model that can be associated with the components of the PV chain and simplified so as to accurately reproduce the behavior of a real battery around a typical system operating point.

Accordingly, the battery model developed by "*Olivier Tremblay*" and "*Louis-A Dessaint*" [97] is used. This model is implemented by *MathWorks* to create the MATLAB battery model in the *SimPowerSystems* toolbox. In this application context, the model can be considered sufficiently simple and satisfactory, as it combines accuracy, simplicity, and speed.

Figure IV.6 presents the schematic representation of the electrical battery model used. It mainly consists of a voltage source in series with an internal resistance. The model assumes a fixed battery internal resistance, whereas the voltage varies with the charge and discharge cycles and as a function of the current battery state of charge SOC.

The model is mathematically expressed by the following relations:

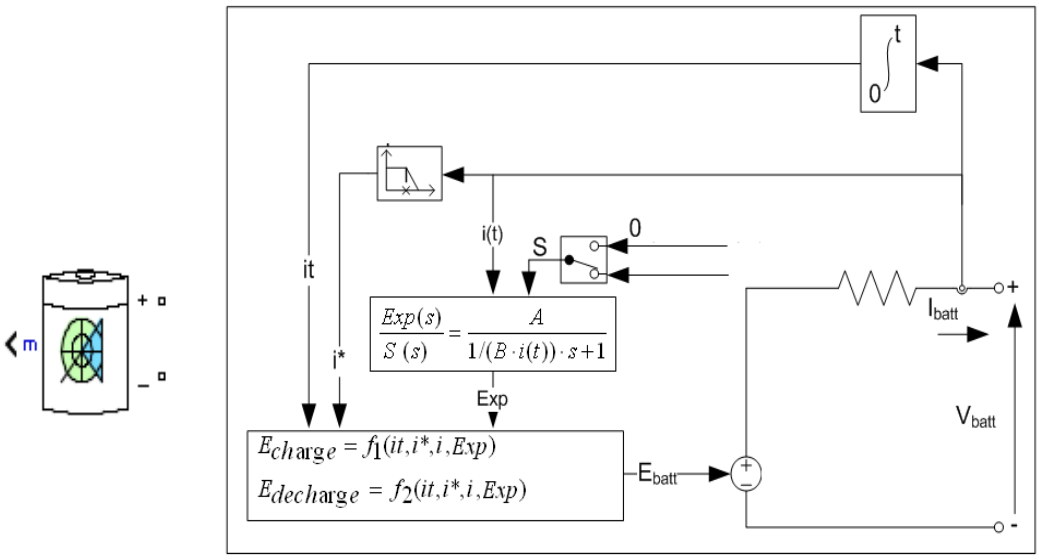
During the charging phase:

$$V_{bat} = E_0 - R\,i - K\,\frac{Q}{it - 0.1Q}\,i^* - K\,\frac{Q}{Q - it}\,it + Exp(t) \tag{IV.19}$$

During the discharging phase:

$$V_{bat} = E_0 - R\,i - K\,\frac{Q}{Q - it}\,(i^* + it) + Exp(t) \tag{IV.20}$$

© Ferdaous Marnoudi ;2016_ All rights reserved



(a) (b)

Figure IV.6: Electrical battery model from the *SimPowerSystems* toolbox. (a) Symbol. (b) Electrical diagram.

where:

$$\dot{Exp}(t) = B \ \mid i(t) \mid \ (-Exp(t) + A\ S(t)) \tag{IV.21}$$

and:

$$i^* = \frac{1}{\frac{T_r}{3}s + 1}\ i \tag{IV.22}$$

with:

- V_{bat}: Current total battery voltage (V).
- E_0: Constant battery voltage (V).
- K: Polarization constant (V/Ah).
- Q: Battery capacity (Ah).
- it: $\int idt$, current battery charge (Ah).
- i: Current total battery current (A).
- i^*: Filtered battery current (A).
- $Exp(t)$: Exponential-zone voltage (V).
- $S(t)$: In charging mode $S(t) = 1$ and in discharging mode $S(t) = 0$.
- A: Amplitude of the exponential zone.
- B: Inverse time constant of the exponential zone.

© Ferdaous Masmoudi, 2016 – All rights reserved

- T_r: Battery time constant, generally estimated at 30 seconds.

The development and use of this model require the following assumptions to be considered under typical operating conditions:

- The internal resistance remains constant during operation.
- The parameters are deduced from the discharge curve and are assumed to be similar to those of the charge curve.
- The battery capacity does not change with the magnitude of the current.
- Temperature does not affect battery behavior.

The accuracy of this model depends mainly on the choice of its parameters. The following paragraphs propose the identification of the battery parameters using two methods: a graphical method based on the manufacturer's datasheet data and a fitting method established from actual experimental measurements of the battery used.

IV.4 .2 .1 Parameter Extraction from Manufacturer Data

The main advantage of the proposed model is the simplicity with which the battery parameters are extracted. Indeed, the required parameters can be graphically deduced from only five points of the discharge curve provided in the manufacturer's datasheet. The manufacturer data for the battery used in practice, reference "Power Kingdom PS7-12", are summarized in Table IV.3.

Table IV.3: Electrical specifications of the "Power Kingdom PS7-12" Lead-Acid battery.

Quantity	Value
Overall Nominal Voltage V_{NG} (V)	12
Rated Capacity$^{(f)}$ C_N (Ah)	(25°C,20HR) 7.0
Internal Resistance$^{(g)}$ R_I ($m\Omega$)	(25°C,SOC=100%) 22
Maximum Capacity C_M (Ah)	(25°C,5HR,1.19A) 5.95
Maximum Discharge Current I_M (A)	(25°C,5s) 105
Charging Voltage V_{cycle} (V)	(25°C,–24mV/°C) 14.5∼15
Maximum Charging Current I_{cycle} (A)	(25°C) 2.1

The discharge-characteristic curve from the datasheet of the battery under study is shown in Figure IV.7.

The model parameters can be extracted from points (a,b,c,d,e) indicated in Figure IV.7. Thus, point (a), which marks the end of the linear zone, makes it possible to determine the nominal voltage V_N and its corresponding capacity C_N. Point (b) is used to identify the maximum capacity C_M, whereas point (c), which marks the end of the exponential zone, is used to determine the fully charged voltage V_C. Point (d) represents the nominal discharge current, assumed constant, I_N, used by the manufacturer to determine the maximum capacity C_M. Point (e), which marks the end of the linear zone, makes it possible to identify the exponential voltage V_E and its corresponding capacity C_E. In addition, the internal resistance R_I and the rated capacity C_N are generally given numerically (data f and g in Table IV.3).

© Ferdaous Namouchi, 2016 - All rights reserved

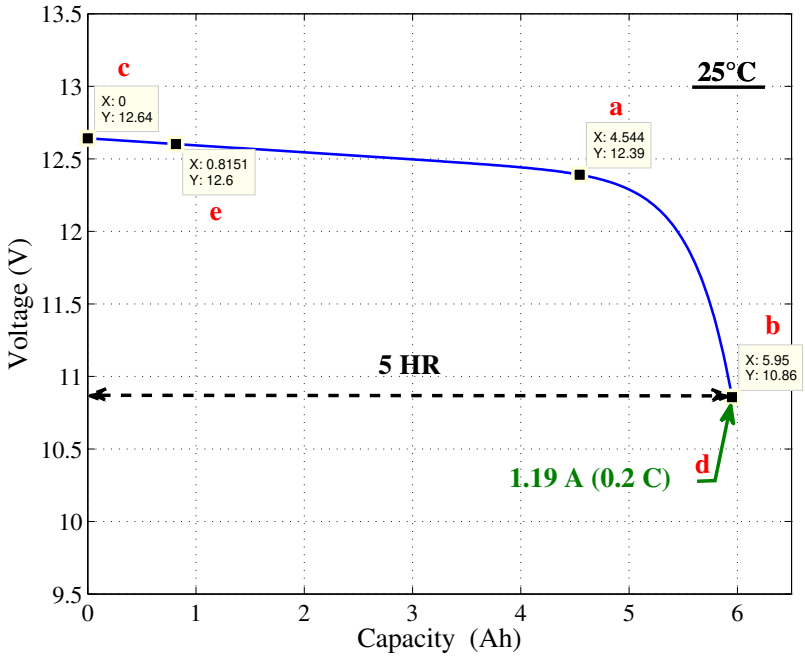


Figure IV.7: Discharge characteristic of the "Power Kingdom PS7-12" Lead-Acid battery at 25°C.

The graphical-identification results obtained from the manufacturer's datasheet are presented in Table IV.4.

IV.4 .2 .2 Parameter Extraction from Experimental Measurements

To improve the accuracy of the battery model, the discharge characteristic is experimentally investigated under typical PV-system operating conditions and using typical loads [98]. The experimental measurements of the currents and voltages supplied by the battery (initially charged) during its discharge are recorded automatically. Figure IV.8.a shows the explanatory diagram of the current- and voltage-measurement method, and Figure IV.8.b presents the experimental battery-measurement test bench.

The battery-model parameters are fitted so that the model coincides with the experimental discharge characteristic. For this purpose, the curve-fitting procedure (Section II.2.2) is used with the evolved-gradient algorithm, as illustrated in Figure IV.9.

The results of identifying the parameters of the "Power Kingdom PS7-12" battery by fitting and using experimental measurements are presented in Table IV.4.

IV.4 .2 .3 Results and Interpretation

The results of extracting the parameters of the "Power Kingdom PS7-12" battery used in practice by adopting the two methods described above are summarized in Table IV.4.

To compare the accuracy of the parameters determined by the two methods studied, Figure IV.10 presents the discharge curves simulated by the battery model using the identified parameters together with the experimentally obtained discharge curve.

© Ferdaous Masmoudi, 2016 — All rights reserved

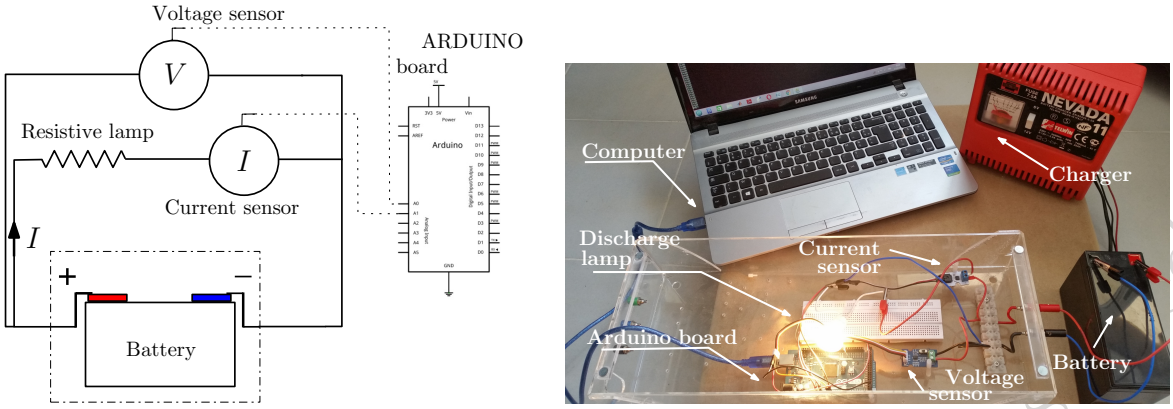


Figure IV.8: Experimental measurements of the "Power Kingdom PS7-12" battery. (a) Explanatory measurement diagram. (b) Experimental test bench.

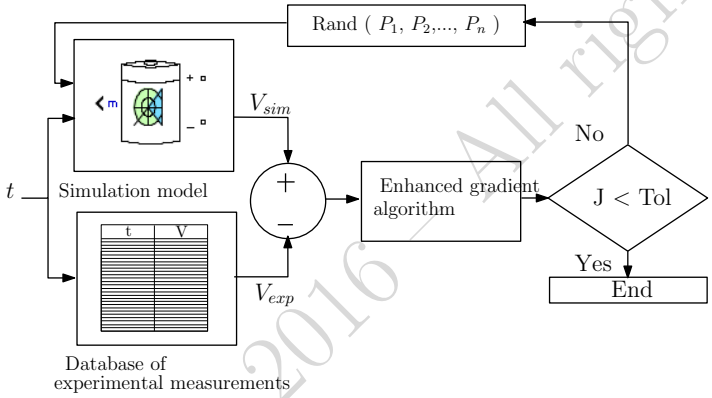


Figure IV.9: Explanatory diagram of the curve-fitting method used to identify the parameters of the "Power Kingdom PS7-12" battery.

Table IV.4: Results of the parameter-extraction methods for the "Power Kingdom PS7-12" Lead-Acid battery.

Parameter	Value from datasheet	Value from experiment
Nominal Voltage V_N (V), "*Nominal Voltage*"	$12.39^{(a)}$	12.3327
Rated Capacity C_N (Ah), "*Rated Capacity*"	$7^{(f)}$	6.9571
Maximum Capacity C_M (Ah), "*Maximum Capacity*"	$5.95^{(b)}$	6.2597
Fully Charged Voltage V_C (V), "*Fully Charged Voltage*"	$12.64^{(c)}$	12.8821
Nominal Discharge Current I_N (A), "*Nominal Discharge Current*"	$1.19^{(d)}$	0.5527
Internal Resistance R_I ($m\Omega$), "*Internal Resistance*"	$22^{(g)}$	22
Capacity at Nominal Voltage C_{VN} (Ah), "*Capacity @ Nominal Voltage*"	$4.544^{(a)}$	3.6211
Exponential Voltage V_E (V), "*Exponential Voltage*"	$12.6^{(e)}$	12.7491
Exponential Capacity C_E (Ah), "*Exponential Capacity*"	$0.8151^{(e)}$	0.5470

The experimental-measurement curve represents the actual behavior of the battery used under typical PV-system operating conditions. A comparison of the simulated curves with the experimental curve shows the limitations of the battery model, which proves unable to reproduce the entire experimental curve, particularly during deep discharge. The graphical parameter-identification method based on datasheet data provides an accuracy of 2% when SOC is 90%

© Ferdaous Idamoud 2016 – All rights reserved

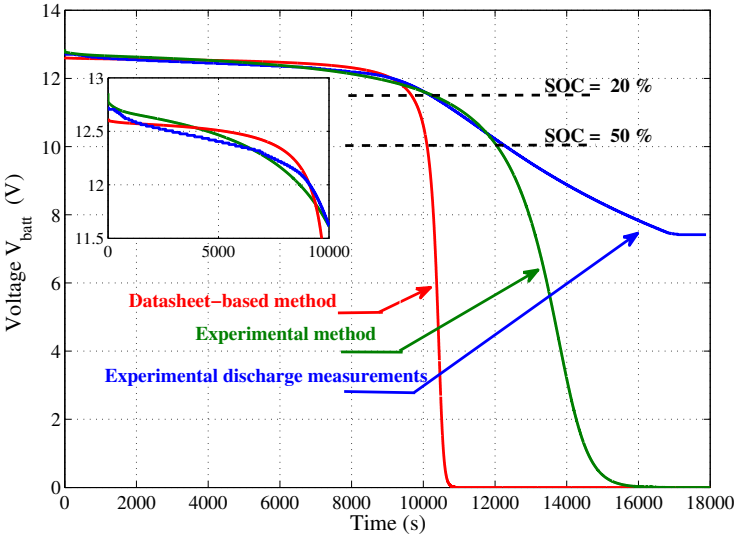


Figure IV.10: Comparison of the discharge characteristics of the "Power Kingdom PS7-12" battery.

and decreases to 10% when SOC is 80%. Beyond this SOC value, the model is considered invalid and no longer reproduces the actual battery behavior. For the identification method based on experimental measurements, better accuracy of 1% is observed down to a state of charge SOC equal to 50%; below this value, the model becomes invalid. The experimental method therefore provides better identification of the battery-model parameters, and the accuracy is sufficiently satisfactory over the operating interval, especially considering that the designed battery observer protects against deep discharge and does not allow the battery to discharge to an SOC below 50%.

IV.4 .3 Battery Observation System:

This section presents a battery observer designed to estimate the state of charge and protect the battery against excessive overcharge and deep discharge [99]. Figure IV.2 previously presented the electrical circuit developed to control the relays remotely by opening or closing them according to the estimated state-of-charge value. Figure IV.11 presents the flowchart of the algorithm used to estimate the state of charge (SOC) at each measurement sample and to control the relays.

The battery state of charge SOC is generally evaluated by the following mathematical expression:

$$SOC(\%) = 100 \left(1 - \frac{1}{Q} \int i(t)dt\right) \tag{IV.23}$$

© Ferdaous Maamoudi, 2016 – All rights reserved

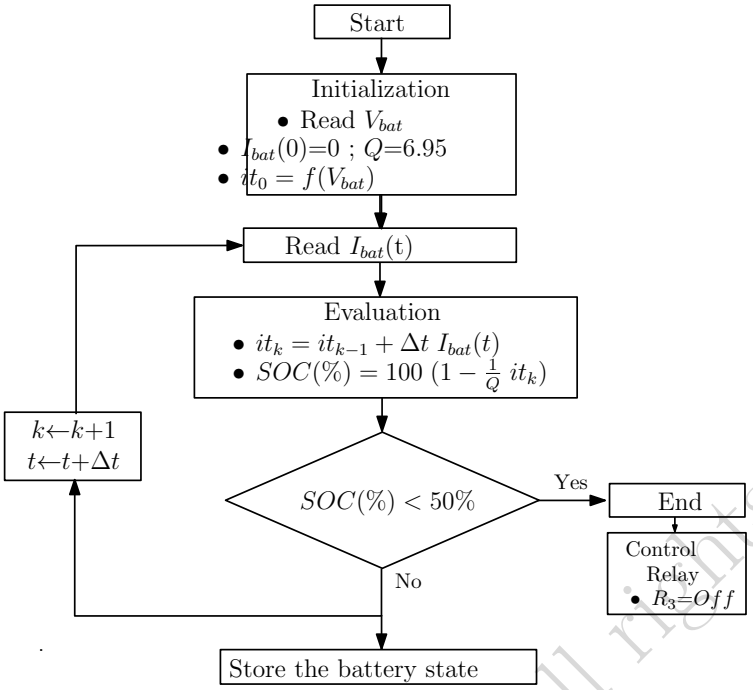


Figure IV.11: Battery-observer algorithm.

IV.5 Design, Modeling, and Sizing of the DC–DC Converter

In the previous sections, a linearization of the PV source and then of the output load around the maximum power point (MPP), considered the ideal point for optimizing the PV system, was carried out.

In this section, the $DC-DC$ conversion stage inserted between the PV module and the load is studied and sized by taking into account the linearizations previously established.

A chopper is a DC–DC power converter that transforms a DC input voltage into another DC output voltage of a different value. The output- voltage value mainly depends on the selected converter topology [100].

For variable-input converters dedicated to PV applications, the output voltage V_S is fixed by the voltage of the storage element V_{bat}, while the input voltage V_{pv} varies from 0 to V_{oc} (open-circuit voltage). In this case, the choice of topology depends on the choice of storage element. If $V_{bat} > V_{pv}$, the converter must be step-up, and if $V_{bat} < V_{pv}$, the converter must be step-down. Step-up/step-down converters also exist and can adapt to any battery choice solely by acting on their duty cycles.

IV.5 .1 Optimal Sizing of Power Converters

In the literature, there are many $DC-DC$ converter topologies that can be implemented [101, 102, 103]. In this work, only the so- called fundamental topologies, which constitute the basic cores of all other topologies, are considered. These converters are called Buck, Boost, and Buck–Boost. They were proposed in 1977 by "*Robert Middlebook*" and "*Slobodan'Cuk*" [106]. Subsequently, "*Cuk*" proposed improvements to the Buck–Boost structure and designed

© Ferdaous Masmoudi, 2016 – All rights reserved

the Cuk and Sepic converters [107, 108]. The Zeta converter, also called the inverse Sepic, and other advanced structures were later introduced by the same research team [109].

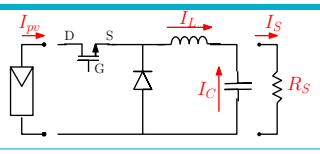
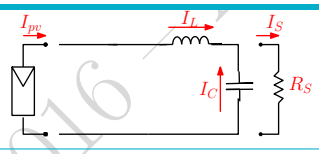
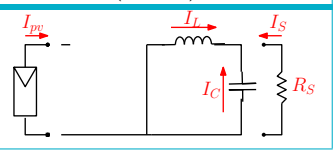
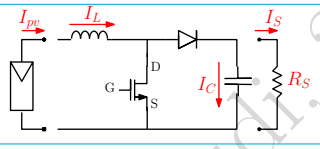
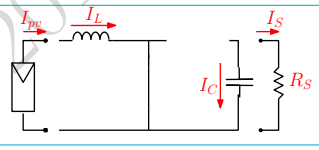
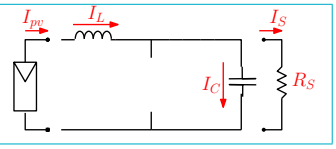
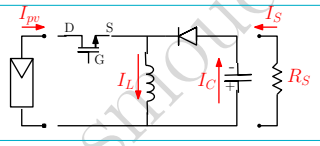
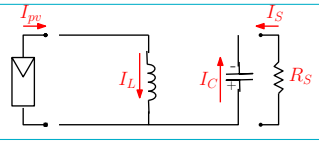
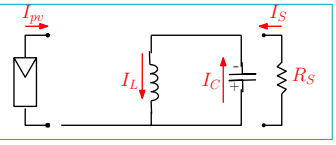
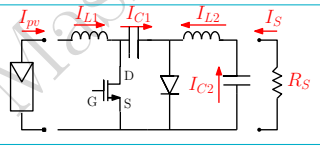
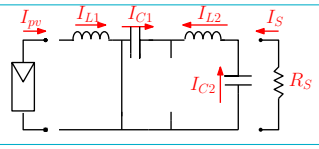
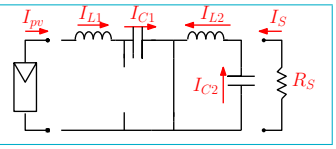
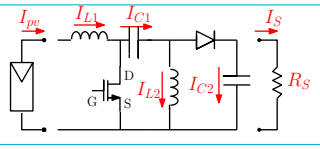
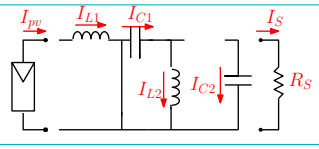
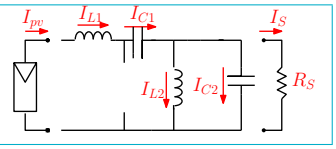
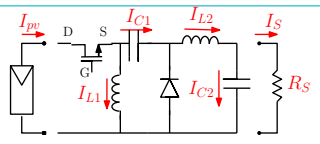
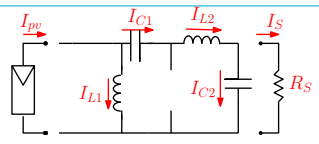
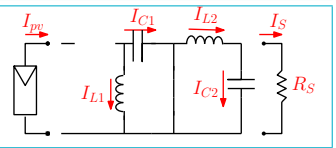
The electrical diagrams of the topologies studied in this work are grouped in Table IV.5, and their state matrices are presented in Table IV.6.

The objective of optimal converter sizing is to determine the converter design parameters, essentially the switching-cell components, inductance values, capacitance values, and switching frequency, in an appropriate manner leading to the best efficiency of the conversion stage.

The optimal choice of switching frequency is a multidimensional problem. Indeed, it depends mainly on the following parameters:

- The control board: the selected microcontroller determines the limitation of the frequency range used. For a basic MPPT control (P&O, incremental, etc.), the use of a PIC or AVR is largely sufficient. For more elaborate approaches (fuzzy technique, neural approach, etc.), the use of a DSP or FPGA board, which is significantly more expensive, is recommended.

Table IV.5: Electrical diagrams of the converter topologies considered. [104]

Topology	Overall diagram	During $d\,T$	During $(1-d)\,T$
Buck			
Boost			
Buck−boost			
Cŭk			
SEPIC			
ZETA			

- Power components: these are selected to withstand the switching frequency used. In other words, the switching period must not be shorter than the sum of the rise, fall, and recovery times of the power component, and a time margin must also be provided to avoid overlap.

© Ferdaous Hasnaoui, 2016 – All rights reserved

- Cooling system: increasing the switching frequency causes excessive heating of the power components, which requires the design of a cooling circuit. This circuit considerably increases the size of the system and also increases the cost of the converter.
- Converter weight and volume: the choice of frequency influences the size of the passive components used (inductors, capacitors, etc.). The lower the frequency, the larger the components. It is therefore advantageous to increase the frequency in order to reduce the converter size. Nevertheless, this increase is penalized by the cooling circuit required to dissipate heat.
- Overall converter cost: optimization of system efficiency is related to the available project budget. It is obviously pointless to optimize the energy gain by 5% at the expense of a large multiplication of the system cost. Thus, the cost of the desired converter must be set consistently with the overall cost of the application.

Consequently, the choice of switching frequency is a technical–economic compromise. In this study, the switching frequency f was set to 62.5 kHz, as this is the maximum frequency offered by the microcontroller used (Arduino 2560). This frequency is acceptable for the majority of power components available on the market and does not require a specific cooling circuit. The overall weight of the converter board is approximately 150 g and the cost is limited to about 100 €; this can be considered an acceptable choice.

The components of the switching cell for a power converter operating in a single quadrant are generally a naturally commutating power diode and a MOSFET transistor controlled at turn-on and turn-off. The components are selected to withstand the frequency f and the power applied to them at each instant. Components with the lowest possible internal resistances should preferably be selected in order to minimize conduction losses, together with the shortest rise and fall times in order to minimize switching losses, while remaining within the allowable budget (the most robust components that produce the lowest losses are the most expensive on the market).

Likewise, the filtering elements (inductors and capacitors) are appropriately evaluated to guarantee, on the one hand, operation of the converter in continuous conduction mode and, on the other hand, minimum ripple of the output quantities (current I_S and voltage V_S). These elements are calculated from the relations summarized in Table IV.7, considering a current-ripple amplitude $\Delta I_L = 2\%\ I_m$ and voltage-ripple amplitudes $\Delta V_{pv} = 2\%\ V_m$ and $\Delta V_S = 2\%\ V_S$. The numerical values calculated for the inductances and capacitances of all the considered topologies are summarized in Table IV.8.

The modeling and simulation of the different converter topologies, using the 50 W PV module at the input and the 24 V storage battery at the output while taking into account the various parasitic elements and conduction losses, are carried out in the MATLAB–Simulink environment using the "*SimPowerSystems*" toolbox.

A comparison of the efficiencies of the different topologies shows that the boost converter is the most appropriate in this context, because it has the highest conversion efficiency, exceeding 82%.

© Ferdaous Messaoudi, 2016 – All rights reserved

Table IV.6: State matrices of the converter topologies considered [104].

Topology	State-space model
Buck	$\frac{d}{dt}\begin{bmatrix} I_L \\ V_C \end{bmatrix} \begin{bmatrix} 0 & \frac{-1}{L} \\ \frac{1}{C} & \frac{-1}{R_S\,C} \end{bmatrix} \begin{bmatrix} I_L \\ V_C \end{bmatrix} + \begin{bmatrix} \frac{d}{L} \\ 0 \end{bmatrix} \begin{bmatrix} V_{pv} \end{bmatrix}$
Boost	$\frac{d}{dt}\begin{bmatrix} I_L \\ V_C \end{bmatrix} = \begin{bmatrix} 0 & \frac{-(1-d)}{L} \\ \frac{1-d}{C} & \frac{-1}{R_S\,C} \end{bmatrix} \begin{bmatrix} I_L \\ V_C \end{bmatrix} + \begin{bmatrix} \frac{1}{L} \\ 0 \end{bmatrix} \begin{bmatrix} V_{pv} \end{bmatrix}$
Buck−boost	$\frac{d}{dt}\begin{bmatrix} I_L \\ V_C \end{bmatrix} = \begin{bmatrix} 0 & \frac{-1}{L(1-d)} \\ \frac{1-d}{C} & \frac{-1}{R_S\,C} \end{bmatrix} \begin{bmatrix} I_L \\ V_C \end{bmatrix} + \begin{bmatrix} \frac{d}{L} \\ 0 \end{bmatrix} \begin{bmatrix} V_{pv} \end{bmatrix}$
Cŭk	$\frac{d}{dt}\begin{bmatrix} I_{L1} \\ I_{L2} \\ V_{C1} \\ V_{C2} \end{bmatrix} = \begin{bmatrix} 0 & 0 & \frac{d}{L_2} & 0 \\ 0 & 0 & \frac{d-1}{L_2} & \frac{-1}{L_2} \\ \frac{d}{C_1} & \frac{1-d}{C_1} & 0 & 0 \\ 0 & \frac{-1}{C_2} & 0 & \frac{-1}{C_2\,R_S} \end{bmatrix} \begin{bmatrix} I_{L1} \\ I_{L2} \\ V_{C1} \\ V_{C2} \end{bmatrix} + \begin{bmatrix} \frac{(1-2d)}{L_1} \\ 0 \\ 0 \\ 0 \end{bmatrix} \begin{bmatrix} V_{pv} \end{bmatrix}$
SEPIC	$\frac{d}{dt}\begin{bmatrix} I_{L1} \\ I_{L2} \\ V_{C1} \\ V_{C2} \end{bmatrix} = \begin{bmatrix} 0 & 0 & \frac{1-d}{L_1} & \frac{1-d}{L_1} \\ 0 & 0 & \frac{1-d}{L_2} & \frac{1-d}{L_2} \\ \frac{1-d}{C_1} & \frac{d-1}{C_1} & 0 & 0 \\ \frac{1-d}{C_2} & \frac{1-d}{C_2} & 0 & \frac{1-2d}{C_2\,R_S} \end{bmatrix} \begin{bmatrix} I_{L1} \\ I_{L2} \\ V_{C1} \\ V_{C2} \end{bmatrix} + \begin{bmatrix} \frac{1-2d}{L_1} \\ \frac{d-1}{L_2} \\ 0 \\ 0 \end{bmatrix} \begin{bmatrix} V_{pv} \end{bmatrix}$
ZETA	$\frac{d}{dt}\begin{bmatrix} I_{L1} \\ I_{L2} \\ V_{C1} \\ V_{C2} \end{bmatrix} = \begin{bmatrix} \frac{-1}{L_1} & 0 & \frac{d-1}{L_1} & 0 \\ 0 & \frac{-1}{L_2} & \frac{d}{L_2} & \frac{-1}{L_2} \\ \frac{1-d}{C_1} & \frac{-d}{C_1} & 0 & 0 \\ 0 & \frac{1}{C_2} & 0 & \frac{-1}{C_2\,R_S} \end{bmatrix} \begin{bmatrix} I_{L1} \\ I_{L2} \\ V_{C1} \\ V_{C2} \end{bmatrix} + \begin{bmatrix} \frac{d}{L_1} \\ \frac{d}{L_2} \\ 0 \\ 0 \end{bmatrix} \begin{bmatrix} V_{pv} \end{bmatrix}$

In the following, the operation of the designed charge controller built around a boost-type step-up converter for the 50 W photovoltaic module is studied.

IV.5 .2 Design of the PV Conversion Chain Using a Boost Converter

This section models the PV conversion chain presented in Figure IV.2 using a boost converter schematized in Figure IV.13. This converter is a two-port network whose input quantities are V_{pv} and I_{pv} (PV-source voltage and current) and whose output quantities are V_S and I_S. The low-pass filter consists of an inductance L and an output capacitance C_S. The input capacitance

© Ferdaous Masmoudi, 2016 – All rights reserved

Table IV.7: Mathematical expressions of the parameters of the different converter topologies considered [104].

	Buck	Boost	Buck-boost	Cŭk	SEPIC	ZETA
$G_V(d)$	d	$\frac{1}{1-d}$	$\frac{d}{1-d}$	$\frac{d}{1-d}$	$\frac{d}{1-d}$	$\frac{d}{1-d}$
d_m	$\frac{V_{S_m}}{V_m}$	$1-\frac{V_m}{V_{S_m}}$	$\frac{V_{S_m}}{V_{S_m}-V_m}$	$\frac{V_{S_m}}{V_{S_m}-V_m}$	$\frac{V_{S_m}}{V_{S_m}+V_m}$	$\frac{V_{S_m}}{V_{S_m}+V_m}$
R_{S_m}	$(d_m)^2\ R_m$	$\frac{R_m}{(1-d_m)^2}$	$\left(\frac{-d_m}{1-d_m}\right)^2 R_m$	$\left(\frac{-d_m}{1-d_m}\right)^2 R_m$	$\left(\frac{-d_m}{1-d_m}\right)^2 R_m$	$\left(\frac{d_m}{1-d_m}\right)^2 R_m$
L_1	$\frac{d_m\ (1-d_m)\ V_m}{f\ \Delta I_L}$	$\frac{d_m\ V_m}{f\ \Delta I_L}$	$\frac{d_m\ V_m}{f\ \Delta I_L}$	$\frac{d_m\ V_m}{f\ \Delta I_{L1}}$	$\frac{d_m\ V_m}{f\ \Delta I_{L1}}$	$\frac{d_m\ V_m}{f\ \Delta I_{L1}}$
L_2	–	–	–	$\frac{d_m\ V_m}{f\ \Delta I_{L2}}$	$\left(\frac{V_m}{\Delta I_{L2}}\right)\frac{d_m\ (1-d_m)}{d_m-1}$	$\frac{d_m\ V_m}{f\ \Delta I_{L2}}$
C_e	$\frac{(1-d_m)\ I_m}{f\ \Delta V_m}$	$\frac{d_m\ V_m}{8\ L\ \Delta V_m\ f^2}$	$\frac{(1-d_m)\ I_m}{2\ \Delta V_m\ f}$	$\frac{(1-d_m)\ I_m}{2\ \Delta V_m\ f}$	$\frac{(1-d_m)\ I_m}{2\ \Delta V_m\ f}$	$\frac{(1-d_m)\ I_m}{\Delta V_m\ f}$
C_1	$\frac{(1-d_m)\ V_{S_m}}{8\ L\ \Delta V_{S_m}\ f^2}$	$\frac{d_m\ I_{S_m}}{f\ \Delta V_{S_m}}$	$\frac{d_m\ I_{S_m}}{f\ \Delta V_{S_m}}$	$\frac{d_m\ I_{S_m}}{f\ \Delta V_{c1}}$	$\frac{d_m\ I_{S_m}}{f\ \Delta V_{c1}}$	$\frac{d_m\ I_{S_m}}{f\ \Delta V_{c1}}$
C_2	–	–	–	$\frac{-d_m\ V_m}{L2\ \Delta V_{c2}\ f^2\ d_m}$	$\frac{(1-d_m)\ (I_m\ L_2-d_m\ V_m)}{\Delta V_{c2}\ f\ L_2}$	$\frac{\Delta I_{L1}}{(8\ \Delta V_{c2}\ f)}$

Table IV.8: Numerical calculation of the parameters of the different converter topologies studied.

	Buck	Boost	Buck-boost	Cŭk	SEPIC	ZETA
V_{S_m} (V)	7.5	30	−15	−15	15	15
G_{V_m}	0.310	1.24	0.62	0.62	0.62	0.62
d_m	0.388	0.3556	0.4369	0.4369	0.4369	0.4369
I_{S_m} (A)	7.1284	1.7821	−3.5642	−3.5642	3.5642	3.5642
$R_{S_m}(\Omega)$	1.0521	16.8342	4.2085	4.2085	4.2085	4.2085
L_1 (mH)	0.515	2	1.1	2.4	2.4	2.4
L_2 (mH)	– – –	– – –	– – –	1.9	2.4	2.4
$C_e(F)$	70.044	0.286	64.441	32.221	32.221	64.441
C_1 (F)	3.8018	33.798	166	72.573	128.88	166.1
C_2 (F)	– – –	– – –	– – –	17.403	128.88	0.737

C_e is a decoupling capacitor used to mitigate the PV-source voltage ripple. The basic switching cell consists of a MOSFET M and a freewheeling diode D. The converter operates through periodic controlled switching of the MOSFET and is a step-up converter because the output voltage is always greater than the input voltage.

The MOSFET is controlled in the on-state during the period $d\ T$ and in the off-state during

© Ferdaous Maamoudi, 2016 _ All rights reserved

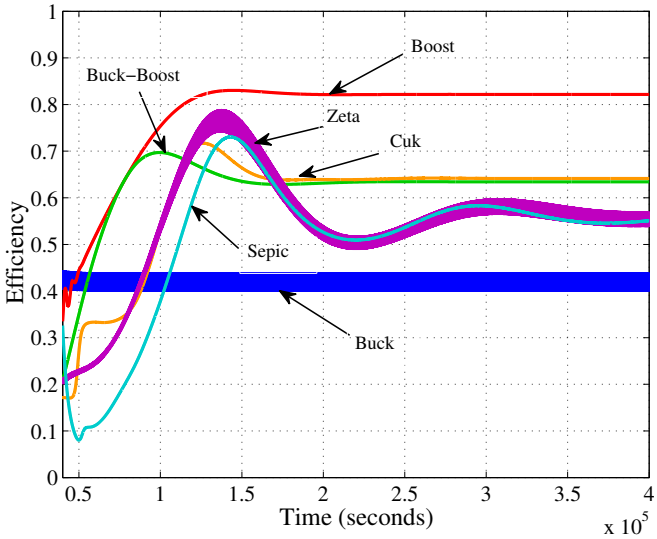


Figure IV.12: Efficiency comparison of the different converter topologies.

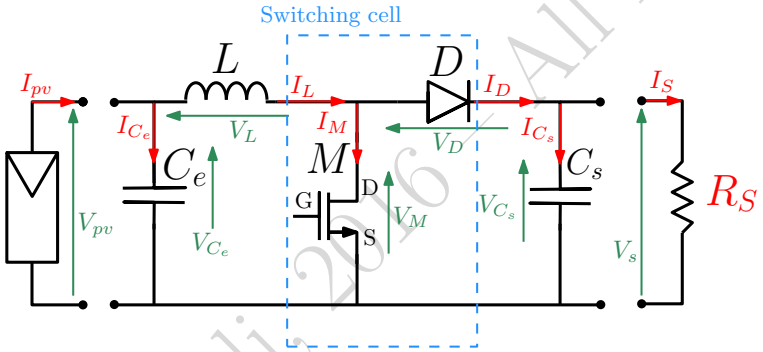


Figure IV.13: Structure of the boost converter.

the period $(1-d)\,T$, where d is the duty cycle, which varies between 0 and 1 ($T = \frac{1}{f}$ is the switching period).

The derivation of the mathematical relations linking the converter state variables to the input and output quantities, as well as the expressions of L and C as functions of ΔI_L and ΔV_S, are widely discussed in the literature [105]. The different relations required for sizing the considered converters are presented in Table IV.7.

The following provides a reminder of these relations for the boost converter. The operating sequences of the Boost converter are shown in Figures IV.14.a and IV.14.b.

- Analysis when the MOSFET is turned on (During dT):

  When the controlled switch M is conducting, the current through the inductor L increases linearly. The mathematical expressions relating the converter state variables to the input and output quantities are written as follows:

$$i_{Ce}(t) = C_e \frac{d\, v_{pv}(t)}{dt} = i_{pv}(t) - i_L(t) \tag{IV.24}$$

© Ferdaous Masmoudi, 2016 - All rights reserved

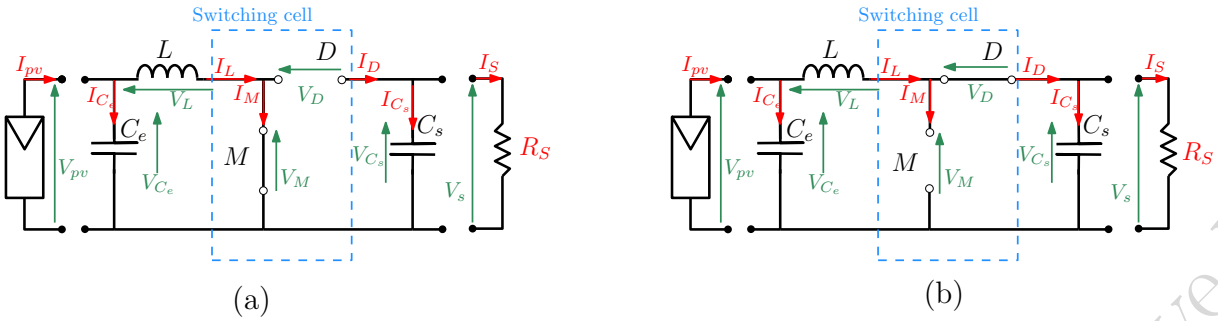


Figure IV.14: Diagrams of the boost-converter operating sequences.

$$i_{Cs}(t) = C_s \frac{d\, v_S(t)}{dt} = -i_S(t) \tag{IV.25}$$

$$v_L(t) = L \frac{d\, i_L(t)}{dt} = v_{pv}(t) \tag{IV.26}$$

- Analysis when the MOSFET is turned off (During $(1-d)T$):

  When the controlled switch M is off, the energy stored in the inductor is transferred through the forward-biased diode to the output capacitance C_S and the load. The current in the inductor and the voltages across the capacitors are written as follows:

$$i_{Ce}(t) = C_e \frac{d\, v_{pv}(t)}{dt} = i_{pv}(t) - i_L(t) \tag{IV.27}$$

$$i_{Cs}(t) = C_s \frac{d\, v_S(t)}{dt} = i_L(t) - i_S(t) \tag{IV.28}$$

$$v_L(t) = L \frac{d\, i_L(t)}{dt} = v_{pv}(t) - v_S(t) \tag{IV.29}$$

- The converter state matrix is written as:

$$\frac{d}{dt} \begin{bmatrix} I_L \\ V_{C_s} \end{bmatrix} = \begin{bmatrix} 0 & \frac{-(1-d)}{L} \\ \frac{1-d}{C_S} & \frac{-1}{R_S\, C_S} \end{bmatrix} \begin{bmatrix} I_L \\ V_{C_s} \end{bmatrix}$$

- The inductance is expressed as a function of the desired ripple amplitude ΔI_L as follows:

$$L = \frac{d\, V_{pv}}{f\, \Delta I_L} \tag{IV.30}$$

- The output capacitance is expressed as a function of the desired ripple amplitude ΔV_S as follows:

$$C_s = \frac{d\, I_S}{f\, \Delta V_S} \tag{IV.31}$$

- The input capacitance is expressed as a function of the desired ripple amplitude ΔV_{pv} as follows:

$$C_e = \frac{d\, V_{pv}}{8\, L\, \Delta V_{pv}\, f^2} \tag{IV.32}$$

© Ferdaous Masmoudi, 2016 _ All rights reserved

- For optimal converter sizing, the ratio d is selected equal to d_m. The appropriate inductance and capacitance values are therefore evaluated using the following relations:

$$L_m = \frac{d_m\, V_m}{f\, \Delta I_L} \tag{IV.33}$$

$$C_{s_m} = \frac{d_m\, I_{S_m}}{f\, \Delta V_{S_m}} \tag{IV.34}$$

$$C_{e_m} = \frac{d_m\, V_m}{8\, L\, \Delta V_m\, f^2} \tag{IV.35}$$

The numerical calculations of the Boost-converter parameters, as well as those of the other considered topologies, are presented in Table IV.8.

IV.5 .2 .1 Simulation of the PV Conversion Chain Using Ideal Components

The work carried out in this section consists of implementing the boost-converter model in MATLAB and associating it with the other blocks of the previously developed PV chain (PV and battery). An ideal power transfer $P_S = P_{pv}$ is considered (where P_S is the output power, $P_S = V_S\, I_S$, and P_{pv} is the input power, $P_{pv} = V_{pv}\, I_{pv}$). The various power losses that actually exist (parasitic elements, conduction losses, wiring losses, etc.) are therefore neglected.

The simulation model of the PV chain in the MATLAB–Simulink environment is presented in Figure IV.15.

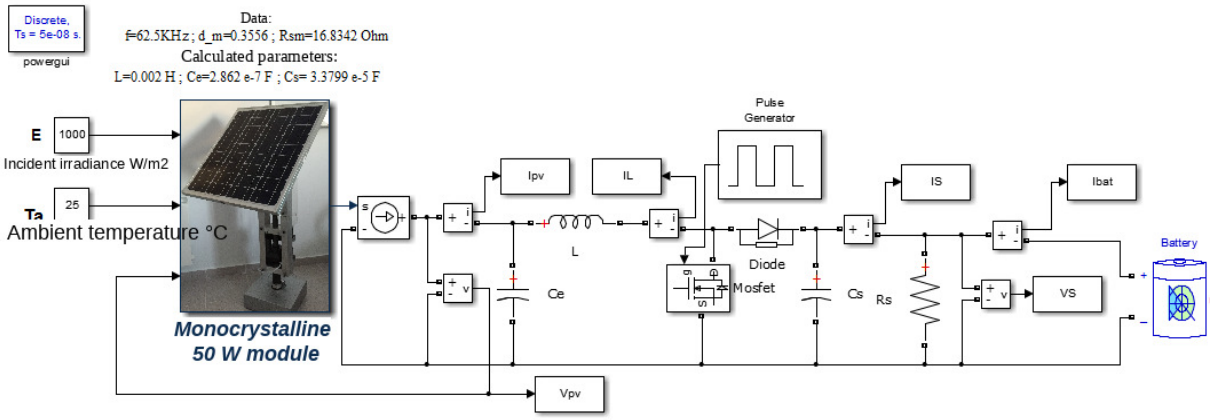


Figure IV.15: Simulation model of the PV chain using ideal components.

The simulation work focuses on analyzing the time variation of the input and output electrical quantities of the conversion chain while maintaining the PV-module irradiance and temperature at $1000 W/m^2$ and $25°C$ and applying a fixed duty cycle $d_m = 35.56\%$ at a frequency of 62.5 kHz. First, an optimal resistive load R_{S_m} equal to 16.8342Ω is considered. Next, a half-charged storage battery (SOC=50%) is integrated, and finally a fully charged battery (SOC=100%) is considered.

The purpose of this section is to ensure that the component-sizing work carried out leads to the desired output-quantity values and to the desired ripple amplitudes of the different quantities.

© Ferdaous 2016 – All rights reserved

The simulation results are presented in Figure IV.16, and analysis of the different quantities leads to the following observations:

- For a resistive load R_S equal to the optimal value R_{S_m} and supplied individually by the PV conversion chain, the input quantities settle around the MPP after a certain transient period, where V_{pv} is nearly equal to V_m, I_{pv} is nearly equal to I_m, and the power P_{pv} is effectively the maximum power P_m of the PV module. This result shows that the circuit sized around the MPP leads exactly to the desired values. The current in the inductor oscillates linearly within the desired range ΔI_L; likewise, the output voltage V_S oscillates within the desired range ΔV_S and reaches the expected value of 30 V. The output current I_S is nearly equal to I_{S_m}, and the output power P_S is nearly equal to the input power P_e. It is obvious that the current in the battery is zero (battery disconnected). The PV-module voltage oscillates strongly during the transient regime and reaches negative values. This effect can be limited by integrating a bypass diode across the PV module.

- If the half-charged battery (50%) is connected, a complete change in all quantities is observed. This is because the battery is considered by the system as an additional load, and the overall output load (the parallel connection of R_{S_m} and the battery) is no longer the optimal load R_{S_m}. Consequently, the input quantities V_{pv} and I_{pv} no longer converge toward V_m and I_m, and the power delivered by the PV module P_{pv} is no longer the maximum value P_m. The current in the inductor decreases, although the ripple remains acceptable. Regarding the output quantities, the output voltage is fixed by the battery, whereas the output current and power show strong ripple and become zero for a short portion of the period T. However, their average values seen by the load are acceptable, and the average output power is identical to the input power. The battery current I_{bat} is negative during the transient regime, which shows that the battery is discharging into the load R_S when the voltage V_S is lower than the battery voltage V_{bat}.

- If a fully charged battery (100%) is connected, results similar to the previous case are obtained, except that the voltages are slightly higher because the battery voltage level is at its maximum. The strong ripple in the current I_{bat} is not recommended by the battery manufacturer because it causes premature aging of the storage element. To overcome this problem, an additional output filter can be designed to limit output-current ripple.

© Ferdaous Masmoudi, 2016 _ All rights reserved

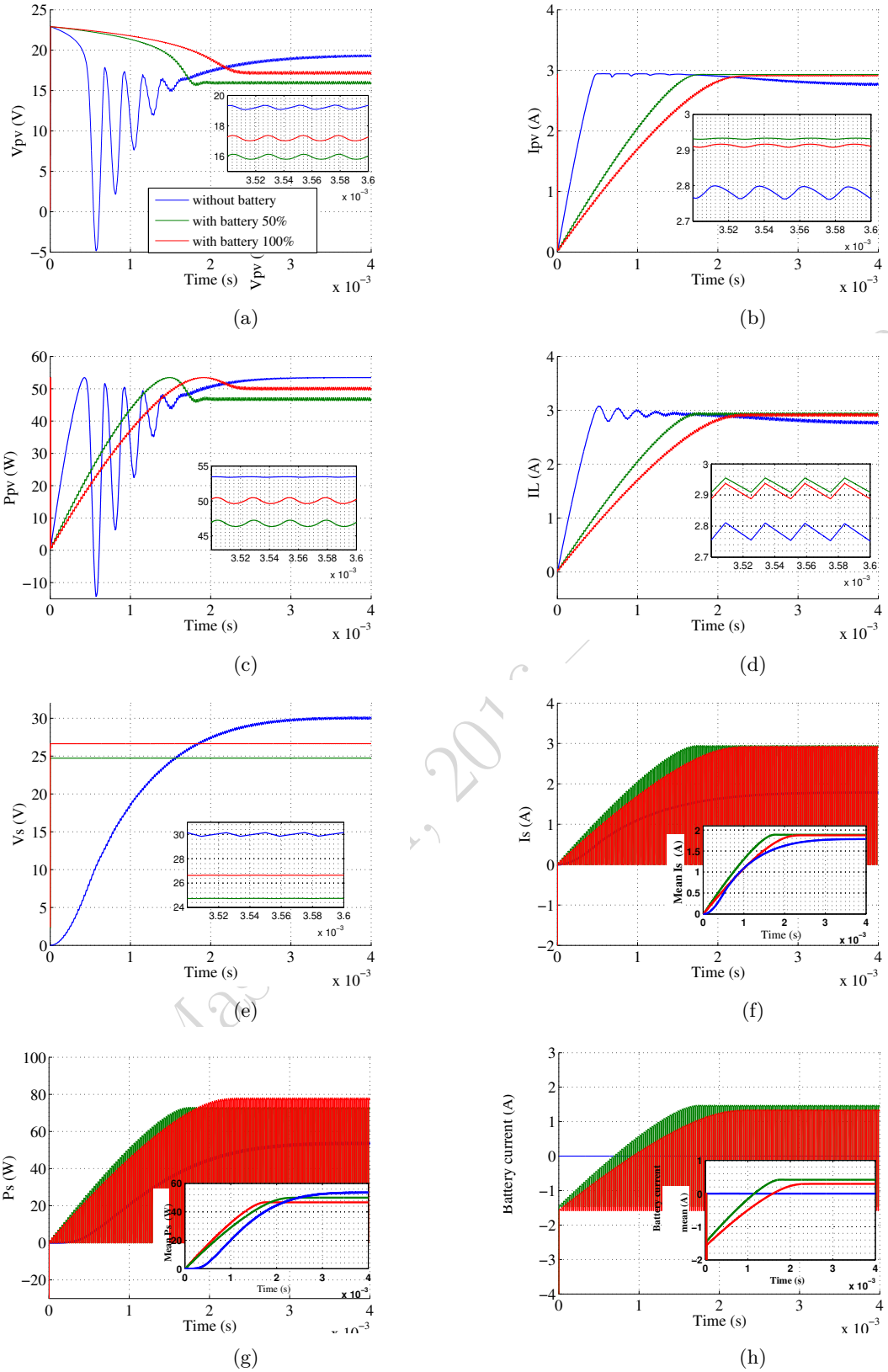


Figure IV.16: Simulation results of the boost converter using ideal components. (a) PV-module voltage V_{pv}. (b) PV-module current I_{pv}. (c) PV-module power P_{pv}. (d) Inductor current I_L. (e) Output voltage V_S. (f) Output current I_S. (g) Output power P_S. (h) Battery current I_{bat}.

© Fe... ...served

IV.5 .2 .2 Simulation of the PV Conversion Chain Taking Converter Losses into Account

The simulation model presented in Figure IV.17 consists of modeling the PV conversion chain while taking into account the parasitic effects in the various components, the conduction losses introduced by the power components, and wiring losses. In this section, an output filter was designed, a bypass diode was added at the input of the PV module, and a blocking diode was added at the converter output.

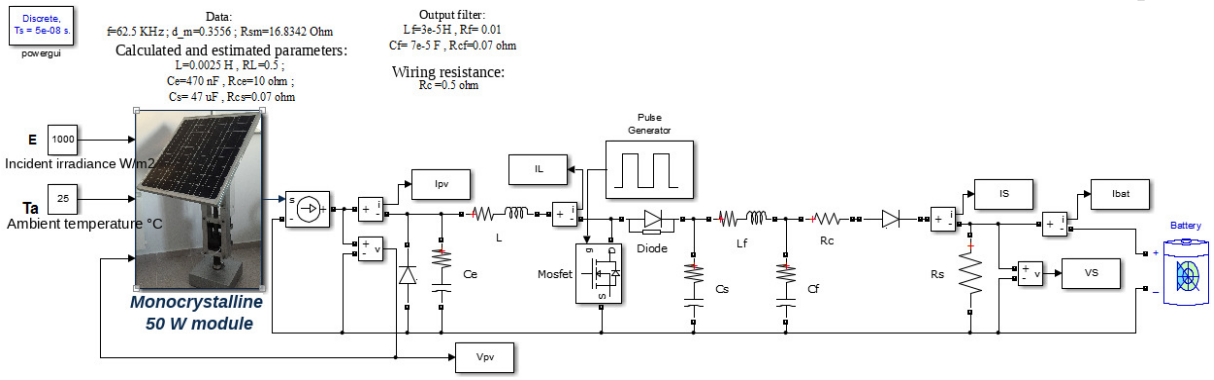


Figure IV.17: Simulation model of the PV chain taking power losses into account.

The purpose of this part of the work is to ensure correct converter operation and to examine variations in its electrical quantities while taking into account the various power losses that actually exist. Under real operating conditions, it is necessary to provide a tolerance margin when sizing passive components in order to reduce stress, avoid saturation, and guarantee smooth circuit operation. Accordingly, the passive components of the entire chain are oversized by 30%.

The same operating conditions for irradiance, temperature, and duty cycle are maintained. The simulation results are presented in Figure IV.18, and analysis of the different quantities leads to the following observations:

- For a resistive load R_{S_m} supplied individually by the PV chain, accounting for converter losses causes a decrease in the power P_{pv} generated by the PV module. This is because the parasitic resistances are considered as additional loads to the load R_S, and the duty cycle d_m is no longer appropriate for the resulting load.

- The output quantities are reduced compared with the previous results. This is particularly visible in the output power, which is significantly lower than the input power because of the system losses.

- Connecting the battery makes it possible to impose and fix the output voltage V_s. The output current I_s is properly smoothed by the designed output filter. The output power is considerably lower than the input power, which reflects the actual efficiency of the conversion stage.

© Ferdaous Mamoudi, 2016

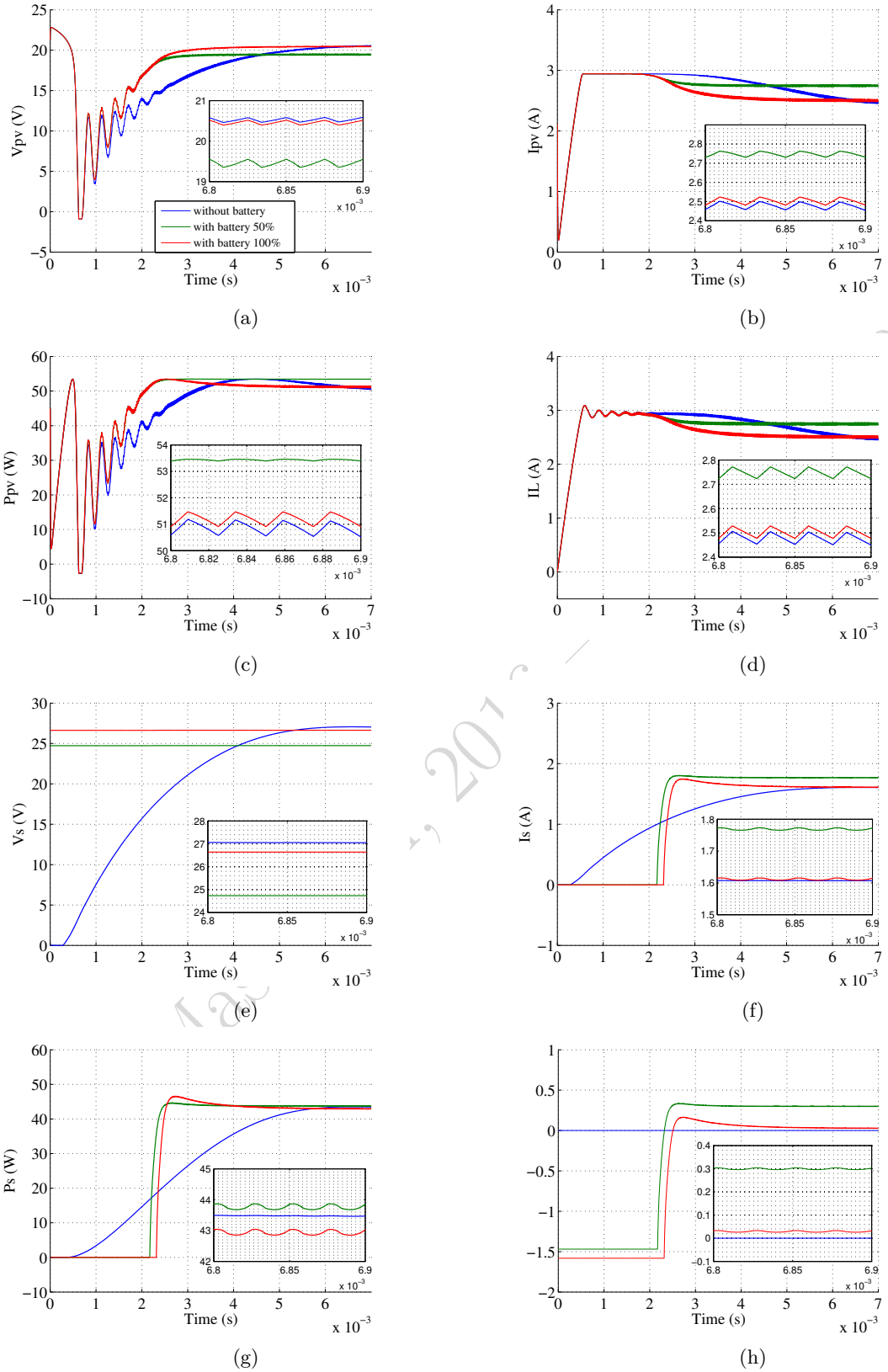


Figure IV.18: Simulation results of the boost converter taking power losses into account. (a) PV-module voltage V_{pv}. (b) PV-module current I_{pv}. (c) PV-module power P_{pv}. (d) Inductor current I_L. (e) Output voltage V_S. (f) Output current I_S. (g) Output power P_S. (h) Battery current I_{bat}.

© Fe ... ; 20 ... served

- The delay that appears in the output-current curve is due to the blocking diode. Indeed, the blocking diode plays a fundamental role in preventing current from flowing back from the battery into the converter during the transient regime. When V_S becomes greater than V_{bat}, the battery becomes a load and absorbs the residual current.

- It can be observed that the converter modeled while taking parasitic elements into account does not allow extraction of the maximum power P_m from the module because the fixed duty cycle d_m is not adapted to the actual system load. At this stage, it can be concluded that integrating an MPPT control strategy is essential for optimizing the power generated by the PV solar module.

IV.6 Design and Modeling of the MPPT Control

This section is devoted to the analysis and synthesis of the MPPT control strategy integrated into the photovoltaic conversion chain presented in Figure IV.2, which controls the duty cycle d of the Boost converter [83].

IV.7 Principle of the MPPT Control Strategy

To extract the maximum power from the PV module, control of the boost converter requires varying the duty cycle d to shift the system operating point toward the MPP. Such control is based on measuring the voltage V_{pv} and current I_{pv} at instants t and $t+\delta t$. Thus, the variations in voltage V_{pv} and power P_{pv} between these two instants make it possible to decide the direction of change of the voltage V_{pv} at instant $t+\delta t$, by decreasing, maintaining, or increasing the duty cycle d.

Thus, to regulate the converter input voltage, the power switch (MOSFET) must be properly controlled in order to ensure adequate adjustment of the duty cycle d of the converter control signal. The idea consists of comparing the voltage and power values generated by the PV module with those measured during the previous cycle. This comparison makes it possible to decide whether the power switch M should be turned on or off according to the observed differences ΔV and ΔP.

Referring to Figure IV.19, four critical situations can be distinguished, namely:

- Situations (a) and (c), where $\frac{\Delta P}{\Delta V} > 0$: in order to reach the point with coordinates (V_m, P_m), the voltage V_{pv} across the PV module must be increased.

- Situations (b) and (d), where $\frac{\Delta P}{\Delta V} < 0$: in order to move toward the point with coordinates (V_m, P_m), the voltage V_{pv} delivered by the PV module must be decreased.

The variation (increase or decrease) of the voltage V_{pv} is based on modifying (increasing or decreasing) the duty cycle d.

To achieve the appropriate variation of the voltage V_{pv}, it is necessary to determine the relationship between the variation of the duty cycle d and that of the voltage V_{pv}. For this

© Ferdaous Masmoudi, 2016 – All rights reserved

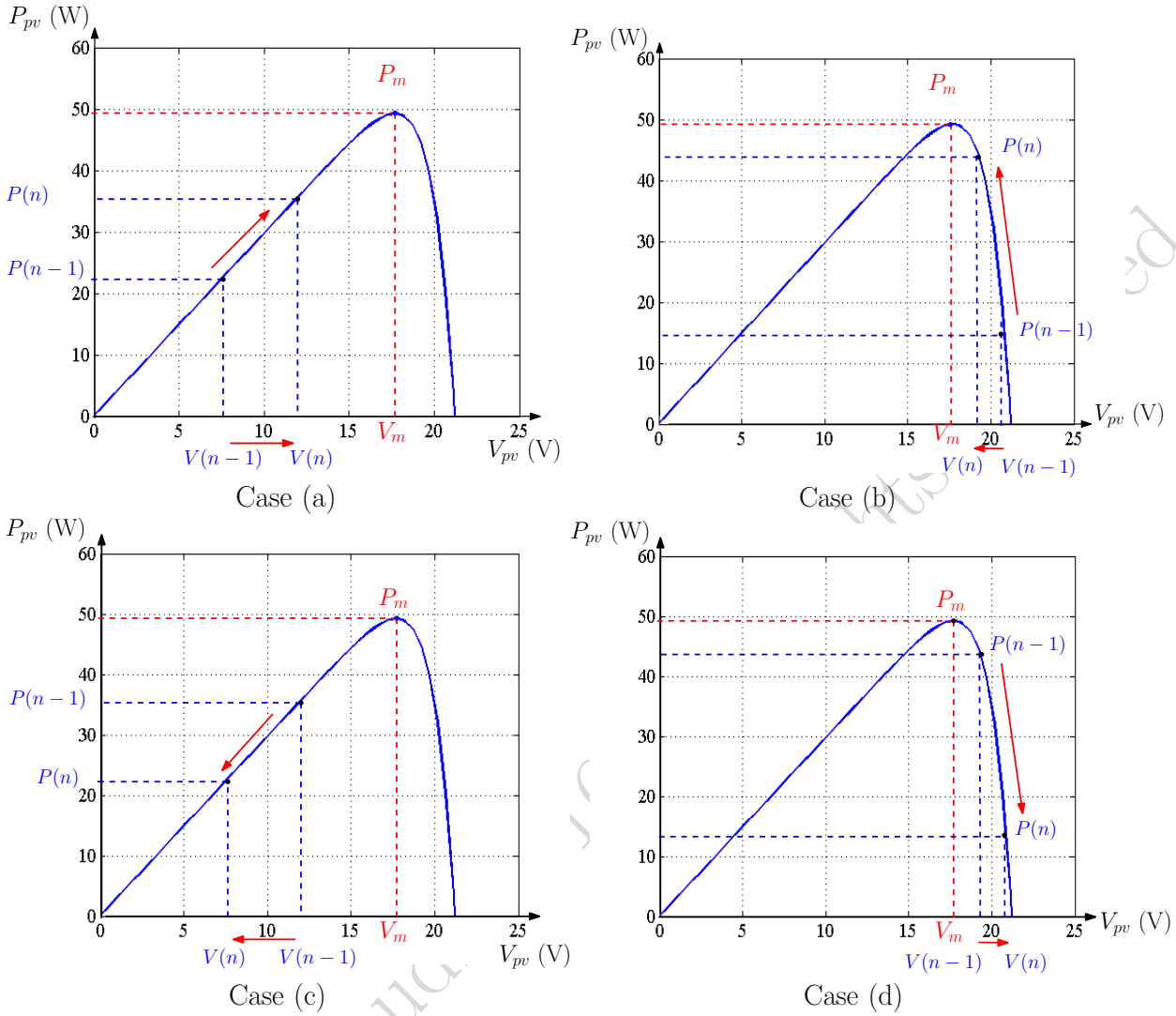


Figure IV.19: Different situations considered by the MPPT strategy.

purpose, the variation of the voltage V_S across the battery during one modulation period T is neglected.

$$V_{pv} = (1 - d)\, V_S \tag{IV.36}$$

$$\frac{dV_{pv}}{dd} = -V_S \tag{IV.37}$$

For all converters, the variation of voltage V_{pv} as a function of duty cycle d is a decreasing function. Thus, increasing V_{pv} requires decreasing the duty cycle d, whereas decreasing V_{pv} is achieved by increasing the duty cycle d.

IV.7 .1 P&O-Type MPPT Control

The Perturb and Observe (P&O) control strategy [110, 111, 112, 113] is the most widely used strategy in photovoltaic conversion applications because of its simplicity in practical implementation. The principle of such a control strategy is based on perturbing the system by increasing

© Ferdaous Masmoudi

or decreasing the duty cycle d, then generating a control signal based on Pulse Width Modulation PWM to drive the power switch M within the converter. The decision to increase or decrease the duty cycle d is based on the four situations (a), (b), (c), and (d) explained previously. To increase the voltage V_{pv}, the duty cycle d must be decreased by a value δd, and to decrease the voltage V_{pv}, it is sufficient to increase the duty cycle d by the same value δd. Let $d(t)$ and $d(t-1)$ be the values of the duty cycle d at instants t and $t\delta t$, respectively, where δt is the measurement period of the voltage V_{pv} and the current I_{pv} at the output of the PV module. The duty-cycle signal d is given by the following relation:

$$d(t) = d(t-1) + q\ \delta_d \tag{IV.38}$$

where q is defined by:

- $q = -1$ for situations (a) and (c), corresponding to an increase in the voltage V_{pv},
- $q = +1$ for situations (b) and (d), corresponding to a decrease in the voltage V_{pv}.

Comparing the duty-cycle signal d with a sawtooth signal of frequency f makes it possible to generate the PWM control signal capable of regulating the voltage V_{pv}.

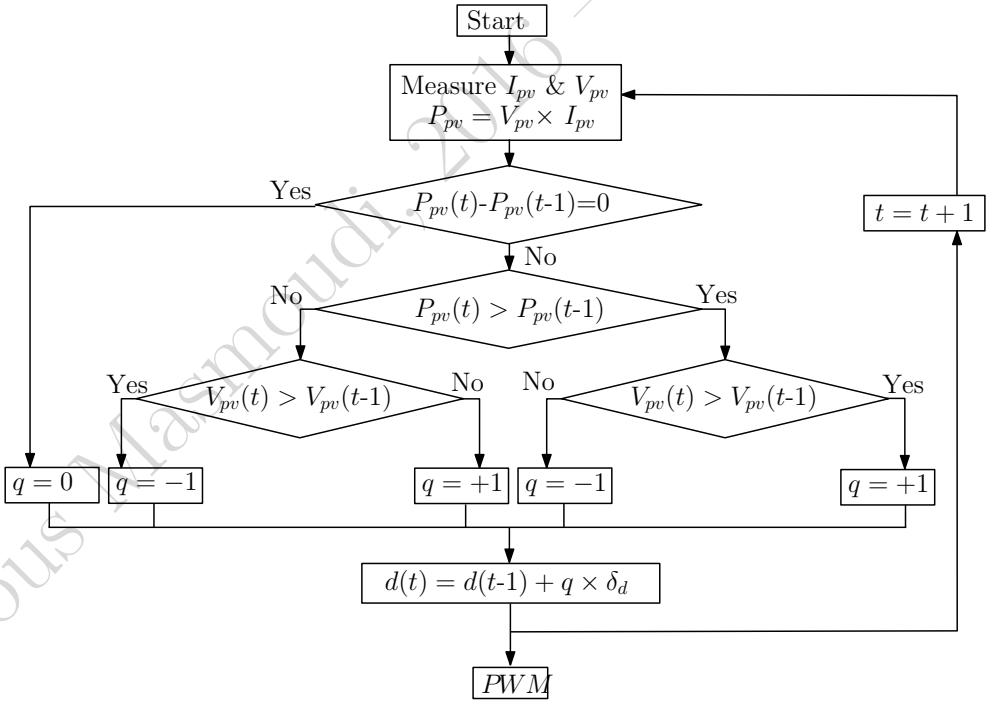


Figure IV.20: Algorithm of the P&O-type MPPT control strategy.

Figure IV.20 illustrates the algorithm of the P&O control strategy for the photovoltaic system. Once the point corresponding to maximum power is reached, the voltage V_{pv} oscillates around this point through action on the duty cycle d. If the perturbation value δd is large, the algorithm responds rapidly to abrupt changes in operating conditions. However, power losses and oscillations around the point corresponding to maximum power become significant.

© Ferdaous Hamoudi, 2016 – All rights reserved

Conversely, if δd is small, the losses are reduced in steady state, but the dynamic response of the system becomes very slow.

The simulation model of the MPPT control strategy implemented in the MATLAB–Simulink environment is presented in Figure IV.21.

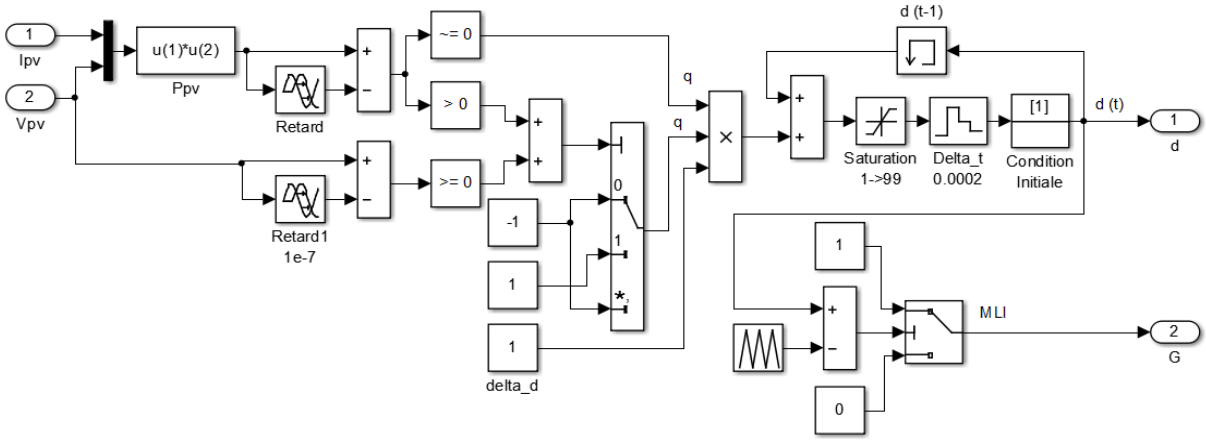


Figure IV.21: Implementation of the MPPT model in the MATLAB–Simulink environment.

IV.7 .2 Simulation of the PV Conversion Chain Controlled by the P&O-Type MPPT Strategy

The PV chain considered in the simulation work is the same as the one considered in the previous section (Figure IV.17), with the previously designed MPPT strategy integrated. Analysis of the simulation results is organized into three parts.

IV.7 .2 .1 Effect of Load Variation

The objective of this section is to discuss the effect of the output load on the electrical quantities of the PV conversion chain.

The study consists of increasing the output load at instant $t = 0.025$ s and observing the behavior of the system under this change. Stable climatic conditions $G = 1000W/m^2$ and $T_a = 25°C$ are maintained.

The simulation results are presented in Figure IV.22, and analysis of the different quantities leads to the following interpretations:

- The electrical quantities of the PV chain exhibit a relatively slow transient regime because of the filters considered in the circuit. Nevertheless, the delay observed particularly in the input-voltage and input-power curves V_{pv} and P_{pv}, extending from 0.001 s to 0.01 s, is caused by the slow dynamics of the MPPT algorithm. Indeed, Figure IV.22.a shows the variation of the duty cycle d, which increases progressively with a small variation δd. The MPPT algorithm carefully acts on d by searching for the appropriate value for tracking the MPP. At instant 0.01 s, the MPPT algorithm converges toward an oscillatory duty-cycle value around 49%.

© Ferdaous Maamoudi, 2016 – All rights reserved

- Because of the blocking diode, the output quantities I_S and P_S appear only from instant 0.007 s. It is at this instant that the converter begins to supply the output load R_S.
- Between instants 0.01 s and 0.025 s, the load R_S is kept fixed. It can be observed that the duty cycle imposed by the MPP algorithm oscillates regularly around a well-defined value. At instant 0.025 s, an auxiliary load is imposed on the circuit. First, disturbances are observed in the input and output electrical quantities, particularly the current and power peaks (I_S and P_S). After a considerable transient time (0.003 s), the MPPT algorithm succeeds in finding the new value of the duty cycle d corresponding to the MPP. The duty cycle settles around 32%, and the power generated by the PV module is optimal and equal to P_m.

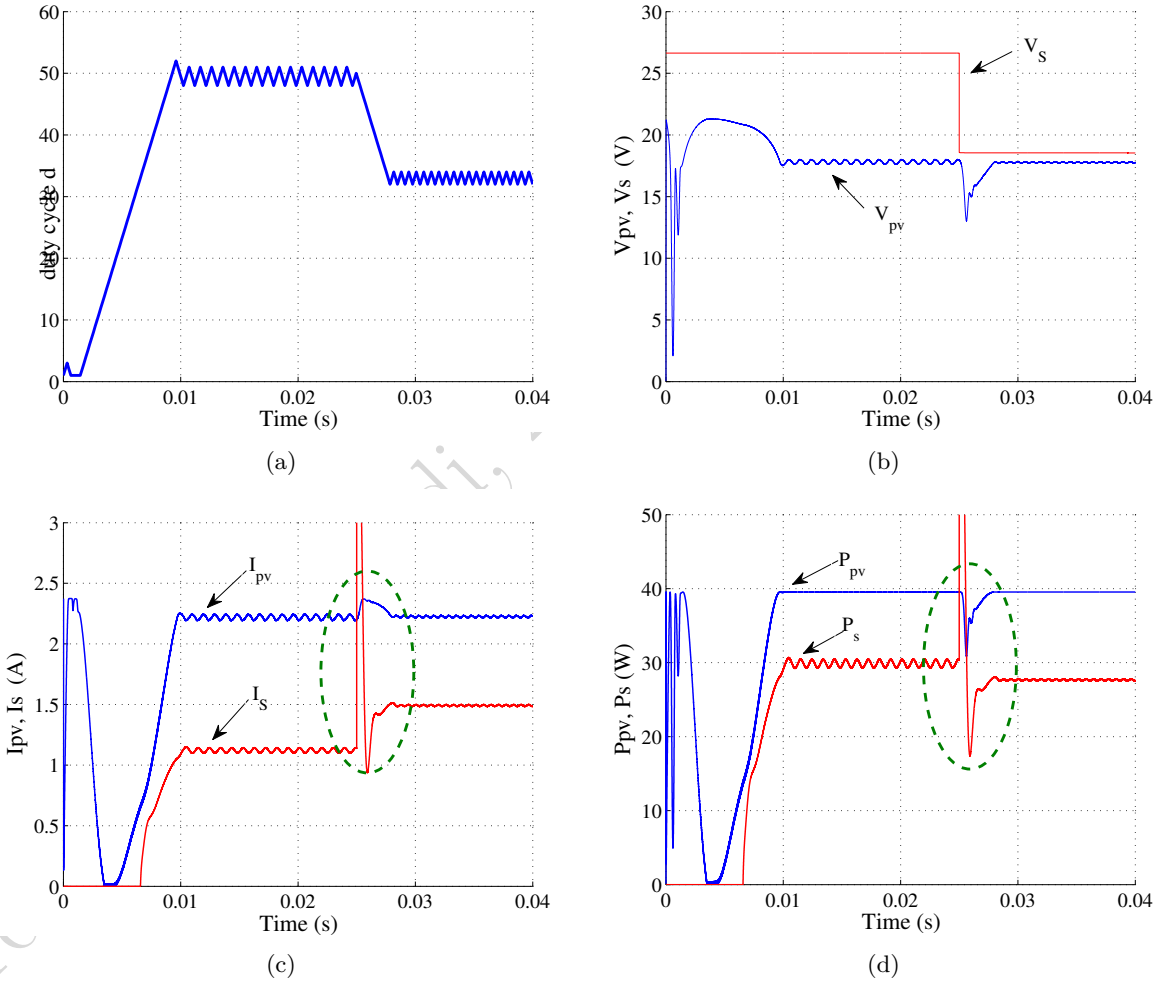


Figure IV.22: Effect of load variation on the electrical quantities of the PV conversion chain. (a) Duty cycle. (b) Input voltage V_{pv} and output voltage V_S. (c) Input current I_{pv} and output current I_S. (d) Input power P_{pv} and output power P_S.

IV.7 .2 .2 Effect of Irradiance Variation

In this section, the effect of variation in the irradiance profile G on the electrical quantities of the PV conversion chain is analyzed.

© Fer... reserved

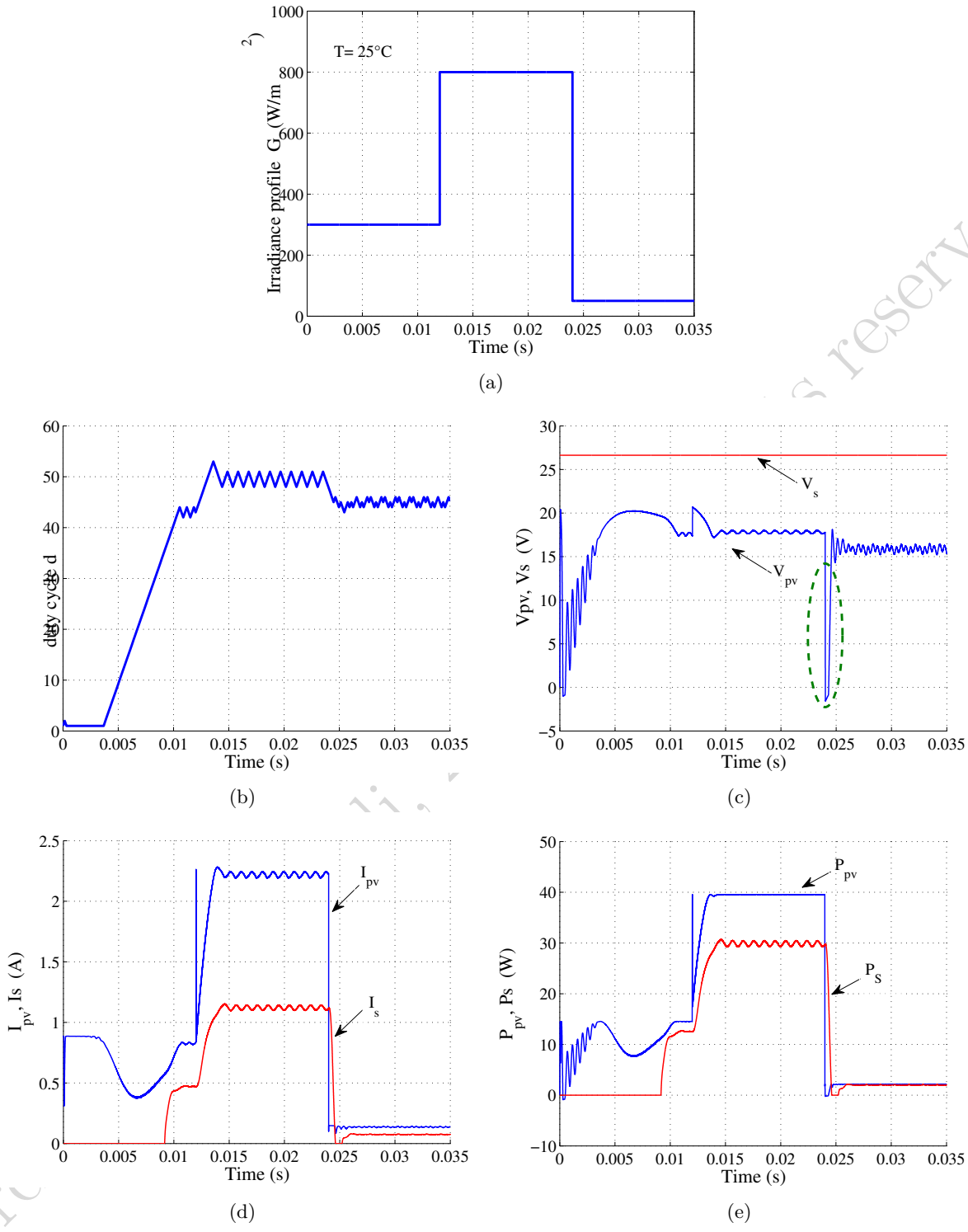


Figure IV.23: Effect of irradiance variation on the electrical quantities of the PV conversion chain. (a) Irradiance profile. (b) Duty cycle. (c) Input voltage V_{pv} and output voltage V_S. (d) Input current I_{pv} and output current I_S. (e) Input power P_{pv} and output power P_S.

The study consists of varying the irradiance value at instants $t = 0.012$ s and $t = 0.024$ s and observing the system behavior under this change. A constant load and an ambient temperature $T_a = 25°C$ are maintained.

© Fer... reserved

The simulation results are presented in Figure IV.23, and analysis of the different quantities leads to the following interpretations:

- Initial system start-up passes through a relatively slow transient regime. However, in steady state the system acquires faster dynamics and begins to follow the imposed variations more smoothly.

- The abrupt increase in irradiance at instant 0.012 s, from $300W/m^2$ to $800W/m^2$, causes a significant overshoot visible in the input-current curve I_{pv} and a less intense overshoot in the voltage curve V_{pv}, which may constitute a disturbing element for PV-module operation. Nevertheless, this change does not affect the output quantities.

- The abrupt decrease in irradiance at instant 0.025 s, from $800W/m^2$ to $50W/m^2$, causes a severe overshoot in the input voltage V_{pv} and a less intense one in the current I_{pv}. Consequently, the input power P_{pv} and output power P_S become zero for a few seconds. The steady state is established after a few instants, and the MPPT succeeds in tracking the maximum power point MPP by searching for the appropriate duty cycle.

IV.7 .2 .3 Effect of Temperature Variation

For this section, a variation in the temperature profile T_a is considered, and the effect of this variation on the electrical quantities of the PV conversion chain is discussed.

The study consists of varying the temperature profile at instants $t = 0.012$ s and $t = 0.024$ s and observing the system behavior under this change. A constant load and irradiance $G = 800W/m^2$ are maintained.

The simulation results are presented in Figure IV.24, and analysis of the different quantities leads to the following observations:

- In general, the influence of temperature variation on the electrical quantities is always less significant than the effects of irradiance and load variation.

- The effect of temperature variation is opposite to the effect of irradiance variation. Indeed, increasing the temperature causes a degradation in power, whereas decreasing the temperature causes an increase in power.

- Abrupt variations in temperature, with an increase at instant 0.012 s and a decrease at instant 0.024 s, disturb the electrical quantities of the system. However, this disturbance is not severe compared with those caused by irradiance or load variation.

- For this type of variation, as well as for the other types, the MPPT algorithm succeeds in adapting to the different changes and finding the appropriate duty cycle d to force the PV module to generate the maximum available power.

© Ferdaous Masmoudi, 2016 _ All rights reserved

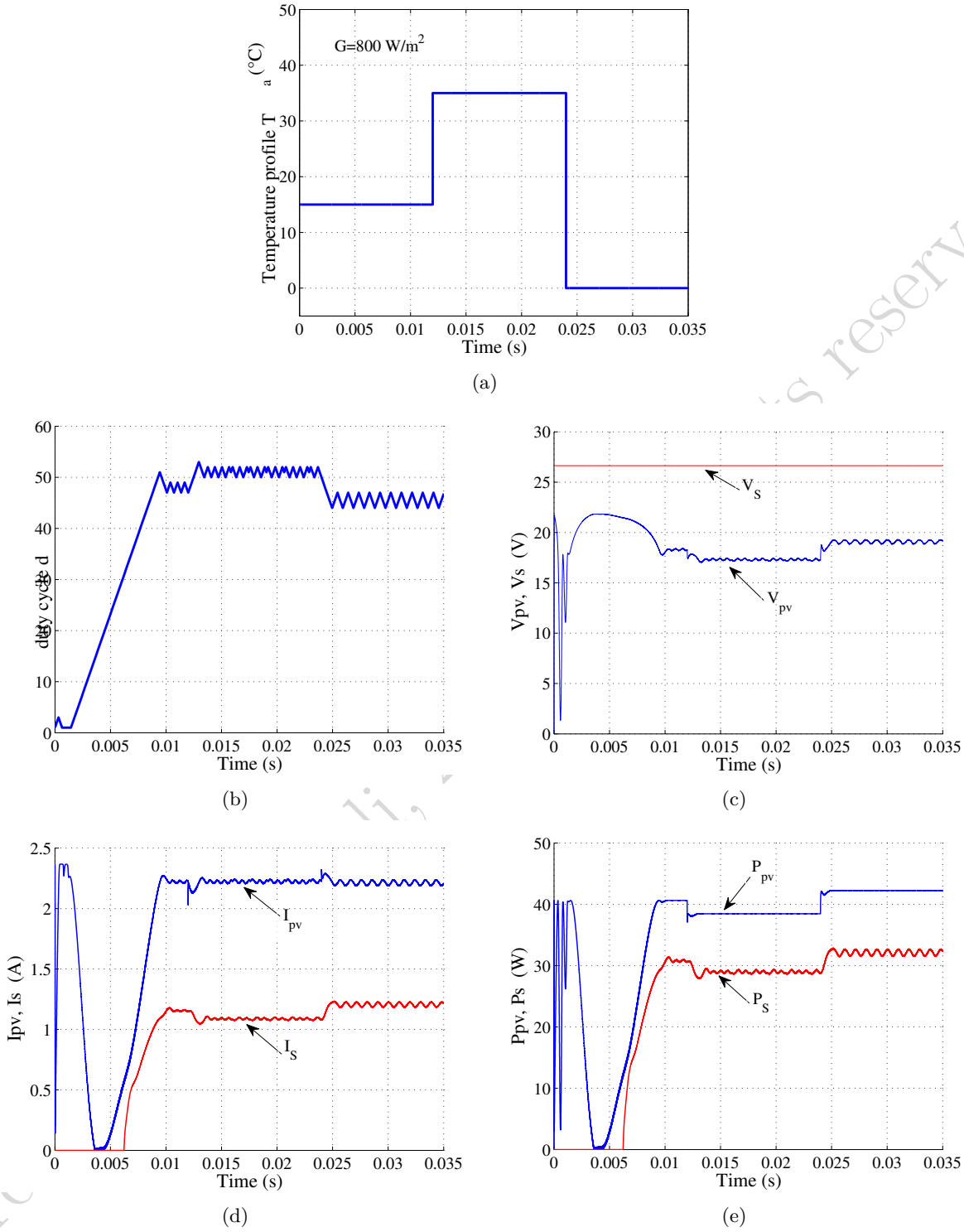


Figure IV.24: Effect of temperature variation on the electrical quantities of the PV conversion chain. (a) Temperature profile. (b) Duty cycle. (c) Input voltage V_{pv} and output voltage V_S. (d) Input current I_{pv} and output current I_S. (e) Input power P_{pv} and output power P_S.

© Fer ... s reserved

IV.8 Conclusion

This chapter was devoted to the optimal design of a PV conversion chain consisting of the association of a PV solar module, a converter- type conversion stage, an output load, and a storage battery, with the integration of an MPPT control strategy. Emphasis was placed on linearization around the maximum power point (MPP), allowing the various components of the power-electronic circuit to be optimally sized. A method for identifying the parameters of the lead-acid battery model from experimental measurements was also presented. Modeling the DC–DC conversion stage enabled a comparison of the different fundamental topologies in terms of efficiency and led to the proposal of the boost architecture as an optimal choice for maximizing system efficiency. In this work, the various power losses that actually occur in conversion circuits and their effects on the degradation of the overall efficiency of the PV chain were discussed. In the final part of this chapter, integration of the P&O-type MPPT control strategy was considered in order to improve the efficiency of the PV module and the conversion system in general. This design, sizing, and simulation work made it possible to optimize the choice of electronic components during the experimental implementation of the power board and led to a better understanding of the electrical behavior resulting from the association of the various electrical devices with nonlinear characteristics (PV module–boost converter–batteries).

© Ferdaous Masmoudi, 2016 _All rights reserved

Chapter V

Experimental Work and Results

Abstract : *This fifth and final chapter of the thesis work focuses on the practical implementation and experimental realization of the theoretical studies carried out in the previous chapters. It presents the first version of the prototype of the PV power-supply system developed for embedded applications, while reporting some experimental measurements obtained from the real tests performed up to this stage.*

Keywords: PV power-supply system prototype,
Dual-axis solar tracker prototype,
Charge-controller prototype,

© Ferdaous Masmoudi, 2016 – All rights reserved

V.1 Introduction

The previous chapters of this thesis discussed, through theoretical studies and simulation work, methods for optimizing the power generated by the photovoltaic solar module. The design of a dual-axis solar-tracking system was presented, and the sizing and design of a charge controller with an appropriate MPPT strategy for controlling the Boost converter were developed.

The knowledge acquired through these studies is essential for mastering the subject, on the one hand, and, on the other hand, provides the knowledge required for the initial design of the desired system. However, simulation work without experimental validation has little significance and limited scientific value.

Therefore, contributing to the construction of the real mechanical and physical system not only consolidates the learning process, but also highlights the advantages of the engineering process in transforming an idea into a tangible product.

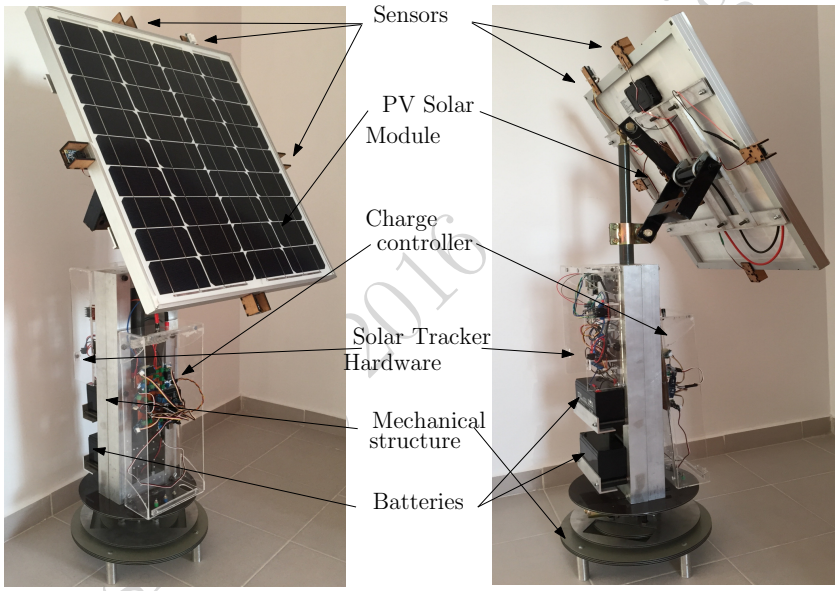


Figure V.1: Prototype of the PV solar-energy power-supply system dedicated to embedded applications.

In this chapter, the outcome of the thesis work is presented. The hardware implementation of the entire photovoltaic solar-energy power-supply system dedicated to embedded applications is therefore addressed. Figure V.1 shows the first version of the manufactured system. The mechanical structure of the solar tracker equipped with its control system can be distinguished. The PV solar module is electrically connected to the charge controller. The entire system is connected to the storage elements formed by two 12 V lead-acid batteries.

This chapter consists of two distinct parts: the first part presents the solar-tracker prototype, followed by the data-acquisition and conditioning method. An excerpt from the first experimental measurements of the solar-trajectory tracking system programmed in open loop is then presented. The second part addresses the design and implementation of the charge controller, namely the power board containing the Boost converter.

© Ferdaous Mas... 2016 ... rights reserved

V.2 Dual-axis solar-tracking system

This section presents the developed solar-tracker prototype. Figure hardwaresystem shows the PV solar module installed on the frame of the mechanical system and equipped with the required sensors. Regarding the hardware part of the system, the electronic layer for data acquisition and transfer mainly uses the Arduino Nano board. This board periodically reads the states of the sensors connected to the analog and digital ports. The Atmega 328 processor converts the analog and digital signals received from the sensors into human-readable values. This electronic layer also transfers the acquired values to the control layer established on the Raspberry Pi SoC board through the I2C protocol. The Raspberry-Pi system-on-chip acts as an interface between the hardware and software parts. This board embeds the ARM11 processor and has the characteristics of a microcomputer equipped with network interfaces such as Wi-Fi and GPIO ports for communication with the electronic layer.

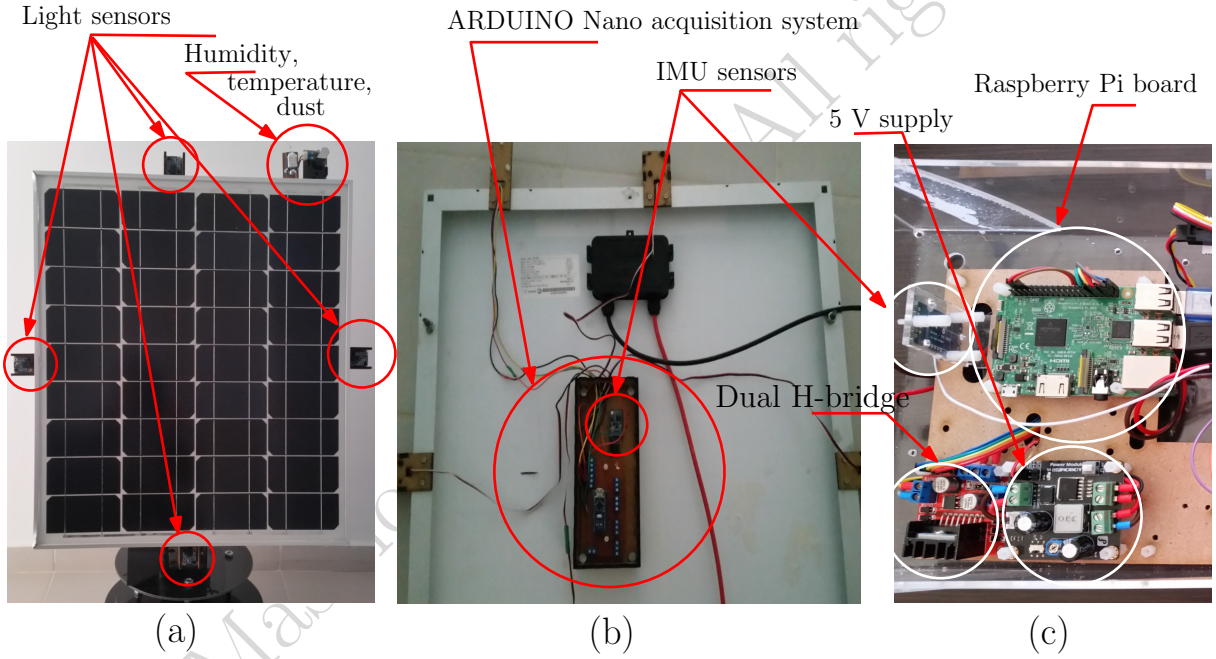


Figure V.2: Hardware part of the solar tracker.

V.2 .1 Real-time data acquisition and conditioning

To automate data conditioning and transfer, the system uses the Wi-Fi interface to upload the acquired data through a Web Service. The latter is handled by a remote Web server that enables data recording and display. At this level, the data are hosted in the cloud for post-processing. This Web service[1] also makes it possible to control the system status remotely. The data-acquisition and processing process is described in Figure V.3. Figure V.4 illustrates the graphical interface of the remote Web server. It enables real-time data display for monitoring and the export of raw data for subsequent post-processing. This cloud-computing technique

[1]Domain name: “www.pvsystem-cellab.com”. Username: “ferdaous”. Password: “ferdaous2016”.

© Ferdaous Ma... All rights reserved

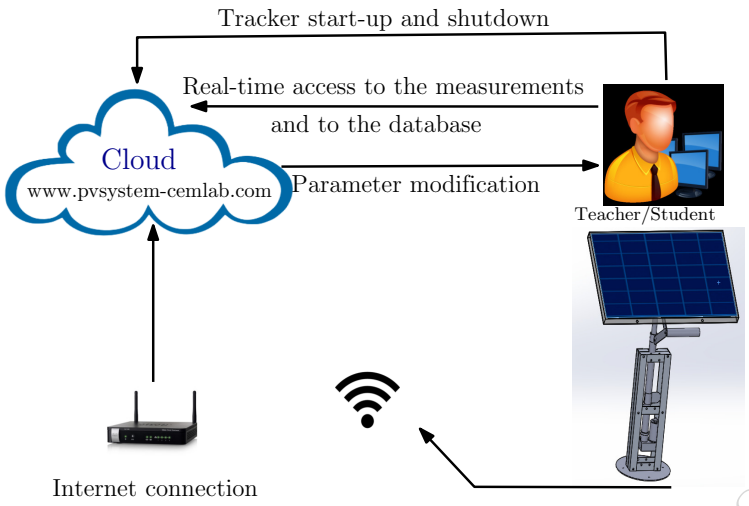


Figure V.3: Data-acquisition process.

("*Cloud Computing*") can be extended to smartphone platforms, ensuring a higher level of data accessibility and control of the designed system.

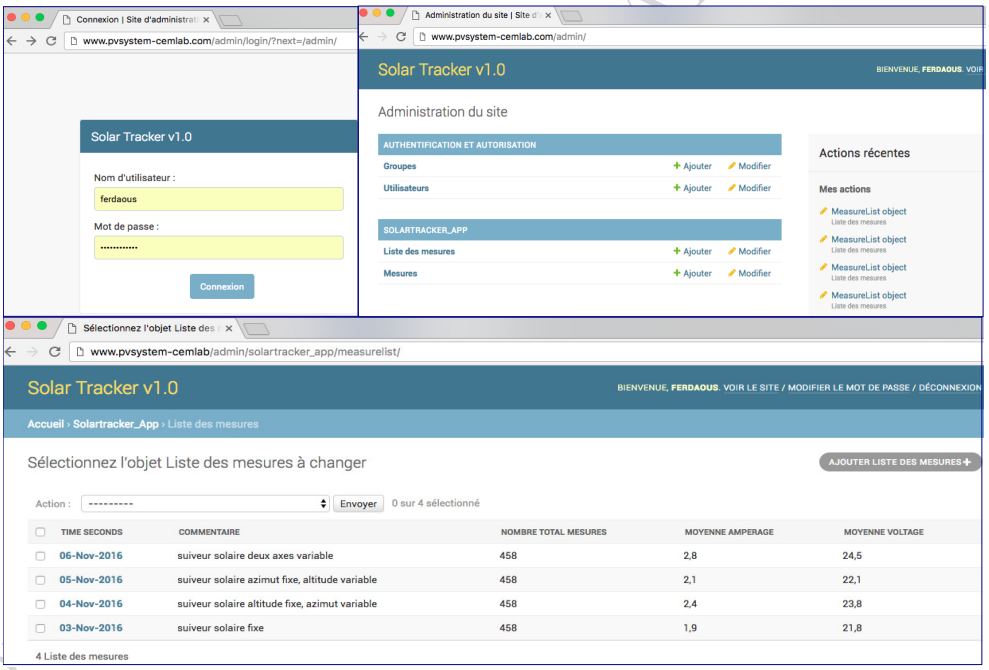


Figure V.4: Graphical interface of the Web Service.

V.2 .2 System installation and experimental results

The previously described system was installed outside the CEM Lab building for one week. The collected results were exported from the remote server described above and plotted, as shown by the curves in Figure V.5. Analysis of these results confirms the simulation results obtained and documented in Chapter III.4.

© Ferdaous All rights reserved

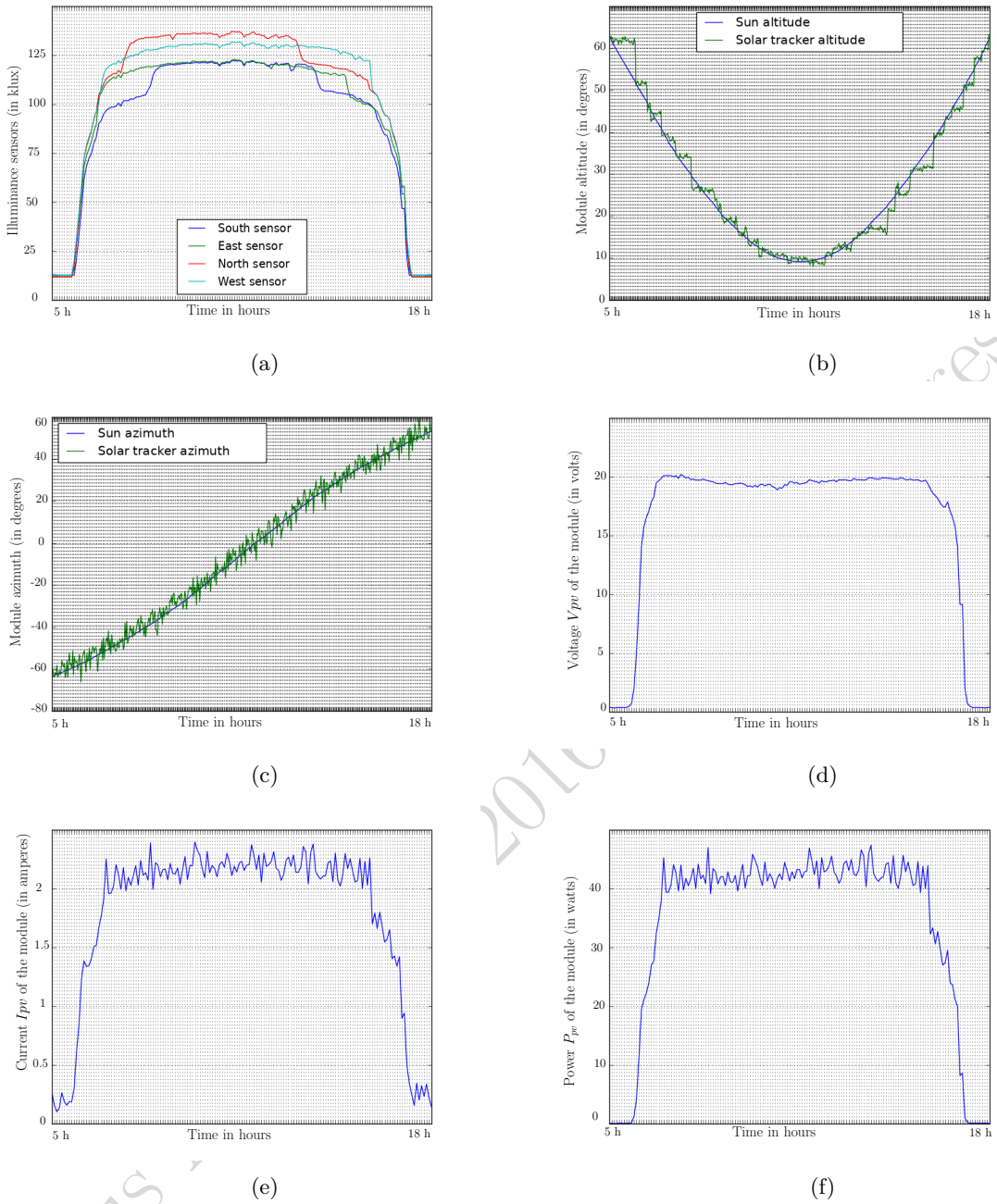


Figure V.5: Experimental results of the solar tracker on November 6, 2016.

V.3 Charge-control system

The charge-controller prototype presented in this section enables the transfer of the energy produced by the PV module to the storage batteries. The system consists of two parts. The power circuit mainly contains the Boost converter sized and designed in Chapter IV. The control circuit is provided by an ARDUINO Mega 2560 board, which acquires data from the current and voltage sensors and then executes the state-machine program of the charge-control system represented by the flowchart in Figure V.6.

© Ferdaous

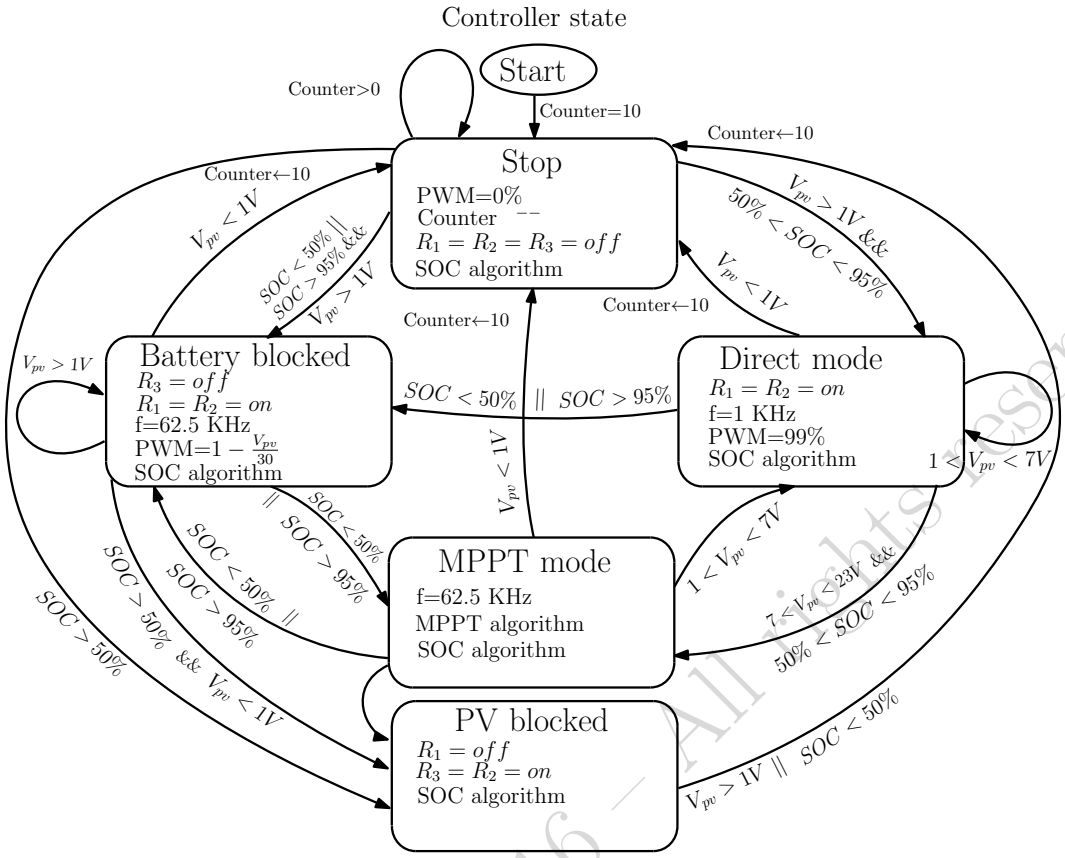


Figure V.6: Flowchart of the states and transitions of the charge-controller program state machine.

V.3 .1 Design and implementation of the printed circuit board

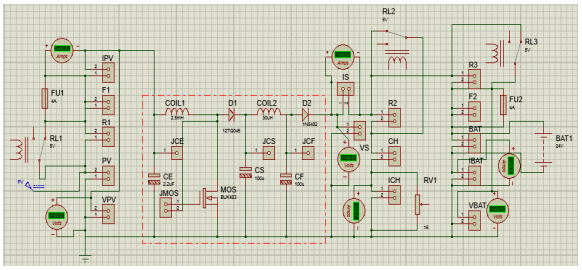
The development of the electronic board of the "Boost" power converter was first carried out by implementing the system using the schematic simulator of the "Proteus ISIS" software, as shown in Figure V.7.a. Then, Figure V.7.b shows the three-dimensional configuration developed for virtual visualization of the board design. Routing of the printed-circuit-board tracks was performed using the "Proteus ARES" software platform, which helps minimize the size of the assembly and optimize conductor lengths between components, as shown in Figure V.7.c. The artwork used to prepare the final double-sided printed circuit board is shown in Figure V.7.d, and the practical implementation of the circuit is shown in Figure V.7.e.

The voltage and current sensors, as well as the remotely controlled relays used in this work, are "surface-mounted" components. This advanced electronic-component technology requires rigorous equipment for printed-circuit-board manufacturing. Therefore, ready-made modules from the "*Seedstudio*" brand were adopted. The modules are integrated into the circuit as shown in Figure V.7.f.

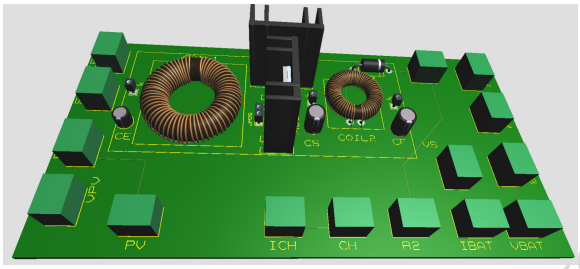
The complete printed circuit board contains the following components.

- "ACS714" Hall-effect current sensors.
- "ACS712" Hall-effect voltage sensors.

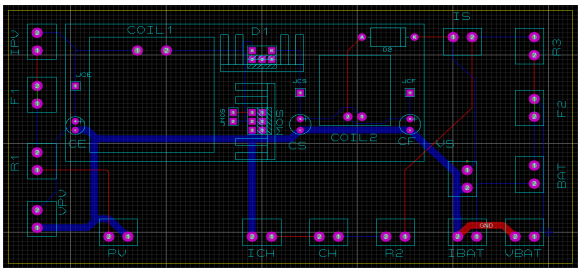
© Ferdaous Maamoudi, 2016 — All rights reserved



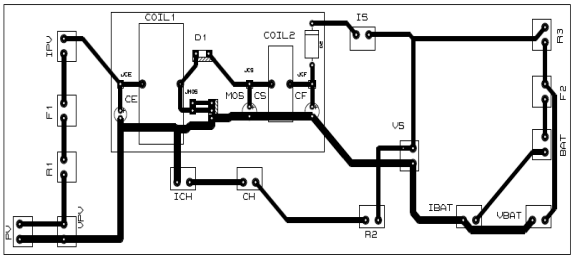
(a) Schematic circuit of the power board containing the Boost converter using Proteus ISIS.



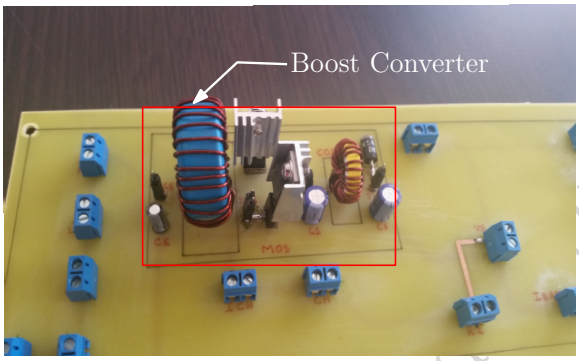
(b) 3D design of the Boost-converter electronic board.



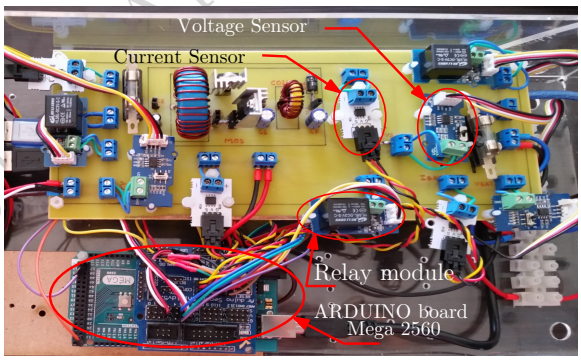
(c) Printed-circuit-board track routing using Proteus ARES.



(d) PCB artwork of the charge controller.



(e) Practical implementation of the printed circuit board.



(f) Assembly of the complete charge-controller system.

Figure V.7: Design and manufacturing stages of the charge-controller system.

- Remotely controlled relay modules.
- Ferrite-core radial inductor.
- Aluminum electrolytic capacitors.
- "MBRF10H100" Schottky diodes.
- "CSD18532KCS" logic-level MOSFET.

To minimize power losses in the inductors and power components, the following rules were adopted:

- Use of short conductors, especially between the controller and the gates of the MOSFET power switches.

© Ferdaous Masmoudi - All rights reserved

- Use of shielded or twisted conductors for the control circuits and minimal use of unshielded wires.
- Minimization of conductor lengths between the power components and the input and output capacitors (minimization of the switching-cell area).
- Use of heat sinks when mounting the power switches for efficient heat dissipation.

V.3 .2 Experimental tests

The developed charge-controller prototype was tested in the laboratory, as shown in Figure V.8. The following instruments were used:

- HMO1022 digital oscilloscope.
- 60 V, 3 A regulated power supply.
- 100-ohm, 5 A variable-resistance rheostat.
- Computer for programming the ARDUINO control board through a dedicated SDK, and then acquiring the traces of the implemented MPPT algorithm.

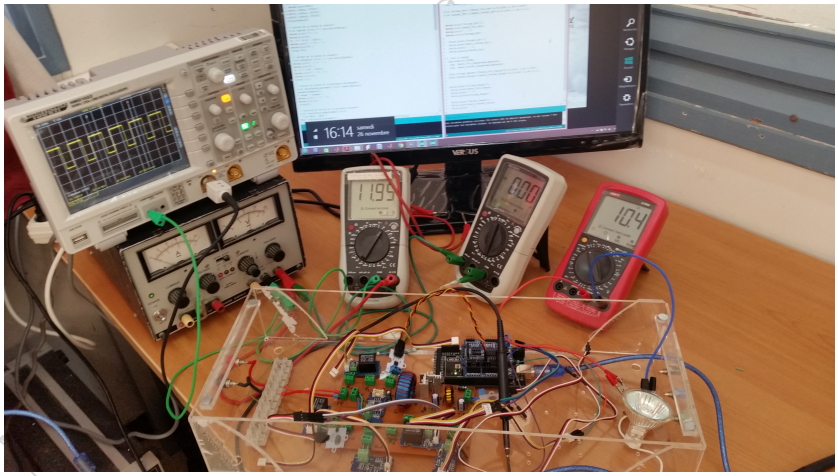


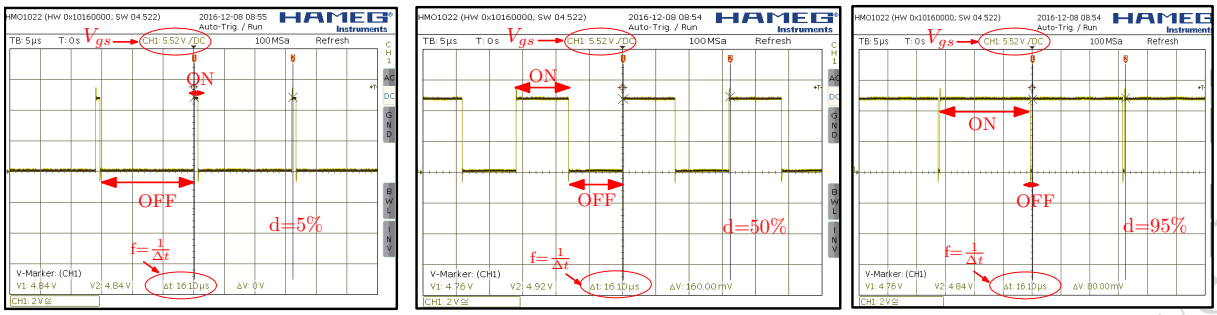
Figure V.8: Test of the charge-control system.

PWM signals for controlling the MOSFET gate are generated through the PWM analog output ports of the ARDUINO board using the "analogWrite(port,d)" function. Figure V.9 shows the oscilloscope display of the V_{gs} PWM gate-control signals and the MOSFET switching frequency.

The first start-up of the system, using a DC voltage source generated by a regulated power supply, made it possible to observe the switching of the voltage V_{ds} across the MOSFET, as shown in Figure V.10.a. The output voltage V_s is stepped up by the Boost converter from 15 V to 26 V for a duty cycle of 60%, as shown in Figure V.10.b.

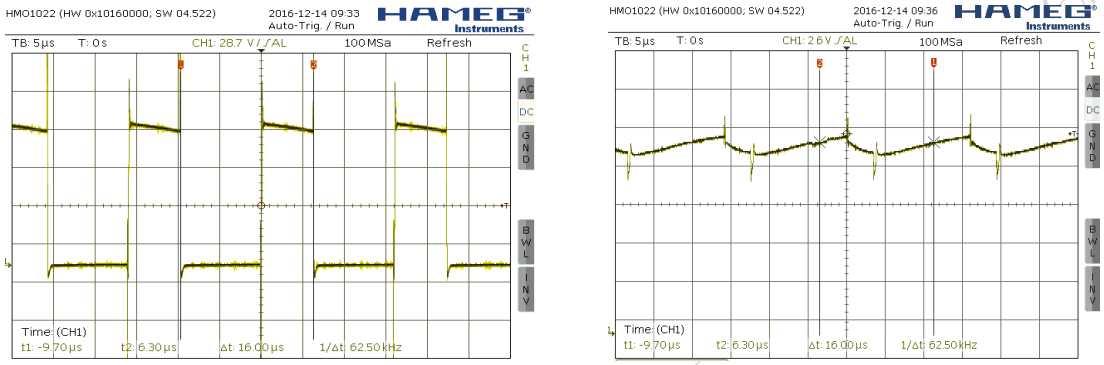
Starting the system using the 50 W photovoltaic generator made it possible to observe the electrical signals V_{gs}, V_{pv}, V_{ds}, and V_s presented in Figure V.11, using a 16 Ω resistive load.

© Ferdaous [illegible] — All rights reserved



(a) (b) (c)

Figure V.9: Frequency and duty cycle of the MOSFET PWM control.

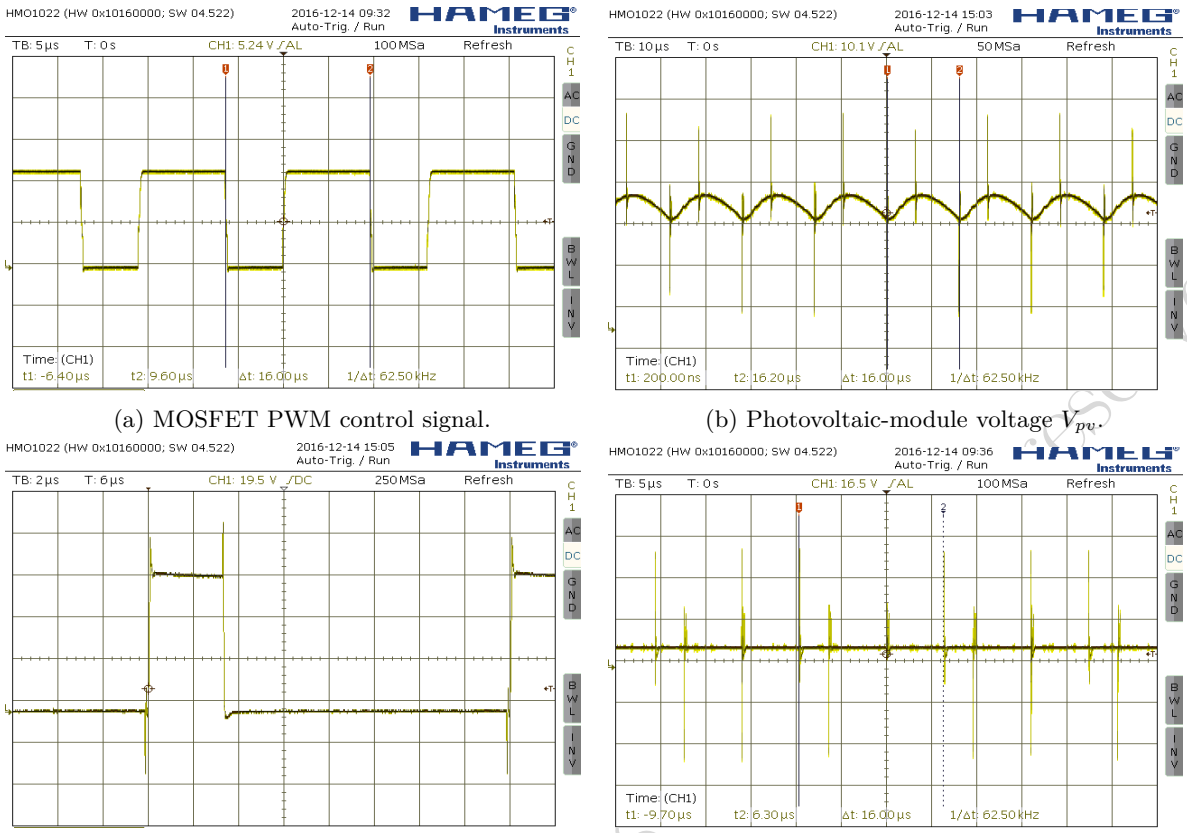


(a) MOSFET drain-to-source voltage V_{ds}. (b) Output voltage across the load V_s.

Figure V.10: Oscilloscope display of the experimental test of the Boost converter with a 15 V voltage source.

The observed voltage waveforms show a strong similarity with the simulation results. This similarity is particularly evident in the oscillatory nature of the module voltage V_{pv} and the switching of the MOSFET voltage V_{ds}. The duty cycle is approximately 63%. The voltage values are lower than the simulated voltages. This difference is explained by the presence of greater losses in practice than in simulation.

© Ferdaous Mamouni, 2016 – All rights reserved



(a) MOSFET PWM control signal.

(b) Photovoltaic-module voltage V_{pv}.

(c) MOSFET drain-to-source voltage V_{ds}.

(d) Output voltage across the load V_s.

Figure V.11: Oscilloscope display of the experimental test of the Boost converter with the PV module.

V.4 Conclusion

The work carried out in this chapter presented the experimental implementation and hardware realization of the optimized photovoltaic system.

The results obtained through this work are very encouraging. The designed system was tested for one week and demonstrated its robustness, efficiency, and autonomy, particularly with respect to remote data transmission and reception. Nevertheless, the system requires a longer testing period in order to guarantee the desired quality and overcome external constraints (wind, dust, rain).

The developed prototype made it possible to collect a database of experimental measurements. The results obtained confirm part of the expected simulation results. Thus, the theoretical studies could be validated by practical results. The real implementation of the system made it possible to highlight new technical problems affecting the endurance and reliability of the system, particularly the problem of sensor calibration.

© Ferdaous Masmoudi, 2016

General Conclusion

This conclusion aims to summarize the work carried out throughout this thesis, with emphasis on the main results obtained during the synthesis and optimization of the photovoltaic conversion chain. It concludes by presenting some possible perspectives for further development of the completed research.

1 Summary of the Work

In this thesis work, which was carried out within the framework of the project on autonomous photovoltaic power supply for an embedded system (a mobile robot as an example), the objective was to build a prototype of an optimized photovoltaic conversion system capable of providing the maximum energy available from the photovoltaic module used.

This work was structured around three main research axes. First, work on the modeling of the photovoltaic solar cell and its associations leading to the formation of the PV module was presented. Then, the optimization of the PV module efficiency through the tracking of incident solar radiation and the development of a prototype of a two-axis motorized solar tracker was addressed. Finally, work was developed on the optimization of the power conversion and electrical-energy storage system, leading to the implementation of a charge-controller prototype based on the Boost converter topology.

The theoretical modeling and simulation work occupied a large part of the project and contributed to mastering the electrical energy produced by photovoltaic technology. The flow of PV solar energy was studied in detail, while using methods for production optimization, from the elementary unit (the solar cell) to energy storage in accumulator batteries. The entire PV conversion chain was modeled, starting from the solar-cell model associated to form a solar module, followed by the solar-trajectory tracking system, up to the power-conversion system equipped with MPPT control. The effects of shading and mismatch in associated solar cells on the PV-module efficiency were also simulated. The importance of theoretical studies highlighted through modeling and simulation work was emphasized. Indeed, this work made it possible to understand and master the physical phenomena occurring in reality, and also to estimate and predict the evolution of the electrical quantities of the PV system over time and under various changes in operating conditions.

The knowledge theoretically developed through in-depth research was experimentally implemented through the fabrication of a real prototype of the complete autonomous PV power-supply

© Ferdaous Machmoudi, 2016 - All rights reserved

system dedicated to embedded systems. The experimental results obtained from this prototype contributed to the validation of part of the theoretical approaches investigated. However, the implemented system requires more testing time and improvements, particularly at the level of the data-acquisition and filtering system.

In summary, this work succeeded in giving rise to a practical study platform that can be used in the future to validate possible work on the control and optimization of PV conversion chains. Moreover, the system is ready to be integrated into the mobile-robot platform, thus allowing it to benefit from clean energy while ensuring its autonomy in terms of electrical-energy production and consumption.

2 Main Results

In the second chapter, five different electrical models of the photovoltaic solar cell applied to monocrystalline-silicon technology were studied. Iterative methods were developed to determine the internal parameters of each model as functions of the variations in temperature T and irradiance G. Comparison among the studied models made it possible to conclude that the one-diode equivalent electrical model is the most accurate and the most suitable for a typical monocrystalline solar cell.

The third chapter was devoted to exploiting the solar-cell model to represent series and parallel associations of a set of cells, thereby making it possible to form a PV module. For this model, the various problems imposed by cell interconnection were considered, and the effect of partial shading on the total power generated at the PV-module output was integrated. The PV-module model was used together with the *SOLPOS* algorithm for the simulation and estimation of the power gain obtained when using a solar tracker. In this study, the importance of the dual-axis solar tracker for maximizing the energy produced by the solar module was demonstrated, and a closed-loop algorithm was developed for managing the movements of the solar tracker, making it possible to detect the effect of partial shading and avoid it through appropriate orientation.

During the fourth chapter, the design of the power-conversion stage required to transfer energy to the load was discussed. In this work, a method for sizing the chopper-type converter around the maximum power point MPP was proposed. This method makes it possible to optimize the efficiency of the conversion stage while ensuring continuous-conduction mode and the quality of the output electrical quantities for any operating condition. In this work, six chopper topologies were studied, and it was shown that the Boost topology has the best efficiency factor for low-power applications. A basic P&O-type MPPT control strategy integrated into a Boost converter was considered, and the effectiveness of such control in maximizing the electrical energy produced by the solar module was demonstrated.

Finally, in the fifth chapter, the implemented prototype of the PV power-supply system was presented together with some experimentally obtained results.

© Fernando Mastronardi, 2016 – All rights reserved

3 Perspectives

The perspectives of this work are numerous and diverse, since the problem addressed in this thesis brings together several contexts related to the use of solar equipment.

The attempts made in the second chapter to contribute to improving the equivalent electrical model of the photovoltaic solar cell were validated for only one type of solar technology (monocrystalline cell). It is therefore intended to continue these investigations for other more cost-effective and more advanced technologies (Figure I.2). In addition, the developed models can be improved to take into account the spectral quality of the incident light, and it is also intended to develop a thermal model relating the junction temperature to the amount of light received at the cell surface.

In this work, some problems related to solar-cell interconnection were discussed. Further investigation in this direction is therefore envisaged by studying the effect of mismatch on cell aging, and diagnostic work on photovoltaic junctions is also intended.

In future work, it is intended to study the association of several solar modules and to continue investigations on partial shading of PV modules and on methods for shadow detection and recognition. In addition, it is intended to study other important phenomena affecting the efficiency of PV systems, such as the effects of wind, humidity, and reflected radiation.

Through the work carried out for the design of the power converter, it is proposed to develop other conversion topologies with higher efficiencies, making it possible to maximize the profitability of the system. In addition, other, more advanced types of MPPT control are intended to be investigated in order to avoid the overshoots observed when using the basic P&O algorithm and to implement them in more robust microcontrollers.

Finally, it should be noted that the development of other versions of the system prototype is envisaged in order to correct the existing mechanical and electrical faults and to provide the tools required to guarantee system robustness in the presence of various sources of disturbance and accidental faults.

© Ferdaous Masmoudi, 2016 - All rights reserved

Abstract

This thesis deals with the modeling and maximum power extraction (MPE) control of a photovoltaic generator. The first chapter is devoted to the modeling of a photovoltaic module (PVM) and to the synthesis of an equivalent electrical model of the PVM. We then address the association of the PVM with different types of DC–DC converters for supplying a storage battery, with the study focusing on the influence of the duty cycle on the behavior of such an association. We conclude our work with the synthesis and analysis of MPE control strategies; the analysis is based on a comparative study of the performance of the synthesized strategies.

The work proposed in this thesis focused on three main areas. The first part is centered on the photovoltaic generator, mathematical models of photovoltaic panels, and the arrays developed and built for testing MPPT algorithms and for diagnostic purposes, as described in Chapter 1. The second part is devoted to the study of the Balance of System (BOS) in order to maximize the energy efficiency of photovoltaic generators, Chapter 2. The third part brings together the experimental work carried out in this thesis and detailed in Chapter 3.

In Chapter 1, an overview of photovoltaic cells, their definitions, history, different technologies, and their most common current application fields is provided. An overview of the existing mathematical models used to describe the electrical behavior of photovoltaic panels is then given, followed by the determination of the parameters of the five-parameter single-exponential model established from datasheet values and used for the implementation of a PV simulator that takes into account the shape, size, and intensity of partial shading with respect to the bypass diodes. In order to eliminate iterative calculations for determining the parameters, a simplified three-parameter model is used, dedicated to diagnostic functions for photovoltaic panels. Simple analytical expressions for models of important parameters, which could reflect deviations from the normal I–V characteristic (for example, from the datasheet or a reference measurement), are proposed.

A considerable part of this thesis is devoted to diagnostic functions for crystalline photovoltaic panels, aimed at detecting failures related to increased series resistance and partial observation, the two main factors responsible for the reduction in the efficiency of residential photovoltaic systems. By combining model calculations with measurements, a method for detecting changes in the series resistance of panels based on the slope of the I–V curve near open-circuit conditions and scaled to Standard Test Conditions (STC) is proposed. The results

© Ferdaous Mamroudi, 2016 — All rights reserved

confirm the advantages of the proposed method in terms of robustness to irradiance changes and partial shading.

In order to detect partial shading on photovoltaic panels, a method based on monitoring the equivalent thermal voltage (V_t) is proposed. V_t is calculated using the simplified three-parameter model based on the experimental curve. The main advantages of the method are the simple expression for V_t, high sensitivity even to a relatively small partially shaded area, and very good robustness against variations in series resistance.

Finally, in order to quantify power losses due to different failures, for example partial shading or increased series resistance, a model-based approach is proposed to estimate the rated power of the panel under STC. Although it is known that the single-exponential model has low approximation accuracy under low-irradiance conditions, with the previously determined parameters it was possible to obtain relatively good accuracy. The main advantage of the method is that it relies on already determined parameters (LRM, V_t) based on measurements, thereby reducing the errors introduced by the limitations of the single-exponential model, particularly under low-irradiance conditions.

© Ferdaous Masmoudi, 2016 – All rights reserved

Bibliography

[1] International Energy Agency. IEA, "Technology Roadmap, Solar Photovoltaic Energy", OECD-IEA, 2014 edition.

[2] International Energy Agency. IEA, "World Energy Outlook 2013, Global Energy Trends", Renewable Energy Outlook, OECD-IEA, 2013.

[3] International Energy Agency. IEA, "Trends 2015 in Photovoltaic Applications", Survey Report of Selected IEA Countries between 1992 and 2014, Report IEA-PVPS, T1. 27, 2015.

[4] U.S. Department of Energy's National Renewable Energy Laboratory (NREL), "2014 Renewable Energy Data Book", Office of Energy Efficiency and Renewable Energy, DOE-GO. 102015. 4724, November 2015.

[5] Agence Nationale de Maîtrise de l'Energie. ANME, Deutsche Gesellschaft für Internationale Zusammenarbeit. GIZ, DZ, "Énergie renouvelable et efficacité énergétique en Tunisie: emploi, qualification et effets économiques", Tunis, décembre 2012.

[6] M.E. Becquerel. "La lumière ses causes et ses effets", Academie des sciences de l'institut de France, Paris, 1867. Edition: London: Forgotten Books, 2013.

[7] K. Mertens, "Photovoltaics fundamentals, technology and practice", First edition, John Wil ey & Sons Ltd, 2014.

[8] T. Markvart and L. Castafier "Solar Cells: Materials, Manufacture and Operation", ELSEVIER Ltd, 2006.

[9] P. Y. Yu and M. Cardona, "Fundamentals of semi-conductors physics and materials properties", Fourth Edition, Springer-Verlag, Berlin Heidelberg, 2010.

[10] S. M. Sze and K. K. Ng, "Physics of Semiconductor Devices", John Wil ey & Sons Ltd, 2007.

[11] H. Mathiru. "Physique des semi-conducteurs et des composants électroniques", Edition : Masson, pp. 464-475, 2012.

© Ferdaous Mamouni, 2016 – All rights reserved

[12] T. Markvart and L. Castafier, “Practical handbook of Photovoltaics fundamentals, technology and practice”, Elsevier Ltd, 2003.

[13] K. Jager, O. Isabella, A. H.M. Smets, R. A.C.M.M. van Swaaij and M. Zeman, “Solar Energy Fundamentals, Technology, and Systems”, Delft University of Technology, 2014.

[14] V.Lemaur, M. Steel, D. Beljonne, J. L. Brédas, and J. Cornil, “Photoinduced Charge Generation and Recombination Dynamics in Model Donor/Acceptor Pairs for Organic Solar Cell Applications:A Full Quantum-Chemical Treatment”, Georgia Institute of Technology, Journal of the American Chemical Society, April 2005, Vol. 127 , pp. 6077-6086.

[15] J.G. Fossum, D.S. Lee. “A physical model for the dependence of carrier lifetime on doping density in nondegenerate silicon”.J. Elsevier, Solid-State Electronics, Vol. 25, pp. 741-747, 1982.

[16] A. D. Jones and C. P. Underwood, “A Thermal Model for Photovoltaic Systems”, School of the Built Environment, University of Northumbria, Elsevier, Solar Energy, Vol. 70, Issue 4, pp. 349-359, 2001.

[17] Z.H. Lu, Q. Yao. “Energy analysis of silicon solar cell modules based on an optical model for arbitrary layers”, Elsevier, Solar Energy, Vol. 81, Issue 5, May 2007, pp. 636-647.

[18] Vun Jack Chin, Zainal Salam, Kashif Ishaque. “Cell modelling and model parameters estimation techniques for photovoltaic simulator application: A review”. J.Applied Energy, Vol. 154, pp. 500-519,2015.

[19] D.T.Cotfas, P.A.Cotfas, S.Kaplanis. “Methods to determine the dc parameters of solar cells: A critical review”. J.Renewable and Sustainable Energy Reviews, Vol. 28, pp. 588-596, 2013.

[20] V.Jack Chin, Z. Salam and K. Ishaque, “Cell modelling and model parameters estimation techniques for photovoltaic simulator application: A review”, Applied Energy, Vol. 154, pp. 500-519, 29 May 2015.

[21] J. Appelbaum n and A.Peled, “Parameters extraction of solar cells - A comparative examination of three methods”, Solar Energy Materials & Solar Cells, Vol. 122, pp. 164-173, 28 December 2013.

[22] A. M. Humada, M. Hojabri and S. Mekhilef, “Solar cell parameters extraction based on single and double-diode models: A review”, Renewable and Sustainable Energy Reviews, April 2016.

© Ferdaous Masmoudi, 2016 _ All rights reserved

[23] Basil Jacob et al. “Solar PV modelling and Parameter Extraction using Artificial Immune system”, ELSEVIER, The 7th International Conference on Applied Energy, ICAE 2015, Energy Procedia, Vol. 75, pp. 331-336, 2015.

[24] M. G. Villalva, J. R. Gazoli, E. Ruppert.“Modeling and circuit-based simulation of photovoltaic arrays”. Brazilian Journal of Power Electronics, Vol. 14, No. 1, pp. 35-45, 2009.

[25] W. Xiao, W. G. Dunford, A. Capel, “A novel modeling method for photovoltaic cells”, 35th Annual IEEE Power Electronics Specialists Conference, Germany, 2004.

[26] K. L. Kennerud. “Analysis of performance degradation in CdS solar cells”. IEEE Transactions on Aerospace and Electronic Systems, Vol. Aes-5, No. 6, November 1969.

[27] J. C. H. Phang, D. S. H. Chan, J. R. Phillips, “Accurate analytical method for the extraction of solar cell model parameters”, Electronics Letters, Vol. 20, No. 10, 10th May 1984.

[28] S. H. Chan, C. H. Jacob, “Analytical methods for the extraction of solar-cell single and double diode model parameters from I-V Characteristics”, IEEE Transactions on Electron Devices, Vol. 34, No. 2, February 1987.

[29] J. A. Gow, C. D. Manning, “Development of a photovoltaic model for use in power-electronics simulation studies”, IEE Proc-Electr. Power Appl, Vol. 146, No. 2, Mars 1999.

[30] J. Jun Soon and K. Soon Low, “Optimizing Photovoltaic Model for Different Cell Technologies Using a Generalized Multidimension Diode Model”, IEEE trans. on industrial electronics, Vol. 62, October 2015.

[31] V. Khanna, B.K. Das, D. Bisht and P.K. Singh,“A three diode model for industrial solar cells and estimation of solar cell parameters using PSO algorithm”, Renewable Energy, Vol. 78, pp. 105-113, 17 January 2015.

[32] S. Li Sheng,“The Theoretical and Experimental Study of the Temperature and Dopant Density Dependence of Hole Mobility, Effective Mass, and Resistivity in Boron-Doped Siliconèè, NBS special publication, pp. 400-47, 2015.

[33] S. S. Li, “Semiconductor Measurement Technology: The Dopant Density and Temperature Dependence of Electron Mobility and Resistivity in N-Type Silicon”, Nbs special publication, pp. 400-33, March 1977.

© Ferdaous Mosmoudi, 2016 _ All rights reserved

[34] S. S. Li, "Semiconductor Measurement Technology: The Relationship Between Resistivity and Dopant Density for Phosphorus and Boron Doped Silicon", Nbs special publication, pp. 400-64, May 1981.

[35] P. Y. Yu and M. Cardona, "Fundamentals of semi-conductors physics and materials properties", Fourth Edition, Springer-Verlag, Berlin Heidelberg, 2010.

[36] J. Bai, S. Liu, Y. Hao, Z. Zhang, M. Jiang and Y. Zhang, "Development of a new compound method to extract the five parameters of PV modules", Energy Conversion and Management, Vol. 79, pp. 294-303, 8 January 2014.

[37] G. Ciulla, V. Lo Brano,V. Di Dio and G. Cipriani, "A comparison of different one-diode models for the representation of I-V characteristic of a PV cell", Renewable and Sustainable Energy Reviews, Vol. 32, pp. 684-696, 8 February 2014.

[38] J. Bikaneria, S. Prakash Joshi and A. R. Joshi, "Modeling and Simulation of PV Cell using One-Diode model", International Journal of Scientific and Research Publications, Vol. 3, 2013.

[39] D. Bonkoungou, Z. Koalaga and D. Njomo, "Modelling and Simulation of photovoltaic module considering single-diode equivalent circuit model in MATLAB", International Journal of Emerging Technology and Advanced Engineering, Vol. 3, 2013.

[40] T. Ma, H. Yang and L. Lu, "Development of a model to simulate the performance characteristics of crystalline silicon photovoltaic modules/strings/arrays", Solar Energy, Vol. 100, pp. 31-41, 20 December 2013.

[41] S. Lineykin, M. Averbukh, A. Kuperman, "An improved approach to extract the single-diode equivalent circuit parameters of a photovoltaic cell/panel", Renewable and Sustainable Energy Reviews, Vol. 30, pp. 282-289, 8 November 2013.

[42] Y. Shi-Guang, Z. Wan-Hui, A. Bin, S. Jing-Wei and S. Hui, "Analysis of each branch current of serial solar cells by using an equivalent circuit model", Chin. Phys. B, Vol. 23, 20 December 2013.

[43] Y. Li, W. Huang, H. Huang, C. Hewitt, Y. Chen, G. Fang and D. L. Carroll, "Evaluation of methods to extract parameters from current-voltage characteristics of solar cells", Solar Energy, Vol. 90, pp. 51-57, 4 February 2013.

[44] L. Peng, Y. Sun, Z. Meng, Y. Wang and Y. Xu, "A new method for determining the characteristics of solar cells", Journal of Power Sources, Vol. 227, pp. 131-136, 27 July 2012.

© Ferdaous M'asmoudi, 2016 – All rights reserved

[45] D. Sera, "Series resistance monitoring for photovoltaic modules in the vicinity of MPP", Aalborg University, Department of Energy Technology Pontoppidanstraede, Vol. 101, Denmark, 2009.

[46] P. Saha, S. Kumar, S. Kr. Nayak and H. Sekhar Sahu, "Parameter Estimation of Double Diode Photo-Voltaic Module", 1st Conference on Power, Dielectric and Energy Management at Nerist (ICPDEN), 2015.

[47] A. Marrekchi, S.Sallem, G. Marco Tina and M.B.A Kammoun, "A new five parameters estimation method for two-diode model of PV module", 6th International Renewable Energy Congress (IREC), 2015.

[48] M. Herman, M. Jankovec and M. Topič, "Optimal I-V Curve Scan Time of Solar Cells and Modules in Light of Irradiance Level", International Journal of Photoenergy, 25 October 2012.

[49] B. Alsayid, "Modeling and Simulation of Photovoltaic Cell/Module/Array with Two-Diode Model", International Journal of Computer Technology and Electronics Engineering (IJCTEE), Vol.1, 2012.

[50] G.H. Yordanov, O.M. Midtgård, and T.O. Saetre, "Two-diode model revisited : parameters extraction from semi-log plots of I-V data", 25th European Photovoltaic Solar Energy Conference and Exhibition, 5th World Conference on Photovoltaic Energy Conversion, Valencia, Spain, pp. 6-10 September 2010.

[51] W. Shockley. "The theory of p-n junctions in semiconductors and p-n junction transistors", Bell Systems Technical Journal, Vol. 28, pp. 435.

[52] B.G. Streetman and S. Banerjee, "Solid State Electronic Devices", 5th Edition, Prentice Hall (2000), Chapter 5.6.2, Recombination and generation in the transition region.

[53] H. Rezk and El-Sayed Hasaneen, "A new MATLAB/Simulink model of triple-junction solar cell and MPPT based on artificial neural networks for photovoltaic energy systems", Ain Shams Engineering Journal, Vol. 6, pp. 873-881, 20 April 2015.

[54] P. Kumar Pandey and K.S. Sandhu, "Multi Diode Modelling of PV Cell", NIT Kurukshetra, Haryana, India, 2014.

[55] K. Nishiokaa, N. Sakitanib, Y. Uraokab and T. Fuyukib, "Analysis of multicrystalline silicon solar cells by modified 3-diode equivalent circuit model taking leakage current through periphery into consideration", Solar Energy Materials & Solar Cells, Vol. 91, pp. 1222-1227, 7 May 2007.

© Ferdaous Masmoudi, 2016 – All rights reserved

[56] T. Markvart and L. Castafier, "Solar Cells: Materials, Manufacture and Operation", ELSEVIER Ltd, 2006.

[57] M. Gen and R. Cheng, "Genetic Algorithms and Engineering Optimization", John Wiley & Sons Inc, 2000.

[58] R.J.Kuo, Ferani E.Zulvia. "The gradient evolution algorithm: A new metaheuristic". J.Information Sciences, Vol. 316, pp. 246-265.

[59] M. Garcia, L. Marroyo, E. Lorenzo, "Soiling and other optical losses in solar-tracking PV plants in Navarra". John Wiley & Sons, 2010.

[60] Atronometrics Inc, "The effects of soiling on PV performance, A brief literature survey", DN. 880027, 2012.

[61] M. R. Maghani, & Al,"Power loss due to soiling on solar panel: A review". Elsevier, Renewable and Sustainable Energy Reviews, Vol. 59, pp. 1307-1316, 2016.

[62] M. Mani, R. Pillai, "Impact of dust on solar photovoltaic (PV) performance". Elsevier, Renewable and Sustainable Energy Reviews, Vol. 14, pp. 3124-3131, 2010.

[63] Sean White, "Solar Photovoltaic Basics: A Study Guide for the NABCEP Entry Level Exam", Routledge taylor & francis group, london and new york, 2015.

[64] A. Ryer,"The light measurement handbook", Second printing, The united states of America, ISBN 0-9658356-9-3, 1997.

[65] M. Drif, P.J. Perez, "A new estimation method of irradiance on a partially shaded PV generator in grid-connected photovoltaic systems", Elseier, Renewable Energy, Vol. 33, pp. 2048-2056, 2008.

[66] P.D. Santos, E.M. Vicente, E.R. Ribeiro, "Relationship between the shading position and the output power of a photovoltaic panel", IEEE, 2011.

[67] R. Ramaprabha, B.L. Mathur, "MATLAB based Modeling to study the influence of shading on series connected SPVA". IEEE-ICETET, 2009.

[68] H. Patel, V. Agarwal, "MATLAB based modeling to study the effects of partial shading on PV array characteristics", IEEE Transaction Energy Conversion, Vol. 23, No. 1, March 2008.

[69] J. Guerrero, Y. Munoz, F. Ibanez, A. Ospino, " Analysis of mismatch and shading effects in a photovoltaic array using different technologies". IOP conf.series: Materials Science and Engineering, Vol. 59, SN. 012007, 2014.

© Ferdaous Masmoudi, 2016 – All rights reserved

[70] H. Haberlin, “Photovoltaics system design and practice”, First edition, John Wil ey & Sons Ltd, 2012.

[71] S.A. Spanoche, J.D. Stewart, “Model based method for Partially shaded PV module Hot-Spot Suppression”, IEEE Journals of Photovoltaics, August 2012.

[72] Michalsky, J. J. “The Astronomical Almanac’s Algorithm for Approximate Solar Position(1950-2050)”. Solar Energy. Vol. 40, No. 3, pp. 227-235, USA, 1988.

[73] I. Reda, A. Andrea, “Solar Position Algorithm for solar radiation applications”, NREL, Technical Report, January 2008.

[74] N.A. Engerer, F.P. Mills, “Kpv: A Clear-Sky Index for photovoltaics”, Solar Energy, April 2014.

[75] C. Marty, R. Philipona, “The Clear-Sky Index to separate Clear-Sky from Cloudy-Sky situations in Climate Reasearch”, Geophisical Reasearch Letters, Vol. 27, No. 17, pp. 2649-2652, September 2000.

[76] G. Prinsloo, R. Dobson, “Solar Tracking...”, ISBN 978-0-620-61576-1, February 2016.

[77] Z. Jayoo, “Tracking Solar Concentrators, A low budget solution”, Springer Briefs In Energy, ISSN 2191-5539, 2013.

[78] L. Guo, J. Han, A.W. Otieno, “ Design and Simulation of a Sun Tracking Solar Power System”, 120th ASEE Annual Conference and Exposition, ATLANTA, June 2013.

[79] F.A. Salem, “Mechatronics Design of Solar Tracking System”, IJCET, June 2013.

[80] D. Rekioua and E. Matagne, “Optimization of Photovoltaic Power Systems: Modelization, Simulation and Control”, Springer-Verlag London, ISBN 978-1-4471-2348-4 2012.

[81] R. Teodorescu, M. Liserre and P. Rodríguez, “Grid converters for photovoltaic and wind power systems”, First edition, John Wiley & Sons, Ltd. Publication, ISBN: 978-0-470-05751-3, 2011.

[82] “A guide to Photovoltaics (pv) system design and installation”, Endecon Engineering with Regional Economic Research, June 2001.

[83] N. Femia, G. Petrone, G. Spagnuolo and M. Vitelli, “Power Electronics and Control Techniques for Maximum Energy Harvesting in Photovoltaic Systems”, CRC press, Taylor & Francis Group, LLC, 2013.

© Ferdaous Mahmoudi, 2016 – All rights reserved

[84] F. jackson, “Stand-Alone Solar Electric Systems”, Earthscan, 2010.

[85] P. Gevorkian, “Solar power in building design”, The McGraw-Hill Companies, Inc., 2008.

[86] S. White, “Solar Photovoltaic Basics: A Study Guide for the NABCEP Entry Level Exam”, Routledge taylor & francis group, London and New York, 2015.

[87] C. Doyle, A. Truitt, D. Inda, R. Lawrence, R. Lockhart and M. Golden, “Best Practices in PV System Installation” Version 1, NREL: national Renewable Energy laboratory, March 2015.

[88] Washington states university extension energy program, “Solar Electric System Design, Operation and Installation”, NREL: national Renewable Energy laboratory ,October 2009.

[89] Sandia National laboratories, “Stand-alone photovoltaic systems a handbook of recommended design practices”, Photovoltaic Design Assistance Center, NEW MEXICO, March 1995.

[90] J. V. M. Caracas, L. F. M. Teixeira, G. C. Farias, L. A. S. Ribeiro, “Implementation of a High efficiency and low Cost Converter for a Photovoltaic Water Pumping System”, University of Maranhao Sao Luis, Brazil, 978 1 4577 1216, IEEE 2012.

[91] C. Ngai-Man Ho, H. Breuninger, S. Pettersson, G. Escobar, L. Augusto Serpa, and A. Coccia, “Practical Design and Implementation Procedure of an Interleaved Boost Converter Using SiC Diodes for PV Applications”, IEEE trans. on industrial electronics, Vol.62, No. 6, June 2012.

[92] F. Nejabatkhah, S. Danyali, S. H. Hosseini, M. Sabahi and S. M. Niapour, “Modeling and Control of a New Thre Input DC/DC Boost Converter for Hybrid PV/FC/Battery Power System”, IEEE transactions on industrial electronics, Vol. 27, No. 5, MAY 2012.

[93] M. G. Villalva , E. R. Filho, “Buck converter with variable input voltage for photovoltaic application”, Universidade Estadual de Campinas (UNICAMP) Campinas. SP. Brasil, 2010.

[94] A. Fasih, “Modeling and Fault Diagnosis of Automotive Lead Acid Batteries”, The Engineering Honors Committee 119 Hitchcock Hall College of Engineering. The Ohio State University Columbus, OH 43210, April 2006.

[95] G. L. Plett, “Battery management systems Volume 1”. Artech House Publishers, Semptember 2015.

© Ferdaous Msmoudi, 2016 _ All rights reserved

[96] G. L. Plett, “Battery management systems Volume 2”. Artech House Publishers, Nouvember 2015.

[97] O.Tremblay, L.A. Dessaint, “A Generic Battery Model for the Dynamic Simulation of Hybrid Electric Vehicles”, IEEE, December 2009.

[98] Y. Riffonneau, S. Bacha, F. Barruel, and S.Ploix, “Optimal power flow management for grid connected PV systems with batteries”, IEEE Transactions on Sustainable Energy, Vol. 2, No. 3, pp. 309 320, 2011.

[99] Gregory L. Plett, “Extended Kalman filtering for battery management systems of LiPB-based HEV battery packs Part1”. State and parameter estimation, ELSEVIER Journal of Power Sources, Vol.134, pp. 277 292, 2004.

[100] L. Lasne, “Électronique de puissance: Cours, étude de cas et exercices corrigés”, 2ème édition, Dunod, Paris, ISBN 978 2 10 072135 1, 2015.

[101] S. Roberts, “DC/DC book of knowledge, Practical tips for the User”, RECOM Engineering GmbH & Co KG, Austria, 2015.

[102] F. L. Luo, H. Ye and M. Rashid, “Digital power electronics ans applications”, Elsevier academic press (USA), 2005.

[103] K. Billings and T. Morey, “Switch mode power supply handbook”, The McGraw-Hill Companies, 2011.

[104] R. W. Erickson and D. Maksimovic, “Fundamentals of Power Electronics”, Second Edition, Kluwer Academic/plenum Publishers, New York, 2001.

[105] D. W. Hart, “Power Electronics”, The McGraw-Hill Companies, Inc., 2011.

[106] R. D. Middlebrook and Slobodan Cuk, “A General Unified Approach to Modelling Switching-Converter Power Stages”, IEEE Power Electronics Specialists Conference, 1976 Record, pp. 18-34 (IEEE Publication 76 CH 1084 3 AES); also International Journal of Electronics, vol. 42, no. 6, pp. 521-550, June 1977.

[107] Solbodan M. cuk, “Modelling, analysis, and design of switching converters”, Doctorat of Philosophy, 29 november 1977.

[108] S. CUK, “General Topological properties of switching structures”, CH 1461 379 0000-010900.75, IEEE, California, 1979.

© Ferdaous Mosmoudi, 2016 – All rights reserved

[109] R. Erickson and D. Maksimovic, “High Efficiency DC-DC Converters for Battery-Operated Systems with Energy Management”, Department of Electrical and Computer Engineering, University of Colorado, Boulder 80309-0425.

[110] D. Sera, “Real time modeling, diagnostics and optimized MPPT for residential PV systems”, Institute of energy technology-Alborg university, Denmark, January 2009.

[111] M. Youjie, C. Deshu, Z. Xuesong and G. Runrui, “MPPT Control of photovoltaic system based on hybrid modeling and its simulation”, IEEE Sustainable Power Generation and supply Conf., pp.1–5, Avril 2009.

[112] N. Femia, G. Petrone, G. Spagnuolo and M. Vitelli, “A Technique for Improving P&O MPPT Performances of double-stage gird-connected photovoltaic systems”. IEEE Trans. on Industrial Electronics, 56(11), November 2009.

[113] F. Lui, S. Duan and Y. Kang, “A variable step size INC MPPT method for PV systems”. IEEE Trans. on Industrial Electronics, 55(7), Juillet 2008.

© Ferdaous Masmoudi, 2016 – All rights reserved

Tunisian Republic
Ministry of Higher Education,
Scientific Research
and Technology

University of Sfax
National Engineering School of Sfax

Doctoral School
Sciences and Technologies

DOCTORAL THESIS

Electrical Engineering
Order No.: 69 - 2016

Optimization of Stand-Alone Photovoltaic Systems

Ferdaous MASMOUDI

الخلاصة: تتناول هذه الأطروحة بالبحث و النقاش إشكاليات إستخلاص و تركيز أنظمة تحويل الطاقة الفوطوضوئية المستقلة بصورة مثلى. الغاية الاساسية من تطوير مثل هذه الأنظمة تكمن في توظيفها ضمن الأنظمة المدمجة كأنظمة الآليات الذكية و الانسان الآلي بطريقة تسمح بالإستفادة من الطاقة الكهربائية المتجددة مع إستعمال مصادر نظيفة و هادئة و مرنة في كنف الاستقلالية المطلقة لعملية التشغيل من حيث إنتاج و استهلاك الكهرباء.

Résumé : Les travaux menés dans cette thèse visent à exposer les problématiques de synthèse et d'optimisation des systèmes de conversion Photovoltaïque autonome. L'objectif principal du développement de tels systèmes consiste à les intégrer au sein des systèmes embarqués (Robots et systèmes intelligents) de manière à les permettre de se bénéficier de l'énergie électrique renouvelable tout en utilisant des sources propres, silencieuses et maniables, ceci en garantissant l'autonomie absolue de production et de la consommation de l'énergie électrique au cours du fonctionnement.

Abstract: The work carried out in this thesis aims to present the issues related to the synthesis and optimization of stand-alone photovoltaic conversion systems. The main objective of developing such systems is to integrate them into embedded systems (robots and intelligent systems) so as to enable them to benefit from renewable electrical energy while using clean, quiet, and manageable sources, thereby ensuring complete autonomy in the production and consumption of electrical energy during operation.

المفاتيح: نظام فوطوضوئي مستقل، تصميم، الطرق المثلى، خلية / وحدة شمسية، متعقب للشمس، محول طاقة متواصل، نظام تخزين، متتبع نقطة الطاقة القصوى.

Mots clés: Système Photovoltaïque autonome, modélisation, optimisation, cellule / module solaire, suiveur solaire, hacheur, système de stockage, charge, MPPT.

Key-words: Stand-alone photovoltaic system, modeling, optimization, solar cell/module, solar tracker, DC-DC chopper, storage system, load, MPPT.

© Ferda